Chapter 7: The Earth's energy budget, climate feedbacks, and climate sensitivity

Coordinating Lead Authors:
Piers Forster (UK), Trude Storelvmo (Norway)

Lead Authors:
Kyle Armour (USA), William Collins (UK), Jean-Louis Dufresne (France), David Frame (New Zealand), Daniel Lunt (UK), Thorsten Mauritsen (Sweden, Denmark), Matthew Palmer (UK), Masahiro Watanabe (Japan), Martin Wild (Switzerland), Hua Zhang (China)

Contributing Authors:
Kari Alterskjær (Norway), Govindasamy Bala (India), Nicolas Bellouin (UK), Sandrine Bony (France), Laurent Bopp (France), Natalie Burls (South Africa), Aaron Donohoe (USA), Mark Flanner (USA), Ryan Padron Flasher (Ecuador), Seiji Kato (USA), Chihiro Kodama (Japan), Zhanqing Li (China), Johannes Quaas (Germany), Anna Possner (Germany), Cristian Proistosescu (Romania), Thomas Richardson (UK), Daniel Rosenfeld (Israel), Bjørn Samset (Norway), Chris Smith (UK), Jessica Vial (France), Mark Zelinka (USA), Shuyun Zhao (China)

Chapter Scientists:
Kari Alterskjær (Norway), Chris Smith (UK)

Review Editors:
Robert Coleman (Australia), H Damon Matthews (Canada), Venkatachhalam Ramaswamy (USA)

Date of Draft:
29/04/2019

Note:
TSU compiled version

Table of Content

Executive Summary

Human activity has substantially perturbed Earth's energy budget [*very high confidence*]. Improved understanding of time-varying climate feedbacks since IPCC AR5 leads to an energy budget that is closed over 1971-2014 and consistent across observations, estimates of effective radiative forcing (ERF) and equilibrium climate sensitivity(ECS) [*high confidence*]. Observations, theory and model simulations demonstrate that total Earth system warming (i.e. total Earth system heat content change) has less variability than global surface temperature change and represents a more robust metric of the rate of global climate change on decadal and shorter timescales [*high confidence*]. [7.1, Box 7.2, 7.3.5, 7.4.3, 7.5.3]

The Earth system gained substantial energy over the period 1971-2014, with a best estimate of 297 ZJ, or 0.42 W m^{-2} expressed relative to Earth's surface area and period length [*very high confidence*]. Observations indicate that the Earth's energy imbalance was larger in the 2000s than in the 1990s [*high confidence*]. Ocean warming dominates the energy inventory change accounting for ~93% of the observed energy change for the period 1971-2014, and the upper ocean (0-700m) accounting for ~60% [*high confidence*]. There is also *medium confidence* that the upper ocean warmed from the 1870s to 1971. Longer observational records, improved and new independent methods to estimate ocean heat content change and consistent closure of the global sea level budget, all promote increased confidence relative to AR5. Heat will continue to accumulate in the Earth system over the 21st Century [*high confidence*] and there is *medium confidence* this will continue until 2300, even under strong mitigation. [7.1, Box 7.2, Chapter 9 Box 9.2]

Multidecadal dimming and brightening trends in surface solar radiation occurred at widespread locations which are not a local phenomenon nor a measurement artefact [*high confidence*]. There is *low confidence* in trend estimates of the other components of the Earth's surface energy budget. [7.2.1]

It is unequivocal that human activity has had a warming effect on the planet since 1750. Human-induced surface temperature rise for the period 1750-2017 is 1.1 °C [0.9 to 1.3 °C 5% to 95% range]. This warming is comprised of a greenhouse warming of 1.7 °C [1.3 to 2.3 °C 5% to 95% range] that has an increasing trend and an aerosol cooling of 0.6 °C [0.3 to 1.1 °C 5% to 95% range] that has remained relatively constant over the last 20 years. Changes in solar and volcanic activity are assessed to have had a negligible effect. [*high confidence*] [7.3.5]

Under greenhouse gas forcing, poleward atmospheric heat transport is expected to increase, compensating decreased mid-latitude poleward ocean heat transport and resulting in modest changes in total poleward heat transport. Since AR5 there is improved understanding of the causes of heat transport changes under climate change. Ocean heat transport changes arise from a reduction in the Atlantic Meridional Overturning Circulation, and from the transport by ocean currents of excess heat taken up at the surface. Atmospheric heat transport changes and associated circulations are responses to energetic demands set by radiative feedbacks and ocean heat uptake. [*high confidence*] [7.2.1, 7.2.2]

The effective radiative forcing (ERF) framework introduced in AR5 has become well established and it has been shown to provide a useful way of estimating temperature response and testing climate models. The ERF for a doubling of carbon dioxide since preindustrial is 4.0 ± 0.7 W m^{-2} [5% to 95% range]. Climate models' radiative transfer representation has improved since AR5, and they have ERFs that are generally within 20% of the assessed best estimate. [*high confidence*] [7.3.1, 7.3.2].

The total anthropogenic ERF over the industrial era (1750-2017) was 2.48 W m^{-2} [1.65 to 3.26 Wm^{-2} 5% to 95% range]. This is an 8% increase over AR5 estimates for 1750-2011. Changes in atmospheric concentrations of greenhouse gases since 2011 and upwards revisions of their forcing efficiencies has led to a 14% increase in their ERF. This is partly offset by a new assessment of total aerosol ERF that is 22% more negative compared to AR5. [*high confidence*]. [7.3.5]

Greenhouse gases contribute an ERF of 3.64 ± 0.42 Wm^{-2} [5% to 95% range] over the industrial era. An ERF of 3.22 ± 0.38 Wm^{-2} comes from the well-mixed greenhouse gases, with ozone changes

contributing the remainder. Carbon dioxide continues to contribute the largest part of this forcing [*high confidence*]. There has been a significant increase in the estimated shortwave forcing from methane [*high confidence*] somewhat countered by a negative rapid adjustment [*medium confidence*]. There is also a ~5% upwards revision due to inclusion of tropospheric adjustments for CO_2 [*medium confidence*]. [7.3.2]

Aerosols contribute an ERF of -1.1 W m^{-2} [-1.8 to -0.5 W m^{-2} 5% to 95% range] over the industrial era [*high confidence*] Aerosol-cloud interactions contribute most (~80%) to the magnitude of the total ERF, with the remainder due to aerosol-radiation interactions [*high confidence*]. There has been a 22% increase in the estimated magnitude but a marked reduction in the uncertainty of the total aerosol ERF relative to AR5, supported by a combination of increased process-understanding, progress in modelling and observational analyses and revised constraints from energy-balance considerations. Compared to AR5, there has been a ~100% upward revision to the magnitude of ERF due to aerosol-cloud interactions, and a ~50% downward revision of the magnitude of ERF due to aerosol-radiation interactions [*medium confidence*]. [7.3.3]

Understanding of cloud processes has improved since AR5, based on new observations, theory, and modelling. Combining all lines of evidence leads to an assessment that the net cloud feedback under future climate change is positive. Process understanding of tropical-marine low cloud feedbacks within GCMs has been complemented by emergent constraints on the cloud controlling factors and explicit simulations using cloud-system resolving models, altogether leading to strong evidence that the total cloud feedback amplifies global climate warming. It is also *very unlikely* that the feedback exceeds 1.1 W m^{-2} °C^{-1}. This major advance assesses a positive cloud feedback to be more likely and reduces the uncertainty range by 50% compared to AR5. [*high confidence*] [7.4.2, Figures 7.4. 3, Table 7.4.1]

Cloud feedbacks are the dominant source of uncertainty in this century's transient global warming under increasing or stable emission scenarios, **whereas uncertainty is dominated by aerosol ERF in strong mitigation scenarios**. Global ocean heat uptake is a relatively minor source of uncertainty in long-term warming. Carbon cycle feedbacks provide an increasing fraction of uncertainty on longer timescales. [*high confidence*] [7.6.1]

Radiative feedbacks will become more positive in the future as the spatial pattern of warming evolves, leading to an ECS that is substantially higher than that inferred from warming over the historical record [*high confidence*]. This new understanding reconciles previously disparate ECS estimates. Historical surface temperature change since 1900 has shown little warming in several key regions of positive feedbacks, including the eastern equatorial Pacific Ocean and the Southern Ocean, with greater warming in key regions of negative feedbacks, including the Western Pacific warm pool. Based on process understanding, climate modelling, and paleoclimate reconstructions, it is expected that future warming will become enhanced over the eastern Pacific Ocean [*medium confidence*] and Southern Ocean [*high confidence*] on centennial timescales. While there is robust agreement across climate model simulations that radiative feedbacks will become more positive in the future, there is currently insufficient evidence to assess whether the magnitude of those projected feedback change is realistic. [7.4.3, 7.5.3, Figures 7.22, 7.6.4]

Based on multiple lines of evidence the best estimate of ECS is 3 °C, the *likely* range is 2.5 to 4 °C and the *very likely* range is 2 to 5 °C. It is *virtually certain* that ECS is larger than 1.5 °C
Substantial advances since AR5 have been made in quantifying ECS inferred from feedback process understanding (including dependence on climate state), the instrumental record, paleoclimates (including accounting for long-term Earth system feedbacks) and emergent constraints. There is a high level of agreement among the different lines of evidence. It remains challenging to rule out low-probability but high-impact upper-end ECS, which is indicated by the notable asymmetry of the assessed ranges. [*high confidence*] [7.5.7]

Based on a process understanding, warming over the instrumental record, and emergent constraints, the best estimate of Transient Climate Response (TCR) is 1.7 °C**, the *likely* range is 1.4 to 2.0** °C **and the *very likely* range is 1.2 to 2.2 °C**. There is a high level of agreement among the different lines of evidence. [*high confidence*] [7.5.7]

It is now well understood that the Arctic warms more quickly than the Antarctic due to a combination of asymmetries in radiative feedbacks and ocean heat uptake between the poles. Since AR5, progress has been made to understand the mechanisms of polar amplification and its uncertainty. A variety of factors all contribute to Arctic amplification, making it a ubiquitous feature of climate model simulations and observations. The Antarctic warms more slowly than the Arctic owing primarily to upwelling in the Southern Ocean. [*high confidence*] [7.6.2, 7.6.3, 7.6.4]

There is *very high confidence* that eventual surface warming will be polar amplified in both hemispheres. Polar amplification is supported across multiple lines of evidence, including the paleoclimate proxy record and GCM simulations of past warm climates and the climate response to CO_2 forcing. GCMs also give *high confidence* that Antarctic amplification will emerge as the Southern Ocean surface warms on centennial timescales, although only *low confidence* of the feature emerging this century. [7.6.4].

CO_2 equivalent emissions aggregated across short and long-lived greenhouse gases using global warming potentials (GWPs) are ambiguous regarding their implications for surface warming. This leads to uncertainty in future warming from targets based on such equivalence, such as those arising from net zero greenhouse gas emissions targets, and most Nationally Determined Contributions. New metrics comparing pulse emissions of long-lived greenhouse gases with sustained emission changes in short-lived gases do lead to appropriate equivalences. Alternatively, emissions of short and long-lived greenhouse gases should be considered separately**.** Long-lived greenhouse gas emission metrics are larger compared to AR5, due to the methodological change of accounting for carbon-cycle responses becoming standard. [*high confidence*] [7.7.1, 7.7.2]

7.1 Introduction, conceptual framework and innovations since IPCC AR5

This chapter assesses the major physical processes that drive changes in the Earth's energy budget thereby affecting global warming. It focuses on documenting advances in scientific understanding of radiative forcing, climate feedbacks and climate sensitivity, and covers observations, theoretical developments and climate model evaluation. The chapter integrates elements that were dealt with separately in previous reports. Aggregate measures of climate response such as equilibrium climate sensitivity (ECS) and the *transient climate response* (TCR) are also assessed here (Box 7.1).

Climate change arises when the Earth's top of atmosphere energy budget is perturbed, and this energy imbalance determines whether the climate system, as a whole, cools or warms. The processes discussed here provide a link between observations (Chapter 2), modelling estimates of historic warming (Chapter 3), and global temperature projections (Chapter 4). They also quantify the relationship between anthropogenic emissions (Chapters 5 and 6) and climate system response. The chapter is primarily concerned with global measures of change, but also assesses regional changes in the energy budget and changes to atmospheric heating insofar as they support the assessments of the hydrological cycle (Chapter 8) and ocean circulation (Chapter 9). Thereby this chapter aids understanding of regional patterns of response (Chapters 10, 11,12 and the Atlas). This chapter builds on material assessed across all chapters of the AR5 WG1 assessment, but principally draws on the radiative forcing assessment within Chapters 7 (Boucher et al., 2013) and 8 (Myhre et al., 2013b), the assessment of feedbacks and model evaluation in Chapters 7 (Boucher et al., 2013) and 9 (Flato et al., 2013), the observed estimates of energy budget change in Chapters 2 (Hartmann et al., 2013) and 13 (Church et al., 2013), and the assessment of climate sensitivity within Chapter 12 (Collins et al., 2013a) of that report.

The *total earth system warming* introduced here is quantified by the total heat content change in the Earth system. It is a measure of global warming that provides a more robust indication of Earth's energy imbalance than globally averaged surface temperature (Von Schuckmann et al., 2016). Research since AR5 has improved scientific understanding of this measure, and its changes through time (Section 7.2). Improved understanding of rapid adjustments to radiative forcing and of aerosol-cloud interactions have led to substantial revision of forcing estimates (Section 7.3). New approaches to the quantification and treatment of feedbacks (Section 7.4) have improved the understanding of the nature and time-evolution of feedbacks so that climate sensitivity has become a more a transient property of the climate system which isn't immediately relatable to the ECS. This change has helped to reconcile disparate estimates of ECS from different lines of evidence (Section 7.5). Regional aspects of the energy budget help the understanding of model responses and their regional variation, informing the climate impacts assessed in WGII (Section 7.6). Finally, innovations in the use of emissions metrics have clarified the relationships between metric choice and policy goals, linking the Chapter to WGIII (Section 7.7).

In Box 7.1 an extended energy budget framework is introduced, which forms the basis for the discussions and scientific assessment in the remainder of this chapter and across the report. The framework reflects advances in the understanding of the Earth system response to climate forcing agents since the publication of the AR5. A schematic of this framework and the key changes relative to the science reported in AR5 is provided in Figure 7.1.

[START FIGURE 7.1 HERE]

Figure 7.1: A conceptual energy budget framework to describe the state-of-the-art understanding of Earth's energy budget, climate feedbacks and the policy implications. The new elements relative to IPCC AR5 are highlighted in red.

[END FIGURE 7.1 HERE]

The phrase "climate metrics" can carry a range of implications, depending on the context. This report distinguishes between "climate metrics" (e.g. ECS) and "emissions metrics" (such as the global warming potential) but this distinction is not clear cut. Climate metrics are generally used to summarise aspects of the overall climate system response (Box 7.1). Emissions metrics are generally used to summarise the relative effects of emissions of different forcing agents, usually greenhouse gases (see Section 7.7). Figure 7.2 shows how the various climate metrics and emission metrics assessed in this chapter fit within the overall chain of processes from human activities to climate impacts. The climate metrics used in this report typically evaluate how the Earth system response varies with atmospheric concentration or radiative forcing change. Whereas emission metrics evaluate how radiative forcing or climate is affected by the emissions of a certain amount of gas. Emission-related metrics are extensively employed in mitigation policy decisions such as trading greenhouse gas reduction measures to compare their effect on climate. Climate metrics are useful to gauge the range of future climate impacts for adaptation decisions under a given emission pathway. The TCR to emissions is used in both contexts: for gauging future surface temperature change under specific emission scenarios and to estimate remaining carbon budgets that are used to form mitigation policies (see Chapter 5, Section 5.5).

[START FIGURE 7.2 HERE]

Figure 7.2: A conceptual chain of processes linking human activity to climate impacts, showing where the climate indicators and emission metrics assessed in this chapter fit within the chain and how they associate with other Working Groups.

[END FIGURE 7.2 HERE]

[START BOX 7.1 HERE]

BOX 7.1: Forcing, feedbacks and sensitivity definitions

The forcing-feedback framework provides a methodology to assess the impact of individual drivers of global mean surface air temperature change, and to facilitate the understanding of the key phenomena that set the magnitude of this temperature change. The framework used here is developed from that adopted in previous IPCC reports. *Effective Radiative Forcing* (ERF), introduced in IPCC AR5 (Boucher et al., 2013; Myhre et al., 2013b) is more explicitly defined in this report and is employed as the central definition of radiative forcing. The framework has also been extended to allow variations in feedbacks over different timescales (Section 7.4.2.6; Section 7.4.3) and with climate state (Section 7.4.4).

The global mean surface temperature response to perturbations to the Earth energy budget can be summarized in the following equation, in which ΔN ($W\ m^{-2}$) represents the top of atmosphere (TOA) energy imbalance, ΔF ($W\ m^{-2}$) is an ***effective radiative forcing*** perturbation to the energy budget, α ($W\ m^{-2}\ {}^{\circ}C^{-1}$) is an aggregated ***feedback parameter*** and ΔT (°C) is the change in ***global mean near-surface air temperature***:

$$\Delta N = \Delta F + \alpha \Delta T \qquad \text{Box 7.1, Equation (7.1)}$$

The **ERF** (Section 7.3) ΔF quantifies the change in the net radiative budget of the Earth system due to some imposed perturbation (e.g. change in carbon dioxide concentration, change in solar incoming radiation). ERF is adopted as the standard definition for quantifying radiative forcing of the climate system. ERF is expressed as a change in net downward radiative flux at the TOA following the initial rapid adjustments in both tropospheric and stratospheric temperatures, water vapour, clouds, and some surface properties. These rapid adjustments affect the energy balance both at the TOA and at the surface. Accounting for such processes gives an estimate of radiative forcing that is more representative of the climate change response associated with forcing agents than previous definitions of radiative forcing (Allan et al., 2014b; Andrews et al., 2010; Sherwood et al., 2015). The timescale of rapid adjustments generally ranges from hours to a few days, and feedbacks generally refer to longer timescale processes. However, there is no clear separation of timescale of processes between rapid adjustments and feedbacks. Therefore, following Sherwood et al. (2015) this report defines rapid adjustments as energy budget changes that are not associated with surface temperature change and feedbacks as those that are. The effect of these rapid adjustments can be estimated/quantified from climate model simulations with sea-surface temperature and sea-ice set to their climatological values (Forster et al., 2013; Pincus et al., 2016). ERF can be quantified as the equilibrium TOA energy imbalance in these experiments, although the effects of any global surface temperature change from changes in land surface temperatures need to be removed or assumed to be small to match the definition of rapid adjustments (Smith et al., 2018b). The stratospheric-temperature-adjusted radiative forcing and the instantaneous radiative forcing (IRF) extensively used in earlier assessments remain useful to quantify components of ERF and are also used to approximate ERF for small forcing agents, where the forcing signal is often swamped by the climate model internal variability, making a reasonable assessment of ERF difficult.

The near-surface air temperature is a common model diagnostic used to infer global warming. Climate models have global coverage of this diagnostic which makes an estimate of their globally averaged surface warming straightforward, yet observations of temperature typically have incomplete coverage of the Earth's surface. Further, estimates of globally averaged trends from observations combine sea-surface temperature measurements over open ocean with near-surface air temperatures over land and sea-ice, effectively blending two types of measurements together (see Chapter 2, Section 2.3 for further details). Modelling studies since AR5 have identified stronger historical trends in global near-surface air temperature than in this blended measure. When accounting for both this blending effect and that of incomplete coverage, biases of up to 16% are seen in global warming estimates between models and common observation-based datasets such as HadCRUT4, such that models give stronger trends (Richardson et al., 2016, 2018a). These biases were partly responsible for the divergent estimates of climate sensitivity across different lines of evidence in AR5 (Collins et al., 2013a). In this assessment, potential biases are avoided by using a standard measure of surface change to compare global warming from models and observations. For compatibility with previous climate projections and most previous estimates of feedback and climate sensitivity, this report adopts the globally averaged near-surface air temperature measure when assessing globally averaged trends in surface warming, climate feedbacks and climate sensitivity (see Chapter 2, Section 2.3).

The ***feedback parameter*** α (Section 7.4) quantifies the sensitivity of the radiative flux at the TOA when the global mean near-surface air temperature changes. Many climate variables affect the radiative flux at the TOA, and the feedback parameter can be formally decomposed, at the first order, into a sum of terms $\alpha = \sum_x \alpha_x$, where x represents a climate variable, or more generally a variable of the Earth system, that has a direct impact on the flux at the TOA. When surface temperature increases, a fundamental response of the climate system is an increase of the emitted longwave radiation, which corresponds to the Planck response for which the temperature change is assumed vertically uniform in the atmosphere and equal to that at the surface. The other climate variables commonly used for the feedback decomposition are the water vapour concentration, the temperature lapse rate, the surface albedo and the clouds. Earth System Models (ESM) now also include biogeochemical feedbacks and some of them include processes relevant at very long term (millennia, e.g. ice sheet changes). The sum of the feedback terms is a measure of how the real Earth might respond to a change in atmospheric CO_2 concentration. All earth system feedbacks that do not alter the atmospheric CO_2 concentration should be included in the sum, such as vegetation response and changes to natural aerosol emissions. However, many model estimates exclude some of the biogeochemical feedbacks and should be regarded as incomplete estimates of the total feedback sum. A change in variable x amplifies the temperature change (positive feedback) when the associated feedback parameter α_x is positive, and damps the temperature change (negative feedback) when α_x is negative (Caldwell et al., 2016; Dufresne and Saint-Lu, 2016; Hansen et al., 1984; Sherwood et al., 2015). New research since AR5 emphasises how feedbacks can vary over different timescales (Section 7.4.2.6; Section 7.4.3) and with climate state (Section 7.4.4). Note there is no standardised notation or sign convention for feedbacks in the literature.

The ***ECS*** (Section 7.5, units: °C) is defined as the value of ΔT at equilibrium ($\Delta N = 0$) for a doubling of the CO_2 concentration relative to a pre-industrial reference state. As it is referenced to a CO_2 concentration change it does not include carbon concentration change-processes but is defined here to include all other Earth System processes that operate on ~150 year timescales (see the climate feedback definition above). Previous IPCC reports have quantified ECS according to the main physical processes (Planck response, water vapour feedbacks, lapse rate feedback, surface albedo feedbacks and cloud feedbacks), also known as the Charney sensitivity. These key physical processes are expected to dominate the response, but the definition used here now allows for other potential Earth system feedbacks such as atmospheric chemistry changes from changes in emissions from vegetation. As coupled atmosphere-ocean climate models are not typically run over a long enough period of time to reach a new equilibrium and internal variability on multiple timescales makes it difficult to define a true equilibrium state, the ECS is estimated hereinafter as half the value of the point where the linear slope of ΔN against ΔT over the first 150 years of an abrupt $4\times CO_2$ climate model simulation crosses the x axis at $\Delta N = 0$.

Evidence since AR5 increasingly shows how feedbacks vary with timescales and climate state (Section 7.5). This means the ECS as defined is less applicable as an aggregate measure of climate feedbacks outside of the 150-year CO_2 change considered in its definition. The *inferred climate sensitivity* is used as a measure equivalent to ECS for shorter, typically historic, periods (Section 7.5.3) and the *long-term Earth sensitivity*, an equivalent measure to ECS applicable to longer paleo-relevant timescales that include shifting vegetation patterns and potential ice-sheet change (Section 7.5.4). Care has to be taken when comparing climate sensitivity across different lines of evidence to translate them onto the ECS standard (Sections 7.5.3 and 7.5.5).

The **TCR** (Section 7.5, units: °C) is defined as the change in the global mean near surface air temperature, averaged over a 20-year period, centred at the time of atmospheric CO_2 doubling (year 70), in a climate model simulation in which CO_2 increases at 1% yr^{-1} from pre-industrial and compared to the same time period within a preindustrial control simulation. It is a measure of transient warming accounting for the strength of climate feedbacks and ocean heat uptake. The ***transient climate response to emissions*** (TCRE) is defined as the transient globally averaged near-surface air temperature change per 1000 Gt C of cumulative CO_2 emissions. TCRE combines both information on the airborne fraction of cumulative CO_2 emissions (the fraction of the total CO_2 emitted that remains in the atmosphere, which is determined by carbon cycle processes) and on the TCR. TCR is assessed in this chapter, whereas TCRE is assessed in Chapter 5, Section 5.5.

[END BOX 7.1 HERE]

7.2 Earth's energy budget and its changes through time

The Earth's energy budget encompasses the major energy flows of relevance for the climate system (Figure 7.3). All the energy that enters or leaves the system does so in the form of radiation at the TOA. The energy budget at the TOA is determined by the amount of incoming solar (shortwave) radiation and the outgoing radiation that is composed of reflected solar radiation and outgoing thermal (longwave) radiation emitted by the climate system. In an equilibrium climate, the outgoing and incoming radiative components are essentially in balance, although there are still fluctuations around this balanced state that arise through internal climate variability (Brown et al., 2014; Palmer and McNeall, 2014) . However, anthropogenic forcing has given rise to a persistent imbalance in the TOA radiation budget, known as Earth Energy Imbalance (Trenberth et al., 2014; Von Schuckmann et al., 2016). The Earth's energy Imbalance is the fundamental driver of the various aspects of observed climate change and a critical metric determining the present rate of global warming.

Earth's energy budget also constitutes the internal flows of energy within the climate system, which characterize the current climate state. Figure 7.3 (left) shows a schematic representation of Earth's energy budget including quantitative estimates of the magnitudes of its individual components averaged over the globe. A corresponding representation of the energy budget, but without consideration of clouds is given in Figure 7.3 (right), as a base state to enable an estimation of the effects of clouds on the energy flows in the climate system. The partitioning of the energy within the climate system plays a key role as driver of atmospheric and ocean dynamics, the global water cycle as well as a variety of surface processes. In the following sections, Earth's energy budget and the internal energy flows are assessed both in terms of the mean state, variability and long-term response under climate change.

[START FIGURE 7.3 HERE]

Figure 7.3: Schematic representation of the global mean energy budget of the Earth (left), and its equivalent without consideration of cloud effects (right). Numbers indicate best estimates for the magnitudes of the globally averaged energy balance components in W m-2 together with their uncertainty ranges in parentheses (95% confidence range), representing present day climate conditions at the beginning of the 21st century. Adapted from (Wild et al., 2015, 2019). [placeholder: change to 90% confidence range for SOD]

[END FIGURE 7.3 HERE]

7.2.1 Present-day energy budget

AR5 (Church et al., 2013; Hartmann et al., 2013; Myhre et al., 2013b) highlighted the progress in quantifying the TOA radiation budget following new satellite observations that became available in the early 21st Century (Clouds and the Earth's Radiant Energy System, CERES; Solar Radiation and Climate Experiment, SORCE). Progress in the quantification of the magnitude and changes in incoming solar radiation at the TOA since AR5 is discussed in Chapter 2, Section 2.2. Since AR5, the accuracy of the reflected solar and outgoing thermal fluxes at the TOA has been further enhanced with the release of the CERES Energy Balance EBAF Ed4.0 product, which includes algorithm improvements and consistent input datasets throughout the record (Loeb et al., 2018a). However, the overall accuracy of these fluxes (regional mean 1 sigma uncertainties of 2.5 W m^{-2} in the all sky fluxes) is not sufficient to monitor the Earth's energy imbalance in absolute terms. Therefore, one-time adjustments have been made to the solar and thermal TOA fluxes of the CERES EBAF dataset within their uncertainty ranges to ensure that the global mean net TOA flux for July 2005–June 2015 is consistent with an Earth's energy imbalance of 0.71 ± 0.10 W m^{-2} (5% to 95% confidence range) inferred from ocean heat content (OHC) measurements using 10 years of Argo measurements and energy uptake by the lithosphere, cryosphere and atmosphere (Johnson et al., 2016; Riser et al., 2016) (Section 7.2.2). Most climate models closely match the TOA radiative exchanges given by CERES-EBAF on a global mean basis, since they are typically tuned to these values, yet show significant discrepancies on regional scales, often related to their representation of clouds (Dolinar et al., 2015; Hwang and Frierson, 2013; Li et al., 2013b; Trenberth and Fasullo, 2010; Wild et al., 2015).

The surface energy budget is associated with substantially larger uncertainties than the TOA energy budget. The components of the surface energy budget cannot be directly measured by passive satellite sensors from space and require retrieval algorithms and ancillary data for their estimation which gives rise to additional uncertainties (Kato et al., 2018; Raschke et al., 2016). On a global mean basis, confidence in the quantification of the surface energy budget has increased, since independent recent estimates converge to within a few W m^{-2} for different surface radiation components (Wild, 2017). These estimates are based on complementary approaches which make use of satellite products from active and passive sensors (Kato et al., 2018; L'Ecuyer et al., 2015) as well as of the information contained in surface observations and climate models (Wild et al., 2015). Inconsistencies in global annual mean fluxes between available satellite-derived surface energy data products and precipitation estimates noted in AR5 (Hartmann et al., 2013) remain, but it has become possible to reconcile the apparent discrepancies between the magnitudes of the global energy and water budgets within the uncertainty ranges of their components (L'Ecuyer et al., 2015; Wild et al., 2013, 2015). On regional scales, the closure of the surface energy budgets remains a challenge with currently available satellite-derived datasets (Kato et al., 2016; L'Ecuyer et al., 2015; Loeb et al., 2014). Annual and seasonal energy budgets for seven continents and nine ocean basins for the period 2000 to 2009 have been estimated by L'Ecuyer et al. (2015) making use of a variety of satellite-derived products. To reintroduce energy and water cycle closure information lost in the development of these independently derived products, the authors developed a variational method that explicitly accounts for the relative accuracies in all component fluxes. A quantification of the energy budget over land and oceans taking into account the information contained in direct observations from both surface and space is given in (Wild et al., 2015) .

Since AR5, quantification of the uncertainties inherent in the different surface energy flux datasets has improved. Uncertainties in global monthly mean downward solar and thermal fluxes in the CERES-EBAF surface dataset are, respectively, 10 W m^{-2} and 8 W m^{-2} (converted to 5% to 95% confidence level) (Kato et al., 2018). When these satellite-based surface solar and thermal fluxes are compared with surface observations, the difference between satellite-based and observed fluxes averaged at 36 Baseline Surface Radiation Network (Ohmura et al., 1998) sites and 46 moored buoys is nearly equivalent to the uncertainty of surface observations of approximately 5 W m^{-2} for both solar (Colbo and Weller, 2009; Michalsky et al., 1999, 2003) and thermal (Groebner et al., 2014) downward fluxes. The uncertainties in latent and sensible heat fluxes averaged over global oceans are approximately 14 W m^{-2} and 6 W m^{-2} (converted to 95% confidence level) (L'Ecuyer et al., 2015), respectively, which correspond to about 8% and 11% of their respective global mean values and are consistent with the uncertainty in daily mean latent and sensible heat fluxes measured at a buoy observatory (Kubota et al., 2008). A recent review of the latent and sensible heat flux accuracies highlights significant differences between several products, while differences between mooring data and a multi-product ensemble reached up to 25 W m^{-2} for latent heat and 5 W m^{-2} for sensible heat (Bentamy et al., 2017). The uncertainty stems from the retrieval of flux-relevant meteorological variables, as well as from differences in the flux parameterizations (Yu, 2019). Turbulent flux uncertainty estimates consider the uncertainties in near surface wind speed, temperature and humidity, but generally exclude the uncertainty associated with the use of bulk parameterizations. Estimating the uncertainty in sensible and latent heat fluxes over land is difficult because of their large temporal and spatial variabilities. The spread of these fluxes over land computed with three global datasets is between 10% to 20% (L'Ecuyer et al., 2015). The uncertainty in the surface energy budget in polar regions is larger than the uncertainty of other regions (e.g. Kato et al., 2018). The uncertainty estimate in the polar energy budgets remains challenging due to limited number of surface sites and larger uncertainty in surface observations (Previdi et al., 2015).

Also climate models show substantially larger discrepancies in their simulated energy budgets at the surface than at the TOA, with a spread of 10-20 W m^{-2} in their surface energy budget components averaged globally, and an even greater spread on more regional scales (Boeke and Taylor, 2016; Li et al., 2013b; Wild et al., 2013; Wild, 2017; Zhang et al., 2018a). The downward thermal and solar radiation in the CMIP5 climate models when averaged over the entire land surfaces varies by more than 30 and 40 W m^{-2}, respectively (Wild et al., 2015).

Several studies noted hemispheric contrasts in the present-day TOA radiation budget measured from space, namely a net gain of radiative energy of 1.4 W m^{-2} in the Southern Hemisphere (SH) and a net loss in the Northern Hemisphere (NH) of 0.2 W m^{-2} (Figure 7.4). This hemispheric difference is due to more outgoing longwave radiation in the NH than the SH, whereas the absorption of solar radiation is hemispherically symmetric (Liu et al., 2017a; Loeb et al., 2016; Marshall et al., 2014; Stephens et al., 2016; Voigt et al., 2013). This results in a net cross-equatorial heat transport of 0.2 PW from the SH to the NH. The cross-equatorial heat transport simulated by the CMIP5 models is on average twice as large as observed because they absorb more solar radiation in the SH than the NH, and also emit more outgoing LW radiation in the NH (Loeb et al., 2016; Voigt et al., 2013). Loeb et al. (2016) further inferred the regional distribution of the TOA, atmospheric and surface energy budget terms over the globe, by combining satellite-derived TOA and surface radiation budget observations with mass corrected vertically integrated atmospheric energy divergence and tendency from reanalyses. Their estimates imply that the cross-equatorial heat transport of 0.2 PW from the SH to the NH is achieved by a cross-equatorial heat transport of 0.44 PW in the ocean from the SH to the NH, and an atmospheric heat transport of 0.24 PW in the opposite (southward) direction (Figure 7.4) (Loeb et al., 2016; Stephens et al., 2016). Liu et al. (2015, 2017a) estimated the global distribution of the net surface (air-sea) heat flux, based on a combination of satellite-derived radiative fluxes at the TOA, and the atmospheric energy tendencies and transports from the ERA-Interim reanalysis. Their derived northward cross-equatorial heat transport in the oceans, at 0.32 ± 0.13 PW (5% to 95% confidence level), is somewhat smaller than estimated by Loeb et al. (2016), due to the consideration of differential heat accumulation in the NH and SH oceans. To accomplish the southward cross-equatorial atmospheric heat transport, the location of the tropical rainfall peak in the Intertropical Convergence Zone (ITCZ) must be located in the NH in the annual mean (Bischoff and Schneider, 2014; Donohoe et al., 2013; Frierson and Hwang, 2012; Kang et al., 2008). There is thus *high confidence* that the northward cross-equatorial oceanic heat transport, owing to meridional overturning in the Atlantic Ocean, is the primary reason that the annual mean rainfall peak is located to the north of the equator (Frierson et al., 2013; Marshall et al., 2014). Cross-equatorial energy transport derived from data products thus provides a key metric for the evaluation of energy budgets in climate models (Lembo et al., 2019; Loeb et al., 2016). Many CMIP5 models do not capture the correct sign and magnitude of the atmospheric cross equatorial heat transport, owing primarily to biases in absorbed shortwave radiation at the TOA, with an ensemble-mean cross-equatorial atmospheric heat transport near zero (Loeb et al., 2016). Too little simulated southward cross-equatorial atmospheric heat transport reflects a double ITCZ bias with too much rainfall to the south of the equator in the annual mean, which has been a persistent problem in multiple generations of climate models (Adam et al., 2016; Hwang and Frierson, 2013; Loeb et al., 2016).

[Placeholder for possible CMIP6 assessment]

[START FIGURE 7.4 HERE]

Figure 7.4: Implied cross-equatorial energy transports in the atmosphere and ocean inferred from hemispheric asymmetries in CERES TOA and surface energy budgets and mass corrected divergence in ERA-Interim atmospheric total energy transport. From Loeb et al. (2016).

[END FIGURE 7.4 HERE]

CMIP5 models capture the overall structure of the observed total (atmosphere + ocean) meridional heat transport, with peak poleward heat transport of about 6 PW in both hemispheres (Trenberth and Stepaniak, 2003), as well as the structure of atmospheric and oceanic heat transports separately (Figure 7.5). However, as for CMIP3 (Donohoe and Battisti, 2012), many CMIP5 models show large (~1 to 2 PW) errors in the mid-latitudes where the magnitude of total heat transport peaks (Figure 7.5a). Model errors in the total heat transport arise from errors in both atmospheric and oceanic heat transport components, with the majority of models showing too little poleward ocean heat transport in mid-latitudes (Figure 7.5c). The differences in peak total heat transport between models have been linked to their differences in the latitudinal structure of absorbed shortwave radiation suggesting that the heat transport errors arise from cloud biases (Donohoe and Battisti, 2012). The ability of models to reproduce the latitudinal structure of TOA radiation has been proposed as a constraint on projected warming over the 21st century (Section 7.5.6) (Brown and Caldeira, 2017).

In summary, since AR5, progress has been made in the estimation of the global mean energy budget, not only at the TOA, but also at the Earth's surface, where independent estimates of the radiative components have converged (*high confidence*). Considerable uncertainties remain in regional surface energy budget estimates, particularly from climate models, as well as in their simulation of the cross-equatorial atmospheric heat transports and the magnitudes of total meridional heat transports in mid-latitudes.

[START FIGURE 7.5 HERE]

Figure 7.5: Observed and CMIP5 climatological energy transports in the atmosphere and ocean (top) and projected heat transport changes at year 100 following CO2 quadrupling (bottom). (a) Climatological total heat transport inferred from CERES TOA (Armour et al., 2019) and simulated by CMIP5 models. (b) Climatological atmospheric heat transport calculated from the NCEP Reanalysis (Trenberth and Stepaniak, 2003) and simulated by CMIP5 models. (c) Climatological oceanic heat transport inferred from surface energy budgets (calculated as a residual between atmospheric heat transport divergence and TOA radiation fluxes). Grey shading shows 5% to 95% range on observational estimates. For total meridional heat transport the range is estimated from inter-annual variability and total CERES calibration error added in quadrature at each latitude. For atmospheric heat transport the range is estimated from inter-annual variability and for oceanic heat transport the range is estimated as a residual from the total and atmospheric heat transports with errors propagated in quadrature. (d-f) Anomalies in total, atmospheric, and implied oceanic heat transports simulated by CMIP5 models under abrupt CO2 quadrupling relative to pre-industrial control simulations which define their climatologies in (a)-(c) (following Armour et al., 2019). Implied ocean heat transport changes shown are those derived by net sea-surface heat fluxes and thus do not account for the pattern of ocean heat storage. [placeholder redo for CMIP6 once available and update to new analyses.]

[END FIGURE 7.5 HERE]

7.2.2 Observed changes in Earth's energy budget

7.2.2.1 Changes in TOA radiative fluxes

Since 2000, changes in the TOA energy fluxes can be tracked from space due to the CERES program (Figure 7.6). The variations noted in the TOA energy fluxes reflect both radiative forcing of the climate system, climate feedbacks, and the influence of internal variations, particularly that of ENSO (Allan et al., 2014a; Loeb et al., 2018a) . For example, globally, the reduction in both outgoing thermal and reflected solar radiation during La Nina conditions in 2008/09 lead to an energy gain for the climate system, whereas enhanced outgoing thermal and reflected solar radiation lead to an energy loss during the El Niños of

2002/03 and 2009/10(Figure 7.6) (Loeb et al., 2018a). Substantial anomalies in the global mean solar reflected radiation can also be attributed to anomalous sea ice cover in the Arctic and Antarctica. For the estimation of trends, the period for which CERES data is available (March 2000–September 2016) is still fairly short and dominated by internal variability of the climate system. Over this period a decrease in global mean solar reflectance of 0.57 ± 0.16 W m^{-2} per decade under all-sky and 0.36 ± 0.14 W m^{-2} per decade under clear sky conditions is observed (5% to 95% confidence level). The global mean TOA thermal outgoing radiation shows no significant changes over this period, neither under all-sky nor under clear-sky conditions (Loeb et al., 2018a). This implies an increase in the global mean net TOA radiation (Earth's energy imbalance) induced largely by the decreasing TOA solar reflectance since 2000 (Figure 7.6). The reconstruction of Allan et al. (2014a) and Liu et al. (2017a) offers insights into TOA radiative flux variability back to 1985, based on a combination of satellite data, atmospheric reanalyses, and climate model simulations. They estimated that over the 1985–1999 period the Earth's energy imbalance is lower on average, at 0.27 ± 0.38 W m^{-2}, than over the period 2000–2015, at 0.59 ± 0.14 W m^{-2} (5% - 95% confidence level). Their reconstruction is further able to capture the interannual variability in Earth's energy imbalance caused by the volcanic eruption of Pinatubo in 1991 and the ENSO events before 2000. In a similar reconstruction based on a combination of successive satellite missions, (Dewitte and Clerbaux, 2018) note a rise in thermal outgoing radiation at the TOA since 1985.

In summation, the energy exchange between Earth and space can be accurately tracked since the turn of the millennium (*high confidence*), and solar reflectance has decreased over this period, while reconstructions indicate that the Earth's energy imbalance has *likely* been higher in the 2000s than in the 1990s (*high confidence*).

[START FIGURE 7.6 HERE]

Figure 7.6: Anomalies in global mean all-sky TOA fluxes from EBAF Ed4.0 in terms of reflected shortwave (upper panel), emitted longwave (middle panel) and net TOA flux (lower panel). Thin lines are monthly anomalies. The thick line through monthly anomalies is the 12-month running mean. Larger reflected shortwave and emitted longwave flux anomalies are defined as positive in upper and middle panels. Net TOA flux is defined as incoming shortwave flux minus reflected and emitted fluxes (i.e. downward positive). Adapted from (Loeb et al., 2018a).

[END FIGURE 7.6 HERE]

7.2.2.2 Changes in ocean heat content

On annual and longer timescales, changes in the Earth's heat inventory are dominated by changes in global ocean heat content (GOHC) (Johnson et al., 2016; Palmer et al., 2011; Palmer and McNeall, 2014; Wijffels et al., 2016). Recent studies estimate an uncertainty of approximately ± 0.5 W m^{-2} on year-to-year changes in OHC, which falls to about ± 0.1 W m^{-2} for decadal trends (Johnson et al., 2016; Roemmich et al., 2015). The satellite measurements and in situ measurements of OHC are therefore complementary elements of the Global Climate Observing System, with the former constraining short-term variability in Earth's energy imbalance and the latter providing longer-term estimates of the absolute magnitude and its changes over time.

IPCC AR5 stated that there is *high confidence* that 93% of the excess heat accumulated in the climate system between 1971 and 2010 has been stored in the World's oceans (Rhein et al., 2013), demonstrating a key role of the oceans in Earth's energy budget on multi-decadal timescales. Confidence in this assessment is strengthened in AR6 through demonstration of consistent closure of both global sea level and energy budgets for the period 1971-present (Chapter 9, Box 9.2).

Past IPCC assessments of OHC change have focussed on estimates based on in situ subsurface ocean observations and have therefore been fundamentally limited by the availability and quality of in situ ocean temperature profile observations (Abraham et al., 2013; Palmer, 2017). Additional observation-based insights into OHC change are now available from a number of innovative approaches that employ methods that are independent of subsurface observations (Gebbie and Huybers, 2019; Resplandy et al., 2018; Zanna et al., 2019). These new methods strengthen the evidence for OHC change between the 1870s and 1971 and provide independent verification of the in situ-based estimates for the periods 1971–present and 2005–present. Incorporating this new evidence, there is *medium confidence* that global ocean warmed from the 1870s to 1971 and *very high confidence* that the global ocean warmed between 1971 to present.

In-situ subsurface ocean temperature measurements provide the most direct estimates of observed OHC change. However, both the observing technologies and their sampling capabilities and characteristics have evolved over time (Abraham et al., 2013; Palmer, 2017), which must be accounted for in our assessment of observed ocean warming. Prior to the widespread deployment of expendable bathythermographs (XBTs) in the late 1960s, there are very large uncertainties in estimates of OHC change (Lyman and Johnson, 2008).Therefore, past IPCC assessments of GOHC change (e.g. Rhein et al., 2013) have focussed on the period since 1970. XBTs typically sample only the upper few hundred metres and most annually-resolved time series estimates of GOHC change are limited to the upper 700 m (Abraham et al., 2013; Lyman et al., 2010). Insights into OHC changes for 700-2000 m has generally relied on generating pentadal averages or fitting trends to the available observations in order to mitigate the poorer sampling of the deep ocean (Cheng et al., 2017; Rhein et al., 2013). OHC changes below 2000 m rely on geographically and temporally sparse hydrographic research sections, and warming rates for this “abyssal” ocean are only available from the 1990s onwards (Desbruyères et al., 2017; Purkey and Johnson, 2010, 2013).

The early 2000s saw a revolution in ocean observing capability in the form of the Argo array of autonomous profiling floats (Riser et al., 2016). Since about 2005–2006 this array has provided routine, quasi-global 10-day sampling of in situ temperature and salinity for the upper two km of the open ocean with a nominal float separation of three degrees latitude/longitude. As well as providing more robust estimates of OHC change over the last decade or so (Johnson et al., 2016; Roemmich et al., 2015), Argo has enabled valuable insights into OHC change since the late 20th Century in combination with data collected as part of the pioneering *Challenger* expedition of 1872–1876 (Roemmich et al., 2012), albeit with much larger uncertainties than are associated with the recent period. Stringent delayed-mode quality control procedures in Argo data streams means that these data are much less prone to biases than XBT observations (Wong et al., 2018).

Observation-based estimates of OHC change have tended to employ statistical approaches to mapping the available temperature profiles (Abraham et al., 2013; Boyer et al., 2016; Lyman et al., 2010). However, ocean state estimates and ocean reanalyses, which make use of a dynamical ocean model, have increasingly been used to gain insights into OHC change and Earth’s energy imbalance (Balmaseda et al., 2013; Palmer et al., 2017; Trenberth et al., 2014). These systems are designed to provide a dynamically consistent estimate of the evolving ocean state and can potentially bring additional insights into underlying processes and mechanisms of observed changes. However, they are also subject to additional uncertainties, biases and other limitations associated with the underlying model physics and data assimilation schemes.

Gebbie and Huybers (2019) and Zanna et al. (2019) have taken novel approaches to reconstructing OHC changes back to the 19th Century. Both methods make use of estimates of ocean circulation to propagate the relatively well-constrained ocean surface conditions into the ocean interior. The agreement between these independent studies leads to a more robust assessment of the historical ocean warming than reported in AR5. There is *medium confidence* that the 0-700 m layer warmed from the 1870s to 1971 and *very high confidence* that this layer warmed over the periods 1971 to present and 2005 to present.

7.2.2.3 Changes in Earth’s surface energy budget

AR5 not only reported changes in the components of the Earth’s energy budget at the TOA and within the oceans, but also at the Earth’s surface (Hartmann et al., 2013). Pronounced changes were reported in multidecadal records of in situ observations of surface solar radiation, which encompass a decline at widespread locations between the 1950s and 1980s, known as "global dimming", and a partial recovery thereafter, termed "brightening".

Since AR5, additional evidence for dimming and/or subsequent brightening based on direct surface observations has been documented in previously less explored areas of the globe, such as in Iran, Bahrain, Teneriffe, Hawaii, the Taklaman desert and the Tibetan Plateau (Elagib and Alvi, 2013; Garcia et al., 2014; Longman et al., 2014; Wild, 2016; You et al., 2013). Strong decadal variations in surface solar radiation remain evident also after careful data quality assessment and homogenization of long-term records in Europe and China (He et al., 2018; Manara et al., 2015, 2016, Sanchez-Lorenzo et al., 2013, 2015; Yang et al., 2018b). Thus, there is *high confidence* that these variations are not measurement artefacts. Since AR5, further investigations on potential impacts of urbanization on solar radiation trends were carried out, indicating that the urbanization effects are generally small, with the exception of some specific sites in Russia and China (Imamovic et al., 2016; Tanaka et al., 2016; Wang et al., 2014). Climate models do not reproduce the full extent of dimming and brightening (Allen et al., 2013; Storelvmo et al., 2018; Wild and Schmucki, 2011), potentially pointing to inadequacies in the representation of aerosol mediated effects or related emission data. *[Placeholder: may assess MERRA for SOD]*

As noted in AR5 (Hartmann et al., 2013) and substantiated in more recent studies, the tendencies in surface solar radiation are less coherent at the beginning of the 21th century, with continued brightening in different parts of Europe and in the US, some stabilization in China and India, and dimming in other areas such as in Iran (Augustine and Dutton, 2013; Jahani et al., 2018; Manara et al., 2016; Pfeifroth et al., 2018; Sanchez-Lorenzo et al., 2015; Soni et al., 2016; Wang and Wild, 2016). The CERES-EBAF satellite-derived dataset of surface solar radiation (Kato et al., 2018), does not indicate a globally significant trend over the period 2001–2012 (Zhang et al., 2015), whereas a statistically significant increase in surface solar radiation of +3.4 W m^{-2} per decade over the period 1996–2010 has been noted over the area in view of the geostationary satellite Meteosat in the record of the Satellite Application Facility on Climate Monitoring (CM SAF) (Posselt et al., 2014). It should be noted that there is uncertainty associated with satellite-derived trends in surface solar radiation, and that they are partially reliant on modelling, particularly when it comes to aerosol effects.

Since AR5 there is additional evidence that strong decadal variations in surface solar radiation occur also under cloud-free conditions, as shown for long term records in Europe, USA, China and India (Gan et al., 2014; Manara et al., 2016; Soni et al., 2016). This suggests that changes in the composition of the cloud-free atmosphere, primarily aerosols, contribute to these variations, particularly since the second half of the 20th century (Wild, 2016). For Europe and East Asia, modelling studies also point to aerosols as an important factor for the variations in surface solar radiation by comparing simulations including and excluding historical aerosol variations (Folini and Wild, 2015; Golaz et al., 2013; Nabat et al., 2014; Persad et al., 2014; Turnock et al., 2015). On the other hand, further evidence for the influence of changes in cloudiness on dimming and brightening is emphasized in some studies (Augustine and Dutton, 2013; Parding et al., 2014; Pfeifroth et al., 2018; Stanhill et al., 2014). Thus, the relative contribution of aerosol and clouds to dimming and brightening is still debated. The influence of cloud-mediated aerosol effects and aerosol radiative effects on dimming and brightening in a specific region may depend on the prevailing pollution levels (Wild, 2016).

Uncertainties in the surface turbulent fluxes continue to limit the feasibility of determining their decadal changes. Nevertheless, over the oceans, reanalysis-based estimates of linear trends from 1948 to 2008 indicate an increase of 4–7 W m^{-2} $decade^{-1}$ for latent heat and 2–3 W m^{-2} $decade^{-1}$ for sensible heat in the western boundary current regions, while trends in extreme fluxes can be higher than 15 W m^{-2} $decade^{-1}$ (Gulev and Belyaev, 2012). In addition, a satellite-based product shows a global ocean latent heat flux trend of around 5.15 W m^{-2} $decade^{-1}$ between 1988 and 2008 (Gao et al., 2013).

Over land, the terrestrial latent heat flux is estimated to have increased by 0.09 W m^{-2} $decade^{-1}$ from 1989 to 1997, and subsequently decreased 0.13 W m^{-2} $decade^{-1}$ from 1998 to 2005 due to enhanced soil moisture limitation mainly in the SH (Mueller et al., 2013). These trends are small in comparison to the uncertainty obtained from satellite-derived and in-situ observations, as well as from land surface models forced by observations and atmospheric reanalyses. Temporal and spatial variability in surface solar radiation and precipitation can affect the variability in terrestrial latent heat flux (Douville et al., 2013; Greve et al., 2014; Oliveira et al., 2011). Changes in evapotranspiration (latent heat flux) during the second half of the 20th century were greater than those in precipitation in the Mediterranean, Africa and northern China, whereas the opposite was the case in Eastern US and La Plata Basin (Greve et al., 2014). Ongoing advances in remote sensing of evapotranspiration from space (Fisher et al., 2017; Mallick et al., 2016; McCabe et al., 2017b, 2017a), as well as terrestrial water storage (Rodell et al., 2018) may contribute to constrain changes in latent heat flux. Meanwhile, there was also progress in benchmarking the terrestrial sensible heat flux (Siemann et al., 2018).

In summary, since AR5, multidecadal variations in surface solar radiation have been detected at many more locations also in remote areas. There is *high confidence* that these variations are of widespread nature, and not only a local phenomenon or a measurement artefact. The origins of these variations need further investigation, although there are indications that anthropogenic aerosols have substantially contributed to these variations (*medium confidence*). Confidence in the trends in surface sensible and latent heat remains *low*.

[START BOX 7.2 HERE]

BOX 7.2: The Global Energy Budget and its Future Changes

The net ERF of the Earth System since 1971 has been positive (Box 7.2, Figure 1; Section 7.3), mainly as a result of increases in atmospheric greenhouse gas concentrations (Section 2.2.8, 7.3.2). These positive forcing agents have been partly offset by negative radiative ERFs, primarily due to anthropogenic aerosols (Section 7.3.3). The net energy inflow to the Earth system from ERF since 1970 is estimated to be 1200 ZJ (1 ZJ = 10^{21} J) with a *very likely* range of 860 to 1510 ZJ.

The ERF-induced warming of the climate system results in increased thermal radiation to space via the Planck response, but the picture is complicated by the variety of other climate and Earth system feedbacks (Section 7.4) that also influence Earth's radiative response (Box 7.2, Figure 1c). The combined effects of these feedbacks can be estimated using atmospheric general circulation model (GCM) simulations using prescribed historical sea-surface temperatures (SSTs) and sea-ice concentrations, resulting in a net feedback parameter, α, that varies as the SST pattern evolves over the historical record (Section 7.4.3). Combining these model-based estimates of time-evolving α with the observed near-surface temperature change provides an estimates of the Earth radiative response (Box 7.2, Figure 1c). The net energy outflow from the Earth system associated with the radiative response since 1971 is estimated to be 860 ZJ with a *very likely* range of 670 to 1210 ZJ.

The combination of the ERF-induced changes and those associated with the radiative response lead to an implied change in Earth's energy storage of 360 ZJ [-85 to 750 5% to 95% range]. This agrees well with an independent observation-based assessment of Earth's energy storage change of 297 ZJ for the period 1971-2014, which is dominated by the increase in OHC. Confidence in the observed energy storage change is strengthened by a consistent analysis and closure of the observed global sea level budget (Chapter 9, Box 9.2). Overall, there is *high confidence* that Earth's energy budget is closed within the estimated uncertainties and this provides strong evidence for our understanding of anthropogenic climate change and estimates of climate sensitivity (Section 7.5). *[Placeholder: uncertainties computed for SOD]*

Recent studies have compared observation-based estimates of multi-decadal GOHC change with those simulated by CMIP5 climate models (Cheng et al., 2016, 2019; Gleckler et al., 2016). In general, there is good agreement in both total ocean heat uptake and its vertical structure between the observations and CMIP5 multi-model mean (Box 7.2, Figure 1f; Chapter 3, section 3.5). However, there is a large spread among CMIP5 models compared to the observations, indicating that in some of the models the historical climates have not evolved in the same way as reality. This implies a broad range of net radiative forcings and/or spread in climate feedbacks over the 20th Century among climate models. In addition, the magnitude of internal variability in OHC and Earth's energy imbalance simulated by each model varies substantially across the ensemble (Gleckler et al., 2016; Palmer and McNeall, 2014).

Smith et al. (2015) presented a comparison of the evolution of Earth's energy imbalance between CMIP5 climate models and observation-based reconstructions of Earth's energy imbalance and GOHC change. The reconstructions of ERB and GOHC change (based on 5-year rolling trends) generally showed good agreement and both exhibited a general tendency towards an increase in Earth's energy imbalance that was punctuated by short-lived cooling episodes associated with major volcanic eruptions. The CMIP5 ensemble mean showed good agreement in both the timing and magnitude of the main signals seen in the observations, with a close correspondence between the time-evolution of Earth's energy imbalance and GOHC change.

Future projections show that Earth's energy imbalance remains positive under all RCP scenarios for several centuries, contributing directly to long-term committed sea level rise through the associated thermal expansion of the global oceans (Box 7.2, Figure 2, e.g. Nauels et al. (2017); Palmer et al. (2018)). While GHG ERF acts initially through suppression of outgoing longwave radiation it is ultimately the increase in absorbed shortwave radiation that dominates the response of Earth's radiation budget (Donohoe et al., 2014a; Trenberth and Fasullo, 2009). This arises because longwave emission to space increases with surface warming while shortwave radiation absorbed increases with warming due to reduced ice cover and increased atmospheric water vapour (Donohoe et al., 2014a). The behaviour of total Earth system warming is in contrast to that of global surface temperature change in two fundamental ways. The first is the long-term commitment, with the total warming continuing for centuries even under strong mitigation scenarios under which GMST stabilises or even reduces. The second is that GMST is much more prone to inter-annual-to-multi-decadal variability than total warming, making the latter a more suitable basis for monitoring the rate of anthropogenic global warming on decadal and shorter timescales (Palmer et al., 2011; Palmer and McNeall, 2014; Wijffels et al., 2016).

[START BOX 7.2, FIGURE 1 HERE]

Box 7.2, Figure 1: Estimates of the net cumulative energy change (ZJ = 10^{21} Joules) for the period 1971-2015 associated with: (a) Earth System Energy Change; (b) Effective Radiative Forcing; (c) Earth System Radiative Response. Shaded regions indicate the 5^{th} to 95^{th} percentile uncertainty range. Panels (d) and (e) show the breakdown of components for energy storage and effective radiative forcings, respectively. Panel (f) shows the comparison of CMIP5 model simulations of 0-2000m heat content change with several observation-based estimates, following Cheng et al. (2019). The shaded regions indicate the 5^{th} to 95^{th} percentile range of model simulations, assuming a normal distribution. [placeholder: Observed Storage Change to be properly assessed for SOD).

[END BOX 7.2, FIGURE 1 HERE]

[START BOX 7.2, FIGURE 2 HERE]

Box 7.2, Figure 2: Two-layer model simulations of global mean surface temperature (left) and ocean thermal expansion (right) under the RCP2.6 and RCP4.5 scenarios, following Palmer et al (2018). Shaded regions indicate the 90% confidence interval based on the ensemble standard deviation. Dotted lines indicate the ensemble mean response. Solid lines show a single CMIP5 model simulation to illustrate the characteristics of variability in each variable. Projections are shown relative to a 1986-2005 baseline period. [placeholder: baseline to be changed inline with AR6 standard period of 1995-2014 at SOD].

[END BOX 7.2, FIGURE 2 HERE]

Changes in meridional heat transport have important consequences for the large-scale patterns of surface warming in response to greenhouse gas forcing (Section 7.6.2). Figure 7.5 illustrates heat transport changes within CMIP5 models at a century after abrupt CO_2 quadrupling. Models simulate several consistent features including increased poleward atmospheric heat transport and decreased oceanic heat transport in both hemispheres (Figure 7.5d, f), except near 70°N where the majority of models show increased poleward oceanic heat transport and decreased poleward atmospheric heat transport (Hwang et al., 2011). Models do not agree on the sign of the total heat transport changes, which are generally small owing to strong compensations between atmospheric and oceanic heat transport changes at all latitudes (Armour et al., 2019; He et al., 2019; Huang and Zhang, 2014).

Improved process understanding of heat transport since AR5 increases the degree of evidence to provide *high confidence* in several key aspects of oceanic heat transport changes under global warming. Anomalous northward ocean heat transport in the Southern Ocean arises primarily from northward-flowing surface waters carrying anomalous heat from where it is taken up around 60°S to where it is stored in the ocean further north (Armour et al., 2016; Froelicher et al., 2015; He et al., 2019; Liu et al., 2018; Marshall et al., 2015; Morrison et al., 2016; Stouffer et al., 2006). Decreased northward oceanic heat transport in the NH mid-latitudes is associated with a reduction in the strength of the Atlantic Meridional Overturning Circulation (AMOC) (Gregory et al., 2005; Marshall et al., 2015; Oldenburg et al., 2018; Rugenstein et al., 2013; Stouffer et al., 2006; Weaver et al., 2007; Winton et al., 2013b). The increase in oceanic heat transport into the Arctic Ocean seen in most models is associated with the northward transport of anomalous heat taken up within the North Atlantic subpolar gyre and with changing ocean currents in the Nordic Seas (Bitz et al., 2006; Holland and Bitz, 2003; Jungclaus et al., 2014; Koenigk and Brodeau, 2014; Mahlstein and Knutti, 2011; Marshall et al., 2015; Nummelin et al., 2017; Oldenburg et al., 2018). Ocean heat transport changes depend on the radiative forcing scenario considered, particularly in the NH where AMOC changes are influenced by aerosol forcing (Shi et al., 2018). CMIP5 models do not show a robust reduction in poleward ocean heat transport in the NH mid-latitudes under historical forcing (Huang and Zhang, 2014), but a reduction is projected to occur as AMOC declines over the 21st century (Chapter 4, Section 4.3.2; Cheng et al., 2013) (*high confidence*).

There is improved understanding of atmospheric heat transport processes since AR5 as well. Atmospheric heat transport changes are commonly understood in terms of the heat flux divergence required to balance the anomalous energy input into the atmosphere at each latitude by radiative forcing, the radiative response to surface warming (i.e., radiative feedbacks), and ocean heat uptake (Armour et al., 2019; Feldl and Roe, 2013b; Huang et al., 2017; Huang and Zhang, 2014; Zelinka and Hartmann, 2012). ERF from CO_2 peaks in the tropics, contributing to increased poleward atmospheric heat transport in both hemispheres. Those radiative feedbacks that preferentially add energy to the tropical atmosphere (water-vapour and cloud feedbacks) contribute to increased poleward atmospheric heat transport in mid-latitudes, while those that preferentially remove energy from the tropical atmosphere (lapse-rate feedback) oppose that increase. The net TOA radiative changes under CO_2 forcing are relatively uniform with latitude owing to weak latitudinal structure in both the ERF and the radiative response to warming (Armour et al., 2019), resulting in the near-invariance of total meridional heat transport (Figure 7.5d) and thus requiring strong compensation between oceanic and atmospheric heat transport changes (Figure 7.5e,f). In this view, because TOA radiation changes relatively little with surface warming in the Arctic (owing to positive regional feedbacks; Section 7.6.2), atmospheric heat transport changes into the Arctic are required to balance the local energy input by CO_2 forcing and ocean heat transport changes. The degree of compensation between atmospheric and oceanic heat transport depends on the latitudinal structure of radiative feedbacks (Dai et al., 2017; Rose and Ferreira, 2013; Yang et al., 2017) and thus varies across models.

Atmospheric heat transport changes also reflect compensations between large changes in the poleward transport of latent energy and dry-static energy (sum of sensible and potential energy) (Held and Soden, 2006; Hwang et al., 2011; Hwang and Frierson, 2010). Large increases in poleward latent energy transport are compensated by large decreases in dry-static energy transport in the mid-to-high latitudes where transient eddies dominate the heat transport. Large increases in equatorward latent energy transport are compensated by large increases in poleward dry-static energy transport in the tropics where the Hadley Circulation dominates the heat transport. These latent energy transport changes correspond to changes in moisture convergence and thus shape the patterns of rainfall under global warming (Held and Soden, 2006; Siler et al., 2018b) (Section 8.4). Moist diffusive energy balance models that approximate heat transport in terms of a flux down the near-surface moist static energy (sum of sensible and latent energy) gradient are able to replicate the atmospheric heat transport changes seen within climate models (Flannery, 1984; Hwang et al., 2011; Hwang and Frierson, 2010; Roe et al., 2015; Rose et al., 2014), including the partitioning of latent and dry-static energy transports (Armour et al., 2019; Siler et al., 2018b). In this view, increased poleward latent heat transport in mid-to-high latitudes with global warming is a consequence of an increase in the meridional moisture gradient while decreased dry-static energy transport in mid-to-high latitudes is a consequence of a decrease in the meridional surface temperature gradient (i.e., polar amplification) (Alexeev et al., 2005; Hwang et al., 2011; Hwang and Frierson, 2010; Merlis and Henry, 2018). The success of this diffusive approximation suggests that relatively simple principles may govern atmospheric heat transport such as maximization of entropy production (Dyke and Kleidon, 2010; Ozawa et al., 2003; Pascale et al., 2012).

There remain open questions regarding how energetic and diffusive perspectives on atmospheric heat transport can be reconciled with the perspective that invokes specific atmospheric circulations (Armour et al., 2019). Much research since AR5 has focused on establishing causal links between changes in regional atmospheric energy budgets and the response of atmospheric circulation (e.g., Ceppi and Hartmann, 2015; Ceppi and Shepherd, 2017; Donohoe et al., 2013, 2014b; Feldl and Bordoni, 2016; Mbengue and Schneider, 2018; Merlis, 2015; Voigt and Shaw, 2015, 2016). A key uncertainty is how atmospheric heat transport changes can be understood in terms of the changes in atmospheric circulation that occur under CO_2 forcing – such as a narrowing and shifting of the ITCZ (e.g., Huang et al., 2013; Neelin et al., 2003), a slowdown and poleward expansion of the Hadley Cell (Held and Soden, 2006; Lu et al., 2007), poleward shifts of mid-latitude jets and storm tracks (e.g, Barnes and Polvani, 2013; Yin, 2005), or changing planetary wave activity (e.g., Graversen and Burtu, 2016; Lee, 2014; Liu and Barnes, 2015).

[END BOX 7.2 HERE]

7.3 Effective Radiative Forcing

7.3.1 Methodologies and representation in models; overview of rapid adjustments

As introduced in BOX 7.1, the IPCC AR5 report (Boucher et al., 2013; Myhre et al., 2013b) recommended ERF as a more useful measure of the climate effects of a physical driver than stratospheric temperature-adjusted radiative forcing (SARF) adopted in earlier assessments. ERF extended the SARF concept to account for not only adjustments to stratospheric temperatures, but also responses in the troposphere to the heating profile induced by the relevant forcing mechanism, termed rapid adjustments. These rapid adjustments include changes in the atmospheric temperature profile, as well as the consequences of these temperature changes on clouds and water vapour. Microphysical effects of aerosol on clouds are also included in the total ERF, and within the literature can either be associated with a rapid adjustment and/or part of the initial IRF. The changes in evapotranspiration and sensible heat fluxed due to the CO_2-physical effect are also considered as components of rapid adjustments (Cao et al., 2010; Doutriaux-Boucher et al., 2009; Richardson et al., 2018b).

The assessment of ERF in AR5 was preliminary as there was no agreed standard for estimating ERF and ERFs were only available for a few forcing agents, so for many forcing agents the report made the assumption that ERF and SARF were equivalent. A body of work since has computed ERFs across many more forcing agents and models, closely examined the methods of computation, quantified and probed the processes involved in delivering rapid adjustments and examined how well ERFs represent the ultimate temperature response. These have led to a much-improved understanding and gives increased confidence in the quantification of radiative forcing across the report. Importantly, the same techniques allow for a much fuller evaluation of radiative forcing within climate models as a key test of their ability to represent both historical and future temperature changes (Chapters 3, Section 3.3 and Chapter 4, Section 4.3).

There have been two main methods used to calculate ERF. The first method is to regress the net TOA radiation flux against global surface air temperature following a step change in the concentration of the forcing agent (Gregory et al., 2004), with the ERF derived from the intercept with the Y axis. Regression-based estimates of ERF depend on the time resolution of the data used (Modak et al., 2016, 2018). For the first few months of a simulation both surface temperature change and stratospheric temperature adjustment occur at the same time leading to misattribution of the stratospheric temperature adjustment to the surface temperature feedback. At longer timescales the curvature of the relationship between TOA flux and surface temperature can also lead to biases in the ERF estimated from the regression method (Andrews et al., 2015; Armour et al., 2013; Knutti et al., 2017) (Section 7.4). A second method for computing ERF is to remove the climate feedback by prescribing the SSTs and sea-ice (Hansen et al., 2005). The prescribed SST method is found to be more certain than the regression method. Nevertheless a 30-year integration needs to be conducted to reduce the uncertainty range to within 0.1 W m^{-2} (Forster et al., 2016).

For the definition of ERF employed here (Section 7.1), the land surface temperature change is considered part of the response. This response can be removed from the prescribed SST and sea-ice TOA energy budget change through the use of radiative kernels or by extrapolating the surface temperature feedback to a temperature change of zero (Chung and Soden, 2015a; Forster et al., 2016; Richardson et al., Submitted; Sherwood et al., 2015). In some definitions of ERF land-surface responses are included, in others they are associated with climate feedbacks (Chung and Soden, 2015a; Richardson et al.; Sherwood et al., 2015). In regression based ERF estimates, patterns of sea-surface temperature change additionally affect the forcing (Andrews et al., 2015). The definition adopted aims to have the cleanest separation between forcing (energy budget changes that are not mediated by surface temperature) and feedbacks (as energy budget changes that are mediated by surface temperature). The definition is also found below to have the most constant feedback parameter across forcing agents.

The ERF can be broken down into the IRF plus the rapid adjustments. In theory this can be constructed bottom-up by calculating the IRF and adding in the rapid adjustments one-by-one or together. The stratospheric temperature adjustment can be calculated in offline radiative transport models (RTMs), for instance using fixed dynamical heating (Fels et al., 1980; Maycock, 2016), but there is no simple way to derive the other adjustment terms without using a full climate model. Methods to determine ERF therefore use top-down diagnoses of the total change in radiative fluxes in a full climate model following an applied forcing, allowing for rapid adjustments, but not climate feedbacks. The principle means for distinguishing between rapid adjustments and climate feedbacks is the dependence on surface temperature rather than the timescale of the response. Rapid adjustments are assumed to be independent of surface air temperature changes whereas climate feedbacks are the dependence of radiative fluxes on surface air temperature (Box 7.1).

The rapid adjustments can be calculated from models by calculating the difference between an IRF (using a double call to the radiative transfer scheme) and a climate model estimate of ERF (from a prescribed SST and sea-ice experiment); or by using radiative kernels (Chung and Soden, 2015b, 2015a; Smith et al., 2018b; Vial et al., 2013; Zelinka et al., 2014; Zhang and Huang, 2014) or a partial radiative perturbation approach (Colman, 2015). The radiative kernel approach is easier to implement through post-processing of climate model output and allows for a comparison of radiative kernels computed from different radiative transfer schemes, whereas the partial perturbation approach would be expected to give a more accurate estimate of the adjustments within the setup of a single model and its own radiative transfer code. Radiative kernels can also be used to estimate the ERF from prescribed SST and sea-ice experiments by removing the land-surface temperature response from the TOA energy budget change (Richardson et al., Submitted; Tang et al., accepted). IRFs and rapid adjustments computed from radiative kernels are shown for five forcing experiments across nine models in Figure 7.7 (Smith et al., 2018b). IRFs provide a useful test of models' radiative transfer codes but few recent experiments have tested IRFs computed within climate models (Pincus et al., 2016). Chung and Soden's (2015b) kernel analyses suggested a large spread in CO_2 IRF and

SARF across models, but this spread could also be attributable to the kernel method employed in estimating IRF. Smith et al. (2018b) find a similar spread in IRF for 2xCO_2 and show that kernel methodological errors are typically smaller than 10%. This suggests the kernel method is a useful but not perfect way of estimating IRF and that the larger than expected spread in IRF in climate models compared to earlier estimates from line by line models could point to real errors in climate models radiative transfer codes (Pincus et al., 2016; Soden et al., 2018) (Section 7.4.2). Table 7.1 shows the estimates of IRF, SARF and ERF from the climate models analysed in Richardson et al. (submitted). This shows improved agreement over previous studies (Pincus et al., 2016 and references therein) and relatively good agreement with the overall assessment of CO_2 ERF in Section 7.3.2. The level of agreement in this and earlier intercomparisons gives *high confidence* in climate models' representation of radiative forcing from greenhouse gases.

[START Table 7.1 HERE]

Table 7.1: IRF at the tropopause, SARF and ERF diagnosed from climate models for a 2xCO2 experiment. Data taken from Richardson et al (submitted). An ERF is also given from prescribed sea-surface temperature and sea-ice experiments, where the effects of land-surface temperature changes are not removed (ERF with land changes).

2xCO_2 (W m^{-2})	**IRF (Tropopause)**	**SARF**	**ERF**	**ERF** With land change
HadGEM2	4.55	3.45	3.44	4.00
NorESM	4.44	3.67	3.50	3.82
GISS	4.41	3.98	4.05	4.58
CanESM2	4.44	3.68	3.54	3.97
MIROC-SPRINTARS	4.62	3.89	3.70	4.10
CESM1-CAM5	4.28	3.89	4.04	4.60
HadGEM3	4.35	3.48	3.64	4.27
IPSL-CM5A	-	3.50	3.32	3.73
MPI-ESM	4.47	4.27	4.13	4.64
CESM1-CAM4	-	3.50	3.57	4.02
ECHAM-HAM	-	-	4.32	-
Multi-model Mean and std.dev.	**4.45 ± 0.11**	**3.73 ± 0.27**	**3.75 ± 0.33**	**4.17 ± 0.33**

[END Table 7.1 HERE]

[Placeholder for possible analysis of IRF RFMIP experiments for SOD]

[START FIGURE 7.7 HERE]

Figure 7.7: The ERF, IRF and rapid adjustment (a) and breakdown of the rapid adjustment using radiative kernels (b) for five idealised forcing experiments across nine models. The 95% confidence range is shown. Note that the land-surface response is included in ERF as an adjustment. Data modified from Smith et al. (2018b).

The results are computed from idealized single forcing experiments with the following abrupt perturbations from present day conditions; doubling CO2 concentration (2xCO2), tripling methane concentration (3xCH4), two percent increase in insolation (2%Sol), ten times black carbon concentrations or emissions (10xBC), five times sulphate concentrations or emissions (5xSul). [For SOD land response will be removed from the ERF in the figure]

[END FIGURE 7.7 HERE]

ERFs have been found to provide a more consistent measure of global temperature change per W m^{-2} of forcing compared to SARF, i.e. α values show less variation across different forcing experiments. (Hansen et al., 2005; Marvel et al., 2015; Richardson et al., submitted). However, even for ERF, studies find that α is not indentical across all forcing perturbations (Duan et al., 2018; Marvel et al., 2015; Modak et al., 2016, 2018; Richardson et al. submitted; Shindell, 2014; Shindell et al., 2015). The latitudinal and altitudinal distribution of the forcing and the additional physiological effects of CO_2 on plants cause variations in α (Kang and Xie, 2014; Modak et al., 2018; Richardson et al. submitted; Shindell, 2014; Shindell et al., 2015). The most comprehensive multi-model analyses compares 12 forcing types across nine models and explores how α varies for different definitions of forcing, including different ways of measuring ERF (Richardson et al., Submitted). They find that the multi-model mean of α is relatively constant (within ~20%, Figure 7.8) across different forcing experiments when computed using ERF from prescribed sea-surface temperature and sea-ice experiments. Additionally, removing the land-surface temperature response from the TOA energy imbalance using a radiative kernel methodology brings α for $2xCO_2$ into closer agreement with other forcing perturbations. When computed using regression-based ERF, α exhibited both more variation in the model-mean and a greater model spread, as did α values computed from SARF (Figure 7.8). When examining single models in Richardson et al. (Submitted) there are variations in α across forcings but the variation was not found to be consistent across models. Other single-model studies published since AR5 (Marvel et al., 2016; Modak et al., 2018; Shindell et al., 2015) and studies examining the effectiveness of solar radiation management geoengineering (Crook et al., 2015; Duan et al., 2018) all show some variation in α across different forcing agents. For more localised forcings α shows greater variation between forcing agents and models (Richardson et al. (Submitted), Figure 7.8). However, as none of these variations are robust across models, this report's assessment is that feedbacks derived from $2xCO_2$ are within a 20% range of that from other forcing agents (*medium confidence*).

This report adopts an estimate of ERF based on rapid adjustments computed from prescribed SST and sea-ice experiments, and additionally removing the TOA energy budget change from the land surface temperature response (Box 7.1). This is firstly for a theoretically cleaner separation between forcing and feedbacks in terms of factors respectively unrelated and related to surface temperature change. Secondly, the new studies highlighted above suggest climate feedback parameters computed within this framework have less variation across forcing agents. From high agreement and medium evidence there is *high confidence* that ERF as defined here represents a useful estimator of equilibrium surface temperature change across a range of typical forcing agents. For localised forcing patterns there are fewer studies and less agreement between them, resulting in *low confidence* that ERF is a suitable measure of surface temperature response.

[START FIGURE 7.8 HERE]

Figure 7.8: Values of climate feedback parameter (α) derived from ERF and SARF for twelve forcing experiments. Multi-model means and full model ranges are shown. ERF is derived from prescribed SST and sea-ice experiments. The number of models analysed differs between experiments as indicated on the bars. Data from Richardson et al. (Submitted). The results are computed from idealized single forcing experiments with the following abrupt perturbations from present day conditions; doubling CO2 concentration ($2xCO_2$), tripling methane concentration (3xCH4), two percent increase in insolation (2%Sol), ten times black carbon concentrations or emissions (10xBC), five times sulphate concentrations or emissions (5xSul), ten times sulphate concentrations or emissions over Asia only (10xSulasia), ten times sulphate concentrations or emissions over Europe only (10xSuleur), change in CFC-12 mixing ratio to 5ppb (CFC-

12), change in CFC-11 mixing to 5ppb (CFC-11), change in N2O mixing ratio to 1ppm (N2O1p), five times tropospheric ozone concentration (Ozone), change in vegetation to pre-industrial conditions (LandUse).

[END FIGURE 7.8 HERE]

7.3.2 Well-Mixed Greenhouse Gases, ozone and stratospheric water vapour

[*note these are assessed from 1750-2017 currently but will be updated to 2018 for the SOD*]

Line-by-line (LBL) models provide the most accurate calculations of the radiative perturbations due to well mixed greenhouse gases (WMGHGs) with errors in the IRF of less than 1% (Mlynczak et al., 2016). They can calculate IRFs with no adjustments, or SARFs by accounting for the adjustment of stratospheric temperatures using a fixed dynamical heating. It is not possible with offline radiation models such as LBL to account for other rapid adjustments, so such models cannot calculate ERFs. The LBL calculations of SARF for carbon dioxide, methane and nitrous oxide have been updated since AR5, which were based on (Myhre et al., 1998). The new calculations (Etminan et al., 2016) include the shortwave forcing from methane and updates to the water vapour continuum (increasing its total SARF by 25%) and account for the overlaps between carbon dioxide and nitrous oxide., The associated simplified expressions are given in Table 7.1. The results for methane have been confirmed independently (Collins et al., 2018). Since they incorporate known missing effects we assess the new calculations as being a more appropriate representation than (Myhre et al., 1998).

As described in Section 7.3.1, ERFs can be estimated solely using climate models, however the radiation schemes in climate models are approximations to LBL models with large variations and biases in results between the schemes (Soden et al., 2018). Hence climate models alone should not be used to the make best estimates of the ERFs for the WMGHGs. This assessment therefore estimates ERFs from a combined approach, using the SARF from LBL codes with the tropospheric rapid adjustments added to this derived from climate models.

The main information used in AR5 to assess components of ERFs was Vial et al. (2013) using 4×CO_2 experiments in CMIP5 models, who found a near-zero non-stratospheric adjustment with an uncertainty on this of 10% of the total CO_2 ERF. The near-zero adjustment comes from an approximate balance between an increase due to water vapour and clouds and a decrease due to increased tropospheric and land surface temperatures. Since then, Zhang and Huang (2014) also analysed CMIP5 model results with similar conclusions to Vial et al. (2013). A more recent analysis from Smith et al. (2018b) of 2×CO_2 experiments found agreement with these earlier two and separated the temperature adjustment into land-surface temperature and tropospheric temperatures (Table 7.2). Excluding the land-surface temperature response to follow the definition in Box 7.1 gives a tropospheric adjustment of +5% which we add to the Etminan et al. (2016) formula for SARF. Due to the agreement between the studies and the understanding of the physical mechanisms there is *high confidence* in the mechanisms underpinning the tropospheric adjustment. However, due to rapid adjustments of different signs there is only *medium confidence* that the overall tropospheric adjustment is positive.

[START Table 7.2 HERE]

Table 7.2: Rapid adjustments to CO_2 forcing due to changes in stratospheric temperature, surface and tropospheric temperatures, water vapour, clouds and surface albedo, as a fraction of the SARF. Note that surface temperature changes are excluded from the forcing in out definition.

Fraction of SARF	Surface temperature	Tropospheric temperature	Stratospheric Adjustment	Surface albedo	Water vapour	Cloud adjustment

	response	adjustment		adjustment	adjustment	
Vial et al. (2013)	-0.2			0.02	0.06	0.11
Zhang and Huang (2014)	-0.23		0.26		0.06	0.16
Smith et al. (2018)	-0.06	-0.16	0.30	0.03	0.06	0.12

[END Table 7.2 HERE]

7.3.2.1 Carbon Dioxide

The $2xCO_2$ ERF is assessed to be 4.0 ± 0.7 W m^{-2} (5% to 95% range). Its assessed components are given in Table 7.3. The combined spectroscopic and radiative transfer modelling uncertainties give an uncertainty in the CO_2 SARF of around 10% or less (Etminan et al., 2016; Mlynczak et al., 2016). The overall uncertainty in CO_2 ERF is assessed as 10%, as the more uncertain rapid adjustments only account for a small fraction of the ERF. The ERF estimate has increased by 8% since AR5 partly due to revised LBL calculations (contributing 3% increase), but mostly due to the combined effects of a series of rapid adjustments. The historical ERF estimate from CO_2 is revised upwards by a total of 16% from a combination of these revisions and the 4% rise in atmospheric concentrations between 2011 and 2017.

[START Table 7.3 HERE]

Table 7.3: Assessed ERF, SARF and tropospheric rapid adjustments to $2xCO_2$ change since preindustrial times compared to the AR5 assessed range (Myhre et al., 2013b). Rapid adjustments are due to changes in tropospheric temperatures, water vapour, clouds and surface albedo and land cover.

$2xCO_2$ forcing	AR5 SARF/ERF	SARF (W m^{-2})	Tropospheric temperature adjustment (W m^{-2})	Water vapour adjustment (W m^{-2})	Cloud adjustment (W m^{-2})	Surface albedo and land cover adjustment (W m^{-2})	ERF (W m^{-2})
$2xCO_2$ ERF components	3.7	3.81	-0.58	0.23	0.43	0.12	4.01
5%-95% uncertainty ranges as percentage of top row	10% (SARF) 20% (ERF)	<10%	40%	70%	100%	50%	17%

[END Table 7.3 HERE]

7.3.2.2 Methane

CH_4 rapid adjustments have been calculated in nine climate models in Smith et al. (2018b). Since CH_4 is known to absorb in the shortwave only adjustments from those models including shortwave absorption are taken into account. For these models the adjustments are robustly acting as a negative forcing as the shortwave absorption leads to tropospheric heating and changes in clouds. The adjustment is -14% ± 9% which counteracts much of the increase in SARF identified by Etminan et al. (2016). Modak et al. (2018) also found negative forcing adjustments from a methane perturbation including shortwave absorption, supporting the above assessment. We caution that since the climate models are not able to represent the shortwave absorption in the detail of Etminan et al. (2016) this introduces further uncertainty. This assessment increases the uncertainty in the rapid adjustment to include zero: -14% ± 14%. The spectroscopic uncertainty in the shortwave component is determined to lead to a 10% uncertainty in the SARF (Etminan et al., 2016) leading to an overall uncertainty of 17% [5%- 95% range]. There is *high confidence* in the spectroscopic revision but only *medium confidence* in the rapid adjustment modification.

7.3.2.3 Nitrous oxide

There have been no studies of the rapid adjustments to N_2O. An idea of the physical responses to N_2O forcing can be gained from the responses CH_4 without shortwave absorption which is 15% ± 8% driven by changes in clouds. The rapid tropospheric adjustments to N_2O are therefore assessed to be 0 ± 10% with *low confidence*. The spectroscopic uncertainty is expected to be small (Etminan et al., 2016).

7.3.2.4 Halogenated species

The stratospheric-temperature adjusted radiative efficiencies for halogenated species were reviewed extensively using LBL models in (Hodnebrog et al., 2013) as used in AR5. That study used a consistent procedure for analysing each species and therefore is assessed as providing the most useful comparison between the species. More recent studies have updated some individual species (Le Bris et al., 2018; Le Bris and Graham, 2014; Lu et al., 2017; Papanastasiou et al., 2018; Totterdill et al., 2016) but do not cause sufficient changes in understanding to require updates to the AR5 ERF values (Myhre et al., 2013b).

The overall uncertainty in the ERFs of halogenated species is estimated to 20% (including 13% from spectroscopic uncertainty (Hodnebrog et al., 2013). The ERF from CFCs is slowly decreasing, but this is more than compensated for by the increased forcing from the replacement species. The ERF from HFCs (which will be controlled under the Kigali agreement) has increased by 0.012 W m^{-2}. Thus, the concentration changes mean that the total ERF from halogenated species has increased since AR5 from 0.363 W m^{-2} to 0.374 W m^{-2} (Table 7.4).

7.3.2.5 Ozone

Determining the tropospheric ozone radiative forcing since 1750 or 1850 is hampered by our lack of measurement of ozone at that time. Estimates are therefore entirely based on models. There have been two studies of ozone ERFs, each based on a single model (MacIntosh et al., 2016; Xie et al., 2016). These did not report corresponding IRFs or SARFs so it is not possible to quantify the effects of tropospheric adjustments. MacIntosh et al. (2016) did present associated changes in cloud cover suggesting increases in stratospheric or upper tropospheric ozone would decrease high clouds and increase low clouds (giving a negative forcing from rapid adjustment), whereas an increase in lower tropospheric ozone decreases low cloud (a positive rapid adjustment). Changes in circulation due to decreases in stratospheric ozone are found to affect SH clouds and the atmospheric levels of sea salt aerosol which would contribute additional rapid adjustments, possibly of comparable magnitude to the SARF from stratospheric ozone depletion (Grise et al., 2013, 2014).

Without sufficient information yet to assess the ERFs, this assessment relies on offline radiative transfer calculations of SARF for both tropospheric and stratospheric ozone. Since AR5, the Coupled Chemistry Model Initiative (CCMI) project has used 20 coupled chemistry-climate models to simulate historical trends in tropospheric and stratospheric ozone (Morgenstern et al., 2017). The SARFs from these models were calculated with an offline radiative transfer model (Checa-Garcia et al., 2018). The values for the 1850 to 2014 SARF were 0.33 W m^{-2} for changes in tropospheric ozone, and –0.03 W m^{-2} for changes in stratospheric ozone. These are in agreement with the AR5 values of 0.36 W m^{-2} (0.18 to 0.54 W m^{-2} 5% to 95% range) and –0.05 (–0.15 to 0.05) W m^{-2} for the period 1850 to 2011 (Myhre et al., 2013b). For tropospheric ozone the assessed central estimate follows Checa-Garcia et al. (2018) and maintains the 50% uncertainty (5%-95% range) from AR5 to give 0.33 (0.16 to 0.50) W m^{-2}. For reference to 1750 an additional 0.04 W m^{-2} should be added (Skeie et al., 2011), giving an overall assessed estimate of 0.37 (0.20 to 0.54) W m^{-2} over 1750-2017.

Stratospheric ozone has been observed since 1979 (Stolarski and Frith, 2006), covering the period over which much of the stratospheric ozone changes have occurred. However, these measurements are not able to constrain the forcing. A comparison of three stratospheric ozone reconstructions, none of which could be excluded by the observational record, showed a large variation (–0.33 W m^{-2} to –0.12 W m^{-2}) (Hassler et al., 2013). This assessment therefore increases the central estimate to be in the middle of the Hassler et al. (2013) range with a 5%-95% uncertainty of ± 0.075 W m^{-2} to give –0.075 (–0.15 to 0.0) W m^{-2} for 1850 to 2014 ERF. The same estimate is adopted for 1750–2017. This assessment finds no evidence to support an upper bound above zero.

7.3.2.6 Stratospheric water vapour

This assessment considers direct anthropogenic impacts on stratospheric water vapour by oxidation of methane. Stratospheric water vapour may also change as a rapid adjustment to species that warm or cool the UTLS region, in which case it should be included as part of the ERF for that species. Changes in global temperatures will also impact on stratospheric water vapour as part of the water vapour climate feedback. There have been no updates to the SARF estimate of 0.07 W m-2 of water vapour from methane oxidation by Myhre et al. (2007), and no estimate of associated tropospheric rapid adjustments. The AR5 SARF estimate (Myhre et al., 2013b) is retained as an estimate of the ERF.

7.3.2.7 Synthesis

CO_2 has increased from 284 µmol mol^{-1} in 1850 to 405 µmol mol^{-1} in 2017 (Chapter 2, Section 2.2), an increase in ERF of 0.21W m^{-2} compared to the time of AR5 (2011). CH_4 has increased from 808 nmol mol^{-1} in 1850 to 1850 nmol mol^{-1} in 2017, an increase in ERF of 0.02 W m^{-2} compared to 2011, but an increase of 0.06 W m^{-2} compared to using the AR5 SARF formula with the 2011 concentration (Myhre et al., 2013b). N_2O has increased from 273 nmol mol^{-1} in 1850 to 330 nmol mol^{-1} in 2017, an increase in ERF of 0.02 W m^{-2} compared to 2011 (Table 7.4).

[START Table 7.4 HERE]

Table 7.4: Present-day mole fractions in pmol mol^{-1} (ppt) except where specified) and ERF (in W m^{-2}) for the WMGHGs. Data taken from Chapter 2, Section 2.2. The data for 2011 (the time of the AR5 estimates) are also shown. Some of the concentrations vary slightly from those reported in AR5 owing to averaging different data sources. Radiative efficiencies for the minor gases are given in the appendix. Uncertainties in the RF for all gases are dominated by the uncertainties in the radiative efficiencies [data and uncertainties will be revised for SOD].

	Concentration		ERF vs 1850		ERF vs 1750	
	2017	2011	2017	2011	2017	2011
CO_2 (µmol mol^{-1})	405	390	2.00±0.34	1.79	2.12±0.36	1.91
CH_4 (nmol mol^{-1})	1850	1803	0.49±0.08	0.47	0.54±0.09	0.52
N_2O (nmol mol^{-1})	330	324	0.18±0.02	0.16	0.19±0.02	0.17
CFC-11	229	237	0.059	0.062	0.059	0.062
CFC-12	511	528	0.163	0.169	0.163	0.169
CFC-13	3.18	3.04	0.001	0.001	0.001	0.001
CFC-113	70.9	74.6	0.021	0.022	0.021	0.022
CFC-115	8.49	8.39	0.002	0.002	0.002	0.002
HCFC-22	241	213	0.051	0.045	0.051	0.045

HCFC-141b	24.5	21.4	0.004	0.003	0.004	0.003
HCFC-142b	22.3	20.8	0.004	0.004	0.004	0.004
HFC-23	29.9	24.1	0.005	0.004	0.005	0.004
HFC-32	14.71	5.15	0.002	0.001	0.002	0.001
HFC-125	23.1	10.3	0.005	0.002	0.005	0.002
HFC-134a	95.6	62.7	0.015	0.010	0.015	0.010
HFC-143a	20.8	12.0	0.003	0.002	0.003	0.002
HFC-152a	6.80	6.55	0.001	0.001	0.001	0.001
SF_6	9.25	7.30	0.005	0.004	0.005	0.004
SO_2F_2	2.32	1.71	0	0	0	0
NF_3	1.62	0.83	0	0	0	0
CF_4	83.6	79.0	0.004	0.004	0.004	0.004
C_2F_6	4.66	4.17	0.001	0.001	0.001	0.001
CH_3CCl_3	2.22	6.29	0	0	0	0
CCl_4	79.6	86.1	0.014	0.015	0.014	0.015
CFCs[1]			0.254	0.263	0.254	0.263
HCFCs			0.059	0.052	0.059	0.052
HFCs			0.033	0.021	0.033	0.021
Halogens			0.374±0.075	0.363	0.374±0.075	0.363
Total			3.02±0.24	2.77	3.21±0.24	2.97

[END Table 7.4 HERE]

7.3.3 Aerosols

Anthropogenic activity, and particularly burning of biomass and fossil fuel, has led to a substantial increase in the atmospheric aerosol loading since pre-industrial times. This is particularly true for sulphate and carbonaceous aerosols, as discussed in Chapter 6 (Section 6.2.1). This has in turn led to changes in the scattering and absorption of incoming solar radiation, and also affected cloud micro- and macrophysics and thus cloud radiative properties. The aerosol changes have been strongly heterogeneous in both space and time and have impacted not just Earth's radiation budget but also air quality, as discussed in detail thrroughout Chapter 6. Here, the assessment is focused on the global impacts of aerosols on Earth's energy budget. Consistent with the terminology introduced above, the effective radiative forcing due to changes in direct aerosol-radiation interactions (ERFari) is equal to the sum of the instantaneous TOA radiation change (RFari) and the subsequent rapid adjustments. The rapid adjustments in ERFari are principally caused by cloud changes, and also by lapse rate and atmospheric water vapour changes, all mainly associated with absorbing aerosols (e.g., black carbon, organic carbon, soil dust). Likewise, the increase in cloud droplet number concentrations associated with an increase in aerosols with the ability to act as cloud condensation nuclei (CCN) can be divided into an instantaneous forcing component (RFaci) due to smaller but more numerous cloud droplets and subsequent adjustments to cloud water content or extent (spatial and/or temporal), which together give an effective radiative forcing due to aerosol-cloud interactions (ERFaci). In theory, a change in the abundance of ice nucleating particles (INPs), and thus ice crystal number concentration, may also have occurred since pre-industrial times, but whether anthropogenic activity in fact leads to appreciable changes in INP abundance remains controversial. However, if such changes have occurred, they could have had an impact on the properties of mixed-phase and cirrus (ice) clouds, and thus contributed to the ERFaci. In the following, an assessment of the RFari and ERFari (7.3.3.1) focusing on process-based evidence (7.3.3.1.1), satellite-based evidence (7.3.3.1.2) as well as model-based evidence

[1] Includes CFC-114, Halon-1211, Halon-1301 and Halon-2401

(7.3.3.1.3) is presented. The same lines of evidence are presented for RFaci and ERFaci in 7.3.3.2. All of the above lines of evidence are thereafter combined with energy balance constraints on the total aerosol ERF (7.3.3.3) to arrive at an overall assessment of the total aerosol ERF (ERFari+aci) in 7.3.3.4.

7.3.3.1 Aerosol-radiation interactions

7.3.3.1.1 Process-based lines of evidence

Aerosol radiative properties are described by the aerosol optical depth (AOD), the single-scattering albedo, and the asymmetry factor. These quantities are determined by the size distribution, the mixing state, the chemical composition (Haywood and Boucher, 2000; Forster et al., 2007), and the geometric shape of the aerosol particles (Dubovik et al., 2006; Kok et al., 2017; Mishchenko et al., 2003; Wang et al., 2013; Yang et al., 2007; Zhao et al., 2003). Since AR5, deeper understanding of the processes that govern the above properties, and thus RFari, has emerged. Combined with new insight related to rapid adjustments to aerosol forcing, this progress has informed new satellite-based and model-based estimates of RFari and ERFari and associated uncertainties (Sections 7.3.3.1.2, 7.3.3.1.3).

Aersosol radiative properties can be computed accurately for spherical particles, but large uncertainties still exist for non-spherical particles. Uncertainties related to particle shape have been estimated to contribute to an RFari uncertainty range from -18% to 26% and from -16.3% to 115.3% at the top and bottom of the atmosphere, respectively (Kahnert and Kylling, 2004), though other studies have reported lower estimates (e.g. Yi et al., 2011). Inconsistencies in the assumption of aerosol particle shape during the retrieval of aerosol radiative properties also introduce errors in satellite-based estimates of RFari. Wang et al. (2013) found that a non-spherical aerosol shape assumption leads to decreases in the absolute values of shortwave (by 13%) and longwave (by 6%) ERFari compared with a spherical shape assumption. Additionally, aerosol particle habit assumptions can also change the simulated ERFari (Wang et al., 2013).

Overall, uncertainties in the estimation of aerosol radiative properties remain the largest source of uncertainties in determining RFari (Li et al., 2009), especially with regard to their vertical distribution (Kahn et al., 2017). Since AR5, the absorbing component of organic aerosols (brown carbon), has been identified as a significant contributor to total aerosol absorption (Samset et al., 2018) which is present even at high altitudes where forcing efficiency is high (Zhang et al., 2017). Brown carbon has since AR5 been more widely included in climate models, thus influencing model-based estimates of RFari and ERFari. For example, Feng et al. (2013) found that brown carbon can contribute up to 20% of the total aerosol absorption, based on the IMPACT chemical transport model. Similar results were found by Jo et al. (2016) using the GEOS-Chem model.

Apart from uncertainties in aerosol emissions, distributions, mixing state and optical properties, it has also been found that the ERFari simulated by climate models is sensitive to model parameterizations of radiative transfer, aerosol mixing treatment (Zhang et al., 2018b; Zhou et al., 2017b, 2018) and the subgrid-scale variability in clear-sky relative humidity (the key factor in calculating particle hygroscopic growth).

Myhre and Samset (2015) showed how the use of 2-stream radiative transfer schemes, as included in many major climate models, leads to a 10% underestimate of RFari, relative to 8-stream calculations employed by some offline calculations. Aerosol radiative properties also depend strongly on the degree to which different chemical species are mixed within the same particle (internal mixing) as opposed to existing in separate particles (external mixing). Regionally, the mixing state of aerosols may influence not only the magnitude but also the sign of the RFari. Significant errors in scattering, absorption, and hygroscopicity are produced if the aerosol mixing state is not properly represented (Ching et al., 2016). Matsui et al. (2018) found that resolving the diversity in black carbon mixing state could amplify the uncertainty range of black carbon RFari due to uncertainties in emission size distribution by five to seven times. Boucher et al. (2016) showed how aerosol uncertainties can be correlated, noting how accelerated ageing of black carbon in polluted environments (Gustafsson and Ramanathan, 2016; Peng et al., 2016) also leads to increased hygroscopicity, rapid wet removal, and, consequently, a modified aerosol distribution, with subsequent impacts on RFari.

Finally, as discussed in Section 7.1, there has been considerable progress in the understanding of rapid adjustments in response to a wide range of forcings since AR5. This is also true for aerosol forcing, and particularly the adjustments to forcings due to black carbon. Stjern et al. (2017) found that for black carbon, about 30% of the RFari is offset by rapid adjustments of clouds (specifically, an increase in low clouds and decrease in high clouds) and lapse rate, by analyzing the simulations of five Precipitation Driver Response Model Intercomparison Project (PDRMIP) models. Similar results have been reported from idealized experiments using modified black carbon wet removal and offline radiative transfer (Hodnebrog et al., 2014; Samset and Myhre, 2015). Smith et al. (2018b) considered more models participating in PDRMIP and suggested that half the RFari was offset by rapid adjustments for black carbon, whereas for sulfate aerosol, rapid adjustments of clouds amplified RFari somewhat. Zhao and Suzuki (submitted) found that about 70% of the RFari of black carbon is offset by rapid adjustments, whereas for sulphate, rapid adjustments amplified RF by about 35% based on climate simulations.

7.3.3.1.2 Satellite-based lines of evidence

The total radiative effect of aerosols on present-day radiative fluxes, REari, is easier to estimate from observations than RFari, because the latter requires knowledge of pre-industrial aerosol distributions. Since AR5, estimates of REari have progressed by including aerosols above land surface and clouds. Using passive and active aerosol remote sensing retrievals, Lacagnina et al. (2017) and Oikawa et al. (2018) both estimate a globally-averaged, all-sky REari of -2.1 W m^{-2}, with a 1-sigma uncertainty range of 0.7 and 0.2 W m^{-2}, respectively. That estimate is less negative than the ocean-only range of -4 to -6 W m^{-2} assessed in AR5 (Boucher et al., 2013) because REari is less negative over more reflective surfaces.

Estimating RFari requires an estimate of industrial-era changes in AOD and absorption AOD, which are often taken from global aerosol modelling. Since AR5, updates to methods of estimating RFari based on aerosol remote sensing or data-assimilated reanalyses of atmospheric composition have been published. Ma et al. (2014) applied the method of Quaas et al. (2008) to updated broadband radiative flux measurements from CERES, MODIS-retrieved AODs, and modelled anthropogenic fractions to find a clear-sky RFari of -0.6 W m^{-2}. This would translate into an all-sky estimate of about -0.3 W m^{-2} based on the clear-to-all-sky scaling implied by Kinne (2019). Rémy et al. (2018) applied the methods of Bellouin et al. (2013b) to the reanalysis by the Copernicus Atmosphere Monitoring Service, which assimilates MODIS total AOD. Their estimate of RFari remains constant around -0.5 W m^{-2} over the period 2008-2014, and then strengthens from 2015 to reach -0.7 W m^{-2} for the year 2017, a trend they attribute to increases in AOD over India and boreal forests. Kinne (2019) updated his monthly total AOD and absorbing AOD climatologies, obtained by blending multi-model averages with ground-based sun-photometer retrievals, to find a best estimate of RFari of -0.4 W m^{-2}. Those three sets of RFari estimates are scattered around the midpoint of the RFari range of -0.35 ± 0.5 W m^{-2} assessed by AR5 (Boucher et al., 2013). None of these studies account for rapid adjustments.

Satellite- and reanalysis-based estimates rely on the hypothesis that constraining total AOD narrows the uncertainty on RFari. There are two challenges against that hypothesis. First, total AOD varies strongly between different reanalyses (e.g. Table 4 of Randles et al. (2017)), indicating that efforts to improve global retrievals remain needed. Satellite aerosol retrieval capabilities have improved since AR5, including extending records back to the early 1980s (Hsu et al., 2017) and maturing retrievals of AOD and absorption AOD under cloudy-sky conditions (Jethva et al., 2013; Waquet et al., 2016). Second, Regayre et al. (2018) found, using a Perturbed Parameter Ensemble based on the Hadley Centre climate model, that uncertainties in the present-day aerosol distributions are not driven by the same parameters as uncertainties in the industrial-era RFari. Consequently, Johnson et al. (2018) found that AOD is a weak constraint on industrial-era RFari, at least over Europe in July. They recommend applying multiple constraints, identifying sulphate concentrations and decadal trends in AOD as especially strong constraints for RFari, which could open the way to improved satellite- and reanalysis-based methodologies.

In summary, updates to satellite-based RFari estimates made since the AR5 are either in close agreement (Kinne, 2019; Ma et al., 2014) or more negative (Rémy et al., 2018) than the AR5 best estimate of –0.35 W m-2 (Boucher et al., 2013). The more negative estimate of Rémy et al. (2018) is due to neglecting a small positive contribution from absorbing anthropogenic aerosols above clouds and obtaining a larger anthropogenic fraction than Kinne (2019). However, Rémy et al. (2018) did not update their assumptions on black carbon anthropogenic fraction and contribution to anthropogenic absorption to reflect recent downward revisions (Section 7.3.3.1.3). If they had, their estimate would be even more negative. Kinne (2019) made those revisions so on balance, more weight is given to that study to re-assess the best estimate of satellite-based RFari to be only slightly stronger than AR5 at –0.4 W m-2. The likelihood confidence interval given by AR5 was ±0.5 W m-2 (Boucher et al., 2013). Continuing uncertainties in the anthropogenic fraction and challenges to the basis of satellite-based approaches mean that this range is adopted again here, despite improved knowledge of anthropogenic absorption. The assessed best estimate and *likely* RFari range from satellite-based evidence is therefore –0.4 ±0.5 W m-2.

7.3.3.1.3 Model-based lines evidence

While satellite-based evidence can be used to calculate RFari, global climate models are needed to calculate the associated rapid adjustments and the resulting ERFari, using the methods described in Section 7.3.1. This calculation is complicated by the fact that the rapid adjustments of lapse rate, water vapour and clouds caused by absorbing aerosols through changes in the thermal structure of the atmosphere, previously termed the semidirect effect of aerosols, are not easily distinguished from cloud adjustments in ERFaci, especially as more models consider internally mixed aerosols that include both absorbing hydrophobic matter and hydrophilic aerosol species.

Model-based estimates of RFari. In AR5, the RFari was assessed to –0.35 ± 0.5 W m^{-2} (Boucher et al., 2013) based on all available lines of evidence. However, a range of developments since the AR5 affect our model-based estimate of RFari. Global emissions of most major species are found to be higher in the current inventories, and with increasing trends, except for the sulphate precursor SO_2, which is similar to the AR5 estimate and with a flat trend (Hoesly et al., 2018). Myhre et al. (2017) showed, in a multi-model experiment, that the net result of these changes is an RFari trend that is flat in recent years. Concurrently, the positive forcing from the absorbing component of organic aerosols has been found to be somewhat stronger than assessed in AR5. In AR5, the assessment of black carbon RFari was markedly strengthened by the assessments provided by Bond et al. (2013), where a key factor was a perceived underestimate of modelled atmospheric absorption when compared to Aeronet observations (Boucher et al., 2013). This assessment has since been modified by new knowledge of the impact of the resolution of emission inventories (Wang et al., 2016), the representativeness of Aeronet sites (Wang et al., 2018), issues with comparing their absorption retrieval to models (Andrews et al., 2017a), and the ageing (Peng et al., 2016), lifetime (Lund et al., 2018b) and average optical parameters (Zanatta et al., 2016) of black carbon.

Consistent with the above updates, Lund et al. (2018a) estimated the net RFari between 1750 and 2014 to be –0.17 W m^{-2}, using CEDS emissions (Hoesly et al., 2018) as input to the chemical transport model OsloCTM3 (Figure 7.9). They attribute the weaker estimate relative to comparable AR5 numbers (Myhre et al., 2013a) to stronger absorption by organic aerosol, updated parameterization of BC absorption, and reduced sulfate cooling.

Mewes et al. (2018) resolved the subgrid variability of relative humidity in the ECHAM6-HAM2 model consistent with the specific humidity probability distribution function assumed in the model cloud scheme; they found that the RFari simulated by the model changed from –0.15 to –0.19 W m^{-2}.

Model-based estimates of ERFari. In AR5, the best estimate of ERFari between 1750–2011, combining models and observational constraints, was –0.45±0.5 W m^{-2} (Boucher et al., 2013). Zelinka et al. (2014) used the Approximate Partial Perturbation (APRP) technique to quantify the ERFari and ERFaci between 1860 and 2000 in nine CMIP5 models; they estimated the ERFari (accounting for a small contribution also for longwave radiation) to be –0.25 ± 0.22 W m^{-2}. However, it should be noted that in Zelinka et al. (2014) the semidirect effect of aerosols is not included in ERFari but in ERFaci. Zhang et al. (2016) found the overall ERFari of three major anthropogenic aerosols (sulfate, black carbon and organic carbon) between 1850 and 2010 to be –0.3 W m^{-2} based on simulations with BCC_AGCM2.0_CUACE/Aero, in which a very small contribution came from rapid adjustments, while Zhou et al. (2017) obtained a very similar value of the ERFari of –0.34 W m^{-2} by considering partial internal mixing (PIM) treatment of aerosols; In their study, the PIM treatment reduced the negative ERFari by 19%. Grandey et al. (2018) simulated the SW RFari between 1850 and 2000 to be –0.18±0.01 W m^{-2} based on the CAM5.3-MARC-ARG simulation. The average ERFari from GCM simulations since 2014 is about –0.26 W m^{-2} (Table 7.5), and thus much smaller in magnitude than the best estimate of ERFari in AR5.

Overall, based on the model-based evidence alone, ERFari is assessed to be –0.2 ± 0.2 W m^{-2}, slightly weaker (less negative) than in AR5. There is no model-based evidence that suggests a positive ERFari.

[START FIGURE 7.9 HERE]

Figure 7.9: Radiative forcing time series for the major anthropogenic aerosol species (1750-2014), based on CEDS emissions. From Lund et al. (2018a). [To be replaced by AeroCom Phsse III and/or AerChemMIP results.]

[END FIGURE 7.9 HERE]

[START Table 7.5 HERE]

Table 7.5: ERFaci from GCM model simulations since 2014.

Number	Models	ERFari (W m^{-2})	ERFaci (W m^{-2})	ERFari+aci (W m^{-2})	reference
1	Nine CMIP5 models: IPSL-CM5A-LR, CanESM2, NorESM1-M, CSIRO-Mk3-6-0, HadGEM2-A, GFDL-CM3, MIROC5, MRI-CGCM3, CESM1-CAM5	–0.25 ± 0.22	–0.92±0.34	–1.17±0.30	Zelinka et al. (2014)
2	ECHAM6-HAM2	—	–0.7 (60°S–60°N ocean)	—	Neubauer et al. (2017)
3	CAM5.3-Oslo	—	–1.07	—	Karset et al. (2018)
4	CAM5.3-MARC-ARG	–0.17±0.01	–1.51±0.05	–1.69±0.05	Grandey et al. (2018)
5	HadGEM3-GA4-UKCA	–0.03 (–0.19, 0.13)	–1.42 (–2.20, –0.61)	–1.46 (–2.18, –0.71)	Regayre et al. (2018)
6	BCC_AGCM2.0_CUACE/Aero	–0.23	–1.01	–1.23	Zhou et al. (2018)
7	IPSL-CM6A-LR	–0.37	–0.28	–0.65	RFMIP, CMIP6
8	MRI-ESM2-0	–0.47	–0.72	–1.19	RFMIP, CMIP6
9	CNRM-ESM2-1	–0.14	–0.61	–0.75	RFMIP, CMIP6
	Post-AR5 Average	–0.24	–0.91	–1.17	RFMIP, CMIP6

[END Table 7.5 HERE]

7.3.3.2 Aerosol-cloud interactions

7.3.3.2.1 Process-based evidence

Aerosols effects on boundary layer clouds. Anthropogenic aerosol particles primarily affect boundary layer water clouds by serving as additional CCN and thus, to an extent that depends on cloud base updraft (W_b), increasing cloud drop concentration (N_d) (Twomey, 1959). Increasing N_d while holding liquid water path (LWP) constant reduces cloud drop effective radius (r_e) and increases the clouds' albedo. This induces an instantaneous negative radiative forcing (RFari). The clouds are thought to adjust to this primary effect of the CCN by slowing the coalescence rate, thus delaying or suppressing rain in precipitating clouds. Rain generally depletes LWP and shortens cloud life time and/or reduces cloud fractional coverage (Cf) (Albrecht, 1989), thus any aerosol-induced rain delay or suppression would be expected to results in increased LWP and Cf. Such aerosol-induced changes are considered rapid adjustments associated with RFaci, and could potentially lead to an ERFaci considerably larger in magnitude than the RFaci alone. However, adding aerosols to non-precipitating clouds has been observed to have the opposite effect on LWP (i.e. a reduction). (Christensen and Stephens, 2011; Lebsock et al., 2008). These findings have challenged the understanding described above and have been explained by enhanced evaporation of the smaller droplets in the aerosol-enriched environments, and resultant enhanced mixing with ambient air.

Our understanding of the processes determining the LWP and Cf effects have improved substantially since AR5 (Fan et al., 2016). The cloud drop coalescence rate increases steeply with r_e^5, which increases monotonically with height above cloud base in developing convective clouds (Freud and Rosenfeld, 2012). The cloud geometrical thickness (CGT) required for rain initiation (D_r) is thought to occur when cloud top r_e reaches 13-14 μm. For warm rain onset, the minimum CGT of a cloud increases with aerosol loading, ranging from tens of meters (ultra clean, small N_d) to several km (severe pollution, large N_d) (Chen et al., 2008; Gerber and Gerber, 1996; Konwar et al., 2012; Pinsky and Khain, 2002; Prabha et al., 2011; Rosenfeld and Gutman, 1994; vanZanten et al., 2005). There is now evidence that the aerosol effects on LWP and Cf in marine boundary layer clouds may be greater than assessed in AR5. Aerosols, through their control on N_d and Dr, influence when marine stratocumulus clouds (MSC) would break up from full overcast to partly cloudy in response to the development of substantial (greater than about 2 mm/day) rain rates (Muhlbauer et al., 2014; Stevens et al., 2005; Wood et al., 2011). This is not limited to MSC in the subtropics, but also occurs over mid-latitude oceans in polar air outbreaks (Abel et al., 2017). The transitions from broken to overcast MSC can be caused by anthropogenic aerosols such as emitted from ships stacks (Goren and Rosenfeld, 2012; Rosenfeld et al., 2006) or advected from the continents (Goren and Rosenfeld, 2015). However, most changes between overcast and broken MSC are observed without any obvious relationship to anthropogenic aerosols, thus not incurring any ERFaci. The difference in cloud radiative effects (CREs)at the TOA between broken and overcast MSC, regardless of the causes to the variability in aerosol, were observed to average 109 ±18 W m^{-2}, composed of Cf (42 ± 8%), LWP (32 ± 8%) and albedo (26 ± 6%) effects (Goren and Rosenfeld, 2014). This decomposition was generally supported by other studies (George and Wood, 2010; Kaufman et al., 2005). The transitions from overcast to broken MSC are thought to occur when N_d decreases below a maximum N_d of about 50 cm^{-3}, associated with large decreases in CCN as observed by in situ aircraft measurements (Cui et al., 2014; Terai et al., 2014; Wood et al., 2011), while breakup has been observed to occur for even larger N_d (about 80cm^{-3}) in deeper clouds with CGT approaching 800 m (Lloyd et al., 2018). Such low values of N_d are well within the aerosol-limited regime, where W_b has little effect on N_d (Chen et al., 2016a), meaning that CCN dominate the variability in N_d. However, processes other than aerosol effects control CGT, which must exceed D_r for precipitation to form and clouds to break up.

Similar to the albedo effect being defined only for changes in N_d for a fixed LWP (Twomey, 1977), it has been argued that the LWP and Cf adjustments should be defined only for changes in N_d for a fixed CGT (Rosenfeld et al., 2019). Because CGT encapsulates much of the meteorological effects, application of this principle has made the problem of isolating aerosol effects from meteorological effects more tractable. Satellite analysis of LWP and Cf adjustments over the ocean between the Equator and 40°S during Austral summers (Rosenfeld et al., 2019) showed that doubling N_d may increase LWP by more than 50% for N_d<150 cm^{-3}. This is applicable equally to MSC and cumulus (CU) clouds, although the absolute magnitude of the effect appears to be twice as strong for MSC compared to CU. Previous observational (Chen et al., 2014; Malavelle et al., 2017; Michibata et al., 2016; Toll et al., 2017) and modelling (Lebo and Feingold, 2014; Sato et al., 2018; Seifert et al., 2015) studies that analysed the LWP effect irrespective of CGT obtained negligible to slightly negative LWP susceptibility ($\lambda=\partial \ln(LWP)/ \partial \ln(N_d)$) and thus inferred much less cooling. This may have been caused by the fact that deeper clouds have larger LWPs, rain more, and thus scavenge aerosols more efficiently. The expected outcome is that clouds with higher N_d appear to have small LWP, which constitutes apparent negative susceptibility, when not measured for a fixed CGT. The same considerations apply to the Cf effect. Sorting by CGT, (Rosenfeld et al., 2019) find that the CRE at the TOA doubles for a doubling N_d, up to N_d of about 150 cm^{-3} where the LWP and Cf effects tend to saturate (Rosenfeld et al., 2019). In contrast to these findings are satellite observations of clouds affected by volcanic plumes and ship tracks, which showed that the reduction of r_e on the background of clouds with already suppressed precipitation can decrease LWP and CRE, possibly due to faster evaporation of the smaller droplets (Chen et al., 2014; Toll et al., 2017) (Section 7.3.3.2.2).

Given enough time (several tens of hours), aerosol-induced cloud changes tend to modify their environment in a way that buffers the aerosol effects on the clouds. For example, in response to aerosol-induced suppression of rain, the clouds would deepen just enough to restore that amount of rain (Stevens and Feingold, 2009). More generally, LESs (Lee et al., 2012; Seifert et al., 2015) run until reaching subsidence radiative-convective equilibrium (SRCE) after a few days, showed that an additional slow cloud adjustment occurs because the environment is modified in a way that buffers the faster adjustment of Cf and LWP effects. Seifert et al., (2015) showed that after reaching SRCE the aerosol effect on mean properties such as Cf, total rain amount, and radiative forcing is negligible. Until SRCE is achieved, however, the aerosol concentration significantly affects the cloud field properties. Satellite observations and reanalysis data show that the conditions of SRCE are not realistic in nature due to the generally short cloud lifetimes (Dagan et al., 2018). The large-scale forcing and SST change frequently enough to prevent the cloud field from ever reaching SRCE and hence cloud fields in nature are in a transient stage for which the aerosol effects on the LWP and Cf are still very important (Seifert et al., 2015).

Buffering arguments have previously been used to exclude the LWP and Cf adjustments from newly developed parameterizations of aerosol effect (Fiedler et al., 2017, 2018; Pincus et al., 2016; Stevens et al., 2017). In fact, the estimated LWP susceptibility was revised to be progressively lower during the last two decades from λ=0.15 to λ=-0.2 (Sato and Suzuki, 2019), along with respectively lower ERFaci. On this background the observed λ=0.58 of marine boundary layer clouds found in Rosenfeld et al. (2019) represents a sharp break with past estimates, although its general validity has yet to be confirmed and reproduced by other studies. If susceptibility is in fact as large as Rosenfeld et al. (2019) suggests, that would imply a considerable increase of ERFaci compared to many previous estimates. However, some of this increase may be offset by positive contribution to ERFaci through deep and ice clouds, for which some evidence has emerged since the AR5 (Kablick et al., 2018; Yan et al., 2014). However, cloud-resolving simulations of the aerosol effects on deep convective clouds have shown mostly neutral radiative effects (Blossey et al., 2018). Convective invigoration effects of ultrafine aerosols that are too small to serve as CCN (diameter smaller than about 60 nm) have been proposed to be important in this context (Fan et al., 2018), but are often neglected.

In contrast to marine boundary layer clouds, boundary layer water clouds over land rarely produce rain (Jiang et al., 2018; Mülmenstädt et al., 2015) due to the much higher CCN and N_d there as compared to over ocean (Li et al., 2018a). Therefore, the adjustment of LWP and Cf in response to aerosol effects on drop coalescence is relatively less important over land.

Aerosol effects on mixed-phase and ice clouds. Aerosols can serve as INPs that initiate the ice phase in supercooled water clouds. Glaciation of supercooled layer clouds, such as prevalent in the arctic, leads initially to conversion of the cloud droplets to fewer and larger ice particles, which reduce the cloud's albedo and hence have a positive shortwave radiative effect. The ice particles often precipitate and lead to cloud dissipation, amplifying the positive shortwave radiative effects. However, during the polar night this leads to a strong surface cooling, because downward longwave radiation is reduced. Addition of anthropogenic INP were observed to glaciate and eventually dissipate supercooled layer clouds (Heymsfield et al., 2010). However, the ability of anthropogenic aerosols to act as INPs have recently been called into question (Vergara-Temprado et al., 2018).

There has been some advancement since AR5 with respect to the effects of aerosols on mixed phase clouds. The importance of mixed phase clouds is manifested by the observations that very little precipitation over land originates from clouds without mixed phase processes (Mülmenstädt et al., 2015). The relative scarcity of INP in the Southern Oceans is the *likely* cause for the relatively larger abundance of persistent supercooled cloud decks compared to the NH and the resultant large solar reflectance from them (Bodas-Salcedo et al., 2016). Adding anthropogenic aerosols from ship stacks to supercooled cloud decks of marine stratocumulus was observed to enhance mixed phase precipitation, which led to a decrease in the LWP and albedo compared to the effect of ship tracks in warmer clouds (Christensen et al., 2014). Secondary ice formation (i.e., not mediated by INP) becomes stronger with larger drops. In marine tropical clouds the secondary ice dominates, thus rendering the INP of little relevance (Yang et al., 2018a). This transition from dominance of INP to dominance of secondary ice nucleation was observed to occur when cloud drop effective radius exceed about 12 μm at -5°C (Rosenfeld et al., 2011).

Implications for ERFaci. A strong negative ERFaci mediated by marine boundary layer clouds was in AR5 mostly attributed to the albedo effect (Boucher et al., 2013). Accumulating evidence shows that there is *very high confidence* in the existence of such an effect. Most of the recent studies have continued to show small negative changes of LWP associated with more aerosols, supporting the view that the albedo effect is dominant, despite some observations clearly showing aerosols enhancing cloud cover and LWP. This apparent discrepancy can potentially be resolved by the notion that deeper clouds have a larger LWP and rain more heavily, thus scavenging the aerosols more efficiently and resulting in clouds that have both larger LWP and less aerosols. This increases the likelihood that LWP and cloud cover effects work in the same direction as the albedo effect, thus increasing the magnitude of the negative ERFaci as assessed in AR5 to a yet poorly known extent. Observational quantification of aerosol effects on mixed phase, deep and ice clouds is challenging and poorly bounded. There is *medium confidence* that the net ERFaci of mixed-phase, deep and ice clouds is positive, thus potentially decreasing the absolute magnitude of the overall ERFaci.

7.3.3.2.2 Satellite-based evidence

Since AR5, the analysis of satellite observations to investigate aerosol-cloud interactions has progressed along several axes: (i) The concept of forcing and adjustments introduced rigorously in AR5 has helped better categorize studies; (ii) advances have been made to infer causality in aerosol-cloud relationships, and (iii) problems and uncertainties in retrievals are better characterized than before.

There are four key cloud parameters that determine the bulk influence of clouds on Earth's radiation budget. These are cloud particle number concentration (droplets or ice crystals), cloud horizontal extent (cloud fraction), cloud water path (vertical integral of cloud liquid- or ice specific mass, mainly determined by the CGT), and – relevant for terrestrial radiation only – cloud top temperature. As described above, the perturbation of cloud particle number concentrations leads to the radiative forcing due to aerosol-cloud interactions, RFaci. Adjustment processes lead to alterations also of cloud fraction, water path, and top temperature, which, together with RFaci, constitute ERFaci. Since AR5, the large body of literature that assessed statistical relationships between aerosol- and cloud retrievals has grown.

Relationship between liquid-cloud droplet concentration and bulk aerosol quantities. Studies exploiting the statistical relationship between cloud droplet concentration and aerosol quantities to infer clues about RFaci follow the early work by Nakajima et al. (2001) and Bréon et al. (2002). In these, a positive relationship between column cloud droplet concentration and aerosol index (AI ; AOD multiplied by Angström exponent) and a negative relationship between cloud droplet effective radius, r_e, and AI, respectively were documented. Several other studies have related cloud quantities to AOD, but it is now well documented that such an approach leads to low estimates of RFaci since AOD is a poor proxy for cloud-base

CCN (Penner et al., 2011; Stier, 2016). Gryspeerdt et al. (2017) demonstrated that the statistical relationship between droplet concentration, N_d, and AOD leads to inferred RFaci that is underestimated by at least 30 %, while the use of AI leads to estimates of RFaci to within ±20 %, if the anthropogenic perturbation of AI is known.

Further, studies assessed in AR5 mostly investigated the linear regression between cloud droplet concentration and aerosol (Boucher et al., 2013). Since in most cases, the relationships are not linear over the entire spatiotemporal distribution, this leads to a further bias (Gryspeerdt et al., 2016). Several studies did not relate cloud droplet concentration, but cloud droplet effective radius to the aerosol (Brenguier et al., 2000). This is problematic since then, in order to infer RFaci, one has to stratify by cloud LWP (McComiskey and Feingold, 2012) or else obtain a biased result. Where LWP positively co-varies with aerosol retrievals (which is often the case, Section 7.3.3.2.1) RFaci inferred from such relationships is biased towards too small values. Also, it is increasingly evident that different cloud regimes show different sensitivities (Stevens and Feingold, 2009). Averaging statistics over regimes thus again biases inferred RFaci (Gryspeerdt et al., 2014b). AR5 concluded that RFaci estimates tied to satellite studies showed comparatively weak RFaci, but on the basis of these newer studies, this statement has to be revised (Boucher et al., 2013).

Statistical relationships for liquid-cloud adjustments. Multiple studies related also cloud fraction and LWP to aerosol (e.g., Nakajima et al., 2001). Most studies document a strongly positive relationship between cloud fraction / LWP and AOD/AI (e.g. Kaufman and Koren, 2006; Quaas et al., 2009). Since AR5, however, it has been documented that factors independent of causal aerosol-cloud relationships heavily influence such statistical relationships. These are specifically the swelling of aerosol in the high relative humidity in the vicinity of clouds (Grandey et al., 2013) and the contamination of aerosol retrievals next to clouds by cloud remnants and cloud-side scattering (Christensen et al., 2017; Várnai and Marshak, 2015). Stratifying relationships by possible influencing factors such as relative humidity (Koren et al., 2010) does not yield satisfying results since observations of the relevant quantities are not available at the resolution and quality required. Another solution to this problem was to assess the relationship of cloud fraction / LWP with droplet concentration (Gryspeerdt et al., 2016; Michibata et al., 2016; Sato et al., 2018). The relationship between satellite-retrieved cloud fraction and N_d was found to be positive (Gryspeerdt et al., 2016), implying an overall adjustment that leads to a more negative ERFaci. However, N_d is biased low for broken cloudiness so that this result is called into question (Grosvenor et al., 2018). Zhu et al. (2018) propose to circumvent this problem by considering N_d of only the brightest 10% of the clouds, on the basis of which Rosenfeld et al. (2019) still obtain a positive cloud fraction – N_d relationship (Zhu et al., 2018) and thus larger indicated LWP and Cf susceptibilities to N_d.

The LWP – N_d relationship is debated. Most studies find negative statistical relationships (Gryspeerdt et al., 2018a; Michibata et al., 2016; Sato et al., 2018). As discussed in Section 7.3.3.2.1, Rosenfeld et al. (2019) suggest that this is attributable to a coalescence sink for N_d for deeper clouds with large LWP, which produce more rain than thinner clouds. Further Rosenfeld et al. (2019) stratify the relationship by the thickness of the brightest, i.e. most adiabatic, clouds in each large-scale scene with the idea that these are unaffected by the aerosol. Doing so, they obtain a large positive relationship between LWP and N_d. This methodology attempts to isolate the effects of aerosols on large-scale LWP from other causes that affect LWP of the adiabatic cores in each scene. Attempts to infer causality by conditioning on specific aerosol sources that did not classify clouds by adiabatic core thickness (see below) suggest a small overall LWP – N_d relationship.

Several studies have documented a negative relationship between cloud -top temperature and AOD/AI (e.g. Koren et al., 2005) However, it has been demonstrated that such relationships are also affected by spurious co-variation (Gryspeerdt et al., 2014a). It remains thus unclear, from satellite data, whether a systematic causal effect exists.

Statistical relationships for ice clouds. For ice clouds, different responses of the ice crystal concentration, Ni, to aerosol perturbations may occur, depending on the freezing mechanism and aerosol type (Kärcher, 2017). Only few satellite studies investigate ice cloud responses to aerosol perturbations so far. Gryspeerdt et al. (2018b) find a positive relationship between aerosol and Ni for cold cirrus under strong dynamical forcing. Zhao et al. (2018) conclude that the sign of the ice crystal size – aerosol relationship depends on humidity. While these studies support modelling results that ice clouds do respond to anthropogenic aerosols, no quantitative conclusions about RFaci for ice clouds can be drawn yet, precluding also conclusions about adjustments.

Attempts to infer causality. Since AR5, there were many efforts to better characterize the causality in aerosol-cloud relationships. In order to explore a clear causal effect of aerosols on clouds, which is impossible from statistical relationships alone, two main aerosol sources external to the physical climate system have been exploited.

(i) The fact that ships emit aerosols and aerosol precursor gases into an otherwise pristine marine air, sometimes visible as ship tracks (Conover, 1966), has been used as a means to assess cloud adjustments to aerosol emissions. Goren and Rosenfeld (2014) suggested that both, cloud LWP and cloud cover increase in response to the ship emissions, contributing three quarters to the total ERF_{aci} for a case of mid-latitude stratocumulus. Christensen and Stephens (2011) found that such a strong adjustment occurs for open-cell regimes, while the adjustments to RFaci are comparatively small in closed-cell regimes. Also exploiting satellite observations of ship emissions, Christensen et al. (2014) demonstrated that ice- and mixed-phase cloud adjustments are such that the overall ERF_{aci} for these clouds is small. Toll et al. (2017) found an overall small response of LWP and cloud fraction, with some discernible change only for raining clouds, especially in moist regimes.

(ii) Volcanic emissions were identified as another source of information (Gassó, 2008). Yuan et al. (2011) document from satellite observations substantially larger cloud fraction, higher cloud tops, reduced precipitation likelihood, and increased albedo in the volcanic plume of the Kilauea volcano in cumulus cloud fields. Ebmeier et al. (2014) confirmed the increased LWP and albedo for other volcanoes. In turn, for the very large eruption of the Holuhraun (Iceland) volcano, Malavelle et al. (2017) did find a strong decrease in cloud droplet effective radius in satellite observations, but no large-scale change in LWP. However, when accounting for meteorological conditions, McCoy et al. (2018) concluded that at least for cyclonic conditions, the extra Holuhraun aerosol did enhance LWP. Toll et al. (2017) examined a large sample of volcanoes and also found a distinct Twomey effect, but found small LWP changes on average. Gryspeerdt et al. (2018a) demonstrate that the negative LWP – Nd relationship becomes very small when conditioned on a volcanic eruption. They conclude that the causal effect of the aerosol on LWP is small in most regions.

Other approaches to identify causality (e.g. from the hemispheric contrast, or from weekly cycles) also allow to identify signals in Nd, but did not identify clear results for adjustments (Feng and Ramanathan, 2010; Quaas et al., 2009a).

In summary of these findings, there is *high confidence* that anthropogenic aerosols lead to an increase in cloud droplet concentrations. In terms of the adjustments, most studies suggest that on average, no large, systematic changes in LWP occur, although there are also studies that suggest a strong negative forcing from adjustments. There is *medium confidence* that liquid-cloud fraction increases in response to aerosol increases. There is no observational evidence at present for a significant response of ice clouds to aerosol perturbations.

[START Table 7.6 HERE]

Table 7.6: Studies quantifying aspects of the global ERFaci that are mainly based on satellite retrievals and were published since AR5. All forcings/adjustments as global annual mean values in W m-2. Most studies split the ERFaci into RFaci and adjustments in LWP and cloud fraction separately. All published studies only considered liquid-water clouds. Some studies assessed the RFaci and the LWP adjustment together and called this "intrinsic forcing" and the cloud fraction adjustment "extrinsic forcing". Published uncertainty ranges are converted to 5-95 % confidence intervals.

RFaci	LWP adjustment	cloud fraction adjustment	Reference
"intrinsic forcing"			Nomenclature from Chen et al. (2014) and Christensen et al. (2016)
–0.6±0.6	n/a	n/a	Bellouin et al. (2013a)
–0.5±0.5		–0.5±0.5	Chen et al. (2014)
–0.4±0.3		n/a	Christensen et al. (2016)
–0.3±0.4		–0.4±0.5	Christensen et al. (2017)
–0.4 (–0.2 to –1.0)	n/a	n/a	Gryspeerdt et al. (2017)
–1.0±0.4	n/a	n/a	McCoy et al. (2017a)
n/a	n/a	–0.5 (–0.1 to –0.6)	Gryspeerdt et al. (2016)
n/a	+0.3 to 0	n/a	Gryspeerdt et al. (2018b) (0 to -60% of RFaci)
–0.8±0.7	n/a	n/a	Rémy et al. (2018)

[END Table 7.6 HERE]

Since AR5, there were several studies that assessed the global effective radiative forcing by aerosol-cloud interactions from satellite observations using different methods (Table 7.6). All studies relied on statistical relationships between aerosol- and cloud quantities to infer sensitivities. Four studies infer RFaci by estimating the anthropogenic perturbation of N_d. For this, Bellouin et al. (2013a) and Rémy et al. (2018) make use of regional-seasonal regressions between satellite-derived N_d and AOD following Quaas et al. (2008). Gryspeerdt et al. (2017) demonstrate that AI is a better proxy to infer RFaci corroborating earlier results by Penner et al. (2011) and Stier (2016) and use this in the regression. McCoy et al. (2017) instead use the sulphate specific mass derived in the MERRA aerosol re-analysis that assimilated MODIS AOD (Rienecker et al., 2011). The other key element is the estimate of the anthropogenic perturbation of the aerosol. Gryspeerdt et al. (2017) and Rémy et al. (2018) use the same approach as Bellouin et al. (2013a) that define anthropogenic fraction using a method adapted from Bellouin et al. (2005). In turn, McCoy et al. (2017) use an anthropogenic fraction from the AEROCOM multi-model ensemble (Schulz et al., 2006). Chen et al. (2014), Christensen et al. (2016) and Christensen et al. (2017) derive the combination of RFaci and the LWP adjustment to RFaci ("intrinsic forcing" in their terminology). They relate statistically AI and cloud albedo and use the anthropogenic aerosol fraction from Bellouin et al. (2013a). The variant by Christensen et al. (2017) is an update compared to the Chen et al. (2014) and Christensen et al. (2016) studies in that it accounts better for ancillary influences on the aerosol retrievals such as aerosol swelling and 3D radiative effects. Chen et al. (2014) and Christensen et al. (2017) use the relationship between cloud fraction and AI to further infer the cloud fraction adjustment. Gryspeerdt et al. (2017) do this in a similar way, but aim to account for non-causal aerosol – cloud fraction correlations by using N_d as a mediating factor. Finally, Gryspeerdt et al. (2018a) derive an estimate of the LWP adjustment using a method similar to Gryspeerdt et al. (2016). They estimate that the LWP adjustment offsets 0 to 60% of the (negative) RFaci.

In summary of the studies, RFaci has a plausible range of –1.0 to –0.3 W m^{-2}. The above estimates suggest that LWP adjustments decrease the ERFaci compared to the RFaci by 0 – 60%. In turn, the cloud fraction adjustment, according to the above studies, amplifies the ERFaci compared to the RFaci by about 130%. This brings the estimated range of ERFaci, considering only liquid-water clouds, to a plausible range of –0.5 to –2.0 W m^{-2}.

On average across the published studies (Table 7.6), RFaci is –0.7 ± 0.5 W m^{-2}. Only one study assessed global LWP adjustments. It concluded that they decrease the ERFaci compared to the RFaci by 0 – 60%. The average for the sum or RFaci and LWP adjustments, as well as published assessments of the "intrinsic forcing") is –0.4 ± 0.4 W $m^{–2}$. Three studies assessed the global cloud fraction adjustment, at –0.5 ± 0.5 W $m^{–2}$. From this assessment, the range of ERFaci considering only liquid-water clouds, is –0.9 ± 0.6 W $m^{–2}$ (5–95% uncertainty range).

7.3.3.2.3 Model-based evidence

In addition to the general methods for calculating ERF described in 7.3.1, ERFaci can be estimated statistically from the susceptibility of cloud albedo to changes in aerosol properties (Christensen et al., 2017; Ghan et al., 2016; Neubauer et al., 2017). Ghan et al. (2016) found that estimates of relationships from recent variability were not applicable to the preindustrial to present-day change, which might affect the estimation of ERFaci. Neubauer et al. (2017) suggested that it was important to remove aerosol water uptake when calculating the susceptibilities of cloud properties to changes of aerosol properties.

In AR5, ERFaci was diagnosed as the residual of the total aerosol ERF and ERFari, as the total aerosol ERF was easier to calculate based on available model simulations (Boucher et al., 2013). The best estimates of total aerosol ERF and ERFari in AR5 were –0.9 and –0.45 W m^{-2}, respectively, yielding an ERFaci estimate of –0.45 W m^{-2}. This value is much less negative than the bottom-up estimate of ERFaci from GCMs presented in AR5. Since AR5, efforts have been made continually to reconcile this difference. Zelinka et al. (2014) estimated ERFaci to be –0.92±0.34 W m^{-2}, based on nine CMIP5 models (Table 7.5). It should be noted that in Zelinka et al. (2014) the semi-direct effect of aerosols is included in ERFaci. This is also true for the three RFMIP models from CMIP6 where data is available (IPSL-CM6A-LR, MRI-ESM2-0, CNRM-ESM2-1, see Table 7.5). Combining these three models with the nine CMIP5 models results in a slightly less negative ERFaci estimate of –0.82 W m^{-2} (Figure 7.10a), with much more spread in model-derived SW aerosol ERF than net aerosol ERF (Figure 7.10b). Regayre et al. (2018) used a single model, the HadGEM3-GA4-UKCA model, and 27 perturbed model parameters to assess the uncertainty range of ERFaci; they estimated ERFaci to be –1.42 W m^{-2}, with a 95% uncertainty range of –2.20 to –0.61 W m^{-2}. Other estimates of ERFaci based on single model simulations are also given in Table 7.5. The average ERFaci from GCM model studies since 2014 is about –0.91 W m^{-2}. Together with the ERFari, the overall aerosol ERF (ERFari+aci) estimated from GCM studies since 2014 is about –1.17 W m^{-2}.

Aerosol-cloud interaction remains a very complex problem for large-scale model studies, because many subgrid-scale processes, from the emissions of aerosols and/or their precursors to precipitation formation, are involved. Large-scale models that simulate ERFaci typically include aerosol-cloud interactions in liquid stratiform clouds only, while very few include aerosol interactions with mixed-phase clouds and/or ice clouds. Several studies have pointed out shortcomings in the representation of aerosol-cloud interactions in GCMs (e.g. Jing and Suzuki, 2018; Seinfeld et al., 2016). Adding to this challenge, process-based constraints and temperature-trend constraints on ERFaci are not necessarily consistent with each other. While the latter place an upper bound on the magnitude of the ERFaci of –1.8 W m^{-2}, adjusting the relationships between N_d and rain formation to observations for MSC in the GFDL CM3 model did not produce any warming since 1860 (Suzuki et al., 2013). Doing the same with the MIROC cloud resolving GCM produced an ERFaci of –3 W m^{-2}, six times larger than the assessed ERFaci in AR5 (Jing and Suzuki, 2018). It is thus possible that accepting a very strong negative ERFaci from marine boundary layer clouds implies missing positive ERFaci mediated by other cloud regimes, for example deep and/or ice clouds (*low confidence*).

In AR5 a positive longwave ERFaci of +0.2 W m^{-2} was proposed, implying a partial compensation for such strong negative shortwave ERFaci estimates (Boucher et al., 2013). However, it was found that the net longwave forcing from cloud and thermodynamic adjustments is small for models without explicit aerosol-ice cloud interaction parameterizations (Heyn et al., 2017); a few models with explicit aerosol-ice interaction commonly yield larger terrestrial spectrum forcing, but also larger solar forcing (Heyn et al., 2017; Salzmann et al., 2010). These studies imply that it was unjustified to assume a +0.2 W m^{-2} offset of ERFaci in the longwave spectrum in AR5.

Based on above model-based evidence alone, ERFaci is assessed to –0.9 ± 0.5 W m^{-2} (5% to 95% uncertainty range)

7.3.3.3 Energy balance constraints on the total aerosol ERF

Energy balance models of reduced complexity have in recent years increasingly been combined with Monte Carlo approaches to provide valuable "top-down" observational constraints on the total ERF, and in some cases for individual forcing components like the highly uncertain total aerosol ERF. When the first top-down estimates (also called inverse estimates) emerged (Knutti et al., 2002), it became clear that some of the early ("bottom-up") GCM estimates of total aerosol ERF were inconsistent with the plausible ranges produced by the new and observationally constrained top-down methods. However, as more inverse estimates have been published, it has increasingly become clear that they too are model-dependent and span a wide range of ERF estimates, with confidence intervals that in some cases do not overlap (Forest, 2018). A recent review of 19 such estimates reported a mean of –0.77 W m^{-2} for the total aerosol ERF, and a 95% confidence interval of –1.15 to –0.31 W m^{-2} (Forest, 2018). Adding to that review, a more recent study using the same approach reported an estimate of total aerosol ERF of –0.89 W m^{-2} and a 90% confidence interval of –1.82 to –0.01 W m^{-2} (Bieltvedt Skeie et al., 2018). However, the estimate was very sensitive to how the increase in OHC was incorporated in the analysis. When incorporating the heat content change of the whole ocean, rather than separating the upper (0 m to 700 m) and deep (below 700 m) OHC change, the study produced a best total aerosol ERF of –1.34 W m^{-2} (90% confidence interval –2.20 to –0.46).

Beyond the inverse estimates described above, several other approaches have since AR5 been used to constrain the total aerosol ERF, and among these the historical record of surface air temperature since pre-industrial times has been the most frequently applied observational constraint. For example, Stevens (2015) used the global mean temperature record from the early 20th century to argue for a lower bound of –1.0 W m^{-2} for the total aerosol ERF. Also, in this study a simplified model was used, but here to represent the historical total aerosol ERF evolution for comparison with the observed temperature record. Given the lack of temporally extensive cooling trends in the temperature record of the 20th century and the fact that the historical evolution of greenhouse gas forcing is relatively well constrained (Chapter 2, Section 2.2), the study concluded that a more negative total aerosol ERF than –1.0 W m^{-2} was incompatible with the historical temperature record. This was countered by Kretzschmar et al. (2017), who argued that the model employed in Stevens (2015) was too simplistic, and could therefore not account for the impact of geographical redistributions of aerosol emissions over time. Following the logic of Stevens (2015) but basing their estimates on a subset of CMIP5 models as opposed to a simplified modelling framework, they argued that a total aerosol ERF as low as –1.6 W m^{-2} was consistent with the observed temperature record. Similar arguments were put forward by Booth et al. (2018), who emphasized that the degree of non-linearity of the total aerosol ERF with aerosol emission is a central assumption in Stevens (2015).

The historical temperature record was also the key observational constraint applied in two additional post-AR5 studies (Rotstayn et al., 2015; Shindell et al., 2015) based on a subset of CMIP5 models. Rotstayn et al. (2015) found a strong temporal correlation (> 0.9) between the total aerosol ERF and the global mean surface air temperature. They used this relationship to produce a best estimate for the total aerosol ERF of –0.97 W m^{-2}, but with considerable unquantified uncertainty, in part due to uncertainties in the Transient Climate Response (TCR). Shindell et al. (2015) came to a similar best estimate for the total aerosol ERF of –1.0 W m^{-2} and a 95% confidence interval of –1.4 to –0.6 W m^{-2} but based this on spatial temperature and ERF patterns in the models in comparison with observed spatial temperature patterns.

A separate observational constraint on the total ERF was proposed by Cherian et al. (2014), who compared trends in downward fluxes of solar radiation observed at surface stations across Europe to those simulated by a subset of CMIP5 models. Based on the relationship between solar radiation trends and the total aerosol ERF in the models, they inferred a relatively strong total aerosol ERF of –1.3 W m^{-2} and a standard deviation of ± 0.4 W m^{-2}. Related to Cherian et al. (2014), Storelvmo et al. (2018) found that the reduction in downward solar radiation fluxes measured at surface stations worldwide since the middle of the last century (known as "global dimming") was severely underestimated by the CMIP5 model ensemble mean. The dimming has been attributed to, and is anticorrelated with, global aerosol emissions (Storelvmo et al., 2016), and an underestimation of the dimming trend therefore likely implies a too weak aerosol radiative effect.

Weighing the above lines of evidence, which are based solely on energy balance considerations or other observational constraints, it is virtually certain that the total aerosol ERF is negative (*high confidence*), and *very unlikely* that the total aerosol ERF is more negative than –1.8 W m^{-2} (*medium confidence*).

7.3.3.4 Overall assessment of total aerosol ERF

In AR5 (Boucher et al., 2013), the overall assessment of total aerosol ERF (ERFari+aci) used the median of all GCM estimates published prior to AR5 of –1.5W m^{-2} (5-95% confidence range of –2.4 W m^{-2} to –0.6 W m^{-2}) as a starting point, but reduced the magnitude of that estimate for the following reasons:

1) Models that accounted for aerosol effects on liquid, mixed-phase and ice clouds tended to produce overall smaller ERFari+aci estimates and were at the time deemed "more complete" in their representation of ACI. This subset of models produced a smaller estimate of –1.38 W m^{-2} for the ERFari+aci and consisted of seven semi-independent models.
2) Studies that constrained models with satellite observations were given extra weight (five estimates in total). They produced a median estimate of –0.85 W m^{-2}. For studies that only reported ERFaci, an ERFari of –0.45 W m^{-2} was added to produce an ERFari+aci estimate. Furthermore, a longwave ERFaci of +0.2 W m^{-2} was added to studies that only reported shortwave ERFaci values (which was true in most cases).
3) Based on higher resolution models, doubt was raised regarding the ability of GCMs to represent the cloud adjustment component of ERFaci with fidelity, and particularly the way in which aerosol effects on warm-rain formation were parameterized. The expert judgement was therefore that aerosol effects on cloud lifetime were too strong in the models, reducing the overall ERF estimate.

The above lines of argument, combined with the GCM estimate quoted above, resulted in an overall assessment of ERFari+aci of –0.9W m^{-2} and a 95% confidence range of –1.9 W m^{-2} to –0.1W m^{-2}.

This assessment revises the best estimate and the range relative to AR5 (Boucher et al., 2013), based on updates and revisions to the above lines of argument in post-AR5 publications. Firstly, the studies that included aerosol effects on mixed-phase and ice clouds (argument (1) above) in AR5 relied on the assumption that anthropogenic black carbon could act as atmospherically relevant ice-nucleating particles (INPs), which has since been challenged by the laboratory community (Kanji et al., 2017; Vergara-Temprado et al., 2018). There is also no observational evidence of appreciable ERFs associated with these effects (Section 7.3.3.2.3), and modelling studies disagree when it comes to both their magnitude and sign (Storelvmo, 2017). Likewise, very few GCMs incorporate aerosol effects on deep convective clouds, and cloud-resolving modelling studies report very different impacts on cloud radiative properties depending on cloud environmental conditions (Tao et al., 2012). Thus, it is not clear whether omitting such effects in GCMs would lead to any appreciable net ERF biases, or if so, what the sign of such biases would be. As a result, and in contrast to (Boucher et al., 2013), all models are given equal weight in this assessment whether they include aerosol impacts on convective, ice and mixed-phase cloud processes or not.

In relation to argument (2), there is now a considerably expanded body of literature which suggests that early modelling studies that incorporated satellite observations may have resulted in overly conservative estimates of the magnitude of ERFaci (Section 7.3.3.2.3). Furthermore, based on an assessment of the longwave ERFaci in the CMIP5 models, the offset of 0.2 W m^{-2} used to adjust the longwave contribution to some model's ERF estimate also appears to be too strong (Heyn et al., 2017).

Argument (3) is still valid when it comes to the general limitations in the ability of GCMs to simulate adjustments in LWP and cloud cover in response to aerosol perturbations, but as discussed in 7.3.3.2.1 it is not clear that this will result in biases that exclusively reduce the magnitude of the total aerosol ERF.

The following assessment of total aerosol ERF is based on four lines of evidence: GCM-based, Process-based and Satellite-based evidence as well as other observational and/or energy balance constraints. The median GCM estimate of total aerosol ERF in AR5 was –1.5 W m^{-2} (Boucher et al., 2013), but there is

preliminary evidence from early models returning data to RFMIP that the latest generation of GCMs will produce ERFari+aci estimates that are slightly smaller in magnitude (currently a mean of –1.17 W m^{-2} based on six models only). Energy balance constraints appear to rule out that the total aerosol ERF is positive, but simultaneously do not support estimates that are less negative (smaller in magnitude) than -1.8 W m^{-2}. Satellite-based studies indicate that the total ERFaci lies in the range –2.0 W m^{-2} to –0.5 W m^{-2} and support a central estimate of –0.9W m^{-2}. The central estimate is consistent with the average based on 9 GCMs in Table 7.6, but the 5% to 95% uncertainty range is narrower (–0.5 to –1.4 W m^{-2}). Recent process-based evidence suggests that cloud adjustments may contribute more to ERFaci than previously thought (Section 7.3.3.2.2). For RFari satellite-based estimates remain consistent with the AR5 assessment, while emission updates and better understanding of the contribution of absorbing aerosols and related rapid adjustments have combined resulted in a model-based ERFari assessment of –0.2+/-0.2 W m^{-2}, representing a downward revision of ERFari relative to the AR5 central estimate of –0.45 W m^{-2}.
Based on the above lines of evidence, the total aerosol ERF is assessed to be larger in magnitude than the assessed (Boucher et al., 2013) estimate, but with a narrower uncertainty range. However, our assessed total aerosol ERF estimate is smaller in magnitude than the GCM-based evidence presented in AR5, due in particular to some of the recent studies that fall in the categories of satellite-based evidence and other observational constraints.

There is strong evidence for a substantive negative aerosol ERF with broad agreement between the three main lines of evidence for aerosol ERF, supported by the energy balance (top down) evidence. This leads to an overall *high confidence* in the estimate of ERF and narrowing of the uncertainty range. Combining all lines of evidence using expert judgement, the ERFari+aci is assessed to be –1.1 W m^{-2}, with a *very likely* range of –1.8 W m^{-2} to –0.5 W m^{-2} and a *likely* range of –1.5 W m^{-2} to –0.7 W m^{-2}. There is *high confidence* that EWFaci contributes most (about 80%) to ERFari+aci, with the remainder due to contributions from ERFari. In contrast to AR5 (Boucher et al., 2013), it is now *virtually certain* that the total aerosol ERF is negative. Figure 7.10 depicts these various lines of evidence and compares them to modelling results from CMIP5 and emergent CMIP6-RFMIP models.

[START FIGURE 7.10 HERE]

Figure 7.10: (a) Net aerosol ERFari+aci from different lines of evidence. Green lines show the very likely range based on satellite observations (solid bar ERFari+aci, dashed bar ERFaci). Blue line shows the very likely range based on observational constraints. Purple bars show the assessed very likely range (thin), likely range (thick), and best estimate (black diamond). Bars show climate model estimates, subdivided into CMIP5 models (Zelinka et al., 2014) and CMIP6 models with individual models depicted by grey dots, and multi-model mean ERFari ("Aerosol") and ERFaci ("Cloud"). Overlaid black diamond and black line shows the multi-model mean and very likely range of model-derived ERFari+aci. (b) Contributions to the shortwave components of model-derived ERFari and ERFaci in (a) from scattering ("Scat"), absorption ("Abs") and cloud amount ("Amt"), with total ERFari and ERFaci best estimates and very likely ranges overlaid as black diamonds and lines.

[END FIGURE 7.10 HERE]

7.3.4 Other agents

In addition to the large anthropogenic ERFs associated with WMGHGs and atmospheric aerosols assessed in Sections 7.3.2 and 7.3.3, land use change, light absorbing particles deposited on snow and ice, and contrails and aviation-induced cirrus have also contributed to the overall anthropogenic ERF and are assessed in Sections 7.3.4.1, 7.3.4.2 and 7.3.4.3. Changes in solar irradiance and volcanic eruptions since pre-industrial combined represent the natural contribution to the total (anthropogenic + natural) ERF and are discussed in Sections 7.3.4.4 and 7.3.4.5.

7.3.4.1 Land use

Land use forcing is caused by changes directly caused by human activity rather than by climate response. Land use change affects the surface albedo and thus imposes a radiative forcing on climate. It also affects the emissions or removal of greenhouse gases from the atmosphere (such as CO_2, CH_4, N_2O). The emission changes have the greatest impact on climate (Ward et al., 2014), however these are already included in greenhouse gas inventories. Land use change also affects the emissions of dust and biogenic volatile organic compounds (BVOCs), which form aerosols and affect the atmospheric concentrations of ozone and methane (Chapter 6, Section 6.2).

Using the definition of ERF from Section 7.1, the rapid adjustment in land surface temperature is excluded from the definition of ERF, but rapid changes in snow cover are included since these adjustments have an immediate effect on the local albedo and radiation budget. Land use change in the mid-latitudes induces a substantial amplifying rapid adjustment in snow cover. Few studies have attempted to quantify the ERF of land use change. Andrews et al. (2017) calculated a very large surface albedo ERF (–0.47 W m^{-2}) in the HadGEM2-ES model although they did not separate out the surface albedo change from snow cover change. HadGEM2-ES is known to overestimate the amount of boreal trees and shrubs in the unperturbed state (Collins et al., 2011b) so will tend to overestimate the ERF associated with land use change. The increases in dust in HadGEM2-ES contributed an extra –0.25 W m^{-2}, whereas cloud cover changes added a small positive adjustment. One estimate of the change due to reduced BVOCs leads to a negative contribution of –0.11 W m^{-2} over the historical period (Unger, 2014) through decreases in ozone and methane, whereas Scott et al. (2017) find that the decrease in aerosols from BVOCs outweighs the forcing contribution from ozone and methane. Rapid adjustments through changes in aerosols and chemistry are *likely* to be very model dependent, and it is not possible to make an assessment based on such a limited number of studies. The contribution of land use change to albedo changes has recently been investigated using MODIS and AVHRR to attribute albedos to geographically-specific land cover types (Ghimire et al., 2014). When combined with a historical land use map (Hurtt et al., 2011) this gives a 1700-2005 SARF of –0.15 ± 0.01 W m^{-2}, of which –0.12 W m^{-2} is from 1850. This study did account for correlations between vegetation type and snow cover, but not the rapid adjustment in snow cover identified in (Andrews et al., 2017b). Since the Ghimire et al. (2014) study supports the central AR5 value (Myhre et al., 2013b) of –0.15 ± 0.10, this estimate of the land use ERF is maintained in this assessment (*medium confidence*), and do not add the effects of snow-albedo until confirmed by other studies.

[*placeholder update with RFMIP analysis for SOD]*

7.3.4.2 Contrails and aviation-induced cirrus

Contrail cirrus form when hot and humid aircraft exhaust mixes with the cold air in the upper troposphere and lower stratosphere (UTLS), creating air that is supersaturated with respect to ice. This in turn leads to homogeneous freezing of small solution droplets, and thus produces narrow bands of cirrus contrail clouds. The contrails can be short-lived or persist for hours, depending on the conditions of the UTLS. In rare cases the contrails can spread out to form horizontally extensive cirrus cloud covers, and the aircraft emissions of water vapour can also generally increase UTLS water vapour concentrations and thereby produce additional cirrus clouds. In both cases, the resulting cirrus clouds are referred to as aviation-induced cirrus. In addition to the above effects, which are manly attributed to aircraft emissions of water vapour, it has also been hypothesized that aircraft emissions of aerosols can influence contrail formation and properties. This topic is assessed along with other ERFs arising from aerosol emissions in Section 7.3.3.

In AR5 the ERF due to contrails and aviation-induced cirrus was assessed to 0.05 (0.02–0.15) W m^{-2}, but a *low confidence* was assigned to that estimate. This positive ERF is the net result of a positive longwave ERF and a smaller negative shortwave ERF, as expected for thin cirrus clouds (Section 7.4). Since AR5, a comprehensive review on the topic (Kaercher, 2018) reported post-AR5 ERF estimates ranging from 0.01–0.06 W m^{-2}, based on three new studies that all used 2005 as their reference period. These estimates support an ERF estimate slightly smaller than that of AR5 (Myhre et al., 2013b). However, due to the rapid growth in air traffic since 2005 (approximately 40%), these numbers probably represent underestimates for the present-day ERF. Post-AR5 updates thus collectively do not support a revision to the best estimate from AR5, but also do not support a range as wide as that of AR5.

There is medium evidence but strong agreement (*high confidence*) that the ERF associated with contrails and aviation-induced cirrus is small but positive. The ERF due to contrails and aviation-induced cirrus is assessed to +0.05 W m^{-2}, with a *very likely* range of 0.01–0.10 W m^{-2}.

7.3.4.3 Light absorbing particles on snow and ice

Light-absorbing particles on snow and ice decreases surface albedo from the cryosphere, contributing a positive radiative forcing. Most previous research has focused on black carbon , although organic carbon and mineral dust can also contribute to the ERF (Skiles et al., 2018).

AR5 assessed black carbon on snow radiative forcing to be 0.04 (0.02 to 0.09) W m^{-2} (Myhre et al., 2013b), with the review from Bond et al. (2013) informing this assessment. Since AR5, one further study of global radiative forcing from black carbon on snow deposition agrees with the AR5 best estimate of 0.04 W m^{-2} (Namazi et al., 2015). Organic carbon deposition on snow and ice has been estimated to contribute a small positive radiative forcing of 0.001–0.003 W m^{-2} (Lin et al., 2014). No comprehensive global assessments of mineral dust deposition on snow are available. More radiative forcing estimates have a regional emphasis, focusing on the Arctic (Jiao et al., 2014), Himalayas (Wang et al., 2015), and to a lesser extent North America, Europe and northern China (Skiles et al., 2018). Black carbon deposition and associated snow-albedo change over the Antarctic continent is considered to be negligible (Bauer et al., 2013; Bisiaux et al., 2012). The regional focus of most studies makes estimating a global mean radiative forcing from aggregating different studies problematic, but the relative importance of each region is *likely* to change if the global pattern of emission sources changes (Bauer et al., 2013). Changes to surface albedo in the cryosphere are difficult to observe with satellites (Warren, 2013), and so modelling studies are often validated using field measurements (e.g. Jiao et al. (2014)).

Owing to the small effect of organic carbon, and no significant revisions to the radiative forcing from black carbon, the best estimate and uncertainty range of radiative from absorbing aerosol on snow and ice is unchanged since AR5, remaining at 0.04 (0.02–0.09) W m^{-2}. The efficacy of black carbon on snow forcing was estimated to be 2 to 4 times as large as for an equivalent CO_2 forcing as the effects are concentrated at high latitudes in the cryosphere (Bond et al., 2013). However, it is unclear, how much of this effect would be accounted for if ERF was calculated, and how much comes from the high latitude nature of the forcing. For the overall ERF the radiative forcing is doubled to partly take the efficacy effects into account, giving an overall assessment of at 0.08 (0.04–0.18) W m^{-2}, with *low confidence*.

7.3.4.4 Solar

Variations in the total solar irradiance (TSI) are a natural external forcing agent. The dominant cycle is the 11-year sunspot activity cycle, which is superimposed on 205–210 and 24,000 year cycles (Section 2.2). Over the last three 11-year cycles, the peak-to-trough amplitude in TSI has differed by about 1 W m^{-2} between solar maxima and minima (Chapter 2, Figure 2.1).

Much of the variance in the solar irradiance, over the solar cycle and between solar cycles, occurs at short wavelengths in the 200–400 nm band (Lean et al., 1997, 2005). The IRF can be derived simply by TSI × (1 – albedo)/4 irrespective of wavelength, where the planetary albedo is taken to be 0.29 (Stephens et al., 2015). The adjustments are expected to be wavelength dependent. Gray et al. (2009) determined a stratospheric temperature adjustment of –22% to spectrally resolved changes in the solar radiance over one solar cycle. This negative adjustment is due to stratospheric heating from increased absorption by ozone at the short wavelengths. A multi-model comparison (Smith et al., 2018b) calculated rapid adjustments of –4% due to stratospheric temperatures and –6% due to tropospheric processes (mostly clouds), for a change in TSI across the spectrum. The smaller magnitude of stratospheric-temperature adjustment is consistent with the broad spectral change rather than the shorter wavelengths characteristic of solar variation. A single model study also found an adjustment that acts to make the forcing more negative (Modak et al., 2016). While there has not yet been a calculation based on the appropriate spectral change, the –6% tropospheric adjustment from Smith et al. (2018b) is adopted along with the Gray et al. (2009) stratospheric temperature adjustment. The ERF due to solar variability over the historical period is therefore represented by 0.72 × TSI × (1 – albedo)/4 using the TSI timeseries from Section 2.2.2.

AR5 (Myhre et al., 2013b) assessed solar SARF from 1750 to 2011 to be 0.05 (0.00–0.10) W m^{-2} which was computed from the 7-year mean around the solar minima in 1745 (being closest to 1750) and 2008 (being the most recent solar minimum). Solar minima are used because they are less variable between cycles and more appropriate to measure changes in activity (Myhre et al., 2013b). The inclusion of tropospheric adjustments that reduces ERF (compared to SARF in AR5) has negligible impact on the overall forcing. Prior to the satellite era, proxy records are used to reconstruct historical solar activity. In AR5, historical records were constructed using sunspot number observations. In this assessment historical time series are constructed from radiogenic compounds in the biosphere and in ice cores that are formed from cosmic rays (Steinhilber et al., 2012).

In this assessment the TSI from the Paleoclimate Model Intercomparison Project Phase 4 (PMIP4) reconstruction is used (Jungclaus et al., 2017). Proxies constructed from the ^{14}C and ^{10}Be radiogenic records for the SATIRE-M model (Vieira et al., 2011) and ^{14}C record for the PMOD model (Shapiro et al., 2011) for the 1745 solar minimum provide 1745 to 2008 ERFs of –0.01, –0.02 and 0.00 W m^{-2} respectively. Several other proxy reconstructions of TSI since AR5 have become available (Egorova et al., 2018; Lean, 2018; Wu et al., 2018), resulting in 1745 to 2008 ERFs ranging from –0.05 to +0.10 W m^{-2}. One substantially higher ERF estimate of +0.35 W m^{-2} derived from TSI reconstructions in Egorova et al. (2018) is based on a later recovery in solar modulation potential from the Maunder Minimum (Muscheler et al., 2016).

The best estimate solar ERF is assessed to be –0.01 W m^{-2}, being the mean of the PMIP4 datasets, with a *likely* range of –0.05 to +0.10 W m^{-2} (*low confidence*). The *likely* range is wider than in AR5 and asymmetric due to the increased diversity in TSI reconstructions prior to 1750, notably those that show a negative forcing due to an upward revision of TSI in the 1740s, and those showing a larger positive forcing due a slow recovery from the Maunder Minimum (Egorova et al., 2018). It is possible that the solar ERF will be revised in the Second Order Draft if a new solar minimum is confirmed in 2018 or 2019.

7.3.4.5 Volcanic

There is large episodic negative radiative forcing associated with aerosols being ejected into the stratosphere from explosive volcanic eruptions, accompanied by smaller eruptions, where only a small amount of aerosol reaches the upper troposphere/stratosphere. The volcanic SARF in AR5 (Myhre et al., 2013b) was derived by scaling the stratospheric aerosol optical depth (SAOD) by a factor of –25 W m^{-2} per SAOD from Hansen et al. (2005). Quantification of the rapid adjustments to SAOD perturbations have determined a significant positive rapid adjustment in the shortwave, leading to estimates of –17 and –20 W m^{-2} per SAOD (Gregory et al., 2016; Larson and Portmann, 2016). A study driven by emissions of SO_2 rather than prescribed SAOD found a positive forcing through effects on upper tropospheric ice clouds, due to additional ice nucleation on the volcanic sulphate particles (Schmidt et al., 2018). With only one study so far, the contribution to volcanic ERF due to sulphate aerosol impacts on ice clouds is not included in the overall assessment.

Non-explosive volcanic eruptions generally yield negligible global ERFs due to the short atmospheric lifetimes (a few weeks) of volcanic aerosols in the troposphere. However, as discussed in Section 7.3.3.2, the massive fissure eruption in Holuhraun, Iceland persisted for months in 2014 and 2015 and did in fact result in a marked and persistent reduction in cloud droplet radii and a corresponding increase in cloud albedo regionally (Malavelle et al., 2017). This shows that also non-explosive fissure eruptions can lead to strong regional and even global ERFs, but because the Holuhraun eruption occurred in NH winter, solar insolation was weak and the observed albedo changes therefore did not result in an appreciable global ERF.

The rapid adjustment component of ERF for volcanic stratospheric aerosols is assessed to be an average of the two climate model based SAOD efficiency calculations: +6.5 W m^{-2} per SAOD with a 5% to 95% range estimated from the total range of rapid adjustment exhibited between the two models. To give a total ERF assessed scaling of –18.5 ± 3.5 W m^{-2} per SAOD (*high confidence*). This is applied to the SAOD timeseries from Chapter 2, Section 2.2 to generate a timeseries of ERF in Figure 7.14, and temperature response in Figure 7.15.

7.3.5 Synthesis of Global Mean Radiative Forcing, Past and Future

7.3.5.1 Summary of Major changes in forcing since IPCC AR5

AR5 introduced the concept of ERF and rapid adjustments and made a preliminary assessment that the tropospheric adjustments were zero for all species other than the effects of aerosol cloud interaction and black carbon. Since AR5, new studies have allowed us to tentatively assess values for tropospheric adjustments to CO_2, CH_4, and stratospheric aerosol, to place a tighter constraint on adjustments from aerosol-cloud interaction and to assess a *likely* sign of the tropospheric adjustments for other forcing agents (section 7.3.2, 7.3.4).

The radiative efficiencies for CO_2, CH_4 and N_2O have been updated since AR5 (Etminan et al., 2016). The differences for CO_2, and N_2O are small at present day concentration, but the radiative efficiency for CH_4 is increased by 25% (see section 7.3.2) (*high confidence*) although the tropospheric adjustment is tentatively assessed to offset around half of that (*medium confidence*).

7.3.5.2 Summary ERF assessment

Figure 7.11 shows the industrial era ERF estimates for 1750 to 2017 for the different forcing agents. It also highlights CMIP6 model results from RFMIP where preliminary results exist. The assessed uncertainty distributions are combined with a 2000 member Monte Carlo sampling of the different distributions assuming they are independent for making the overall assessment of possible ERFs, shown as distributions in Figure 7.13.

[START FIGURE 7.11 HERE]

Figure 7.11: Effective radiative forcing from 1750 to 2017 by contributing forcing agents. CMIP6 model estimates for 1850-2014 are shown as circles where known.

[END FIGURE 7.11 HERE]

[START Table 7.7 HERE]

Table 7.7: Summary table of ERF estimates for AR6 and comparison with the four previous IPCC assessment reports. For AR5 and AR6 these include tropospheric adjustments where known.

	Global Mean Effective Radiative Forcing (W m^{-2})					
	SAR (1750–	*TAR (1750–*	*AR4 (1750–*	*AR5 (1750–*	*AR6 (1750–2017)*	*Comment*

	1993)	*1998)*	*2005)*	*2011)*		
Well-mixed greenhouse gases (CO_2, CH_4, N_2O, and halocarbons)	2.45 (2.08 to 2.82)	2.43 (2.19 to 2.67)	2.63 (2.37 to 2.89)	2.83 (2.26 to 3.40)	3.22 (2.84 to 3.60)	Increases in concentrations. Changes to radiative efficiencies. Inclusion of tropospheric adjustments.
Tropospheric ozone	+0.40 (0.20 to 0.60)	+0.35 (0.20 to 0.50)	+0.35 (0.25 to 0.65)	+0.40 (0.20 to 0.60)	+0.37 (0.18 to 0.56)	Most recent model estimates. No tropospheric adjustment assessed.
Stratospheric ozone	–0.1 (–0.2 to –0.05)	–0.15 (–0.25 to –0.05)	–0.05 (–0.15 to +0.05)	–0.05 (–0.15 to +0.05)	–0.075 (–0.15 to 0.0)	Increased to include an additional dataset. No tropospheric adjustment assessed
Stratospheric water vapour from CH_4	Not estimated	+0.01 to +0.03	+0.07 (+0.02, +0.12)	+0.07 (+0.02 to +0.12)	+0.07 (+0.02 to +0.12)	Estimate unchanged.
Aerosol–radiation interactions	Not estimated	Not estimated	–0.50 (–0.90 to –0.10)	–0.45 (–0.95 to +0.05)	–0.2 (–0.4 to 0)	Reduced by about 55% compared to AR5
Aerosol–cloud interactions	0 to –1.5 (sulphate only)	0 to –2.0 (all aerosols)	–0.70 (–1.80 to –0.30) (all aerosols)	–0.45 (–1.2 to 0)	–0.9 (–1.4 to –0.5)	Increased by 100% compared to AR5
Surface albedo (land use)	Not estimated	–0.20 (–0.40 to 0.0)	–0.20 (–0.40 to 0.0)	–0.15 (–0.25 to –0.05)	–0.15 (–0.25 to –0.05)	No change, but no tropospheric adjustment assessed
Surface albedo (black+organic carbon aerosol on snow and ice)	Not estimated	Not estimated	+0.10 (0.0 to +0.20)	+0.04 (+0.02 to +0.09)	+0.08 (+0.04 to +0.18)	Increased since AR5 to better account for temperature effects
Contrails	Not estimated	+0.02 (+0.006 to +0.07)	+0.01 (+0.003 to +0.03)	+0.01 (+0.005 to +0.03)		
Combined contrails and contrail-induced cirrus	Not estimated	0 to +0.04	Not estimated	+0.05 (+0.02 to +0.15)	+0.05 (+0.01 to +0.10)	Narrower range since AR5
Total anthropogenic	Not estimated	Not estimated	1.6 (0.6 to 2.4)	2.3 (1.1 to 3.3)	**2.48 [1.65 to 3.26]**	Slight increase due to compensating effects of greenhouse gases and aerosol
Solar irradiance	+0.30 (+0.10 to +0.50)	+0.30 (+0.10 to +0.50)	+0.12 (+0.06 to +0.30)	+0.05 (0.0 to +0.10)	–0.01 (–0.05 to +0.10)	Revised historical TSI estimates

Notes:

Volcanic RF is not added to the table due to the episodic nature of volcanic eruptions which makes it difficult to compare to the other forcing mechanisms.

[END Table 7.7 HERE]

The total anthropogenic ERF over the industrial era (1750–2017) is estimated as 2.48 W m^{-2} (1.65 to 3.25 W m^{-2} 5% to 95% range) (Table 7.7). This is an 8% increase over AR5 (Myhre et al., 2013b) estimates for 1750–2011. This modest increase is a result of compensating effects. Atmospheric concentrations of well-mixed greenhouse gases since 2011 and upwards revisions of their forcing estimates has led to a 14%

increase in their ERF. Whereas, the total aerosol ERF is assessed to be 22% more negative compared to AR5, due to revised estimates rather than trends *(high confidence).*

Greenhouse gases, including ozone and stratospheric water vapour from methane oxidation, are estimated to contribute an ERF of 3.64 W m^{-2} (3.22 to 4.06 W m^{-2} 5% to 95% range). 3.22 (2.84 to 3.60) W m^{-2} of this ERF comes from the well-mixed greenhouse gases, with ozone and stratospheric water vapour changes contributing the remainder. Carbon dioxide continues to contribute the largest part of this ERF (*high confidence*). There has been a significant increase in the estimated shortwave forcing from methane (*high confidence*) somewhat countered by a negative rapid adjustment (*medium confidence*). There is also a 5% upwards revision due to inclusion of tropospheric adjustments for CO_2 (*medium confidence*) and 3% increase in the SARF from LBL calculations (*medium confidence*).

Aerosols have in total contributed an ERF of –1.1 W m^{-2} (–1.8 to –0.5 W m^{-2} 5–95% confidence range). Aerosol-cloud interactions contribute –0.9 (–1.4 to –0.5) W m^{-2} to this ERF, with aerosol-radiation interactions contributing the remaining –0.2 (–0.4 to 0) W m^{-2}.

7.3.5.3 Temperature Contribution of forcing agents

The contribution of forcing agents to 2017 temperature change relative to 1750 is shown in Figure 7.12. These estimates were produced using the FaIR simple climate model emulator (Smith et al., 2018a) using a 2000-member Monte Carlo simulation of ERF (as in Figure 7.11), ECS and TCR. Distributions for ECS and TCR were informed by section 7.5 and chosen to approximately maintain the best estimate and *likely/very likely* ranges assessed in that section while also observing a strong positive correlation. The components to temperature change are assessed by removing each forcing component from the pre-industrial to present-day simulation in each ensemble member in FaIR and computing the difference.

Figure 7.12 also shows an estimate of the temperature response to forcing calculated by the MAGICC model (Meinshausen et al., 2011; Nauels et al., 2017) as the bottom panel which is a more established and tested simple climate model emulator (Chapter 1, Section 1.6). Overall the temperature response in Figure 7.12 is dominated by the uncertainty in ERF, yet for WMGHG contribution to warming the uncertainty is dominated by ECS and TCR.

[SOD note, the MAGICC result use preliminary ERF estimates and its own ECS/TCR ranges, hence it warms more. For the SOD either Chapter 4 or this Chapter will have an Appendix with a comparison of simple climate models]

Error bars in Figure 7.12 show the contribution of ERF uncertainty with best estimates of ECS and TCR (solid lines) and total response uncertainty using the section 7.5 assessment of ECS and TCR (dashed lines). Overall the response is dominated by the uncertainty in ERF, yet for WMGHG contribution to warming the uncertainty is dominated by ECS and TCR.

These results show that it is unequivocal that anthropogenic activity has had a warming effect on the planet since 1750. Analyses of radiative forcing and climate sensitivity presented in this chapter give an estimated human induced warming of 1.12°C (0.63 to 1.80°C 5% to 95% range) (*high confidence*). Changes in solar and volcanic activity are assessed to have had a negligible effect (*high confidence*). By applying historical observations of global near surface temperature trends the 1750 to 2017 anthropogenic warming estimate is narrowed to 1.08°C (0.86–1.30°C *very likely* range). This warming is comprised of a greenhouse warming of 1.7°C (1.3–2.3°C) that has an increasing trend and an aerosol cooling of 0.6°C (0.3–1.1°C) that has remained relatively constant in terms of the globally averaged ERF over the last 20 years (Figure 7.15) (*high confidence*).

Figure 7.13 shows the overall assessments from this chapter both before and after applying historical observational constraints. Posterior distributions of ECS and TCR are slightly narrower than their prior distributions taken from Section 7.5.7. The ECS and TCR observationally-constrained posterior distributions give *very likely* ranges of 2.9°C (2.1–4.4°C) and 1.6°C (1.3–2.2°C) respectively (Figure 7.13a). Note, that to avoid double counting historical constraints on ECS and TCR, these posterior distribution are not applied to our overall assessment of ECS and TCR in Section 7.5.7. Applying observational constraints does not greatly change the distribution of aerosol ERF or its contribution to temperature (Figure 7.13b,c) but has more influence on greenhouse-gas induced warming. The anthropogenic warming is highly constrained by the observations owing to the small influence of natural forcers (Figure 7.13c).

[START FIGURE 7.12 HERE]

Figure 7.12: The contribution of forcing agents to 2017 temperature change relative to 1750. (top) These estimates were produced using the FaIR simple climate model emulator (Smith et al., 2018a) where ranges for ERF were taken from Section 7.3 and ranges for ECS and TCR were taken from Section 7.5. Error bars show the contribution of forcing uncertainty with best estimates of ECS and TCR (solid lines) and total response uncertainty. (bottom) the temperature changes simulated by the MAGICC simple climate model (Meinshausen et al., 2011; Nauels et al., 2017), using its own distribution of ECS and TCR, only the effect of forcing error is shown. [Preliminary results from MAGICC based on earlier forcing estimates, will be updated for SOD].

[END FIGURE 7.12 HERE]

[START FIGURE 7.13 HERE]

Figure 7.13: (a) Probability density functions (PDFs) of ECS and TCR; (b) Distributions of effective radiative forcing and (c) distributions of contribution to anthropogenic temperature change from 1750 to 2017. Ranges for ERF were taken from Section 7.3 and ranges for ECS and TCR were taken from Section 7.5. PDFs combine the contribution of forcing uncertainty with ranges of ECS and TCR. In each panel, the solid filled curves show the constrained (posterior) distributions after matching historical temperatures to the surface air temperature from Cowtan and Way (2014) using the FaIR simple climate model emulator (Smith et al., 2018a). In (a), dashed curves show the prior distributions as assessed in this chapter, whereas in (b) and (c) dashed curves represent distributions before constraint to historical temperature observations.

[END FIGURE 7.13 HERE]

7.3.5.4 Historical timeseries from models and observations

Historical timeseries of the assessed ERF and the resulting near surface global temperature changes are shown in Figures 7.14 and 7.15. The historical timeseries of ERFs for the WMGHGs can be derived by applying the ERF calculations of section 7.3.2 to the observed timeseries of WMGHG concentrations in Chapter 2, Section 2.2. Stratospheric ozone ERF is scaled using the present day value in Section 7.3.2 to the observed levels of equivalent effective stratospheric chlorine (EESC) using values from Daniel et al. (2010) up to 1980 and Engel et al. (2018) after 1980. Changes in solar forcing are derived by scaling observed total solar irradiance (TSI) (Section 2.2.2), changes in volcanic forcing are derived by scaling observed stratospheric aerosol optical depth (SAOD) (Section 2.2.3). Tropospheric ozone and aerosol forcing uses model-derived results from ACCMIP (Shindell et al., 2013; Stevenson et al., 2013), which in the latter case is re-scaled to the updated assessment in this section. [*note: will update for SOD.*] The land use ERF timeseries is based on historical land use reconstructions. [*note: currently using AR5, will get surface albedo timeseries from Chapter 2 for SOD*].

These results show that for most of the historic period the overall long term trends closely followed the CO_2 contribution, as non-CO_2 greenhouse gas forcing (from other WMGHGs and ozone) was more-or less cancelled out by the aerosol cooling. However, that is no longer the case and over the last few decades the long-term warming has been occurring at a faster rate than that expected by CO_2 alone (*high confidence*), see also Chapter 2, (Section 2.2).

[START FIGURE 7.14 HERE]

Figure 7.14: Timeseries of total (thick dashed line) and individual components (thin solid lines) of ERF from 1750 to 2017 assessed in this chapter. Some small individual components are grouped for clarity.

[END FIGURE 7.14 HERE]

[START FIGURE 7.15 HERE]

Figure 7.15: Timeseries of near surface global temperature changes, using the time series of ERFs assessed in this section (Figure 7.14) and calculated using the FaIR simple climate model emulator (Smith et al., 2018a) using the distribution of ECS and TCR assessed in section 7.5 and Section 7.3.5.3. The median of a 2000-member Monte Carlo ensemble is shown for the total temperature and the contribution from each component.

[END FIGURE 7.15 HERE]

7.4 Climate and Earth system feedbacks

The amplitude of climate change primarily depends on the magnitudes of the radiative forcings and feedbacks (Box 7.1, Equation 7.1?). The Earth system feedbacks are numerous and may be gathered in three groups: the climate, biogeochemical and long-term feedbacks. The latter includes feedbacks that are relevant only for time scales larger than a few centuries. The climate and biogeochemical feedbacks already act at shorter time-scale, i.e. the time scales that are used in practice to estimate the ECS. The feedback framework used here, and an overview of model-based estimates of feedbacks are presented in section 7.4.1. For each feedback, the basic underlying mechanisms and their assessment are presented in section 7.4.2. It has recently been recognized that the magnitude of climate feedbacks can change as climate evolves, which has implications for understanding the historical period and projected future warming. Progress has been made to understand and clarify the key causes of these changes in terms of the feedback dependence on temperature pattern (Section 7.4.3) and on climate mean state (Section 7.4.4). A synthesis of the feedback assessment is given section 7.4.5.

7.4.1 Framework and methodology

7.4.1.1 Standard framework

The global temperature changes of the climate system are generally analysed with the classical forcing-feedback theory (see also Box 7.1) (Bony et al., 2006; Dessler and Zelinka, 2015; Dufresne and Saint-Lu, 2016; Hansen et al., 1984; Sherwood et al., 2015; Wetherald and Manabe, 1988). As described in Box 7.1 (Equation 7.1?), in response to a radiative forcing ΔF, the global mean surface air temperature changes by ΔT from its initial value. The resulting global energy imbalance ΔN can be written as $\Delta N = \Delta F + \alpha\Delta T$, where α is the feedback parameter that quantifies the change in the radiative flux at the TOA in response to changes in global mean surface temperature.

When surface temperature changes, many climate variables change, thus affecting the radiative flux at the TOA. The feedback parameter can then be formally decomposed, at the first order, into a sum of terms $\alpha = \sum_x \alpha_x$, where x are vectors representing climate variables that have a direct impact on the flux at the TOA and $\alpha_x = \frac{\partial N}{\partial x}\frac{\partial x}{\partial T}$. Climate feedbacks are commonly decomposed into variables associated with a vertically uniform temperature change (named the Planck response, P; Section 7.4.2.1), the water vapour concentration (WV; Section 7.4.2.2), the temperature lapse rate (LR; Section 7.4.2.2), the surface albedo (A; Section 7.4.2.3), clouds (C; Section 7.4.2.4), and biogeochemical and other Earth system feedbacks (section 7.4.2.5). Alternative feedback decompositions have been suggested, in particular to focus on relative humidity (Held and Shell, 2012; Ingram, 2013). The biogeochemical feedbacks arise due to changes in aerosols and atmospheric chemical composition, and Gregory et al. (2009) show that they can be analysed using the same framework.

Most feedback studies consider the radiative response to global mean surface temperature changes, although the response to local surface temperature changes is used for deeper analysis (Feldl and Roe, 2013a, Section 7.6.2). Various methods can be used to estimate α_x (Bony et al., 2006), but most recent modelling studies use a 'radiative kernel' method (Soden et al., 2008, Section 7.3.1) wherein the first term of α_x, the kernel $\frac{\partial N}{\partial x}$, is evaluated by perturbing individual climate variables within the radiation code of a single atmospheric GCM; under the assumption that $\frac{\partial N}{\partial x}$ is approximately constant and representative of other models, multiplication by values of $\Delta x/\Delta T$ simulated by coupled GCMs produces an estimate of each α_x. The kernel method is an approximation which is only valid for small temperature changes (Jonko et al., 2013). Biogeochemical feedbacks need specific methods (Gregory et al., 2009; Heinze et al., 2018).

7.4.1.2 Methodology of the feedback assessments

In climate models the feedback parameters α_x are commonly estimated as the mean differences in the radiative fluxes between atmosphere-only simulations in which the change in SST is prescribed (Cess et al., 1990), or as the regression slope of change in radiation flux against change in global-mean surface temperature (ΔT) using atmosphere-ocean coupled simulations with abrupt CO_2 changes (*abrupt4×CO₂*) (Andrews et al., 2012; Gregory et al., 2004). The regression slope is sometime replaced by a simple difference between two average periods. These simulations are also used to estimate the ERF (see Section 7.3.1). Neither method is perfect as the latter estimate is affected by internal climate variability and time evolving pattern of SST increase, and the former does not include all changes of the surface conditions. Nevertheless, these approaches yield consistent results when the specificity of the experimental design is taken into account (Ringer et al., 2014). At inter-annual time scales, the radiative kernel method allows a direct comparison between observational, reanalysis and model estimates of α_x, although the correlation between N and T is weak at this timescale.

The assessment of feedbacks does not rely solely on the estimation from GCMs as the models inevitably contain errors in mean states and physical processes responsible for the radiative response to temperature changes. Instead, different lines of evidence from observations, theory, and process modelling are combined with the feedback derived from GCMs to make an overall assessment (Section 7.4.2).

Feedback parameters were first assumed to be approximatively constant and independent of each other except for WV and LR feedbacks which are often combined due to a well-established mechanism that couples them (Section 7.4.2.2). Previous assessments have understood that feedbacks would be time, state and forcing dependent but understanding of these dependencies has advanced considerably since AR5 making this topic a major theme of the Chapter (Sections 7.1, 7.3.1, 7.4.3, 7.4.4.3, 7.4.4.4). Nevertheless, when the feedbacks are computed in a consistent way, they allow the main processes that drive the amplitude of climate change to be partitioned and analysed. Overall these developments improve understanding and advance the comparison of models with observations, and the comparison of different model experiments, resulting in an improved assessment.

7.4.1.3 Updates of feedbacks in climate models

Since AR5, many modelling groups have newly participated in CMIP, leading to an increase in the number of models, from 38 in CMIP5 to 101 in CMIP6. Because some of the CMIP6 models share an atmosphere or ocean component, they are not completely independent, and such a structural similarity across models, called the model genealogy, can be identified by clustering them in terms of their climatology (Knutti et al., 2013). Yet, climate models having the same particular component can behave differently when other components of the models are not identical. Furthermore, changing details such as the resolution and internal model parameters can result in differences in climate feedbacks. Because of these reasons, for the purposes of this discussion, all models are displayed.

Estimation of individual feedback terms is compared between CMIP5 and CMIP6 climate models (Figure 7.16). The feedback is calculated using the linear regression between ΔT and ΔN for 150 years in the abrupt CO_2 quadrupling (*abrupt4xCO*$_2$) experiments (Andrews et al., 2012; Caldwell et al., 2016; Gregory et al., 2004). Radiation kernels are also used to eliminate apparent dependence of one feedback on the other due, for example, to cloud masking effects (Soden et al., 2008; Zelinka et al., 2016). In CMIP5 models, the Planck feedback parameter has a mean of –3.16 W m^{-2} °C^{-1} with a *likely* range of 0.08 W m^{-2} °C^{-1} (2.5% of the mean value) because in the GCMs the clear-sky longwave radiation is calculated with small errors compared to the clear-sky shortwave radiation (Pincus et al., 2015). The combined WV+LR component provides the largest positive feedback compensating the negative Planck feedback, and shows a mean value of 1.15 W m^{-2} °C^{-1} and a *likely* range of 0.17 W m^{-2} °C^{-1}. Surface albedo and cloud feedbacks also act to amplify the temperature response. The mean value of the albedo feedback parameter is 0.37 W m^{-2} °C^{-1} and the *likely* range is 0.25–0.44 W m^{-2} °C^{-1}, which accounts for about 50% of the mean. The evaluation of the cloud feedback is more uncertain; the *likely* range of 0.18–0.7 W m^{-2} °C^{-1} is much larger than the mean value of 0.44 W m^{-2} °C^{-1}. The total combined feedback parameter derived from CMIP5 models of –1.1 W m^{-2} °C^{-1} is thus accompanied by a *likely* range from –1.3 to –0.8 W m^{-2} °C^{-1} due largely to spread in the albedo and cloud feedbacks. There is a small discrepancy between the total feedback calculated directly using the time evolutions of ΔT and ΔN in each model and the accumulation of individual feedbacks (shown at the right of Figure 7.16) owing to long-term Earth system processes (Section 7.4.2.5) as well as errors in the radiative kernel method. The above estimations of the feedbacks will be revised with other lines of evidence in Section 7.4.2, in which the confidence levels will also be provided.

[SOD *Placeholder for evaluations of feedbacks in CMIP6 models*]

[START FIGURE 7.16 HERE]

Figure 7.16: Estimates of global mean climate feedbacks in CMIP5 and CMIP6 abrupt4xCO^2 simulations. The box-whisker plot indicates the multi-model mean (horizontal lines), likely range (boxes) and very likely range (whiskers). Individual feedback terms are computed using a radiative kernel by multiplying temperature-mediated changes in the respective field. A residual between the summed feedback and the total climate feedback, the latter directly derived from the models, is shown at the right. The CMIP5 data are adopted from Caldwell et al. (2016). [Note that the CMIP6 values are not yet available, so plotted using the CMIP5 values tentatively.]

[END FIGURE 7.16 HERE]

The ensemble sizes of the CMIP5 and CMIP6 models are not sufficiently large to sample the range of model uncertainty. One way to further explore the range of climate feedbacks that can be obtained from models is to construct perturbed parameter ensembles (PPEs), wherein uncertain parameters in a model are randomly altered (Collins et al., 2011a; Klocke et al., 2011; Sanderson et al., 2008a; Stainforth et al., 2005). Those parameters have repeatedly been changed through a tuning procedure of climate models, so that the PPE can naturally be generated as a consequence of the model tuning (Hourdin et al., 2017). The PPEs have shown commonly considerable variations in climate feedbacks within a single model (Klocke et al., 2011; Stainforth et al., 2005), but the range of uncertainty due to parametric differences in the PPE does not exceed the range due to structural difference in the CMIP multi-model ensemble when the TOA energy balance is constrained (Shiogama et al., 2012). Since many of the parameter values were chosen to compensate errors in the energy budgets, they are not actually independent of each other if the PPE does not allow a large energy imbalance at TOA.

The range of the total climate feedback shown in Figure 7.16 is derived directly from the ensemble of the total feedback in the multi model ensemble. If, however, it is computed by adding in quadrature the *likely* ranges of individual feedbacks assuming that they are independent, the *likely* range of the total feedback becomes wider by 17%. This indicates that the feedbacks in climate models are partly dependent on each other. Besides a well-known co-dependency between the WV and LR feedbacks (Po-Chedley et al., 2018a; Soden and Held, 2006), two more possible co-dependencies have been suggested (Caldwell et al., 2016; Huybers, 2010). One is a negative covariance between the LR and longwave cloud feedbacks, which may be accompanied by a deepening of the troposphere (O'Gorman and Singh, 2013) leading both to more rising of high clouds and a larger upper-tropospheric warming. The other is a negative covariance between albedo and shortwave cloud feedbacks, which may occur due to compensation between a reduced surface albedo and an increase in low-level clouds with the loss of Arctic sea ice (Mauritsen et al., 2013). However, the covariances between these feedbacks are not extremely strong in the CMIP5 ensemble and furthermore not supported yet by sufficient observations. Therefore, assessments of the individual feedbacks are made separately in section 7.4.2 without a particular consideration on the co-dependency between them.

7.4.2 Assessing climate feedbacks

The goal of this section is to provide an overall assessment of individual feedbacks by combining different lines of evidence from observations, theory, process models and GCMs. For achieving this, the understanding of the processes governing the feedbacks, why the feedback estimates differ among models, studies or approaches, and the extent to which these estimates are consistent is presented.

7.4.2.1 Planck response

The Planck response represents the extra emission to space of LW radiation arising from a vertically uniform warming of the surface and the atmosphere. The feedback parameter associated with this warming is strongly negative, playing a fundamental stabilizing role. This parameter has been estimated using climate simulation outputs or meteorological reanalysis (Caldwell et al., 2016; Dessler, 2013; Soden and Held, 2006; Vial et al., 2013) and the value is in line with simple estimates based on Planck radiation. The spread among these estimates is low and is mainly due to differences in climatological cloud and water vapour distributions and the pattern of surface temperature changes. Models with greater high-latitude warming, where the temperature is colder, have smaller values of the Planck feedback. The physical processes that control this response are very well understood and the estimates from observations and climate models are consistent at interannual time scales (Dessler, 2013; Hansen et al., 1984; Soden and Held, 2006; Vial et al., 2013). This leads to an overall *high confidence* in the estimate of the Planck response, that is assessed to be α_P = –3.15 W m^{-2} °C^{-1} with a *very likely* range of –3.4 to –2.9 W m^{-2} °C^{-1} and a *likely range* of –3.3 to –3.0 W m^{-2} °C^{-1}.

7.4.2.2 Water vapour and lapse rate feedbacks

The lapse rate feedback quantifies the change in radiative flux at the TOA due to the non-uniform change in vertical temperature profile associated with a change in global mean surface temperature. In the tropics, the vertical temperature profile is mainly driven by moist convection and thus follows a moist adiabat. The warming is therefore larger in the upper troposphere than in the lower troposphere (Bony et al., 2006; Manabe and Wetherald, 1975; Santer et al., 2005). This leads to a larger radiative emission to space per degree of surface warming and therefore a negative feedback.

At mid and high latitudes, the vertical temperature profile is mainly driven a balance between radiation and meridional heat transport rather than convection, leading to strong temperature inversions characterized by a cold surface and warmer atmosphere above, particularly in winter (Payne et al., 2015). As a consequence, warming is trapped near the surface, leading to a positive lapse rate feedback in polar regions (Manabe and Wetherald, 1975; Pithan and Mauritsen, 2014). However, the tropical contribution strongly dominates and the global lapse rate feedback is a large negative feedback. The 66% range in the CMIP5 climate models is $\alpha_{LR} = -0.65 \pm 0.3$ W m^{-2} °C^{-1} (Caldwell et al., 2016; Dessler, 2013; Soden and Held, 2006; Vial et al., 2013).

The water vapour feedback quantifies the change in radiative flux at the TOA due to changes in atmospheric water vapour concentration associated with a change in global mean surface temperature. As the relative humidity is nearly constant (Held and Shell, 2012; Soden and Held, 2006), specific humidity increases with temperature following approximatively the Clausius-Clapeyron relationship, which increases absorption of both LW and SW radiation and decreases the outgoing radiation. Compared to the assumption of fixed-relative humidity, the water vapour feedback simulated by models is about 5% weaker (Soden et al., 2008; Soden and Held, 2006), the main reason being a decrease of the RH in the tropical upper troposphere (Vial et al., 2013).

Because they are strongly linked by the Clausius-Clapeyron relationship and they are of opposite sign, the LR and WV feedbacks are often summed into one term. This reduces inter-model spread compared to the individual LR and WV feedbacks (Colman, 2003; Soden and Held, 2006). Held and Shell (2012) propose a formulation that explicitly takes into account the Clausius-Clapeyron relationship and that separates the effects of changes in temperature at constant relative humidity from the changes in relative humidity. This allows a better analysis of the role of the change in relative humidity.

The tropics strongly contribute to the individual global LR and WV feedbacks but contribute much less to the combined WV+LR feedback because of the opposite signs of the two feedbacks (Bony et al., 2006; Colman, 2003; Soden and Held, 2006). The cancellation is almost perfect in the tropical upper troposphere (Vial et al., 2013). The inter-model spread in the tropical water vapour feedback is controlled by relative humidity changes (Po-Chedley et al., 2018a; Vial et al., 2013) which can be large (O'Gorman and Muller, 2010). As a result, the coupling between the tropical LR and WV feedbacks across models is weak. The LR and WV feedback are closely tied in the extratropics since relative humidity changes are small there (Po-Chedley et al., 2018a).

Multi-model analyses show that models with relatively larger warming in the tropics have a more negative global lapse rate feedback (Soden and Held, 2006). As the LR feedback is more negative in the tropics than in the mid and high latitudes, it was first assumed that this was a direct consequence of the patterns of warming. However, recent studies demonstrate that this simple explanation was not sufficient (Po-Chedley et al., 2018a). If the local LR feedback is assumed to be constant among models, the spread of warming pattern explains only a small fraction of the global LR feedback spread. The main factor of this spread is the dependence of the local LR feedback to the pattern warming, especially over the sub-Antarctic region (Po-Chedley et al., 2018a). A larger warming in the tropics compared to high latitudes leads to an increase of poleward heat and water vapour transport and an increase of the local LR feedback in the extratropics. As a consequence, both the individual WV and LR feedbacks and the combined WV+LR feedback depend on how models simulate the contrast between the tropical and the extratropical temperature. In particular they depend on how models simulate current sea-ice extent and how this extent decreases with global warming (Po-Chedley et al., 2018a).

Idealized simulations of the radiative-convective equilibrium over large domains using cloud-resolving models (CRMs) or GCMs have shown that in certain conditions, convective atmospheres could spontaneously organize into dry and moist areas, a phenomenon referred to as 'convective self-aggregation', and that the clustering of convection leads to a dramatic drying of the free troposphere on average over the domain (Bretherton et al., 2005; Held et al., 1993). Observations also show that for given large-scale vertical motions and surface temperature, situations of stronger convective aggregation are associated with a drier atmosphere (Holloway et al., 2017; Tobin et al., 2012, 2013). Numerical and theoretical studies suggest that the phenomenon of self-aggregation can depend on surface temperature (Emanuel et al., 2014), raising questions regarding whether a change of convective aggregation with global warming could affect the water vapour feedback, and whether GCMs could take this effect into account. The phenomenon of convective self-aggregation has been shown to also arise in GCMs, and like in CRMs it can be temperature-dependent (Arnold and Randall, 2015; Coppin and Bony, 2015; Held et al., 2007; Popke et al., 2013; Wing et al., 2017). It suggests that the GCMs have the potential to affect the WV feedback through changes in convective organization. However, although GCMs can simulate changes in the organization of deep convection on synoptic to planetary scales, they do not represent the mesoscale organization of convection. Whether or not this may affect the magnitude of the WV feedback in climate change remains unknown.

The strength of the LR and WV feedbacks show statistical correlations among models under climate variability and change (Colman and Hanson, 2017). When analysing the LR and WV feedbacks at interannual time scale, there is a general consistency between GCMs and observations during the observational record (Colman and Hanson, 2017; Dessler, 2013; Po-Chedley et al., 2018a). Models have a behaviour that is fully consistent with observations and theories although observations do not allow to constrain the precise value of these feedbacks.

This leads to an overall *high confidence* in the estimate of the water vapour plus lapse rate feedback, as the main physical processes that drive these feedbacks are well understood, are supported by multiple lines of evidence including models, theory and observations, and the various estimates cover a wide range of approaches. The combined water vapour plus lapse rate feedback is assessed to be α_{LR+WV} = 1.12 W m^{-2} °C^{-1}, with a *very likely* range of 0.85 to 1.40 W m^{-2} °C^{-1} and a *likely* range of 1.0 to 1.25 W m^{-2} °C^{-1}. It is *virtually certain* that the combined water vapour plus lapse rate feedback is positive.

7.4.2.3 Surface albedo feedback

Surface albedo is determined primarily by surface reflectance, but also by the spectral and angular distribution of incident solar radiation. Changes in planetary albedo are roughly one-third the magnitude of surface albedo changes, owing to atmospheric absorption and scattering, with variability and uncertainty arising primarily from clouds (Donohoe and Battisti, 2011). Temperature change induces surface albedo change through several direct and indirect means. In the present climate, the largest contributions by far are changes in the extent of sea ice and seasonal snow cover, as these media are highly reflective and there are large regions that are typically close to the melting temperature. Reduced snow cover on sea ice may contribute as much to albedo feedback as reduced extent of sea ice. Changes in the snow metamorphic rate, which generally reduces snow albedo with warmer temperature, and warming-induced consolidation of light absorbing impurities near the surface, also contribute secondarily to the albedo feedback (Doherty et al., 2013; Flanner and Zender, 2006; Qu and Hall, 2007; Tuzet et al., 2017). Other contributors to albedo change that are modulated indirectly by global temperature include vegetation state (Section 7.4.2.6), soil wetness, and ocean roughness.

CMIP5 models show large spread in α_A (Qu and Hall, 2014; Schneider et al., 2018), motivating attempts to quantify α_A from global observations. Although estimates derived from the satellite record are hampered by interannual variability and its short duration compared with climate equilibration timescales, justification for using these data comes from analysis of transient simulations showing that α_A estimates from time periods when global temperature change exceeds 0.5 K, regardless of the period length, offer good approximations of long-term (century-scale) α_A (Schneider et al., 2018). Global temperature change during the period of consistent space-borne albedo measurements (1979 to present) is on the cusp of this threshold.

Flanner et al. (2011) applied satellite observations to determine that the NH cryosphere contribution to α_A over 1979–2008 was 0.48 (0.29–0.78) W m^{-2} °C^{-1}, with roughly equal contributions from changes in seasonal snow cover and sea ice. Since AR5, and over similar periods of observation, Crook and Forster (2014) found an estimate of 0.8 ± 0.3 W m^{-2} °C^{-1} for the total NH extra tropical surface albedo feedback, when averaged over global temperature change. Pistone et al. (2014) and Cao et al. (2015) estimated the Arctic sea ice contribution alone to be 0.31 ± 0.04 and 0.31 ± 0.08 W m^{-2} °C^{-1}, respectively, substantially larger than the estimate from Flanner et al. (2011). Much of this NH discrepancy can be traced to different estimates of attenuation by Arctic clouds between model-derived radiative kernels and direct measurements of TOA irradiance, with the latter indicating much less attenuation and therefore suggesting that the two more recent studies showing larger α_A are more realistic. All four studies show larger observational estimates of Arctic albedo change than exhibited by most CMIP3 and CMIP5 models over similar time periods, which can be traced to models generally underestimating the rate of Arctic sea ice loss during recent decades (Flato et al., 2013; Stroeve et al., 2012; Chapter 9, Section 9.3.1). Crook and Forster (2014) additionally found that although models underestimated NH feedback values they agreed on similarly sized Southern Hemispheric extratropical values.

Since AR5, Chen et al., (2016b) estimate that NH land snow changes during 1982–2013 contributed (after converting from NH temperature change to global mean temperature change) 0.1 W m^{-2} °C^{-1} to global α_A, smaller than the estimate 0.48 (0.29–0.78) W m^{-2} °C^{-1} of Flanner et al. (2011). Qu and Hall (2014) report a CMIP5 multi-model mean NH land snow contribution to α_A of 0.08 W m^{-2} °C^{-1}. Encouragingly, this is about the same as the average of the 8 models (ranging from 0.05–0.10 W m^{-2} °C^{-1}) whose seasonal cycle of albedo feedback falls within the observational range of uncertainty determined from satellite measurements. The seasonal cycle of α_A offers a promising constraint on α_A in the climate change context because the two are very highly correlated in models (Crook and Forster, 2014; Hall and Qu, 2006; Qu and Hall, 2014).

These studies all focus on the northern hemisphere, though exclusion of the SH only slightly biases estimates of global α_A because seasonal snow cover in the SH is relatively small, and trends in SH sea ice extent are relatively flat or slightly increasing over the satellite record (Comiso et al., 2017; see also Chapter 2, Section 2.3). The multi-model mean global-scale α_A (from all contributions) over the 21st century in CMIP5 models under the RCP8.5 scenario is 0.40 W m^{-2} °C^{-1} with a standard deviation of 0.10 W m^{-2} °C^{-1} (Schneider et al., 2018), closely matching the summed observational contributions from NH sea ice and land snow over the satellite era. Moreover, Schneider et al. (2018) found that modelled α_A does not decline over the 21st century, despite large losses of snow and sea ice, though a weakened feedback is apparent after 2100. Using the idealized *abrupt4×*CO_2 as for the other feedbacks, the estimate of the global-scale albedo feedback in the CMIP5 models is 0.35 W m^{-2} °C^{-1} with a standard deviation of 0.08 W m^{-2} °C^{-1} (Caldwell et al., 2016; Vial et al., 2013).

[*Assessment of the short-term albedo feedbacks due to vegetation will be included in the SOD*]

This leads to an overall *high confidence* in the estimate of the surface albedo feedback based on multiple lines of evidence including observations, models and theory. The basic phenomena that drive this feedback are well understood and the different studies cover a large variety of hypothesis or behaviours, including how the evolution of clouds affects this feedback. The global albedo feedback is therefore assessed to be α_A = 0.35 W m^{-2} °C^{-1}, with a *very likely* range of 0.10–0.60 W m^{-2} °C^{-1} and a *likely* range of 0.25–0.45 W m^{-2} °C^{-1}. It is *virtually certain* that the surface albedo feedback is positive.

7.4.2.4 Cloud feedbacks

Clouds can be formed almost anywhere on the globe when moist air parcels rise and cool, enabling the water vapour to condensate or small water droplets to freeze. The cloud droplets, ice crystals, and their mixture interact with each other to grow into large particles of rain, snow, or drizzle, which fall down to the surface. These microphysical processes are coupled with aerosols, radiation and circulation, resulting in a complexity in the cloud processes, and it has been both observational and modelling challenges to measure them accurately and calculate them adequately, respectively. Regarding the energy budget, clouds affect SW radiation by reflecting solar insolation due to their high albedo (acting to cool the climate system) and also LW radiation by absorbing the energy emitted from the surface and re-emitting at a lower temperature than the surface temperature (i.e., the greenhouse effect, acting to warm the climate system). These effects of clouds on radiation are measured by the CRE, which is the difference in TOA radiation between clear and cloudy skies. Because the SW CRE and LW CRE tend to compensate each other over the equatorial region where deep convective clouds dominate, the net CRE shows a large negative value over the eastern part of the subtropical oceans and the extratropical oceans owing to cooling by marine low clouds. The global-mean net CRE is approximately –18 W m^{-2}, which comes from a SW CRE of –46 W m^{-2} partly cancelled by a LW CRE of +28 W m^{-2} (Loeb et al., 2018b). Albeit current GCMs lack the ability to reproduce some cloud regimes correctly, the overall distribution as well as the global mean of the net CRE derived from the CMIP6 multi-model mean is similar to the satellite observations.

The ability of GCMs to simulate clouds has now been evaluated not only for the cloud cover and CRE, but also for cloud properties directly associated with processes of cloud-radiative feedbacks, by means of the recent satellite observations and the so-called satellite simulators implemented in climate models (Bodas-Salcedo et al., 2011; Tsushima et al., 2017). Measurements from A-Train satellites resolve the vertical distribution of clouds (Stephens et al., 2002), but they cannot be directly compared to the GCM outputs because all of the clouds are not seen from space simultaneously. The simulators apply the satellite retrieval algorithms to the instantaneous cloud fields simulated in a GCM, enabling a like-for-like comparison with the A-Train products. Consequently, a thorough evaluation of the vertical profile of simulated clouds has revealed model errors in the fraction, liquid and ice contents, optical depth, and resultant CRE (Bodas-Salcedo et al., 2012; Konsta et al., 2015; Nam and Quaas, 2012; Suzuki et al., 2015; Tsushima et al., 2013). For example, McCoy et al. (2014a; 2014b) showed that the too week negative SW CRE over the Southern Ocean, a well-known common error in GCMs, was due to a lack of sufficient supercooled cloud liquid droplets that should increase the cloud optical depth. While the cloud properties relevant to CREs have incrementally been improved in recent generations of GCMs (Jiang et al., 2012; Klein et al., 2013), there still remain the common model errors such as in the subtropical low clouds (Nam et al., 2012) and mixed-phase cloud over the Southern Ocean (McCoy et al., 2016). Therefore, the assessment of cloud feedbacks in this section relies not only on GCMs but also on cloud process models and emergent constraints on cloud processes.

Clouds have various types, from thick convective clouds to thin stratus and cirrus clouds, depending upon thermodynamic conditions and large-scale circulation. They are classified into several regimes as schematically shown in Figure 7.17. Over the equatorial warm pool, high SST stimulate the development of deep convective systems, which are accompanied by anvil and cirrus clouds near the tropopause where the convective air outflows. Deep convection also frequently occurs along the ITCZ in the Pacific and Atlantic. The large-scale circulation associated with these convective clouds leads to subsidence over the subtropical cool oceans, where deep convection is suppressed by a lower tropospheric inversion layer maintained by the subsidence and thereby shallow cumulus and stratocumulus clouds form. In the extratropics, mid-latitude storm tracks control cloud fraction, which occurs primarily in frontal bands of the extratropical cyclones. Because liquid droplets cannot freeze spontaneously at temperatures above approximately –40°C and ice nucleating particles that can aid freezing at warmer temperatures are rare, extratropical clouds often consist both of super-cooled liquid and ice crystal, shaping mixed-phase clouds. A challenge for understanding cloud feedbacks with surface warming is to assess the response of clouds not only to changes in local temperature and moisture but also to changes in the large-scale circulation such as the poleward retreat of storm tracks, expansion of subtropical dry zones, and increase of tropopause heights at all latitudes (red arrows in Figure 7.17). While these circulation changes have partly been detected in observations, and the past cloud change patterns derived from satellite records are overall consistent with the projected changes in GCMs (Norris et al., 2016), the broad consistency is not sufficient to quantify the net cloud feedback.

[START FIGURE 7.17 HERE]

Figure 7.17: Schematic cross section of diverse cloud regimes between the tropics and Polar Regions. Thick solid and dashed curves indicate the tropopause, melting level, and the subtropical inversion layer in the current climate. Thin grey arrows represent robust responses in the large-scale circulation to greenhouse warming, supported by independent lines of evidence. Text and arrows in red show the robust part of

cloud responses to the surface warming.

[END FIGURE 7.17 HERE]

In a first attempt to systematically evaluate ECS based on fully coupled GCMs in AR4, diverging cloud feedbacks were recognized as a dominant source of uncertainty. A thorough assessment of cloud feedbacks in different cloud regimes was then carried out in AR5 (Boucher et al., 2013), which provided *high* or *medium confidence* for some of the cloud feedbacks but *low* or no *confidence* for the rest (Table 7.8). Many studies that estimate the net cloud feedback using CMIP5 simulations (Caldwell et al., 2016; Colman and Hanson, 2017; Vial et al., 2013; Zelinka et al., 2016) show slightly different values depending on the methodology and the set of models but commonly report a considerable inter-model spread of the feedback, which has the 90% range spanning from a weak negative to a strong positive feedback (Figure 7.16). Part of this diversity arises from the considerable dependence of the models' cloud feedback on the parameterization of clouds and their coupling to other sub-grid processes (Gettelman et al., 2012; Watanabe et al., 2012).

Since AR5, community efforts have been made to understand the cloud feedbacks in various cloud regimes coupled with large-scale circulation (Bony et al., 2015). For some cloud regimes, different lines of evidence from observations, theoretical arguments, and cloud process modelling using Large Eddy Simulation (LES) help quantifying the temperature-mediated feedbacks. Consequently, the net cloud feedback derived from GCMs has been revised by assessing separately the regional cloud feedbacks and summing them to give the global feedback. This bottom-up assessment is explained below with a summary of updated confidence of individual cloud feedback components in Table 7.8.

Tropical high-cloud altitude feedback. The cloud top altitude increases under global warming, concurrent with the rising of the tropopause at all latitudes. This increasing altitude of high clouds has been observed in early generation GCMs (Hansen et al., 1984) and the tropical high-cloud altitude feedback was assessed to be positive with high confidence in AR5 (Boucher et al., 2013). This is supported by a theoretical argument called the fixed anvil temperature (FAT) mechanism, which ensures temperature at the convective detrainment layer does not change when the altitude of high-cloud top increases with rising tropopause (Hartmann and Larson, 2002; Zelinka and Hartmann, 2010). Because the cloud top temperature does not change significantly with global warming, cloud longwave emission does not increase even though the surface warms, resulting in an enhancement of the high cloud greenhouse effect (a positive feedback). The upward shift of high clouds with surface warming is detected in observed interannual variability and trends in satellite records for 1983-2009 (Chepfer et al., 2014; Norris et al., 2016), and in global cloud-system resolving simulations and LES (Khairoutdinov and Emanuel, 2013; Narenpitak et al., 2017; Tsushima et al., 2014). The high-cloud altitude feedback was estimated to be +0.5 W m^{-2} °C^{-1} based on GCMs in AR5, but is revised, using a recent re-evaluation that excludes effects of other clouds, downward to +0.20 W m^{-2} °C^{-1} with the *very likely* range of 0.05–0.35 W m^{-2} °C^{-1} (Zelinka et al., 2016). The positive high-cloud altitude feedback simulated in GCMs is supported by theoretical, observational, and process modelling studies, and is judged with *high confidence*.

Tropical high-cloud amount feedback. Updrafts in the convective plume lead to detrainment of air mass at a level where the buoyancy diminishes, and thus organized deep convective systems over high SSTs in the tropics are accompanied by so-called anvil clouds in the upper troposphere. The anvil clouds that occupy a wider area than the convective plumes themselves contribute substantially to the positive LW CRE in the present climate, so that they would exert a negative feedback if their area were reduced in the future (Figure 7.17). A hypothesis known as the 'iris effect' that suggests the reduction of anvil clouds due to global warming was first proposed by Lindzen et al. (2001), who advocated that an increased precipitation efficiency with warming results in less condensates in the detrained air mass and consequently a strong negative feedback. This hypothetical microphysical process is not supported to date, but recent observational estimates reveal that variability in the tropical high-cloud area has a weak negative feedback on interannual time scales (Williams and Pierrehumbert, 2017). The reason for decreasing anvil clouds with increasing SST is *likely* different from the iris effect. Observational analyses show that the anvil cloud cover tends to be reduced when convective clouds are clustered, accompanying a drying of the surrounding environment (Stein et al., 2016; Tobin et al., 2013). Simulations using LES and idealized GCM experiments consistently demonstrate that the convective aggregation is enhanced with increased SST and theoretical arguments have been made to explain this enhancement (Bony et al., 2016; Emanuel et al., 2014; Mauritsen and Stevens, 2015; Muller and Held, 2012; Wing and Emanuel, 2014). A thermodynamic mechanism referred to as the 'stability iris effect', independent of convective aggregation, has also been proposed to explain the tendency of many GCMs and CRMs to predict a decrease of the anvil cloud amount with warming (Bony et al., 2016; Cronin and Wing, 2017). However, a large uncertainty remains about the change in convective aggregation with warming. Moreover, the simulation of high-level clouds in GCMs and CRMs (including in global CRMs) strongly depends on the representation of parametrized processes such as cloud microphysics. Finally, anvil clouds represent only part of the upper-level cloudiness. For all these reasons, the behaviour of the high-cloud amount with warming remains quite uncertain. The tropical high-cloud amount feedback is therefore *likely* small and negative, counteracting a small portion of the positive high-cloud altitude feedback, but with a *low* confidence.

Tropical marine low-cloud feedback. It has long been argued that the response of low-latitude marine boundary layer clouds to surface warming was the largest contributor to the cloud feedback uncertainty (Bony and Dufresne, 2005). Because of their low altitude, low clouds in the stratus, stratocumulus, and trade cumulus regimes mainly affect shortwave radiation and would therefore act as a positive feedback if the amount declined with surface warming, and vice versa. Processes that control the low clouds are, however, not simple, and involve coupling with atmospheric motions on multiple scales from the boundary layer turbulence to the large-scale subsidence, which may be represented by a combination of shallow and deep convective mixing (Sherwood et al., 2014). Recent studies have attempted to disentangle the processes into several 'cloud controlling factors' that cause the cloud amount either to increase or decrease in response to the surface warming in a GCM (Brient and Schneider, 2016; McCoy et al., 2017b; Myers and Norris, 2016; Qu et al., 2014, 2015; Zhai et al., 2015). Two dominant factors are identified: a thermodynamic effect due to rising SST that works to reduce low cloud, and a stability effect accompanied by an enhanced inversion strength that works to increase low cloud. These controlling factors compensate with a varying degree in different GCMs, but can be constrained using the observed seasonal or interannual relationship between the low-cloud amount and the controlling factors in the environment, to which long-term changes in the latter from abrupt4xCO_2 simulations are multiplied. The advantage of this approach over conventional calculation of cloud feedbacks is that the temperature-mediated cloud response can be estimated without using information of the simulated cloud responses that are less trustworthy than the changes in the environmental conditions. The synthetic analysis leads to a larger local positive feedback with smaller uncertainty: +1 W m^{-2} °C^{-1} with a *likely* range of 0.6–1.4 W m^{-2} °C^{-1}, compared to the raw GCM estimates of +0.5 W m^{-2} °C^{-1} with the *likely* range from –0.2 to 1.2 W m^{-2} °C^{-1} (Klein et al., 2017) (Figure 7.18). The revision toward a larger positive feedback is supported by explicit simulations using LES applied to trade cumulus and stratocumulus regimes (Bretherton, 2015). Given that the tropical marine low clouds occupy about 25% of the globe, the global feedback due to low clouds is assessed to have the mean value of +0.25 W m^{-2} °C^{-1} and the *very likely* range of 0 to 0.5 W m^{-2} °C^{-1} *with high confidence*.

Tropical land cloud feedback. Intensification of the global hydrological cycle is a robust feature of global warming, but at the same time, many land areas in the subtropics will experience drying at the surface and the atmosphere (Chapter 8, Section 8.1). This occurs owing to a limited water availability over these regions and consequently the cloudiness is also expected to decrease over the warm subtropical land. The reduction of land clouds are consistently identified in the CMIP5 models and also in a super-parameterized GCM (Bretherton et al., 2014; Kamae et al., 2016). Because low clouds are the majority of the subtropical land clouds, this reduced amount of low clouds reflects less solar insolation and leads to a positive feedback similar to the marine low clouds. The mean estimate of the global land cloud feedback in GCMs is much smaller than the marine low cloud feedback, 0.08 W m^{-2} °C^{-1} with the inter-model standard deviation of 0.08 W m^{-2} °C^{-1}. However, the magnitude of this feedback has not yet been supported by other lines of evidence besides GCMs, which have considerable biases in the mean temperature and cloud fraction over land. Therefore, a small positive feedback due to decreasing land clouds is assessed *likely* with *medium confidence*.

Middle latitude cloud amount feedback. Expansion of the subtropical dry zone and poleward shift of the storm tracks are prominent features of the large-scale circulation due to global warming. Because much of the middle latitude clouds are induced by extratropical cyclones in the storm tracks, it has long been suggested that the middle latitude cloud maxima will also move poleward with surface warming. If the cloud maxima are shifted poleward where solar insolation is low, shortwave cloud radiative cooling is weakened and it causes a positive feedback to occur. A long-term trend of the poleward shift of middle latitude clouds has indeed been seen both in observations and GCMs, but the magnitude of the feedback is still uncertain due to several reasons. On the one hand, observational estimates of the shifts in storm tracks and cloud areas (Bender et al., 2012; Eastman and Warren, 2013), though significant, may be partly due to data artefacts resulting in a spurious trend. On the other hand, GCMs predict a decrease of middle latitude cloud coverage with the radiative feedback smaller than observational estimates (Ceppi and Hartmann, 2015; Kay et al., 2014) perhaps due to underestimation of shifts in the jet (Allen et al., 2012). A recent study suggests that the jet shift is caused by an altered radiative heating associated with an upward shift of clouds as in the tropics (Li et al., 2018b), indicating a mutual interaction between changes in the circulation and clouds. Overall, both observations and climate models support the positive mid-latitude cloud amount feedback, but the magnitude depends on the degree of circulation response to warming and it is not agreed between them due to limited accuracy of observations and errors in GCM simulations. This leads to the assessment with *medium confidence* as in AR5.

Extratropical cloud optical depth feedback. It has been argued that the cloud optical depth (opacity) will increase with surface warming in polar low clouds and hence result in a negative feedback. The most plausible explanation for this increase in cloud optical depth is a shift from ice-dominated to liquid-dominated clouds with warming. Liquid clouds generally consist of many small cloud droplets, while the ice crystals in ice clouds are orders of magnitudes fewer and thus much larger, causing the liquid clouds to be optically thicker. However, other causes for the increase in optical thickness have also been proposed (McCoy et al., 2019). Despite the fact that the process responsible for increasing the cloud optical depth is not unique (Storelvmo et al., 2015), GCMs simulate a negative optical depth feedback of –0.27 W m^{-2} $°C^{-1}$ over the SH high latitudes. However, this negative feedback is *very likely* overestimated in the models because they tend to overestimate the relative amount of ice in these clouds (Tan et al., 2016). The feedback may actually be close to neutral considering an observational estimate using satellite datasets (Terai et al., 2016). Because of these disagreements between climate models and observational estimates, the extratropical cloud optical depth feedback is assessed to be small positive with *medium confidence*.

[START FIGURE 7.18 HERE]

Figure 7.18: A synthetic evaluation of the tropical low-cloud feedback, derived from GCMs (blue), observed cloud controlling factors (yellow), and LES (dots). Central estimates are shown by white lines. Boxes and the error bars indicate the likely (66 %) and very likely (90 %) confidence intervals, respectively. The feedbacks are shown as local values but not the global mean. LES results are derived from six simulations for different cloud regimes over the tropical subsidence region. Data obtained from (Klein et al., 2017). [Note that results from CMIP6 models will be added when available.]

[END FIGURE 7.18 HERE]

Synthesis for the net cloud feedback. Our understanding of the response of clouds to greenhouse warming and its radiative feedback has deepened since AR5. Of particular progress is the assessment of marine low cloud feedback, which has continuously been a major contributor to the cloud feedback uncertainty. Different sources of knowledge (theory, observations, and process modelling) are now available to verify or revise the low cloud feedback simulated in GCMs, and the positive low-cloud feedback is consequently assessed with high confidence. Yet, it is challenging to estimate the net cloud feedback by summing known feedbacks associated with individual cloud regimes because the processes involved in some of the cloud feedbacks have been poorly understood to date (Table 7.8).

Using CMIP5 GCMs, a broad agreement has been obtained in the net cloud feedback between different time scales at interannual variability and slow (decadal to centennial) climate change (Colman and Hanson, 2017). This means that the cloud feedback on the interannual time scale, due mostly to natural climate variability, can be a surrogate of the feedback to CO_2-induced warming and the former can be estimated using observations. For the years 2000–2010, the net cloud feedback calculated using two atmospheric reanalysis data (ERA-Interim and MERRA) and TOA radiation budgets derived from the CERES product is +0.54 ± 0.35 W m^{-2} $°C^{-1}$ (Dessler, 2013) (the range indicates one standard deviation). The larger mean value suggests that GCMs underestimate a positive feedback or overestimate a negative feedback in some cloud regimes, but the observational estimate may certainly depend on the period used (see Section 7.4.3). Nonetheless, the net cloud feedback from GCMs becomes closer to the observational estimate when the tropical low-cloud feedback is revised using constraints from observations and LES (Figure 7.18).

In summary, a broad agreement for the positive net cloud feedbacks is obtained from multiple lines of evidence. This leads to an overall *high confidence* in the estimate of the feedback sign, compared to AR5. When the two major cloud feedbacks assessed with high confidence (tropical high-cloud altitude and tropical marine low cloud) are summed, the net cloud feedback is assessed to be α_{cloud} = 0.2+0.25 = 0.45 W m^{-2} $°C^{-1}$, with *medium confidence*. While other cloud feedbacks are difficult to quantify, they are judged small compared to the two major feedbacks, and they will also partly compensate each other because of different signs, so that this value is used as a central estimate. The standard deviation of the combined two major feedbacks is 0.18 W m^{-2} $°C^{-1}$, which is doubled given the uncertainty that the other cloud feedbacks do not cancel each other but are added in quadrature, i.e., the *likely* range of the net cloud feedback from 0.1 to 0.8 W m^{-2} $°C^{-1}$. Two out of five other cloud feedbacks are assessed small negative (Table 7.8), but of magnitudes that are insufficient to affect the sign of the estimated value of α_{cloud} based on expert judgement. It is therefore *very likely* that the net cloud feedback lies between 0 and 1.1 W m^{-2} $°C^{-1}$.

[START Table 7.8 HERE]

Table 7.8: Assessed sign and confidence level of cloud feedbacks in difference regimes, compared between AR5 and AR6. For some cloud regimes, the feedback was not assessed in AR5, indicated by N/A.

Feedback	AR5	AR6
Tropical high-cloud altitude feedback	Positive (*high confidence*)	Positive (*high confidence*)
Tropical high-cloud amount feedback	N/A	Small negative (*low confidence*)
Tropical marine low-cloud feedback	N/A (*low confidence*)	Positive (*high confidence*)
Tropical land cloud feedback	N/A	Small positive (*medium confidence*)
Middle latitude cloud amount feedback	Positive (*medium confidence*)	Positive (*medium confidence*)
Extratropical cloud optical depth feedback	N/A	Small negative (*medium confidence*)
Polar clouds	Small positive (*very low confidence*)	N/A
Net cloud feedback	Positive (*medium confidence*)	Positive (*high confidence*)

[END Table 7.8 HERE]

7.4.2.5 Non-CO_2 biogeochemical feedbacks and long-term Earth system feedbacks

The feedbacks presented in the previous sections (7.4.2.2 to 7.4.2.4) were directly linked to major climate variables (temperature, water vapour, clouds, and surface albedo). The central role of these phenomena has been recognised since the very first studies on past and future climate change. However, in addition to these climate feedbacks, the Earth system includes feedbacks for which the impact of the global mean surface temperature on the radiative budget is mediated by changes in the chemical composition of the dry atmosphere. They may be associated with changes in aerosols such as dust, sea-salt, or dimethylsulfide (DMS or $(CH_3)_2S$), or changes in non-H_2O greenhouse gases or stratospheric ozone. Collectively, they are referred to as *biogeochemical feedbacks*. Among them, the most important is the carbon cycle feedback that describes how a change of the global mean surface temperature affects the carbon cycle, the CO_2 concentration in the atmosphere, the radiative budget and eventually the global mean surface temperature. However, carbon cycle feedbacks are explicitly excluded in a framework where feedbacks are referenced to a CO_2 concentration change. Therefore, carbon cycle feedbacks (including weathering) are not considered here but are assessed in Chapter 5, Section 5.4. In this section only the *non-CO_2 biogeochemical feedbacks* are assessed.

Some feedbacks act on very long timescales, such as those associated with changes in ice sheets, or vegetation distribution, or deep ocean circulation. These *long-term Earth system feedbacks* usually act on timescales longer that the observational record or the century-scale future, and longer than typical simulations carried out by full complexity climate models. The mechanisms associated with long-term Earth system feedbacks, and quantitative estimates of their magnitude from the paleoclimate record, are assessed in Sections (7.4.2.5.2) and (7.4.2.5.3) respectively.

An overall assessment of non-CO_2 biogeochemical feedbacks and long-term Earth system feedbacks is given in Section (7.4.2.5).

7.4.2.5.1 Non-CO_2 biogeochemical feedbacks

Climate-DMS Feedback: DMS is indirectly produced by marine phytoplankton and is emitted to the atmosphere where it can lead to the subsequent formation of sulfate aerosol and CCN. Since the seminal work of (Charlson et al., 1987), the DMS-climate feedback loop has been invoked as a potential important climate-biogeochemical retroaction, with a warmer climate leading to higher DMS emissions, increased CCN and alteration of cloud properties, and subsequent changes in radiative fluxes. A few studies have attempted to estimate the potential climate feedback due to changes in DMS emissions using marine biogeochemical models embedded in climate models (Bopp et al., 2004; Gabric et al., 2013) with large discrepancies even on the sign of the feedback. Since AR5, new studies have used empirical evidence showing that climate-DMS feedback parameter is modulated by ocean acidification, with decreasing pH leading to a decrease of marine DMS emissions, and hence have updated the estimates of climate-DMS feedback parameter in the range 0.12 to 0.16 W m^{-2} °C^{-1} (Schwinger et al., 2017; Six et al., 2013).

Climate-dust feedback: Mineral dust is the most abundant aerosol type in the atmosphere and affects the climate system by directly scattering and absorbing radiation as well as leading to CCN and ice nucleating particles. Overall, current understanding of dust radiative properties suggests a negative radiative forcing with dust increases (Balkanski et al., 2007). Because dust emissions are sensitive to climate variability (e.g. through changes in the extent of dryland), it has been hypothesized that the climate-dust feedback could be an important retroaction loop in the climate system. In response to future climate change, predicted future dust conditions range from a 60% less dusty future (Mahowald and Luo, 2003) to a moderate increase of 10–20% in dust (Tegen et al., 2004), thus leading to high uncertainties even on the sign of the feedback loop. Since AR5, Kok et al. (2018) have estimated the direct dust-climate feedback, from changes in the dust direct radiative effect only, and have constrained this feedback in the range –0.04 to +0.02 W m^{-2} °C^{-1}.

Climate-stratospheric ozone feedback: Ozone is both a key absorber of solar radiation and an important greenhouse gas. Changes in ozone concentrations in response to projected climate change have been shown to lead to a potential climate-atmospheric chemistry feedback. Climate-chemistry models consistently project an increase in the Brewer-Dobson circulation triggered by tropical sea surface warming (Bunzel and Schmidt, 2013) that leads to a decrease in lower stratospheric ozone levels in the tropical belt due to a reduced time for ozone production (Bekki et al., 2013). This would be responsible for a negative global mean ozone radiative feedback (Dietmüller et al., 2014). Since AR5, several studies have estimated the intensity of such a feedback, and obtained contrasted results, from an insignificant (Marsh et al., 2016), low (Dietmüller et al., 2014) to a first-order effect (Nowack et al., 2015) on climate sensitivity. The estimate of this climate-stratospheric ozone feedback is very model dependent, and its range is from –0.2 to 0 W m^{-2} $°C^{-1}$.

Climate-BVOC feedback: BVOCs, such as isoprene and terpenes, are produced by land vegetation and marine plankton. Once in the atmosphere, BVOCs and their oxidation products lead to the formation of secondary organic aerosols and to increased ozone concentrations, with implications on radiative forcing. Because warmer temperatures and increased atmospheric CO_2 levels are expected to increase the emissions of BVOCs by the land biosphere (Arneth et al., 2010; Kulmala et al., 2004), it has been speculated that BVOCs may be involved in a climate feedback loop. Since AR5, Paasonen et al. (2013) and Scott et al. (2018) have estimated the feedback associated with the BVOC-induced effect on clouds and radiation to be about –0.01 W m^{-2} $°C^{-1}$

Climate–CH_4 and climate-N_2O feedbacks: As reported in Chapter 5, Section 5.4.7, global warming modifies CH_4 emissions from wetlands, the CH_4 lifetime in the atmosphere and the N_2O emissions by land and ocean. The estimate of their combine feedback is in the *likely* range from –0.03 to 0.03 W m^{-2} $°C^{-1}$, with low *confidence*.

[Assessment of the short-term vegetation feedbacks, like stomatal conductance feedback, are only included in the long-term feedback in the FOD (7.4.2.5.2) but will be included here in the SOD]

The CMIP6 ensemble provides a number of pairs of 4x CO_2 simulations carried out with models that either do or do not include non-CO_2 biogeochemical feedbacks. The comparison is not always completely clean because these pairs of models may differ by more than just their inclusion of these processes (e.g. they may run at different resolutions), but a comparison of the simulations provides a first-order estimate of the magnitude of the combination of these non-CO_2 biogeochemical processes. (Table 7.9). *[SOD: here will follow an assessment of the CMIP6 model-based estimates of the non-CO2 biogechemical feedbacks]*.

[START Table 7.9 HERE]

Table 7.9: [This table does not exist yet, but for SOD will be a table of those CMIP6 models that have an Earth system and an AO-only version, with the difference in their estimate of feedback parameter from the two versions.]

[END Table 7.9 HERE]

7.4.2.5.2 Long-term Earth system feedbacks: mechanisms and model-based estimates

There are three main components of the Earth system that respond typically on timescales greater than a few decades. These are the deep ocean circulation (in particular the deep ocean overturning), the distribution of vegetation, and ice sheets.

Long term Earth system feedbacks associated with deep ocean adjustment. The timescale for full equilibration global climate in response to a sustained CO_2 forcing is of order several millennia owing to the slow adjustment of the deep ocean (Li et al., 2013a; Zickfeld et al., 2017). While the global-average SST is expected to be nearly equilibrated (within ten percent of equilibrium warming) after 1000 years (Knutti and Rugenstein, 2015), regions of the sea surface take longer to equilibrate owing to their strong connection to the deep ocean. In particular, SSTs in the Southern Ocean adjust more slowly than those in any other region (Li et al., 2013a; Stouffer, 2004) owing to strong circumpolar upwelling of deep ocean waters that have not been in direct contact with the atmosphere for hundreds to thousands of years (Armour et al., 2016; Marshall et al., 2015).

Section 7.4.3 assesses the dependence of Earth's global radiation budget on the spatial pattern of SST changes with a focus on the evolution of surface warming on centennial timescales. Warming of the Southern Ocean surface is thought to affect polar radiative feedbacks associated with the lapse rate, sea-ice cover, and cloud cover. Hence, the feedback parameter, α, is expected to continue to change as the pattern of SSTs evolve as the deep ocean adjusts on millennial timescales. Fully coupled state-of-the-art climate models are rarely integrated for more than several hundred years, making it challenging to assess the magnitude of millennial-scale feedback changes. However, a few very long simulations have been carried out with fully coupled models, and with lower complexity models (Knutti and Rugenstein, 2015; Li et al., 2013). Some indicate that α continues to evolve as the SST pattern changes for several thousand years, while others find that α becomes constant after a few hundred years as the spatial pattern of warming stabilizes (Armour et al., 2013). While there is *high confidence* that feedbacks will increase in the future as the spatial pattern of warming evolves on centennial timescales (Section 7.4.3), there is currently insufficient information to assess how radiative feedbacks will change as the deep ocean adjusts over millennial timescales.

Long term Earth system feedbacks associated with vegetation. Vegetation is sensitive to climate on long timescales, because different species are adapted to different specific climates (e.g. Köppen and Geiger, 1936; Prentice et al., 1992). Furthermore, vegetation is directly sensitive to atmospheric CO_2, which affects plant physiology through changes in stomatal conductance and photosynthesis rates (e.g. Ainsworth and Rogers, 2007). As such, in response to CO_2 and temperature changes (Chapter 5, Section 5.2.3), and changes to the hydrological cycle associated with temperature changes (Chapter 5, Section 5.2.3), the distribution of vegetation can change over time. As vegetation distributions change, there is a radiative effect on the climate system because different species of vegetation typically have different albedos (including when snow-covered; e.g. Essery et al., 2009). Furthermore, different species have different roughness lengths and different evapotranspiration properties, and so changes in vegetation can also influence atmospheric circulation and the hydrological cycle (Bonan, 2008). Here, the associated feedback system is termed "physiological-biophysical vegetation feedbacks". In contrast, biogeochemical vegetation feedbacks, which influence atmospheric CO_2, are explicitly excluded in our concentration-driven framework (Section 7.1; Box 7.1) and are not considered here. The timescale of response of vegetation to CO_2 and climate change is relatively uncertain but can be hundreds of years (Willeit et al., 2014); full equilibrium only occurs when the soil system and associated carbon pools fully equilibrate, which can take longer (Sitch et al., 2008).

Climate models that include a dynamical representation of vegetation (e.g. Harper et al., 2018) can been used to explore the importance of physiological-biophysical vegetation feedbacks (e.g. Alo and Anagnostou, 2017; Armstrong et al., 2019; Arora et al., 2013; Notaro et al., 2007; O'ishi et al., 2009; Port et al., 2012; Willeit et al., 2014; Zhang et al., 2018). Typically, simulations driven by prescribed CO_2 increases are carried out in climate models with and without dynamic vegetation, and the temperature responses compared. In AR5, it was discussed that such model experiments predicted that expansion of vegetation in the high latitudes of the NH would enhance warming due to the associated surface albedo change (Boucher et al., 2013); an effect amplified by sea ice and snow feedbacks. Further, that reduction of tropical forests would also lead to warming, due to reduced evapotranspiration. However, no quantitative assessment was made of the global impact of physiological-biophysical vegetation feedbacks, although CMIP5 simulations at that time indicated a small mean positive warming (+0.42 °C after 140 years of a 1% per year CO_2 increase).

Since AR5, several studies have confirmed that physiological-biophysical vegetation feedbacks lead to enhanced warming in NH high latitudes (*high confidence*), associated with a shift from tundra to boreal forests and the associated albedo change (Armstrong et al., 2019; Willeit et al., 2014; Zhang et al., 2018c). Although regional modelling indicates that vegetation feedbacks may act to cool climate in the Mediterranean (Alo and Anagnostou, 2017), in the tropics and subtropics the regional response is in general not consistent across models.

On a global scale, modelling studies indicate that physiological-biophysical vegetation feedbacks are either positive (Armstrong et al., 2019; Arora et al., 2013; Notaro et al., 2007; O'ishi et al., 2009) or are close to zero (Port et al., 2012; Willeit et al., 2014). Overall, the feedback parameter, α_x, for physiological-biophysical vegetation feedbacks is assessed to be *likely* positive, with *medium confidence*, but there is insufficient evidence at this time to give an assessment of its *likely* range. Higher confidence in the results from coupled climate-vegetation models will be obtained if they are able to better simulate past observed changes in vegetation, such as under orbital forcing in the mid-Holocene, when data indicates extensive vegetation in the Sahara, which models are currently unable to capture (Braconnot et al., 2012).

Long term Earth system feedbacks associated with ice sheets. Earth's ice sheets (Greenland and Antarctica) are also sensitive to climate change (Section 9.4). Their surface mass balance depends on the net energy balance and P-E at their surface, and the stability of the Antarctic ice shelves depends on ocean temperature (Section 9.4.1). The presence of ice sheets affects Earth's radiative budget, hydrology, and atmospheric circulation due to their characteristic high albedo, low roughness length, and high altitude, and they influence ocean circulation through freshwater input from calving and melt (e.g. Fyke et al., 2018). The timescale of response of ice sheets is of the order of thousands of years; due to the long timescales involved, fully coupled climate-ice sheet simulations with full complexity models cannot be run to full equilibrium, and as a result, long-term simulations are often carried out with lower complexity models, and/or are not fully coupled.

In AR5, it was described that both the Greenland and Antarctic ice sheets would continue to melt in a warming world (Collins et al., 2013a), with a continuation in sea level rise beyond the year 2500 being assessed as *virtually certain*. However, there was *low confidence* in the associated feedback mechanisms, and as such, there was no assessment of the magnitude of long-term Earth system feedbacks associated with ice sheets.

The magnitude of the feedback associated with changes to ice sheets can be quantified by comparing the global mean long-term equilibrium temperature response to increased CO_2 concentrations in simulations that include interactive ice sheets with that of simulations that do not include the associated ice-sheet climate interactions (Bronselaer et al., 2018; Goelzer et al., 2011; Golledge et al., 2019; Swingedouw et al., 2008; Vizcaíno et al., 2010). These simulations indicate that on multi-centennial timescales, fresh water fluxes from melting ice sheets modify ocean circulation (Bronselaer et al., 2018; Goelzer et al., 2011; Golledge et al., 2019; Swingedouw et al., 2008), leading to reduced warming, although other work suggests no net global temperature effect of ice sheet melting (Vizcaíno et al., 2010). However, model simulations in which the Antarctic ice sheet is removed completely in a paleoclimate context indicate a positive global mean feedback on multi-millennial timescales due primarily to the surface albedo change (Goldner et al., 2014; Kennedy-Asser et al., 2019). As such, overall, on multi-centennial timescales the feedback parameter, α_x, associated with ice sheets is negative (*medium confidence*), but on multi-millennial timescales by the time the ice sheets reach equilibrium (or completely melt) and freshwater fluxes reduce (or stop), the feedback parameter is positive (*high confidence*). However, there is currently not enough evidence to quantify these feedbacks, or the timescales on which they act.

[SOD will add discussion of any new long simulations with and without ice sheets that are carried out in the framework of ISMIP6 (Goelzer et al., 2018; Nowicki et al., 2016)*]*.

Long-term Earth system feedbacks: paleoclimate observations and modelling. In AR5 (Masson-Delmotte et al., 2013), the only quantitative assessment of long-term Earth system feedbacks was in the context of the paleoclimate record, wherein it was assessed that evidence from the Mid Pliocene Warm Period (MPWP, 3.3 to 3.0 million years ago) implied that, with *medium confidence*, Long-term Earth sensitivity may be up to two times greater than Charney climate sensitivity. This implies a positive value of the feedback parameter, αx, for the combination of vegetation and ice sheet feedbacks.

Since AR5, several studies have further explored long-term Earth system feedbacks using a combination of paleoclimate observations and modelling. In particular, model simulations under CO_2 forcing can be carried out in which the vegetation and ice sheets are prescribed in a way that is informed by paleoclimate observations (Haywood et al., 2013b; Lunt et al., 2009)). For this approach, observations of past sea level (e.g. from paleo shorelines; Dowsett and Cronin, 1990; or from geochemical estimates; Winnick and Caves, 2015) can provide information on ice sheet changes, and observations of past vegetation (e.g. from pollen records; Salzmann *et al.*, 2013) can provide information on land surface changes, associated with past high-CO_2 time periods.

Overall assessment of non-CO_2 biogeochemical feedbacks and long-term Earth system feedbacks. A limited number of studies provided new estimates of the non-CO_2 biogeochemical feedbacks since AR5. The non-CO_2 biogeochemical feedbacks come from a variety of models, with different level of complexity and that generally include only part of these feedbacks. The possible interaction between feedbacks may be lacking. The results vary across the different studies, which are generally based on a limited evidence. As a result, there is *low confidence* in the estimates of both the individual feedbacks and their total effect (Table 7.10).

The combination of model-based estimates, and paleoclimate approaches together indicate with *high confidence* that the feedback parameter associated with long-term Earth system feedbacks (vegetation and ice) is positive on multi-millennial timescales, but there is not enough robust evidence to give a quantitative assessment of its magnitude or the associated timescales *[note:for SOD may change with emerging papers]*.

[START Table 7.10 HERE]

Table 7.10: Assessed estimates of non-CO_2 biogeochemical feedbacks and long-term Earth system

Feedback Parameter, α_x	Combined Feedback Parameter, α_x	Timescale	Assessment	Confidence
DMS		Years	*likely* 0.12 to 0.16 W m^{-2} °C^{-1}	*low*
Dust		Years	*likely* –0.04 to +0.02 W m^{-2} °C^{-1}	*low*
Stratospheric ozone		Years	*likely* –0.2 to 0 W m^{-2} °C^{-1}	*low*
BVOC		Years	about –0.01 W m^{-2} °C^{-1}	*low*
CH_4 and N_2O		Years	*likely* –0.02 to 0.03 W m^{-2} °C^{-1}	*low*
DMS, Dust, Stratospheric ozone, BVOC, CH_4 and N_2O	All non-CO_2 biogeochemical	Years	*likely* –0.1 to 0.1 W m^{-2} °C^{-1}	*low*
Vegetation		Multi-centennial	*likely* positive	*Medium*
Ice sheets		Multi-centennial	*likely* negative	*Medium*
Ice sheets		Multi-millennial	*likely* positive	*High*
Vegetation, ice sheets	All long-term Earth system	Multi-millennial	*very likely* positive	*High*

[END Table 7.10 HERE]

7.4.2.6 Synthesis

Table 7.11 summarises the estimates and the assessment of the individual and the total feedbacks presented in the above sections. The GCMs estimates is computed using one single method whereas the assessed interval also includes uncertainties due to the calculation method. The *medium confidence* in the cloud feedback limited the level of confidence of the total feedback and prevents us from defining the *very likely* range of the total feedback. However, as the net cloud feedback is assessed positive with *high confidence*, the total climate feedback is assessed to be *very likely* more positive than –1.95 W.m^{-2} °C^{-1} with *high confidence.*

[START Table 7.11 HERE]

Table 7.11: Synthesis Assessment of climate feedbacks

Feedback parameter α_x	CMIP5 GCMs 5-95% interval ($W\ m^{-2}\ °C^{-1}$)	CMIP6 GCMs 5-95% interval ($W\ m^{-2}\ °C^{-1}$)	AR6 assessment *very likely* interval ($W\ m^{-2}\ °C^{-1}$)	AR6 assessment *likely* interval ($W\ m^{-2}\ °C^{-1}$)	AR6 assessment level of confidence
Planck	–3.2 to –3.0		–3.4 to –2.9	–3.3 to –3.0	*high*
WV + LR	1.0 to 1.3		0.85 to 1.40	1.0 to 1.25	*high*
Clouds	–0.1 to 0.95			0.07 to 0.83	*high*
Surface albedo	0.2 to 0.55		0.10 to 0.60	0.25 to 0.45	*high*
non-CO_2 biogeochemistry	Not evaluated		Not evaluated	–0.1 to 0.1	*low*
Total (i.e. relevant for ECS)	–1.6 to –0.6			–1.6 to –0.9	*medium*
Additional long term (millennial scale)			> 0.0		*high*

[END Table 7.11 HERE]

7.4.3 Dependence of feedbacks on temperature patterns

Since AR5 there is a much-improved understanding of the dependence of radiative feedbacks on the spatial patterns of surface warming. Multiple generations of climate models have produced changes in the global radiative feedback under transient warming, and a variety of explanations have been proposed for this behaviour (Andrews et al., 2015; Boer and Yu, 2003; Geoffroy et al., 2013a; Murphy, 1995; Rose et al., 2014; Senior and Mitchell, 2000; Williams et al., 2008; Winton et al., 2010). Research since AR5 has focused on the role of evolving SST patterns in driving radiative feedback changes (Andrews et al., 2015, 2018; Andrews and Webb, 2018; Armour et al., 2013; Ceppi and Gregory, 2017; Dong et al., 2019; Gregory and Andrews, 2016; Marvel et al., 2018; Myhre et al., 2018; Proistosescu and Huybers, 2017; Silvers et al., 2018; Zhou et al., 2016, 2017a). In particular, changes in warming patterns provoke changes in global TOA radiation that are not associated with global mean surface warming. Thus, if the warming pattern evolves, so too will global radiative feedbacks. This “pattern effect” (Stevens et al., 2016) is distinct from potential radiative feedback dependencies on the global mean surface warming, which are assessed in Section 7.4.4. This section assesses process understanding of the pattern effect. Section 7.5.3 describes how potential feedback changes affect estimates of ECS based on historical warming.

The radiation changes most sensitive to warming patterns are thought to be those associated with the low-cloud cover (affecting global albedo) and the tropospheric temperature profile (affecting infrared emission to space). The mechanisms and radiative impacts of these changes are illustrated in Figure 7.19a,b. SSTs in regions of deep convective ascent (e.g., in the western Pacific warm pool) govern the temperature of the tropical free troposphere and, in turn, affect low clouds through the strength of the inversion that caps the boundary layer (i.e., the lower-tropospheric stability) in subsidence regions (Klein et al., 2017; Wood and Bretherton, 2006). Surface warming within ascent regions thus warms the free troposphere and increases low-cloud cover, engendering an increase in infrared emission to space and a reduction in absorbed solar radiation. In contrast, sea-surface warming in regions of overall descent preferentially warms the boundary layer and enhances convective mixing with the dry free troposphere, decreasing low-cloud cover (Bretherton et al., 2013; Qu et al., 2014; Zhou et al., 2015) and engendering an increase in absorption of solar radiation but little change in infrared emission to space. As a result, warming in tropical ascent regions actuates negative lapse-rate and cloud feedbacks while warming in tropical descent regions actuates positive lapse-rate and cloud feedbacks (Figure 7.19b; (Andrews and Webb, 2018; Dong et al., 2019; Rose and Rayborn, 2016; Zhou et al., 2017a). Surface warming in mid-to-high latitudes engenders a weak radiative response owing to compensating changes in infrared emission (Planck and lapse-rate feedbacks) and absorbed solar radiation (shortwave cloud and surface-albedo feedbacks) (Figure 7.19b) (Dong et al., 2019; Rose and Rayborn, 2016).

[START FIGURE 7.19 HERE]

Figure 7.19: Illustration of tropospheric temperature and cloud response to enhanced warming in the west Pacific Ocean relative to the east; adapted from (Mauritsen, 2016) based on results from (Zhou et al., 2016). (b) Global TOA radiative response to sea-surface warming at each location while SSTs are held fixed elsewhere in NCAR's Community Atmosphere Model version 5 (CAM5); adapted from (Zhou et al., 2017a). (c) Observed sea-surface temperature linear trend over 1900-2017 (HadISST dataset; Rayner et al., 2003). (d) Sea-surface temperature linear trend over 150 years following abrupt CO_2 quadrupling simulations of CMIP5 GCMs (average of 17 models). [Note SOD will update to show observed 1900-2018 SST trend. For SOD: show (a) as a separate figure and update. In its place add the pattern of warming under 1pctCO_2 or historical for CMIP5/6]

[END FIGURE 7.19 HERE]

Since 1900, observed SSTs in the tropical western Pacific Ocean have increased while those in the tropical eastern Pacific Ocean have changed less (Figure 7.19c; Chapter 9, Section 9.2). Much of this strengthening of the equatorial Pacific temperature gradient has occurred since about 1980 due to strong warming in the west and cooling in the east associated with an intensification of the surface equatorial easterly trade winds that has been driven by a combination of internal variability and aerosol forcing (Chapter 9, Section 9.2). Southern Ocean SSTs have also been slow to warm since 1900 and have cooled since 1980 owing to a combination of upper-ocean freshening from ice-shelf melt, intensification of surface westerly winds from ozone depletion, and variability in ocean convection (Chapter 9, Section 9.2). Concurrent with these SST trends since 1980 has been an increase in the strength of the capping inversion in tropical descent regions, resulting in an observed increase in low-cloud cover over the tropical eastern Pacific (Zhou et al., 2016). Thus, tropical low-cloud cover increased over recent decades even as global-average surface temperature increased – a negative low-cloud feedback which is at odds with the positive low-cloud feedback expected under global warming (Section 7.4.2). Atmosphere-only GCMs run with prescribed observed SST and sea-ice concentrations show pronounced variation in their radiative feedbacks over the last century, with a trend toward strongly negative net radiative feedback in recent decades, owing primarily to negative shortwave cloud feedbacks, as in observations (Figure 7.20a) (Andrews et al., 2018; Dong et al., 2019; Marvel et al., 2018; Zhou et al., 2016). However, coupled versions of the same GCMs, with identical atmospheres, robustly produce more positive values of net radiative feedbacks primarily due to more positive shortwave cloud feedback in response to abrupt CO_2 quadrupling (*abrupt4xCO$_2$*) (Andrews et al., 2018; Marvel et al., 2018). That is, the net radiative feedback within GCMs is more positive (higher ECS) for the long-term pattern of warming under CO_2 forcing than it is over the historical record. This finding can be understood from Figure 7.19b,c,d: historical sea-surface warming has been relatively large in regions of tropical ascent, leading to enhanced radiation to space per degree of global warming and thus an anomalously net negative radiative feedback; however, coupled GCMs project that future warming will be largest in tropical descent regions and at high latitudes (Section 7.6.2), leading to a reduction in radiation to space per degree of global warming and thus a more positive global radiative feedback.

Andrews et al. (2018) analysed available CMIP5/6 climate model simulations (6 in total) comparing feedbacks engendered by prescribed historical warming patterns (atmosphere-only GCMs) against feedbacks under projected *abrupt4xCO$_2$* warming (coupled GCMs). All models show a more positive global radiative feedback under *abrupt4xCO$_2$* than for the historical period (trend since 1870), with an average increase of around +0.6 W m^{-2}°C^{-1} (+0.3 to +1.0 W m^{-2} °C^{-1} range across models) (Figure 7.20d,f). These feedback changes imply that the value of ECS may be substantially larger than that inferred from the historical record (Section 7.5.3.1).

Feedback changes can alternatively be estimated within transient warming simulations of coupled GCMs.

(Armour, 2017) considered changes in radiative feedbacks between the transient response to an idealized 1% yr^{-1} CO_2 ramping (*1pctCO₂*) and the long-term response under *abrupt4xCO₂* in 21 CMIP5 models. The majority of models show a more positive global radiative feedback under *abrupt4xCO₂* than transient warming, with an average increase of around +0.2 W m^{-2} $°C^{-1}$ (–0.1 to +0.6 W m^{-2} $°C^{-1}$ range across models) (Figure 7.19c). The increase in feedbacks within the coupled models is thus not as large as that found when prescribing observed warming patterns (Figure 7.19b,c). This arises from the fact that the spatial pattern of warming within the *1pctCO₂* simulations is distinct from that observed over the historical record and more similar to the pattern under *abrupt4xCO₂*. In general, coupled GCMs are not able to reproduce the observed cooling of the eastern tropical Pacific or Southern Ocean over recent decades, even within historical simulations where non-CO_2 forcings are included (Kostov et al., 2018; Zhou et al., 2016). This suggests that internal climate variability may have played an important role in observed SST trends or that GCMs may have errors in either the applied forcing or forced response (Section 9.2). Simulations with prescribed historical warming patterns (Figure 7.19b) provide a more realistic representation of historical feedbacks and are thus thought to provide more accurate estimates of how feedbacks may change as the warming pattern evolves from present to equilibrium under CO_2 forcing (Andrews et al., 2018).

[START FIGURE 7.20 HERE]

Figure 7.20: (a) Radiative feedback (α) over the historical record derived from atmospheric GCMs with prescribed observed SSTs and sea-ice concentration changes (modified from Andrews et al., 2018). Historical feedback is derived from linear regression of global TOA radiation against global near-surface air temperature over the simulations, with regression starting in year 1870 and ending in the year shown. (b) Radiative feedback derived from historical energy budget constraints (Section 7.5.3). (c) Relationship between historical net feedback in atmospheric GCMs constrained to match the observed pattern of warming over the over the historical record (Figure 7.19c) and the net feedback under abrupt CO_2 quadrupling within coupled versions of the same GCMs (average warming pattern shown in Figure 7.19d). Equilibrium feedback is estimated based on regression of global TOA radiation against global near-surface air temperature over years 1-150 of abrupt4xCO_2 simulations, but similar results are found if the feedback magnitude is estimated as CO_2 ERF divided by ECS. (d) Relationship between historical net feedback and equilibrium net feedback in fully-coupled CMIP5 models. Historical feedback is estimated at year 100 of 1%/yr CO_2 ramping simulations based on the change in global TOA radiation divided by the change in global near-surface air temperature where changes are taken with respect to pre-industrial (Armour, 2017). The equilibrium feedback magnitude is estimated as CO_2 ERF divided by ECS where ECS is derived from linear regression over years 1-150 of abrupt4xCO_2 simulations (Box 7.1). [SOD will add additional CMIP6 models to all panels when available. Calculate feedback changes over historical simulations when forcing become available (RFMIP).]

[END FIGURE 7.20 HERE]

The magnitude of radiative feedback changes, as quantified by GCMs, depends on the accuracy of both the projected patterns of SST and sea-ice concentration changes in response to CO_2 forcing and the radiative response to those patterns (Andrews et al., 2018). It also depends on the accuracy of the historical SST and sea-ice concentration conditions prescribed within atmospheric GCMs to quantify the historical radiative feedback (Figure 7.20), which are uncertain for the early portion of the historical record but less problematic from the late 1970s (Section 2.2). While there are not yet direct observational constraints on the magnitude of the pattern effect, satellite measurements of TOA radiation fluxes show strong co-variation with changing patterns of SSTs, indicating the potential for a strong pattern effect in nature (Loeb et al., 2018c). Cloud responses to observed warming patterns in atmospheric model have also been found to compare favourably with those observed by satellite (Zhou et al., 2016). This suggests that the pattern effect will only be negligible if the observed pattern of warming persists to equilibrium. However, there is medium evidence and high agreement across paleoclimate proxies, GCM simulations, and process understanding that warming in the eastern equatorial Pacific Ocean and Southern Ocean, largely absent over the historical record, will eventually emerge as the response to CO_2 forcing dominates temperature changes in these regions (Sections

7.6.2; 7.6.3; 9.2). This leads to *medium confidence* that the eastern Pacific SSTs will eventually warm by more than the western Pacific SSTs and *high confidence* that SSTs in the Southern Ocean will eventually warm by more than tropical SSTs. Thus, there is *high confidence* that radiative feedbacks will become more positive in the future as the pattern of surface warming evolves. The magnitude of the net radiative feedback changes between the present warming pattern and the projected equilibrium warming pattern in response to CO_2 forcing (Figure 7.19b) estimated to be in the range +0.3 to +1.0 W m^{-2} $°C^{-1}$ (Figure 7.19b) with a *low confidence* in this range because its quantification currently relies solely on GCM results. Section 7.5.3 assesses the implications of changing radiative feedbacks for estimates of ECS based on the historical temperature record.

7.4.4 Dependence of feedbacks on climate mean state

In the standard framework of forcings and feedbacks (Section 7.4.1; Box 7.1), the strength of climate feedbacks are assumed to be independent of the background global mean temperature, i.e., the individual feedback parameters, α_x, are assumed to be constant over a range of climate states. If this approximation holds, then the equilibrium global mean temperature response to a unit forcing will be constant, regardless of the climate state to which that forcing is applied.

In reality, this approximation will break down if climate feedbacks behave sufficiently non-linearly, varying as a function of, for example, background temperature (Bloch-Johnson et al., 2015; Roe and Armour, 2011; Roe and Baker, 2007; Zaliapin and Ghil, 2010). If the real climate system exhibits this so-called "state-dependence", then future temperature change in response to large forcings may be different from that inferred using the standard framework. Climate models do in general include representations of feedbacks that allow non-linear behaviour, and so model results may also differ from the predictions from the standard framework.

In AR5 (Boucher et al., 2013), there was a recognition that the climate system could be state-dependent (Colman and McAvaney, 2009), but modelling studies that explored this (e.g. Manabe and Bryan, 1985; Voss and Mikolajewicz, 2001; Stouffer and Manabe, 2003; Hansen, 2005) were not assessed in detail. However, in AR5 (Masson-Delmotte et al., 2013) paleoclimate evidence was used to assess that climate sensitivity in simulations of the Last Glacial Maximum (LGM, ~19,000 to 21,00 years ago; Table 2.A.1; Cross-Chapter Box 1.4) was less than that in simulations of warm climates (CO_2 quadrupling), due to a state dependency in shortwave cloud feedbacks.

Here recent evidence for state-dependence in feedbacks, from modelling studies (Section 7.4.4.1) and from the paleoclimate record (Section 7.4.4.2) are assessed. Evidence for the dependence of feedbacks on the spatial pattern of warming, independent of global mean temperature change, is assessed in Section 7.4.3.

7.4.4.1 Evidence for state-dependence in feedbacks from modelling studies

There are several modelling studies since AR5 in which models have been used to explore state-dependency (Caballero and Huber, 2013; Good et al., 2015; Hansen et al., 2013; Heinemann et al., 2009; Jonko et al., 2013; Meraner et al., 2013). Typically, multiple simulations are carried out across successive CO_2 doublings; a non-linear temperature response to these successive doublings may be partly due to forcing that increases more rapidly than expected from a purely logarithmic dependence and partly due to state-dependence in feedbacks.

Not all modelling studies have partitioned the non-linearities in temperature response into components due to non-linearities in forcings versus feedbacks. However, there is general agreement amongst GCMs that there is a net increase in overall feedback strength (i.e. the feedback parameter, α, becomes less negative) as temperature increases from preindustrial (Meraner et al., 2013; see Figure 7.21). This increase is due in most models to the water vapour (Section 7.4.2.2) and cloud (Section 7.4.2.4) feedbacks becoming more positive with warming. These changes are offset partially but not completely by the surface albedo feedback becoming less positive with warming (Jonko et al., 2013; Meraner et al., 2013), which is a consequence of reduced snow and sea ice in a warmer climate. At the same time there is little change in the Planck feedback (Section 7.4.2.1), which becomes slightly less negative with decreasing planetary emissivity as global temperature increases (Mauritsen et al., 2019). Analysis of the spatial patterns of the non-linearities in temperature response (Good et al., 2015) suggests that these are also associated with a reduced weakening of the AMOC, and changes to evapotranspiration. There is some limited evidence from models that feedback strength may start decreasing (α becoming more negative) at very high CO_2 concentrations (> 4000ppmv) (Caballero and Huber, 2013; Hansen et al., 2013; Popp et al., 2016).

Several EMICs have been used to assess state-dependence of feedbacks (synthesised by Pfister and Stocker, 2017). The majority of EMICs synthesised either did not exhibit state-dependence or had a net feedback strength that decreased (i.e. α became more negative) with increasing CO_2 forcing, in contradiction to the GCM results. This is perhaps unsurprising since EMICs usually do not represent the water vapour and cloud feedbacks mechanistically. One exception was the FAMOUS model, which had net feedbacks that increased with increasing CO_2 forcing (i.e. α became less negative), and which, in contrast to the other EMICs in that study, is more akin to a low-resolution GCM. Although Pfister and Stocker (2017) showed that care must be taken when interpreting results from current generation EMICs, it did suggest that non-linearities in feedbacks can take a long time to emerge in model simulations, implying that millennial-scale simulations are required to increase confidence in GCM studies examining state-dependence.

The possibility of fundamental changes in state has also been suggested from theoretical studies; such changes in state could lead to substantial changes in climate feedbacks across relatively narrow CO_2 increases (Popp et al., 2016; Steffen et al., 2018; von der Heydt and Ashwin, 2016). However, even if such behaviour does exist, the threshold at which any such threshold might occur is highly uncertain.

Overall, the modelling evidence indicates that there is *medium to high confidence* that the overall net feedback strength increases with background temperature, at least up to atmospheric CO_2 concentrations of about 4000 ppmv, and *medium confidence* that this state-dependence primarily derives from increases in the water vapour and shortwave cloud feedbacks; however, there is *insufficient evidence* to provide a quantification of associated nonlinearities in the feedback parameter, α.

7.4.4.2 Evidence for state-dependence in feedbacks from the paleoclimate record

Several studies have estimated the strength of climate feedbacks from observations of the glacial-interglacial cycles of the last ~2 million years, and found a state dependence, with weaker net feedback (more negative α) during colder periods of the cycles and stronger net feedback (less negative α) during warmer periods (Friedrich et al., 2016; Köhler et al., 2015, 2017; Royer, 2016; von der Heydt et al., 2014); see summaries in Skinner (2012) and von der Heydt *et al.* (2016). However, the nature of the non-linearity derived from these observations is dependent on the assumed ice sheet forcing (Köhler et al., 2015), which is not well known, and the orbital forcing (Köhler et al., 2018); furthermore, modelling studies support both decreased (Yoshimori et al., 2011) and increased (Kutzbach et al., 2013) temperature response to unit forcing during cold climates compared to modern. Overall, there is *medium confidence* that the net feedback is stronger (α is less negative) in the warmer than in the colder episodes of the glacial-interglacial cycles.

There is paleoclimate observational evidence that during time periods warmer than present there is an increase in net feedback strength (i.e. α becomes less negative) with increasing temperature (Anagnostou et al., 2016; Shaffer et al., 2016), but the uncertainties in global mean temperature and forcing at these times are relatively large. This state-dependence in feedbacks in Earth's deep past is also supported by paleoclimate modelling studies of the Eocene (Caballero and Huber, 2013), wherein the state-dependence is associated with changes in shortwave cloud feedback. The paleoclimate evidence indicates that the overall net feedback strength was *likely* greater during warm time periods of the last 65 million years than during colder time periods (*low confidence*).

Overall, independent lines of evidence from models (Section 7.4.4.1) and from the paleoclimate record

(Section 7.4.4.2) indicate that the feedback parameter, α, *likely* becomes less negative as temperatures increase above modern-day values (*high confidence*); see Figure 7.21. *[note for SOD: the overall synthesis of evidence from paleoclimate and models at this point will likely depend on the forthcoming nonlinMIP results* (Good et al., 2016)*, plus any emerging paleo work. The synthesis, summarised in Figure 7.21, could then be quantified with a likely range.]*

[START FIGURE 7.21 HERE]

Figure 7.21: Feedback parameter, α (W m-2 °C-1), as a function of global mean surface air temperature relative to preindustrial, for model simulations (coloured circles and lines), and from paleoclimate data (grey circles and associated uncertainties). [N.B. for SOD some of these values will need checking with the original authors, as they are not all clear from the publications. Additionally, in some cases we have had to make assumptions about the forcing from CO2 doubling, or the ECS, or the LGM temperature].

[END FIGURE 7.21 HERE]

7.5 Estimates of ECS and TCR

ECS and TCR are metrics of the global mean temperature response to forcing (Section 7.1; Box 7.1) which can be estimated by combining several different lines of evidence from observations and GCMs. The constraints on these climate metrics assessed in this section are based on radiative forcing and climate feedbacks evaluated from process understanding (Section 7.5.2), climate change and variability seen within the instrumental record (Section 7.5.3), paleoclimate data (Section 7.5.4), and GCMs and emergent constraints (Sections 7.5.5 and 7.5.6). The overall assessments of the ECS and TCR are presented in Section 7.5.7.

The ECS has been extensively probed through CO_2-doubling experiments using atmospheric GCMs coupled with mixed-layer oceans during CMIP3, and subsequently through standardized CO_2-quadrupling experiments (*abrupt4xCO2*) using fully coupled GCMs during CMIP5 and CMIP6. Conventionally, the ECS is diagnosed by assuming that the radiative forcing of a quadrupling is exactly twice that of a doubling, and extrapolating to equilibrium the regression of global mean TOA radiation against global mean near-surface air temperature over years 1 to 150 within *abrupt4xCO2* simulations (Box 7.1) (Andrews et al., 2012; Gregory et al., 2004), an approximation to the true ECS that would be reached if the model was run to equilibrium. However, methodological limitations do not alter the conclusions drawn here. The ECS of a given model is the net result of the model-specific effective radiative forcing (ERF) of CO_2 doubling ($\Delta F_{2\times CO2}$) and the sum of feedback parameters (α): ECS = $\Delta F_{2\times CO2}/(-\alpha)$. Most of the spread in ECS among models arises from the contribution of cloud feedbacks to variations in α (Section 7.4.2.4).

The TCR has been diagnosed in GCMs from simulations in which the CO_2 concentration is increased at 1% yr^{-1} (*1%CO2*, an approximately linear increase in ERF over time) and defined as the average over a 20-year period, centred at the time of atmospheric CO_2 doubling, which occurs at year 70 (Box 7.1). TCR is always smaller than ECS because ocean heat uptake acts to reduce surface warming. Yet, TCR is correlated (r =0.8) with ECS across CMIP5 models (Armour, 2017; Grose et al., 2018), as expected from the fact that TCR and ECS are inherently related measures of climate response to forcing: both depend on $\Delta F_{2\times CO2}$ and α. The approximately linear relationship between TCR and ECS may become nonlinear for values of ECS higher than those spanned by CMIP5 models (Hansen et al., 1985; Knutti et al., 2005; Millar et al., 2015) owing to ocean heat uptake processes playing a more important role in setting the rate of warming when the radiative response to warming is weak.

7.5.1 Relevance of ECS, TCR for projections and policy

Regional changes in temperature, rainfall, and climate extremes have been found to correlate well with the forced changes in global-mean surface temperature within coupled GCMs (Giorgetta et al., 2013; Seneviratne et al., 2016; Tebaldi and Arblaster, 2014). While this so-called 'pattern scaling' has important limitations arising from, for instance, localized forcings, land-use changes, or internal climate variability (Deser et al., 2012; Luyssaert et al., 2014), global temperature change nonetheless explains a substantial fraction of inter-model differences in projections of regional climate changes over the 21st century (Tebaldi and Knutti, 2018). This section assesses the relationships between the idealized metrics of global climate response assessed above and their relevance for model projections of global-mean surface temperature changes.

Given that TCR and ECS are metrics of global temperature response to idealized CO_2 forcing (Box 7.1), they are not expected to directly correspond to warming under realistic forcing scenarios that include time-varying non-CO_2 forcing agents (such as aerosols and land-use changes). However, their correlation with projected warming across models gives an indication of their usefulness as a predictor of future warming. It has been argued that TCR, as a metric of transient warming, is more policy-relevant than ECS (Frame et al., 2006). However, recent results suggest that the situation is more complicated (Gregory et al., 2015; Grose et al., 2018). Grose et al. (2018) find that TCR is indeed more strongly correlated ($r = 0.8$) with warming to-date than is ECS ($r = 0.7$) across historical simulations of CMIP5 models, and that TCR remains more highly correlated with warming over the 21st century when measured relative to the period 1880 to 1950. However, ECS is more highly correlated ($r = 0.95$) with the long-term (50- and 100-year) linear warming trends in moving windows starting around 2015. This result appears to be robust with respect to emissions scenario, but does not have a clear physical explanation at this time. A potential explanation is that the radiative feedbacks governing transient warming become more similar to those governing ECS over the course of the 21st century as the pattern of surface warming becomes similar to the equilibrated warming pattern (Grose et al., 2018).

Another key metric of changes in the Earth system is the transient climate response to cumulative emissions (TCRE) which measures the global mean surface temperature response as a function of cumulative anthropogenic emissions of carbon dioxide (Chapter 5, Section 5.5). Whereas ECS and TCR consider the climate system response to specific forcing trajectories, TCRE compares the climate system response to (cumulative) emissions of CO_2. By including the carbon cycle, it captures more of the causal chain associated with anthropogenic climate change. Here only ECS and TCR are assessed; TCRE is assessed in Chapter 5, Section 5.5.1.

7.5.2 Process-based estimates

7.5.2.1 ECS using process-based assessments of the forcing and feedbacks

Steady global-mean near-surface air temperature response to a time-invariant perturbation in the CO_2 radiative forcing realizes once the Earth's energy budget regains equilibrium, taking thousands of years. In a climate model, such a response is approximated in *abrupt4xCO2* simulations, to which linear regression of ΔN against ΔT is applied and extrapolated to a point at $\Delta N = 0$. Assuming that ERF scales with the logarithm of the atmospheric CO_2 concentration so that the ERF from CO_2 quadrupling is approximately twice that of doubling, the above temperature response divided by two provides ECS, which is equal to the ratio between ERF to CO_2 doubling and the total climate feedback, i.e., $-\Delta F_{2\times CO2}/\alpha$ (cf. Box 7.1). Because radiative feedbacks can vary as the pattern of warming evolves (Section 7.4.3), the slope of the regression is in general only be an approximation to α; the assessment of feedbacks by regression (e.g., Section 7.4.2) introduces small (<10%) errors that do not affect the conclusions here. The range of ECS values directly calculated from *abrupt4xCO2* simulations by GCMs is referred to as the raw ECS range. However, the raw ECS range may not be identical to a true range of process-constrained ECS because uncertainty in some important climate feedbacks have been underestimated and some processes are not included in the GCMs (Section 7.4.2).

An alternative approach to assess the ECS range presented here, which is less dependent upon GCMs, is to use estimations of $\Delta F_{2\times CO2}$ and α obtained separately from independent lines of evidence (Sections 7.3.2 and 7.4.2). The IRF can be accurately obtained using LBL calculations, to which uncertainty due to rapid adjustments are added for estimating the range in $\Delta F_{2\times CO2}$. The range of α is derived by combining estimates of individual climate feedbacks ($\alpha \equiv \sum_i \alpha_i$, where α_i denotes the *i*th feedback parameter) based on theory, observations, and high-resolution process modelling. From these process-based evaluations, the central estimate of $\Delta F_{2\times CO2}$ is larger than $\Delta F_{2\times CO2}$ from CMIP5 models and has a narrow *likely* range, while α shows a slight negative mean value with a wide range compared to the CMIP5 (Table 7.11). Assuming that each of these two parameters follow an independent normal distribution, the *likely* range of ECS can be obtained by substituting the respective probability density function (PDF) into the expression of ECS. Since α is in the denominator, the Gaussian PDF leads to a long tail in ECS toward high values, indicating the great impact of uncertainty in α in estimating the likelihood of a high ECS (Knutti and Hegerl, 2008; Roe and Baker, 2007). Using the process-based assessment of $\Delta F_{2\times CO2}$=4.0 W m^{-2} and α=–1.25 W m^{-2} °C^{-1} (Section 7.3.2 and 7.4.2.6), the ECS shows the median of 2.9 °C, which is slightly lower than the ensemble mean of raw ECS values from CMIP5 models whereas the 17-83 percentile range is widened by 20% (red and cyan curves in Figure 7.22). *[Note estimate will be made consistent with Section 7.3 in SOD]*

The wide range of the process-based ECS compared with the range from GCMs is not due solely to different estimations of $\Delta F_{2\times CO2}$ and α, but is partly explained by an assumption that $\Delta F_{2\times CO2}$ and α are independent in the process-based estimates. In the CMIP5 ensemble, these two quantities are negatively correlated when they are calculated using the linear regression to *abrupt4xCO2* simulations (r^2 = 0.34, Andrews et al., 2012; Webb et al., 2013; see black dots in Figure 7.22). The correlation acts to compensate the inter-model spreads of $\Delta F_{2\times CO2}$ and α and thereby to narrow the ECS range directly estimated from the models. If the ECS distribution is reconstructed from PDFs of $\Delta F_{2\times CO2}$ and α derived from GCMs assuming that they are not correlated, the range of ECS is greater by 30% without a change in the mean (blue curve in Figure 7.22). Likewise, the process-based ECS distribution becomes narrower by 30% if $\Delta F_{2\times CO2}$ and α were assumed to have the covariance same as the CMIP5 models (pink curve in Figure 7.22).

A significant correlation between ERF and the total feedback occurs when the two parameters are estimated separately from AGCM experiments with prescribed SST or the CO_2 concentration, so is probably not an artefact of calculating them using the single linear regression in *abrupt4xCO2* simulations. The possible physical cause may be a compensation between the cloud rapid adjustment and the cloud feedback over the tropical oceans (Chung and Soden, 2018; Ringer et al., 2014). It has been shown that the change in the boundary layer humidity is a controlling factor for the low-cloud adjustment (Kamae and Watanabe, 2012) and for the low-cloud feedback (Klein et al., 2017), and therefore the responses of these clouds to the direct CO_2 radiative forcing and to the surface warming may not be independent indeed. However, the robust physical mechanisms are not yet clear, and furthermore, process-based assessment of the tropical low-cloud feedback does not refer to the GCMs given that physical processes which control the low clouds are not sufficiently well simulated in models. For these reasons, the co-dependency between $\Delta F_{2\times CO2}$ and α is judged with *low confidence* and the assumption that they are independent for the process-based assessment of ECS is employed, which has the mean of 2.9 °C and is *likely* between 2.3 and 4.1 °C with *high confidence*. It is *very unlikely* that ECS is greater than 5.6 °C or lower than 1.9 °C. [*Note: the assessed values for ECS here are still tentative and subject to change in SOD*]

[START FIGURE 7.22 HERE]

Figure 7.22: Probability distributions of ERF to CO_2 doubling (ΔF2×CO_2, top) and the total climate feedback (α, right), derived from CMIP5 abrupt4xCO2 simulations (blue) and process-based assessments in Sections 7.3.2 and 7.4.2 (red). The joint PDF is calculated on a two-dimensional plane of ΔF2×CO_2 and α (middle), on which the 90% range shown by an ellipse is imposed to the background theoretical values of ECS (color shading). The white dot, thick and thin curves in the ellipse represent the mean, likely and very likely range of ECS. For each set of PDFs of ΔF2×CO_2 and α, two different estimations of the ECS range are presented; one assuming that ΔF2×CO_2 and α are independent (red and blue) and the other

assuming that they have a covariance seen in the CMIP5 abrupt4xCO_2 simulations (pink and cyan). The assumption about the co-dependence between $\Delta F2\times CO_2$ and α does not alter the mean estimate of ECS but affects its likely range. Data for abrupt4xCO_2 simulations are taken from Caldwell et al. (2016).

[END FIGURE 7.22 HERE]

7.5.2.2 Transferring ECS to TCR using a two-layer EBM

In the previous section, ECS was estimated using the radiative forcing and the climate feedback parameter as: ECS = $-\Delta F_{2\times CO2}/\alpha$. To transfer the process-bases assessment from ECS to TCR, the dampening effects of heat uptake by the ocean needs to be taken into account and for this purpose a two-layer energy balance model (EBM) that allows the heat exchange between the upper- and deep-layer oceans (mimicking the ocean heat uptake) has been widely used (Armour, 2017; Geoffroy et al., 2012, 2013a; Gregory, 2000; Held et al., 2010; Mauritsen and Pincus, 2017; Rohrschneider et al., 2019). In the two-layer EBM, several parameters, in addition to ΔF and α, are introduced: heat capacities of the upper and deep oceans (C and C_0), heat exchange coefficient (γ), and the so-called efficacy parameter of ocean heat uptake (ε) that represents the dependence of radiative feedbacks on the evolving SST pattern under CO_2 forcing alone. This simple two-layer model does not include effects of natural internal variability and aerosol radiative forcing, which also affect the transient temperature response in observational records (Section 7.5.3). These parameters have different values in different GCMs, but the EBM was shown to reproduce well the global-mean surface temperature response in a GCM when the parameters are suitably estimated from the corresponding *1%CO2* simulation. The analytical solution of the EBM reveals that the surface temperature change to either abrupt or 1% increase of the atmospheric CO_2 concentration is expressed by a combination of fast and slow responses having time scales of about 4 and 250 years, representing the fast adjustment of the surface components of the climate system and slow response of the deep ocean (Geoffroy et al., 2013a).

In the equilibrium, the response of upper ocean temperature, assumed to be equivalent to surface temperature, reaches the ECS, which, by definition, depends only on $\Delta F_{2\times CO2}$ and α. In CMIP5 models, they both have inter-model spreads representing uncertainty (Figure 7.23), but uncertainty in α substantially (80–90%) contributes to the *likely* range of ECS. If additional parameters in the two-layer model are held fixed at constants taken from CMIP5 model mean estimates, the *likely* range of ECS (Section 7.5.2.1) is straightforwardly transferred to the *likely* range of TCR that is defined by the temperature response at the year 70 (1.4 to 2.2 °C, Figure 7.23b). For the range of TCR, contribution of uncertainty in α is reduced to 50 to 60% while uncertainty in ΔF becomes relatively important (Geoffroy et al., 2013b). TCR reflects the fast response occurring approximately during the first 20 years in the *abrupt 4xCO2* simulation (Held et al., 2010), but the fast response is not independent of the slow response because there is a nonlinear co-dependence between them (Andrews et al., 2015). That is, larger the fast response occurs in a GCM, greater nonlinearity works to amplify the slow response. There are several mechanisms that give rise to the nonlinear amplification of the slow response (Gregory et al., 2015), but an important factor is the dependence of α on the evolving pattern of SST increase (Section 7.4.3). Consequently, the probability of high TCR is not very sensitive to changes in the probability of high ECS.

The transient temperature response, in reality, varies with different estimates of the ocean heat uptake. A fitting of the two-layer model to the transient responses in CMIP5 models shows that uncertainty in heat capacities can be neglected and differences in ε and γ among GCMs explain 10-20% of the inter-model spread of TCR (Geoffroy et al., 2013b). Specifically, their product, εγ, appearing in a simplified form of the two-layer energy budget equations, TCR $\cong -\Delta F_{2\times CO2}/(\alpha - \varepsilon\gamma)$, gives a single parameter quantifying the dampening effects of heat uptake (Jiménez-de-la-Cuesta and Mauritsen, submitted; see also Section 7.5.3). The ocean heat uptake in nature is controlled by multiple processes associated with advection and mixing (Exarchou et al., 2014; Kostov et al., 2014; Kuhlbrodt et al., 2015) but is crudely represented by a single term of heat exchange between the upper- and deep-oceans in the two-layer EBM. Therefore, it is challenging to constrain ε and γ from observations and these parameter values estimated from CMIP5 models are used here (Geoffroy et al., 2013b). Because estimated values of ε and γ are only weakly correlated, the mean value and one standard deviation of $\varepsilon\gamma$ are calculated by ignoring their covariance as $\varepsilon\gamma = 0.86 \pm 0.29$. By incorporating the inter-model spread in $\varepsilon\gamma$, the *likely* range of TCR is widened by 17% (Figure 7.23c). Yet, the dominant contribution to the uncertainty range of TCR arises from the climate feedback, and the previous assessment stating that uncertainty in ocean heat uptake is of secondary importance remains unchanged.

The resultant TCR has the central estimate 1.7 °C, judged with *medium confidence*. It is *likely* in the range from 1.4 to 2.2 °C and is *very unlikely* to be greater than 3.2 °C. The upper bound of the *likely* range was not reduced from of the process evidence alone but can well be constrained using multiple lines of evidence (Section 7.5.7).

[START FIGURE 7.23 HERE]

Figure 7.23: (a) Time evolution of the effective radiative forcing (ERF) to the CO_2 concentration increased by 1% per year until the year 70 (equal to the doubling, grey line) and kept fixed afterword. The range of ERF has been assessed in Section 7.3. (b)-(c) Range of surface ocean temperature response (assumed to be equivalent to the surface air temperature response) to the CO_2 forcing in the two-layer EBM calculated with a given range of ECS, considering uncertainty only in $\Delta F2\times CO_2$ and α (b, shading by red and orange colours) and additionally in two parameters associated with the ocean heat uptake (c, shading by blue and cyan colours). The mean estimate of the response (black curve) is identical in (b) and (c). For comparison, the step response to abrupt doubling of the CO_2 concentration is displayed by grey curves. The mean and ranges of ECS and TCR are shown at the right (the values also presented in the panel).

[END FIGURE 7.23 HERE]

7.5.3 Estimates based on the historical temperature record

This section assesses the estimates of TCR and ECS based on the instrumental record of climate change and variability with an emphasis on evidence since AR5. Section 7.5.3.1 considers estimates based on the global energy budget. Section 7.5.3.2 considers estimates based on the use of simple climate models evaluated against the historical temperature record. Section 7.5.3.3 considers estimates based on internal variability in global temperature and TOA radiation. Section 7.5.3.4 provides an overall assessment of TCR and ECS based on the historical temperature record.

7.5.3.1 Estimates based on the global energy budget

Warming since the pre-industrial period is measured to be around 1°C with small uncertainty (Section 2.2). Together with estimates of Earth's energy imbalance (Section 7.2) and the global ERF that has driven the observed warming (Section 7.3), the instrumental temperature record permits 'global energy budget' estimates of ECS and TCR. While energy budget estimates use instrumental data, they are not based purely on observations. GCM simulations inform estimates of the historical ERF (Section 7.3) as well as the global energy imbalance in the pre-industrial climate (the period against which changes are measured) (Lewis and Curry, 2015; Otto et al., 2013). GCMs are also used to characterize the internal climate variability that may have contributed to observed changes in temperature and energy imbalance. Moreover, a global-mean energy budget model is needed to relate ECS and TCR to the estimates of global warming, ERF and energy imbalance (Forster, 2016; Hegerl and Zwiers, 2011; Knutti et al., 2017). Research since AR5 has shown that the global-mean energy budget that is traditionally used produces values of ECS that are biased low for two main reasons: i) because it does not account for the dependence of radiative feedbacks on the spatial pattern of surface warming (Section 7.4.3) and ii) because there are inconsistencies in how global mean surface temperature trends are estimated.

The traditional global-mean energy balance model employed for global energy budget estimates (Gregory et al., 2002) (Section 7.4.1; Box 7.1) relates the difference between the ERF (ΔF) and the radiative response to observed global warming ($\alpha\Delta T$) to the global energy imbalance (ΔN): $\Delta N = \alpha\Delta T + \Delta F$, where α represents the net global radiative feedback parameter (units of W m^{-2} °C^{-1}). Given the relationship ECS = $\Delta F_{2\times CO2}/(-\alpha)$, where $\Delta F_{2\times CO2}$ is the ERF from CO_2 doubling, ECS can be inferred from historical estimates of ΔT, ΔF, ΔN and $\Delta F_{2\times CO2}$: ECS = $\Delta F_{2\times CO2}\,\Delta T/(\Delta F - \Delta N)$. While TCR is defined as the temperature change at the time of CO_2 doubling under an idealized 1%/yr CO_2 increase, it can be inferred from the historical record as: TCR = $\Delta F_{2\times CO2}\,\Delta T/\Delta F$, under the assumption that radiative forcing increases quickly compared to the adjustment timescales of the deep ocean, but slowly enough that the upper ocean is adjusted, so that ΔT and ΔN increases approximately in proportion to ΔF. Because ΔN is positive, TCR is always smaller than ECS, reflecting lower transient warming than equilibrium warming. TCR is always better constrained than ECS owing the fact that the denominator of TCR, without the quantity ΔN, is more certain and further from zero than is the denominator of ECS. The upper bounds of both TCR and ECS are inherently less certain than their lower bound owing to the fact that ΔF is uncertain and in the denominator.

This traditional global-mean energy balance model assumes globally homogenous feedbacks and forcings, and thus lacks a representation of the radiative feedback dependence on the spatial pattern of warming. Studies that employ this model to infer ECS (Gregory et al., 2002; Lewis and Curry, 2015; Otto et al., 2013) thus inherently assume that radiative feedbacks will remain constant between the period of historical transient warming and the equilibrium response to CO_2 forcing. However, as summarized in Section 7.4.3, there are now multiple lines of evidence suggesting that radiative feedbacks will become less negative as the warming pattern evolves in the future. Extensions to the traditional energy balance model can be made to capture the pattern effect by allowing for multiple radiative feedbacks operating on different timescales (Armour, 2017; Armour et al., 2013; Geoffroy et al., 2013a; Held et al., 2010; Proistosescu and Huybers, 2017; Rohrschneider et al., 2019), by allowing feedbacks to vary with the spatial pattern or magnitude of ocean heat uptake (Rose et al., 2014; Rugenstein et al., 2016; Winton et al., 2010), or by allowing feedbacks to vary with the type of radiative forcing agent (Kummer and Dessler, 2014; Marvel et al., 2016; Shindell, 2014). However, a direct way to account for the pattern effect is to use the relationship ECS = $\Delta F_{2\times CO2}/(-\alpha + \alpha')$, where $\alpha = (\Delta N - \Delta F)/\Delta T$ is estimated from global energy budget changes and α' represents the change in the radiative feedback parameter between the historical period and the equilibrium response to CO_2 forcing, which can be quantified using GCMs (Andrews et al., 2018; Armour, 2017). A trend toward less negative radiative feedbacks in the future ($\alpha' > 0$) implies that the actual ECS will be larger than that inferred from historical warming. An alternative approach estimates feedback changes due in response to CO_2 forcing alone in terms of the ocean heat uptake efficacy (see Section 7.5.2.2).

Energy budget estimates of TCR and ECS have evolved in the literature over recent decades as global warming has continued. Revisions in estimates are also due to improved observations and understanding of global surface temperature trends (Richardson et al., 2016, 2018a), revised energy imbalance estimates (Johnson et al., 2016), and improved estimates of radiative forcing (Forster, 2016; Knutti et al., 2017). Prior to AR5, the global energy budget provided relatively weak constraints, primarily due to large uncertainty in the tropospheric aerosol forcing, giving ranges of ECS that typically included values above 10°C. Improved estimates of aerosol forcing together with a larger greenhouse-gas forcing by the time of AR5 led to an estimate of ΔF that was more positive and better constrained relative to AR4. Using energy budget estimates and radiative forcing estimates updated to 2009, Otto et al. (2013) found that TCR was 0.9°C to 2.0°C (5% to 95% range) with a most *likely* (median) value of 1.3°C, and that ECS was 1.2°C to 3.9°C (5% to 95% range) with a most *likely* value of 2.0°C. Studies since AR5 have confirmed these results or produced narrower ranges for TCR and ECS (Forster, 2016; Knutti et al., 2017).

Accurate estimates of global energy imbalance can be made from around 2002 based on near-global ocean temperature observations from autonomous profiling floats (Section 7.2). Over the period 2002 to 2018 the global energy imbalance is estimated to be 0.75±0.1 W m^{-2} (90% confidence) (Section 7.2). Anomalies are taken with respect to the baseline period 1850 to 1900, although other baselines could be chosen to avoid major volcanic activity (Lewis et al., 2018; Otto et al., 2013). Several lines of evidence, including GCM simulations (Lewis and Curry, 2015), energy balance modelling (Armour, 2017), and ocean GCMs forced by observed SSTs (Zanna et al., 2019) suggest that global energy imbalance for 1850 to 1900 was 0.1±0.2 W m-

[2]. Combined with estimates of internal variability in global energy imbalance within periods of equivalent lengths derived from unforced GCM simulations, the anomalous energy imbalance is estimated to be $\Delta N = 0.65 \pm 0.24$ W m^{-2}. Global near-surface air temperature change between 1850–1900 and 2002–2018 is estimated to be $\Delta T = 1.02 \pm 0.14$ °C (Chapter 2, Section 2.2; Box 7.2), accounting for internal variability derived from unforced GCM simulations. The ERF change between 1850–1900 and 2002–2018 is estimated to be $\Delta F = 2.11 \pm 0.58$ W m^{-2} and the ERF from CO_2 is estimated to be $\Delta F_{2\times CO2} = 4.0 \pm 0.7$ W m^{-2} (Section 7.3.2). Employing these values within the traditional global-mean energy balance model described above produces values of TCR that lie in the range 1.3°C to 2.6°C (5% to 95% range) with a most *likely* (median) value of 1.8°C (Figure 7.24a). The inferred ECS lies in the range 1.7°C to 4.6°C (5% to 95% range) with a most likely value of 2.6°C (Figure 7.24b). These TCR and ECS ranges are comparable to those in the recent literature (Lewis et al., 2018; Lewis and Curry, 2015; Otto et al., 2013) but with higher values owing to updated estimates of observed warming, ocean heat uptake, and ERF. *[Will update for SOD]*

An important part of the upwards revision of the ECS inferred from energy budget studies is the use of global coverage near-surface air temperature indicators to estimate the surface temperature trends. Most studies have relied on HadCRUT4 global warming estimates that had incomplete coverage of some regions, especially the Arctic, and also blended near-surface air temperature observations with temperatures measured below the surface of the oceans. The HadCRUT4 historical trends are around 16% smaller than estimates of global surface air temperature warming and as a result ECS and TCR derived from these have similarly smaller ECS and TCR values (Richardson et al., 2016, 2018a). These surface warming trends are discussed in Chapter 2, Section 2.3 but it is important to note here that for a like-to-like comparison with ECS and TCR estimates derived from models it is necessary to make sure that the same measure of global surface temperature trends is used. The energy budget studies assessing ECS in AR5 employed HadCRUT4 or similar measures of surface warming trends. Other lines of evidence assumed global surface air temperature trends meaning that AR5 based energy budget estimates of ECS were about 16% lower than other lines of evidence adding to the overall disparity (Collins et al., 2013a). In this report, global near-surface air temperature is chosen as the standard measure of global warming to aid comparison with previous model and process-based estimates of ECS, TCR and climate feedbacks (see Box 7.1).

[START FIGURE 7.24 HERE]

Figure 7.24: (a) TCR inferred from global energy budget constraints for the period 2002-2018 relative to 1850-1900; horizontal bar shows median value, box shows 17 to 83% range, and vertical line shows 5% to 95% range. (b) ECS inferred from global energy budget constraints for the period 2002-2018 relative to 1850-1900 (blue) and ECS accounting for the pattern effect (red) (Section 7.4.3) based on feedback changes derived from coupled GCM simulations (Armour, 2017) (middle) or from GCM simulations with prescribed historical sea-surface temperature and sea-ice concentrations (Andrews et al., 2018) (right). (c) Relationship between inferred ECS (blue) and actual ECS (red) in GCMs where the inferred ECS is derived from coupled GCM simulations (Armour, 2017) (left) or from GCM simulations with prescribed historical sea-surface temperature and sea-ice concentrations (Andrews et al., 2018) (right); actual ECS is derived from abrupt4xCO2 simulations and differences between the two are shown in grey. [Eventually redo this with using historical simulations and RFMIP forcings for CMIP6 models rather than 1pctCO$_2$ runs.]

[END FIGURE 7.24 HERE]

Several approaches have been used to estimate the degrede to which the actual ECS may be larger than that inferred from historical warming due to changes in the net radiative feedback parameter (α') as the warming pattern evolves in the future. By comparing radiative feedbacks in GCMs forced by a 1% yr^{-1} CO_2 ramping (*1pctCO$_2$*) (a rough analogue for historical warming) to radiative feedbacks in the same set of GCMs forced by CO_2 quadrupling (*abrupt4xCO$_2$*), Armour (2017) estimated that $\alpha' = +0.2$ W m^{-2} °C^{-1} (–0.1 to +0.6 W m^{-2} °C^{-1} range across models) (Section 7.4.3). This implies modelled values of ECS under *abrupt4xCO$_2$* that are on average about 15% higher (about 5% lower to 50% higher across models) than those inferred under

1pctCO₂ (Figure 7.24c). The strong tendency toward more positive feedbacks (α' > 0) reflects the fact that the transient response to CO_2 forcing shows relatively more warming in key negative feedback regions (e.g., western tropical Pacific Ocean) and less warming in key positive feedback regions (eastern tropical Pacific Ocean and Southern Ocean) than is projected in the near-equilibrium response to *abrupt4x*CO_2 (Section 7.4.3) (Held et al., 2010; Proistosescu and Huybers, 2017).

By comparing radiative feedbacks in atmospheric GCMs run with observed surface warming patterns to radiative feedbacks in coupled versions of the same set of GCMs forced by *abrupt4x*CO_2, Andrews et al. (2018) estimated that α' = +0.6 W m^{-2} °C^{-1} (+0.3 to +1.0 W m^{-2} °C^{-1} range across models) (Section 7.4.3). This implies modelled values of ECS under *abrupt4x*CO_2 that are on average about 60% higher (20% to 100% across models) than those inferred from models using observed warming patterns (Figure 7.24c). These feedback changes reflect the fact that the observed spatial pattern of historical surface warming has been markedly different from the pattern of warming projected under *abrupt4x*CO_2, with observations showing warming in key negative feedback regions (e.g., western tropical Pacific Ocean) and cooling in key positive feedback regions (eastern tropical Pacific Ocean and Southern Ocean) over recent decades (Section 7.4.3; Chapter 9, Section 9.2). This estimate of feedback changes accounts for all factors that have contributed to the observed temperature changes, including radiative forcings, the climate response to those, and internal climate variability (Andrews et al., 2018), but the method assumes that atmospheric GCMs correctly translate patterns of surface warming to changes in the radiation balance.

Using the value α' = +0.2 ± 0.25 W m^{-2} °C^{-1} (5% to 95% range) derived from Armour (2017), ECS lies in the range 1.8°C to 6.6°C (5% to 95% range), with a most *likely* (median) value of 3.0°C (Figure 7.24b). Using the value α' = +0.6 ± 0.4 W m^{-2} °C^{-1} (5% to 95% range) derived from Andrews et al. (2018), ECS lies in the range 1.9°C to 18°C (5% to 95% range), with a most *likely* (median) value of 4.2°C (Figure 7.24b). The low end of these ECS ranges are similar to that inferred using the traditional energy balance model (i.e., assuming α' = 0), reflecting a weak dependence on the value of α' when ECS is small (Andrews et al., 2018; Armour, 2017). However, the high end of the ECS range is strongly dependent on the value of α'.

The values of ECS above are all considerably higher than those estimated from both AR5 and recently published estimates (Collins et al., 2013a; Forster, 2016; Lewis et al., 2018; Lewis and Curry, 2015; Otto et al., 2013) . Four revisions made in this report are responsible for this increase. i) An upwards revision of historic surface temperature trends from the adoption of near surface air temperature measure and newly published trend data (Chapter 2, Section 2.3). ii) An 8% increase in the ERF for $\Delta F_{2\times CO2}$ (Section 7.3.2). iii) A 22% more negative best estimate of aerosol ERF, which acts to weaken estimates of historic ERF trends. iv) Accounting for the pattern effect. The concerted effect of all these revisions has yet to be tested in the published literature and leads to a cautious assessment at this stage [*note: we will watch this space carefully for SOD*].

ECS is *very likely* higher than that inferred from the historical global energy budget changes based on modelled changes in radiative feedbacks, but there is substantial uncertainty in how much higher. The accuracy of the estimated α' hinges on the accuracy of projected changes in the warming pattern under CO_2 forcing and on the radiative response to those warming patterns within GCMs. While several lines of evidence indicate that α' > 0 (Section 7.4.3), the quantitative accuracy of feedback changes is not known at this time (Section 7.4.3; Figure 7.24): GCMs produce a wide range of results for α' (Figure 7.20) and there are currently no observational constraints on its value. Global energy budget constraints thus provide *very high confidence* in the lower bound of ECS: it is *extremely unlikely* to be less than 1.7°C, assuming no change in radiative feedbacks in the future. Estimates of α' that are informed by observed historical warming patterns (Andrews et al., 2018) indicate a most *likely* (median) value of ECS of around 4°C. However, owing to large uncertainties in future feedback changes, the historical energy budget currently provides little information about the upper bound of ECS.

7.5.3.2 Estimates based on simple climate models

Dynamical energy balance models, sometimes known as simple climate models (SCM), are more complex than global-average energy balance models but far less complex than comprehensive GCMs (Bodman and Jones, 2016; Forest, 2018). SCMs generally include a representation of the ocean and thus can simulate the temporal evolution of climate. While some SCMs capture only the global-average warming (Geoffroy et al., 2012; Held et al., 2010; Padilla et al., 2011; Section 7.5.2.2), many SCMs represent warming within a small number of regions, such as at the scale of hemispheres, over land and ocean, and at different vertical levels of the ocean (Aldrin et al., 2012; Andronova and Schlesinger, 2001; Bieltvedt Skeie et al., 2018; Forest, 2002; Forest et al., 2006, 2008; Johansson et al., 2015; Knutti et al., 2002; Libardoni and Forest, 2011; Skeie et al., 2014). A few utilize more complex Earth Models of Intermediate Complexity (EMICS) (Huber et al., 2014; Olson et al., 2013; Tomassini et al., 2007). SCMs thus make use of more spatial and temporal information from the historical record than do estimates based on global-average energy balance model described above. However, lacking the comprehensive physics of GCMs, they rely on simple parameterizations of radiative feedbacks, radiative forcing, ocean heat uptake processes, and internal variability.

The numerical efficiency of SCMs means that they can be empirically constrained by observations: a large number of possible parameter values (e.g., radiative feedback parameter, aerosol radiative forcing and ocean diffusivity) are randomly drawn from prior distributions; forward integrations of the model are performed with these parameters and weighted against observations of surface or ocean warming, producing posterior estimates of quantities of interest such as TCR, ECS and aerosol forcing (see Section 7.3). The choice of prior distributions generally has a large impact on the results (Bieltvedt Skeie et al., 2018; Bodman and Jones, 2016; Hegerl et al., 2006).

Improved estimates of ocean heat uptake over the past two decades (Section 7.2) have diminished the role of ocean diffusivity in driving uncertainty in ECS, leaving the main trade-off between posterior ranges in ECS and aerosol radiative forcing (Forest, 2002; Frame et al., 2005; Knutti et al., 2002). AR5 (Bindoff et al., 2013) assessed a variety of estimates of ECS based on SCMs and found that they were sensitive to the choice of prior parameter distributions chosen and temperature datasets used, particularly for the upper end of the ECS range. However, SCMs generally produced estimates of ECS between 1°C and 5°C and ranges of TCR between 0.9°C and 2.6°C. Padilla et al. (2011) use a simple global-average model with two timescales (see Section 7.5.2) to derive observationally-constrained estimate of TCR to be in the range 1.3°C to 2.6°C (5% to 95% range) with a median value of 1.6°C. Using the same model, Schwartz (2012) finds TCR in the range 0.9°C to 1.9°C (5% to 95% range).

Using an SCM comprised of northern and southern hemispheres and an upwelling-diffusive ocean (Aldrin et al., 2012), with surface temperature and OHC datasets updated to 2014, Skeie et al. (2018) estimate a median value of TCR of 1.4°C with range 0.9°C to 2.0°C (5% to 95% range) and infer a median value of ECS of 1.9°C with range 1.2°C to 3.1°C (5% to 95% range). The median estimate of ECS increases to 2.9°C if the model is not constrained by the depth profile of ocean warming, suggesting that the results depend sensitively on the details of vertical heat transport in the ocean. Using a similar SCM comprised of land and ocean regions and an upwelling-diffusive ocean, with surface temperature and OHC datasets through 2011, Johansson et al. (2015) infer a most *likely* value of ECS of 2.5°C with range 2.0°C to 3.2°C (5% to 95% range). The estimate is found to be sensitive to the choice of dataset endpoint and the representation of internal variability meant to capture the El Niño–Southern Oscillation.

Differences between these two studies arise, in part, from their different surface temperature and OHC datasets, different radiative forcing uncertainty ranges, different priors for model parameters, and different representations of internal variability. This leads to substantially different estimates of ECS, with the median estimate of Skeie et al. (2018) lying below the 5% to 95% range of ECS from Johansson et al. (2015). Neither of these studies account for the bias introduced by blending SST and near-surface air temperature data or spatial coverage effects (Richardson et al., 2016, 2018a), suggesting that their derived values of TCR and ECS may be biased low by about 16%. The Skeie et al. (2018) SCM has a constant value of the radiative feedback parameter, and thus should be compared to values of inferred ECS from global energy budget constraints (Section 7.5.3.2) that do not account for feedback changes with warming pattern (Bieltvedt Skeie et al., 2018). The Johansson et al. (2015) SCM allows distinct radiative feedbacks for land and ocean, *likely* contributing to the different results and making it unclear whether it can be compared directly with ECS values from global energy budget constraints. While neither study provides a constraint on the actual ECS, the most *likely* estimates of ECS inferred from both studies lie within the 5% to 95% range of the ECS inferred from historical warming (1.7°C to 4.6°C), which is consistent with higher values of ECS when accounting for changes in radiative feedbacks as the spatial pattern of warming evolves in the future (Section 7.5.3.2).

7.5.3.3 Estimates based on climate variability

Continuous satellite measurements of TOA radiation fluxes, available since 2000, are now long enough to study inter-annual variations in the global energy budget (Figure 7.6). Although the measurements do not have sufficient accuracy to determine the absolute global energy imbalance (Section 7.2.1), they provide accurate estimates of its variations and trends since the year 2002 that agree well with estimates based on observed changes in GOHC (Johnson et al., 2016; Loeb et al., 2012). When combined with global surface temperature observations and simple models of global energy balance, satellite measurements of TOA radiation afford estimates of the radiative feedback parameter associated with recent climate variability (Dessler and Forster, 2018; Donohoe et al., 2014a; Forster and Gregory, 2006; Murphy et al., 2009; Tsushima and Manabe, 2013). These feedback estimates, derived from the regression of TOA radiation on surface temperature variability, imply values of ECS that are broadly consistent with those from other lines of evidence within large uncertainties (Forster, 2016; Knutti et al., 2017) (Figure 7.24). A history of regression-based feedbacks and their uncertainties is summarized in AR5 in Bindoff et al. (2013).

Since AR5, it has been noted that regression-based feedback estimates depend on whether annual- or monthly-mean data are used and on the choice of lag employed in the regression, complicating their interpretation (Forster, 2016). The observed lead-lag relationship between global TOA radiation and surface temperature, and its dependence on sampling period, is well replicated within unforced simulations of GCMs (Dessler, 2011; Proistosescu et al., 2018). These features arise because the regression between global TOA radiation and surface temperature reflects a blend of different radiative feedback processes associated with several distinct modes of variability acting on different time scales, such as monthly atmospheric variability and inter-annual El Niño–Southern Oscillation (ENSO) variability (Lutsko and Takahashi, 2018; Proistosescu et al., 2018). It thus appears that regression-based feedbacks provide estimates of the radiative feedbacks that are associated with internal climate variability, and thus do not provide a direct estimate of ECS. Moreover, variations in global surface temperature that do not directly affect TOA radiation may lead to an a positive bias in regression-based feedback (Spencer and Braswell, 2010, 2011), although this bias appears to be small (Murphy and Forster, 2010) particularly when annual-mean data are used (Proistosescu et al., 2018). When tested within GCMs, regression-based feedbacks have been found to be weakly correlated with values of ECS (Chung et al., 2010; Lutsko and Takahashi, 2018), but finding such a correlation requires integrations that are much longer than the satellite record. However, correlations between regression-based feedbacks and long-term feedbacks have been found to be higher when focused on specific processes and regions, such as for subtropical low clouds (Zhou et al., 2015) or the water vapour feedback (Dessler, 2013; Section 7.4.2).

Assessing the global radiative feedback in terms of the more stable relationship between tropospheric temperature and TOA radiation offers another potential avenue for constraining ECS, suggesting that CMIP5 GCMs with ECS values between 2.0°C to 3.9°C are within uncertainties based on satellite measurements (Dessler et al., 2018). Using the CMIP5 models to quantify the relationship between feedbacks operating at interannual timescales and feedbacks operating at equilibrium under CO_2 doubling produces an estimate of ECS of 3.3°C (median) with a range of 2.4°C to 4.6°C (17 to 83 percentiles) (Dessler and Forster, 2018).

A number of studies consider the observed climate response to volcanic eruptions over the 20th century (Knutti et al., 2017). However, the constraint on ECS is weak, particularly at the high end, because the temperature response to short-term forcing depends only weakly on radiative feedbacks (Boer et al., 2007;

Wigley et al., 2005) and because it can take decades of a sustained forcing before the magnitude of temperature changes reflects differences in ECS across models (Geoffroy et al., 2013b; Merlis et al., 2014). The radiative feedbacks governing the global temperature response to volcanic eruptions are *likely* different than those governing long-term global warming (Marvel et al., 2016; Merlis et al., 2014). It is also a challenge to separate the response to volcanic eruptions from internal climate variability in the years that follow them (Wigley et al., 2005). Estimates based on the response to volcanic eruptions agree with other lines of evidence (Knutti et al., 2017), but *likely* do not constitute a direct constraint on ECS.

Other studies have attempted to relate ECS to internal climate variability (Knutti et al., 2017) using variants of the fluctuation dissipation theorem, which state that the linear response of the climate system to external forcing is related to its unforced fluctuation properties about equilibrium. Such studies have generally made simplistic assumptions such as the use of a single climate timescale, a single radiative feedback value, and white-noise forcing, leading to biases in their estimates of ECS (Kirk-Davidoff, 2009; Knutti et al., 2017; Knutti and Hegerl, 2008). Using similar assumptions, (Cox et al., 2018a) derive a metric of historical temperature variability, defined as the ratio of temperature variability to a measure of the lag-1 autocorrelation of annual-mean temperature, and show it to scale with ECS within historical simulations of CMIP5 models. Using the observed surface temperature record as an "emergent constraint" on the variability metric, Cox et al. propose a median estimate of ECS of 2.8°C with range of 1.6°C to 4.0°C (5% to 95% range). These results have been questioned on a number of points (Brown et al., 2018; Po-Chedley et al., 2018b; Rypdal et al., 2018). Within CMIP5 historical simulations, the variability metric has been shown to primarily reflect forced temperature variations rather than internal variability as constructed, making it difficult to interpret. Using only the early portion of the 20th century temperature record between volcanic eruptions, where temperature variability is less driven by radiative forcing changes, increases the median estimate of ECS to 3.3°C and broadens the range to 1.9°C to 4.7°C (5% to 95% range) (Po-Chedley et al., 2018b). Many climate models with higher values of ECS fail to match the characteristics of temperature variability in the latter half of the 20th century as measured by the Cox et al. variability metric, pointing to potential model deficiencies, but it is currently unclear whether these deficiencies are related to their values of ECS.

7.5.3.4 Assessment of TCR and ECS based on the historical temperature record

Multiple lines of evidence from the historical temperature record, including estimates using global energy budget changes, simple climate models, and internal climate variability, produce median ECS estimates that range between 3°C and 4°C, but a best estimate value cannot be given owing to a strong dependence on assumptions about how radiative feedbacks will change in the future. However, there is robust evidence and high agreement across the lines of evidence leading to *very high confidence* that ECS is *extremely likely* greater than 1.7°C. There is robust evidence and medium agreement across the lines of evidence that ECS is *likely* greater than 2.3°C (*high confidence)*. While historical global energy budget changes do not provide constraints on the upper bound of ECS, estimates based on climate variability provide *medium confidence* (high agreement, limited evidence) that ECS is *unlikely* greater than 5°C.

Global energy budget constraints indicate a most *likely* value of TCR of 1.8°C (*high confidence*). There is *high confidence* that TCR is *likely* in the range 1.5°C to 2.2°C and *very likely* in the range 1.3°C to 2.6°C.

7.5.4 Paleoclimate estimates of ECS

Evidence from paleoclimate data, and from a combination of paleoclimate data and models, can provide information regarding climate and Long-term Earth sensitivity (see Box 7.1) that is complementary to, and independent from estimates based on: process-based studies (Section 7.5.2); the historical record (Section 7.5.3); and model simulations (Section 7.5.5). The strengths of using the paleoclimate record to estimate climate sensitivity include: (i) The estimates are based on observations of a real-world Earth system response to a forcing, in contrast to using estimates from process-based studies or directly from models. (ii) The forcings are often relatively large (similar in magnitude to a CO_2 doubling or more), in contrast to data from the historical record. (iii) The forcing often changes relatively slowly so the system is close to equilibrium, reducing or eliminating complications associated with accounting for ocean heat uptake, in contrast to the historical record. However, these strengths are balanced by the fact that there can be relatively large uncertainties on estimates of the paleo forcing, and paleo temperature response. Furthermore, uncertainty associated with the state-dependence of feedbacks (Section 7.4.4) means that climate sensitivity during Earth's past may not be the same as it is today.

The AR5 stated that data and modelling of the Last Glacial Maximum (LGM, 21,000 to 19,000 years ago) indicated that it was *very unlikely* that ECS to a doubling of atmospheric CO_2 lay outside the range 1°C to 6°C (Masson-Delmotte et al., 2013). Furthermore, that climate records of the last 65 million years indicated a climate sensitivity range of 1.1°C to 7°C, a range to which they assigned a 95% confidence interval.

Compared with AR5, there is now higher confidence in estimates of the climate sensitivity during Earth's past. The strengthened understanding and improved lines of evidence come from: (i) the use of high-resolution paleoclimate data across multiple glacial-interglacial cycles (Friedrich et al., 2016; Köhler et al., 2015, 2017, 2018; von der Heydt et al., 2014); (ii) better constraints on pre-ice core estimates of atmospheric CO_2 concentrations (Anagnostou et al., 2016; Martínez-Botí et al., 2015) and surface temperature (Hollis et al., submitted); (iii) more accurate paleoclimate boundary conditions for models (Haywood et al., 2016); and (iv) improvements in models themselves (Chapter 4, Section 4.1).

The paleoclimate lines of evidence regarding climate and Long-term Earth sensitivity can be broadly categorised into two types: (i) direct estimates of radiative forcing and temperature response resulting in an estimate of the feedback parameter, α (Box 7.1, Equation 7.1?), and (ii) paleoclimate data constraints on model simulations resulting in an estimate of ECS.

7.5.4.1 Direct estimates of radiative forcing and temperature response

In order to provide direct estimates of climate sensitivity, evidence from the paleoclimate record can be used to estimate forcing (ΔF) and global mean temperature response (ΔT) in Box 7.1, Equation 7.1?, assuming the system is in equilibrium. However, there are complicating factors with using the paleoclimate record, and these challenges and uncertainties are somewhat specific to the time period being used.

The Last Glacial Maximum (LGM) can provide robust direct constraints on climate sensitivity (see Table 7.12 for estimates since AR5). Because the major forcings and feedback processes that led to the cold climate (e.g., CO_2, non-CO_2 greenhouse gases and ice sheets) are relatively well-known (Chapter 5, Section 5.1), orbital forcing relative to preindustrial is negligible, and there are relatively high spatial resolution and well-dated paleoclimate temperature data available for this time period (Chapter 2, Section 2.3.1). Uncertainties in deriving a climate sensitivity from the LGM data arise primarily from uncertainties on the calibration from the paleoclimate data to local annual mean temperature, and uncertainties on the conversion of the local temperatures to a global annual mean surface air temperature. As a result of these uncertainties, estimates of global mean LGM cooling relative to preindustrial vary from 3°C to 7°C (Chapter 2, Section 2.3.2. [*SOD will update according to their final assessment and baseline*]). The LGM climate is often assumed to be in full equilibrium with the forcing. Under this assumption, a calculation of sensitivity using solely CO_2 forcing will give a Long-term Earth sensitivity rather than an ECS (see Box 7.1). In order to calculate an ECS, which is often most comparable to direct estimates from models, the approach of Rohling et al. (2012) is now widely-used. This approach introduces an additional forcing term in Box 7.1, Equation 7.1? that quantifies the resulting forcing associated with various feedbacks (for example for the increase in ice sheets, an estimate of the forcing associated with the change in albedo of the land surface). However, differences between studies as to which processes are considered as forcings, and differing methodologies for estimating the ice sheet forcing, means that even with this approach, estimates are not always directly comparable. Here, only estimates from studies that have accounted for the long-term Earth system feedbacks associated with vegetation and/or ice sheet feedbacks in this manner and therefore estimate ECS are assessed (see Table 7.12).

Since AR5, several studies have extended the Rohling et al. (2012) approach (described above for the LGM) to the glacial-interglacial cycles of the last about 1 to 2 million years (Friedrich et al., 2016; Köhler et al., 2015, 2017, 2018; von der Heydt et al., 2014; see Table 7.7). All the uncertainties that apply to the LGM also apply to this period but are in general amplified due to larger uncertainty in estimates of temperature response and CO_2 forcing in the pre-ice core period. Furthermore, orbital forcing is problematic to account for in the traditional framework of climate sensitivity because, although the orbital forcing over this period is close to zero in the global annual mean, its strong seasonal and latitudinal components result in a relatively large response in the global annual mean temperature (Singarayer and Valdes, 2010; Heinemann et al, 2014) and ice volume (Abe-Ouchi et al., 2013), even in the absence of CO_2 changes. In addition, for time periods in which the forcing relative to modern is small (interglacials), the inferred climate sensitivity has relatively large uncertainties because the denominator in Box 7.1, Equation 7.1? is close to zero.

In the pre-Quaternary (prior to about 2.5 million years ago), the forcings and response are relatively large and are also generally in the same sense as future climate change (i.e. a warming). Similar uncertainties as for the LGM apply, but in this case a major uncertainty relates to the forcing, because prior to the ice core record there are only indirect estimates of CO_2 concentration, and in addition, there are currently no proxies for non-CO_2 greenhouse gases. However, advances in using boron isotopes to reconstruct ocean pH (Foster and Rae, 2016) mean that the uncertainties on pre-Quaternary CO_2 are narrower than they were in AR5, and these time periods can now contribute to an assessment of climate sensitivity. The mid-Pliocene warm period (MPWP, 3.3 to 3.0 million years ago) has been targeted for constraints on climate and Long-term Earth sensitivity (Martínez-Botí *et al.*, 2015; Royer, 2016; see Table 7.12), due to the fact that CO_2 concentrations were high at this time, and because the MPWP is sufficiently recent that topography and continental configuration are similar to modern-day; as such, a comparison of the mid-Pliocene with modern provides probably the closest natural analogue to a classic climate sensitivity simulation from a model. Within the mid-Pliocene, the KM5c interglacial has been identified as a particularly useful time period for assessing climate sensitivity (Haywood et al., 2013a, 2016) because its orbit and topography are very similar to modern-day.

Further back in time, in the Eocene (about 50 million years ago), uncertainties in forcing and temperature change become larger, but the signals in general are larger too (Anagnostou et al., 2016; Shaffer et al., 2016; Hollis et al, submitted; see Table 7.12). However, additional uncertainties arise because differing continental position and topography/bathymetry mean that climate sensitivities derived from these time periods may be less relevant for the future (Fransworth et al., submitted). Furthermore, on even longer timescales of the last 500 million years (Royer, 2016) the temperature and CO_2 measurements are in general asynchronous, and therefore challenging to use to assess climate sensitivity.

7.5.4.2 Paleoclimate data constraints on model simulations

In order to obtain an observational constraint on climate sensitivity, model-derived estimates of warming due to elevated CO_2 (usually from CO_2 doubling or quadrupling experiments) from an ensemble of models are compared with simulations of a particular paleo time period from the same models, and with observational constraints of that time period. This can provide a constraint on climate sensitivity (similar to an emergent constraint, see Chapter 3, Section 3.2) provided there is a statistically significant relationship between the results from the elevated CO_2 and paleo model simulations. The analysis can be carried out with an ensemble of parameter-perturbed instances of a single model, or with an ensemble of different models. Uncertainties in the resulting estimates of climate sensitivity arise from errors in the models used, uncertainties in the proxy observations, and in the boundary conditions used to force the paleo model simulations. Paleoclimate data and model simulations of both the Last Glacial Maximum (Harrison et al., 2014, 2015) and the Pliocene (Hargreaves and Annan, 2016) have been used to estimate climate sensitivity in this way. However, for the LGM, Hopcroft and Valdes (2015) showed that the PMIP3 models do not exhibit a significant relationship between ECS values in the paleo and elevated CO_2 simulations.

7.5.4.3 Summary

This summarises Table 7.12 and provide an overall assessment of, lines of evidence from paleoclimates for constraining ECS and ESS. Although some of the estimates in Table 7.12 are not independent because they use similar proxy records to each other (e.g. von der Heydt *et al.*, 2014; Köhler *et al.*, 2015; Kohler *et al.*, 2017; Kohler et al, 2018), there are still multiple independent lines of paleoclimate evidence regarding climate sensitivity, from differing past time periods (LGM (Harrison et al., 2015); glacial-interglacial (Friedrich et al., 2016; Köhler et al., 2017), Pliocene (Martínez-Botí *et al.*, 2015; Hargreaves and Annan, 2016) and Eocene (Anagnostou et al., 2016; Shaffer et al., 2016)), with differing proxies for estimating forcing (e.g. CO_2 from ice cores or boron isotopes) and response (e.g. temperature from $\delta^{18}O$, Mg/Ca or Antarctic δD), and from differing methodologies (direct or paleo constraints). Furthermore, although different studies have uncertainty estimates that account for differing sources of uncertainty, some studies (Friedrich et al., 2016; Martínez-Botí et al., 2015) do consider many of the uncertainties discussed in Section 7.5.4.1. All the studies based on glacial-interglacial cycles explicitly take into account state-dependence of climate sensitivity (Section 7.4.4) by considering only the warm phases of the Pleistocene, but only two of those (Friedrich et al., 2016; Köhler et al., 2018) take into account orbital forcing.

[START Table 7.12 HERE]

Table 7.12: Estimates of ECS derived from paleoclimates since AR5 that account for at least some of the long-term Earth system feedbacks. Not all of these are independent as some share common underlying datasets. Different studies (column 1) focus on different time periods (column 2) and use a variety of different methods (column 3). Different studies have accounted for different long-term feedbacks in their estimates of ECS, so the type of climate sensitivity reconstructed is also noted (column 4), using the nomenclature of Rohling et al. (2012). As well as a best estimate many studies also give a range (column 5), which includes varying sources of uncertainty (column 6).

Study	Time period	Method	Climate sensitivity classification according to Rohling et al. (2012).	Published best estimate [and uncertainty]	Uncertainty estimate includes uncertainty in:
von der Heydt et al. (2014)	Warm states of glacial-interglacial cycles	Direct	S[GHG, LI, AE, VG]	2.3°C [2.0 – 3.5°C][b]	Range of LGM global mean temperatures.
Köhler et al. (2015)	Warm states of glacial-interglacial cycles	Direct	S[CO2,LI]	5.7°C [3.7 – 8.1°C][b]	Range of LGM global mean temperatures, and uncertainty on regression.
Köhler et al. (2017)	Warm states of glacial-interglacial cycles	Direct	S[CO2,LI]	5.8°C [4.1 – 8.0°C][b]	1 sigma uncertainty on regression
Köhler et al. (2018)	Warm states of glacial-interglacial cycles	Direct	S[GHG, LI, VG, AE]	[1.9 - 3.8°C][c]	Range of 3 different temperature reconstructions.

Friedrich et al. (2016)	Warm states of glacial-interglacial cycles	Direct	S[GHG,LI,AE]	4.9°C [4.3 - 5.4°C][c]	*Likely* range. Range of LGM global mean temperatures, aerosol forcing,
Martínez-Botí et al. (2015)	Pliocene	Direct	S[CO2,LI]	3.7°C [2.4 – 5.1°C][b]	2 sigma uncertainty on regression.
Anagnostou et al. (2016)	Eocene	Direct	S[CO2,LI]	[2.1 – 4.6°C]	Calibration uncertainty in temperature and CO_2.
[PlioMIP data paper]	Pliocene (KM5c)	Direct	-	Does not yet exist	-
[DeepMIP data paper] ; Hollis et al (in review)	Eocene (EECO)	Direct	-	Does not yet exist	-
Shaffer et al. (2016)	Eocene	Direct	S[GHG,AE,LI]	[3.3 – 5.6°C]	Calibration uncertainty in temperature and CO_2.
Royer (2016)	Pliocene	Direct	S[CO2,LI]	7.7℃	
Schmidt et al., (2014)	LGM	Paleo constraint	S^a	3.1°C [1.2 – 4.9°C]	90% interval based on proxy calibration uncertainties and spread on emergent constraint.
Harrison et al. (2014)	LGM	Paleo constraint	S^a	2.7°C	-
Harrison et al. (2015)	LGM	Paleo constraint	S^a	[1.4 - 4.4°C]	spread on emergent constraint
Hargreaves and Annan (2016)	Pliocene	Paleo constraint	S^a	[1.9 – 3.7°C]	spread on emergent constraint
Sherwood et al (in prep)	Glacial-interglacial cycles Pliocene	Synthesis of several lines of evidence	S^a	Not yet known	-

Notes: Note that S^a denotes a classification of climate sensitivity in the table.
(b) = Best estimate and range calculated from published estimate assuming ERF due to CO_2 doubling of 3.7 W m^{-2}.
(c) = estimate from glacial-interglacial cycles that accounts for effect of orbital forcing.

[END Table 7.12 HERE]

None of the studies in Table 7.12 that directly estimate ECS from forcings and feedbacks (as described in Section 7.5.4.1) have a minimum estimate of ECS that is smaller than 1.9°C per CO_2 doubling. The lowest estimate of ECS using the paleoclimate constraint method (as described in Section 7.5.4.2) is 1.2°C. None of the studies have a maximum estimate of ECS that is greater than 8.1°C. Including only those studies that consider some form of uncertainty analysis, and account for orbital forcing, the maximum estimate of ECS is 5.6°C. Overall, taking into account the uncertainties discussed in Section 7.5.4, the non-linearities of feedbacks discussed in Section 7.4.4, and the evidence assessed previously in AR5, the paleoclimate record on its own suggests that ECS is *very likely* in the range 2 to 5°C (*high confidence*). The high confidence comes from the multiple lines of independent evidence in the various studies, and the relative agreement between these studies.

7.5.5 Climate sensitivity in global models

Climate sensitivity has been extensively probed in global climate models through standardized CO_2-quadrupling experiments (*abrupt4xCO2*) and linear regression during CMIP5 (Andrews et al., 2012) and CMIP6 (reference), in CO_2-doubling experiments coupled with mixed-layer oceans during CMIP3 and sometimes using a prescribed SST increase (e.g. *amip4K*). These different methods to estimate ECS in climate models yield slightly different results, though not to an extent that is deemed important for the conclusion to be drawn in this. The ECS of a model is the net result of the models effective radiative forcing from a doubling of CO_2 and the sum of feedback parameters. It is well known that among models most of the spread arises from cloud feedbacks, and of that, most spread among models is related to tropical low-level clouds (Bony and Dufresne, 2005). Since these clouds are small-scale and shallow, the representation of such clouds is foremost controlled by the parameterizations in the models.

Random variations from model to model or between model versions have a symmetric impact of the climate feedback parameter α and, since ECS is inversely proportional to the feedback parameter, an asymmetric impact on ECS. ECS and TCR values are presented in Table 7.13 and also illustrated in Figure 7.25 where the distribution of ECS probed in CMIP3, CMIP5 and CMIP6 models along with a theoretical distribution (Roe and Baker, 2007) adapted to feedback parameters and forcing diagnosed from CMIP5 models (Caldwell et al., 2016). From the figure there is a close agreement between the two distributions near the peak probability, but whereas CMIP3 and CMIP5 models are clearly under-represented in the long upper-end tail, the CMIP6 models are more abundantly present above 4.5°C, though no model has been published to CMIP yet with an ECS above 6°C (see Table 7.13).

[START FIGURE 7.25 HERE]

Figure 7.25: Distribution of ECS from CMIP3 and CMIP5 (light gray) and CMIP6 models (dark gray). The black line is the distribution obtained by Monte-Carlo sampling feedback parameters estimated from CMIP5 models by Caldwell et al. (2016). [This is a preliminary analysis based partly on an informal survey will be updated for SOD]

[END FIGURE 7.25 HERE]

There can be several reasons why the CMIP3 and CMIP5 models tended to not occupy high ECS. First these are ensembles of opportunity and since the number of models overall is relatively low there is the possibility that by coincidence no models with higher ECS were published in CMIP3 and CMIP5. Alternatively, when high ECS models emerge from the development process they can become re-tuned, reconfigured or discarded and so might not see publication (Hourdin et al., 2017): modelling groups might have perceived a high ECS as generally unrealistic, have specific difficulties to reproduce the instrumental record warming, or a sensitive model might be prone to entering run-away warming or cooling for regularly applied forcings. Some modelling groups declare not tuning their modelled ECS (Schmidt et al., 2017a) (Schmidt et al., 2017a), whereas one group reported tuning down a high ECS from about 7 to 3°C in order to improve the match with the instrumental record warming (Mauritsen et al., 2019). About one third of modelling groups participating in a large survey agreed, or somewhat agreed, that the tuning of ECS to improve the match with historical warming is eligible (Hourdin et al., 2017).

[For SOD here will be a paragraph reporting on studies investigating why CMIP6 models are more sensitive]

One way to explore how tuning parameters impact ECS is to construct PPEs, wherein typically tuned or uncertain parameters are randomly altered within expert-solicited ranges (Klocke et al., 2011; Stainforth et al., 2005). Typically, 100 or more perturbed models are constructed this way, and the influence on ECS explored. Uniformly, studies find substantial variations in ECS within a single model of similar magnitude to the CMIP multi-model ensemble, though the distributions are model-dependent and so contain a structural component. Nevertheless, ECS below 2°C occur only infrequently, and no PPE study to date has resulted in a model with an ECS below 1.5°C.

An increasingly widely-used approach is to construct high-resolution convective CRMs or super-parameterisations, in order to dispose of moist convection parameterisation thought to be a major source of uncertainty. Unfortunately, results from such model studies do not indicate convergence with regards to ECS. One study using the global cloud resolving model NICAM found total positive feedback due to increasing upper-level cloudiness (Tsushima et al., 2014), super-parameterised versions of the NCAR family of models suggest mid-range ECS (Bretherton et al., 2014). Support to the notion of a lacking convergence is found in a study where convective parameterisation is disabled in regular climate models (Webb et al., 2015).

Climate models, although comprehensive, cannot resolve or represent all processes that occur in nature with fidelity. The current understanding is that the most important feedback processes are included, but if there are important feedback processes not included in all, or the majority of models, then purely model-based inference may be biased. Proposed missing feedback mechanisms include a missing anvil cloud area feedback (Mauritsen and Stevens, 2015) or missing ozone chemistry (Nowack et al., 2015). Already represented feedback processes may also be systematically biased, here in particular mixed-phase cloud feedbacks are suspect of being too negative (Tan et al., 2016) (Section 7.4.2.4). The strength of these suggested missing- or biased feedback processes remain debated, though together they are deemed too weakly negative to cause modelled ECS below 1.5°C. This is because it requires a large negative change to the feedback parameter to substantially lower an already low ECS, e.g. going from 2.0 to 1.5°C requires additional negative feedback of about –0.6 W m^{-2} $°C^{-1}$.

The direct use of the raw ECS estimated from models is shifting from being the main source of information in early reports to instead playing a more supportive role in the present assessment. Instead, emergent constraints utilise inter model spread to infer either individual feedback mechanisms or aggregate ECS with some success (Section 7.5.6). Based on past model developments it is *extremely likely* that ECS is greater than 1.5°C (*high confidence*), because no model with a lower ECS has been constructed, possible missing feedbacks are not assessed strong enough to cause such low ECS, and available anecdotal evince of climate model tuning has only been to reduce ECS.

[START Table 7.13 HERE]

Table 7.13: Estimates of TCR, ECS, radiative forcing from a doubling of CO^2 and α derived from available CMIP6 models. ECS, radiative forcing and α are obtained based on (Andrews et al., 2012; Forster et al., 2013; Gregory et al., 2004) with uncertainties given as the 95 % confidence intervals from the regression. CMIP5 values from AR5 (Flato et al., 2013; Table 9.5) and CMIP3 values from AR4 (Randall et al., 2007; Tables 8.2 and S8.1 and calculations on numbers therein) are also listed.

		TCR	ECS	Radiative forcing (W m^{-2})	Feedback parameter, α (W m^{-2} °C^{-1})
CMIP6	BCC-CSM2-MR	1.36	3.02	2.79 ± 0.13	0.92 ± 0.06
	CNRM-CM6-1	2.23	4.84	3.72 ± 0.13	0.77 ± 0.04
	CNRM-ESM2-1	1.86	4.76	2.98 ± 0.07	0.62 ± 0.03
	GISS-E2-1-G	1.73	2.72	3.92 ± 0.16	1.44 ±0.08
	IPSL-CM6A-LR	2.41	4.57	3.41 ± 0.16	0.75 ± 0.05
	MICROC6	1.56	2.61	3.63 ± 0.23	1.39 ± 0.12
	MRI-ESM2-0	1.67			
	Model mean	**1.83**	**3.75**	**3.41**	**0.98**
	Std. Dev.	0.34	0.98	0.81	0.32
CMIP5	Model mean of 23 models	1.8	3.2	3.4	1.1
	Std. Dev.	0.4	0.8	0.5	0.3
CMIP3	Model mean of 19 models	1.8	3.2	3.6	1.42[a]
	Std. Dev.	0.4	0.7	0.3	0.32[a]

Notes: (a) Model mean over 20 CMIP3 models and standard deviation from Forster and Taylor (2006).

[END Table 7.13 HERE]

7.5.6 Emergent constraints on ECS

Methods to estimate ECS through emergent constraints that in diverse ways instead embrace model spread in ECS have seen increasing attention in the recent decade. The general methodology of emergent constraints is introduced in Chapter 1, Section 1.4. Table 7.14 summarises the emergent constraints used here.

The perhaps simplest class of emergent constraints regress past global, or near-global, temperature change against modelled ECS to obtain a relationship that can be used to translate an observed climate change to ECS. Examples include using the relationship between ECS and last glacial maximum (LGM) cooling (Hargreaves et al., 2012), warming in the Pliocene epoch (Hargreaves and Annan, 2016), the response to Pinatubo (Bender et al., 2010), and the post-1970s warming (Jiménez-de-la-Cuesta and Mauritsen, submitted). The paleo-climate emergent constraints are particularly useful as they utilize past climates in equilibrium but are limited by structural uncertainties in the proxy-based temperature and forcing reconstructions (Section 7.5.4), possible differences in equilibrium patterns between models and Earth, and a small number of model simulations participating. A study that developed an emergent constraint based on the response to the Mount Pinatubo eruption yielded a best estimate of 2.4°C (*likely* 1.7-4.1) (Bender et al., 2010). When accounting for ENSO variations they found a somewhat higher best estimate of 2.7°C, which is in line with later studies that suggest ECS inferred from periods with volcanic activity are low-biased (Gregory et al., submitted). Thus, this class of emergent constraints yield median ECS of 2.5-2.9°C and fairly tight uncertainty ranges, in particular at the upper end.

Lagged-correlations present in short term variations in the global mean surface temperature can be linked to climate sensitivity through the fluctuation-dissipation theorem which is derived from a mixed-layer model (Cox et al., 2018a; Hasselmann, 1976; Schwartz, 2007). Initial attempts to apply the theorem directly to observations yielded a fairly low ECS estimate of 1.1°C (0.6°C to 1.7°C, 17 to 83 percentiles) (Schwartz, 2007), but recently it was proposed to use variations in the historical experiments of the CMIP5 climate models as an emergent constraint giving a median ECS estimate of 2.8°C (2.2°C to 3.4°C, 17 to 83 percentiles). A particular challenge is to separate short term from long term variability, and slightly arbitrary choices regarding the methodology of separating these in the global mean temperature from long term signals in the historical record, omission of the later strongly forced period, as well as input data choices, can lead to median ECS estimates ranging from 2.5°C to 3.5°C (Brown et al., 2018; Po-Chedley et al., 2018b; Rypdal et al., 2018). Calibrating the emergent constraint using CMIP5 modelled natural variability as measured in pre-industrial control simulations (Po-Chedley et al., 2018b) will inevitably lead to an overestimated ECS due to externally forced short term variability present in the historical record (Cox et al., 2018b). Thus, when the same filter is applied to both the modelled and observed temperature records, the resulting ECS median is robustly close to 3°C and 17 to 83 percentiles not outside 2.2°C to 4.0°C.

Short term variations in the Earth's energy budget, observable from satellites, arising from variations in the tropical tropospheric temperature has been linked to ECS through models, either as a range of models consistent with observations (Dessler et al., 2018) or as a formal emergent constraint by deriving further model-based relationships to yield a median of 3.3°C and a *likely* range of 2.4-4.5°C (Dessler and Forster, 2018). There are major challenges associated with short term variability in the energy budget, in particular how it relates to long-term forced response of clouds (Colman and Hanson, 2017; Lutsko and Takahashi, 2018), and variations in the surface temperature that are not directly affecting the radiation balance leads to an overestimated ECS when using linear regression techniques where it appears as noise in the independent variable (Gregory et al., submitted; Proistosescu et al., 2018). The latter issue is largely overcome when using the tropospheric mean or mid-tropospheric temperature (Dessler et al., 2018; Trenberth et al., 2015).

A substantial number of emergent constraint studies focus on observables that are related to tropical low-cloud feedback processes (Brient et al., 2016; Brient and Schneider, 2016; Sherwood et al., 2014; Volodin, 2008; Zhai et al., 2015). These studies yield median ECS estimates of 3.5°C to 4°C and provide only small probability to values below 3°C. The approach is attractive since most of the spread among climate models arises from low cloud feedbacks (Bony and Dufresne, 2005; Randall et al., 2007; Wyant et al., 2006), but nevertheless assumes that all other feedback processes are unbiased (Klein and Hall, 2015). In particular, accounting for a missing representation of the anvil cloud area feedback (section 7.4.2.4) with an assessed mean of –0.2 W m^{-2} $°C^{-1}$, shifts the median estimates range of this class of emergent constraints down to 2.9°C to 3.3°C and accordingly grants probability to values below 3°C. Thus, the subset of emergent constraints that focus on low-level tropical clouds are not inconsistent with other emergent constraints of ECS, but at the same time an inter-dependence with the process-based estimates (Section 7.5.2) is introduced.

The fidelity of models in reproducing aspects of temperature variability or the radiation budget has also been proposed as emergent constraints on ECS (Bender et al., 2012; Brown and Caldeira, 2017; Covey et al., 2000; Huber et al., 2010; Knutti et al., 2006; Siler et al., 2018a). Here indices based on spatial or seasonal variability are linked to modelled ECS, and overall the group of emergent constraints yield best estimates of 3.3°C to 3.7°C. Some of these emergent constraints are subject to the same issue as identified for the low-level cloud feedbacks-based constraints of assuming processes not probed for, e.g. the longwave feedbacks are unbiased in the underlying model ensemble and are thus assessed to be less reliable than other emergent constraints.

The varied groups of emergent constraints have yielded median ECS estimates across a fairly wide range, however when critically assessed for systematic biases they robustly support best estimates close to 3°C. At the lower end practically all studies find lower bounds (5^{th} percentiles) around 2°C, whereas the upper end is less consistent across studies. Since several of the emergent constraints can be considered nearly independent, a Bayesian approach could have been taken to multiply probability distributions in order to obtain a tighter combined range (Annan and Hargreaves, 2006). Nevertheless, there is sufficient cross-dependencies, as for instance models are re-used in many of the derived emergent constraints, and furthermore the methodology has not yet reached a level of maturity to justify this approach. This therefore leads to the assessment that ECS inferred from emergent constraints is *very likely* 2 to 5°C.

Emergent constraints on TCR with a focus on the instrumental temperature record have also been proposed. In the simplest form Gillett et al. (2012) regressed the response of one model to individual historical forcings to obtain a tight range, but later when an ensemble of models was used the range was widened (Gillett et al., 2013). Another study used the response to the Pinatubo volcanic eruption to obtain a similar range (Bender et al., 2010). A tighter range, notably at the lower end, was found in an emergent constraint focusing on the post-1970s warming exploiting the lower spread in aerosol forcing change over this period (Jiménez-de-la-Cuesta and Mauritsen, submitted). The study also found that a larger median compared to energy budget constraints (Section 7.5.3) is due to the finite heat capacity of the upper ocean that dampen the response in the first years to decades after a forcing is applied. Combining the three studies gives a *very likely* range of 1.2°C to 2.2°C.

[START Table 7.14 HERE]

Table 7.14: Collection of emergent constraint studies estimating ECS.

Study	Emergent constraint description	Published best estimate and uncertainty (°C)	Uncertainty estimate:
(Bender et al., 2010)	Pinatubo integrated forcing normalized by CMIP3 models own forcing versus temperature change regressed against ECS.	[1.7-4.1]	5% to 95%
(Brient et al., 2016)	Shallowness of low-level tropical clouds	[2.4-4.6]	Model range consistent with observations
(Brient and Schneider, 2016)	Cloud fraction variability versus SST anomalies	4 [2.3-5.0]	5% to 95%
(Brown and Caldeira, 2017)	Aspects of the representation of the present-day top-of-atmosphere radiation balance	3.7 [3.0-4.2]	25% to 75%
(Cox et al., 2018a)	Persistence of variability in global mean temperature in instrumental record	2.8 [2.2-3.4]	17% to 83%
(Dessler et al., 2018)	Tropical mean 500 hPa temperature against global top-of-atmosphere radiation balance	[2.1-3.9]	Model range consistent with observations
(Dessler and Forster, 2018)	Similar to (Dessler et al., 2018), but derive additional relationships from models	3.3 [2.4-4.5]	17% to 83%
(Hargreaves and Annan, 2016)	Pliocene tropical SSTs	[1.9-3.7]	5% to 95%
(Huber et al., 2010)	Aspects of the representation of the present-day top-of-atmosphere radiation balance	3.4 [2.9-4.0]	17% to 83%
(Jimenéz-de-la-Cuesta and Mauritsen, submitted)	Post-1970s global warming	2.83 [1.72-4.12]	5% to 95%
(Knutti et al., 2006)	Regional seasonal cycle in land surface temperature	3.3 [2.2-4.4]	5% to 95%
(Sherwood et al., 2014)	Indicators of tropical convective mixing	Around 4 [>3]	Model range consistent with

			observations
(Siler et al., 2018a)	Spatial distribution of planetary albedo (shortwave reflectivity)	3.68 [2.38-4.98]	5% to 95%
(Volodin, 2008)	Tropical variations in cloud fraction and humidity	3.6 [3.3-3.9]	5% to 95%
(Zhai et al., 2015)	Subsidence regime tropical low-level cloud variations	3.9 [3.45-4.35]	17% to 83%

[END Table 7.14 HERE]

7.5.7 Synthesis

Substantial quantitative progress has been made in interpreting evidence of Earth's climate sensitivity since the previous report, through innovation, scrutiny, theoretical advances and a rapidly evolving data base from current, recent and past climates. Noteworthy is that ECS as derived directly from climate models plays a secondary role, and that weight is given to the process-understanding, instrumental record warming, paleo-climate records and emergent constraints in the assessment.

A key advance over the AR5 assessment is that across the nearly independent lines of evidence there is broad agreement that the central estimates of ECS are close to or not inconsistent with 3°C. This advance is foremost following an improved quantification of Earth's imbalance, instrumental record global temperature change, and the strength of anthropogenic forcing, combined with an understanding of how pattern-effects influence ECS inferred from historical warming (Sections 7.4.3 and 7.5.3), improved quantification of paleo climate change from proxy evidence and a deepened understanding of how feedback mechanisms depend on the climate mean state such that they inrease ECS in warmer climates (Sections 7.4.4 and 7.5.4), and also an improved quantification that cloud feedback mechanisms together are *likely* positive based on multiple lines of evidence (Sections 7.4.2 and 7.5.2). The assessed statements are summarized in Table 7.14 for ECS and Table 7.15 for TCR.

Whereas AR5 embraced the bulk of the evidence in the assessed ECS *likely* range (Collins et al., 2013a), the broader evidence-base presented here and the general agreement among the lines of evidence encourages the combination of the evidence to yield a tighter range. This can be done formally using Bayesian statistics (Annan and Hargreaves, 2006; Stevens et al., 2016). However, it is straightforward to understand that if two lines of independent evidence each give a low probability of an outcome being true, e.g. that ECS is less than 1.5°C, then the combined probability that ECS is less than 1.5°C is true is lower than that of either line of evidence. On the contrary, if one line of evidence is unable to rule out an outcome, but another is able to assign a low probability, then there is a low probability that the outcome is true. This logic applies also when there is slight dependency between the lines of evidence, for instance between historical evidence, global models and emergent constraints, though the combined constraint will be closer to the tighter of the individual lines of evidence.

Substantial advances over the previous report have been made in quantifying ECS inferred from a feedback process understanding, the instrumental record, paleoclimates, emergent constraints combined with a solid understanding that feedback processes change with time and depend on the climate state. Therefore, based on multiple lines of evidence the best estimate of ECS is 3 °C, and it is *likely* 2.5°C to 4°C and *very likely* 2°C to 5°C. It is *virtually certain* that ECS is larger than 1.5°C. The assessed ranges are all assigned *high confidence* due to the high level of agreement among the different lines of evidence. It remains challenging to rule out low-probability but high impact upper end ECS, which is indicated by the notably asymmetry of the assessed ranges.

It is worthwhile contemplating whether the consensus of the median ECS estimates is an expression of groupthink, i.e. whether evidence supporting a certain ECS that has long been the consensus (Charney et al., 1979) is being sub-consciously favoured over other values. In this regard it is worth remembering the many failed attempts to challenge an ECS of this magnitude, starting as early as (Ångström, 1900) criticizing the results of (Arrhenius, 1896) arguing that the atmosphere was already saturated in infrared absorption such that adding more CO_2 would not lead to warming. The assertion was understood half a Century later to be incorrect. History has seen a multitude of challenges, e.g. (Lindzen et al., 2001; Schwartz, 2007; Svensmark, 1998), mostly implying lower ECS than the range assessed as *very likely* here, but there are also examples of the opposite (Snyder, 2016) as criticised by (Schmidt et al., 2017b). Looking back, the resulting debates have led to a deeper understanding, strengthened the consensus, and so have been scientifically valuable. Certainly, also in the future there will be studies that will challenge the here presented assessment.

[START Table 7.15 HERE]

Table 7.15: Summary of ECS assessment

ECS	Central value	*Likely* range	*Very likely* range	*Extremely likely*
Process understanding (7.5.2)	2.9°C	2.3-4.1°C	1.9-5.6°C	
Warming over instrumental record (7.5.3)				> 1.7°C
Paleoclimates (7.5.4)			2.0-5.0°C	
Global models (7.5.5)				> 1.5°C
Emergent constraints (7.5.6)	3°C		2.0-5.0°C	
Synthesis	**3°C**	**2.5°C to 4.0°C**	**2.0°C to 5.0°C**	

[END Table 7.15 HERE]

The evidence for TCR is less abundant than for ECS, and for natural reasons it focuses on the instrumental temperature record (Sections 7.5.3 and 7.5.6) and process understanding (Section 7.5.2). TCR and ECS are not unrelated, though, and in any case TCR is less than ECS. Furthermore, unlike ECS, estimates of TCR from the historical record is not strongly influenced by externally forced surface temperature pattern effects since both historical transient warming and TCR are affected (Section 7.4.3).

Based on a process understanding, warming over the instrumental record and emergent constraints the best estimate TCR is 1.7°C, and it is *likely* 1.4°C to 2.0°C and *very likely* 1.2°C to 2.2°C. The assessed ranges are all assigned *high confidence* due to the high level of agreement among the different lines of evidence.

[START Table 7.16 HERE]

Table 7.16: Summary of TCR assessment

TCR	Central value	*Likely* range	*Very likely* range
Process understanding	1.7 °C	1.4-2.2 °C	1.2-3.2 °C

(7.5.2)			
Warming over instrumental record (7.5.3)	1.8 °C	1.5-2.2 °C	1.3-2.6 °C
Emergent constraints (7.5.6)	1.7 °C		1.2-2.2 °C
Synthesis	**1.7 °C**	**1.4-2.0 °C**	**1.2-2.2 °C**

[END Table 7.16 HERE]

7.5.8 Evaluation of ECS and TCR in climate models

The above lines of evidence offer opportunities to evaluate climate model values of climate sensitivity. Because energy budget constraints on ECS rely on climate models at multiple levels and permit a large range of values, they do not provide an independent evaluation of model ECS. However, comparisons can be made between model values of ECS inferred from transient warming simulations with those derived from historical energy budget constraints. Inferred values of ECS estimated within transient warming simulations of CMIP5 GCMs (2.1°C to 3.8°C) lie within the *very likely* range of ECS derived from the global energy budget (1.7°C to 4.6°C) (Section 7.5.3; Figure 7.24; Armour 2017; Proistosescu et al. 2017). However, the inferred ECS values from GCMs do not span the full range of inferred ECS values allowed by energy budget constraints. It is possible that other effects such as internal variability or volcanic forcing (Gregory et al. 2019) have contributed values of inferred ECS over the historical record being lower than the actual ECS. The potential for internal variability to have contributed to inferred ECS is supported by large ensemble experiments, such as the 100-member MPI-ESM1.1 ensemble that produces values of ECS inferred for the historical period ranging from 2.1°C to 3.9°C due to internal variability alone (Dessler et al., 2018). This magnitude of natural variability is taken into account in energy balance inference, but since the real Earth only provides a single realization it is not easy to know if natural variability is actually biasing ECS. A 'like-with-like' comparison can be made between GCM values of inferred ECS derived from simulations with prescribed historical sea-surface temperature and sea-ice concentrations and value of inferred ECS from the historical global energy budget. Inferred ECS from historical warming within the small subset of models that provide these simulations (6 in total) (Andrews et al., 2018) span a range 1.6°C to 2.2°C, consistent with but at the low end the range of ECS inferred from energy budget constraints (Figure 7.23). This suggests that radiative feedbacks within the current models are generally accurate given the observed pattern of warming. [*For SOD: assess CMIP5/6 GCM ECS and TCR against other lines of evidence and against our assessed range.]*

7.6 Process understanding and model evaluation of climate response

This section assesses process understanding of the long-term and large-scale climate response to greenhouse gas radiative forcing and evaluates the ability of models to capture the changes as it is inferred from the paleoclimate record. Section 7.6.1 considers the critical processes determining the global mean surface temperature response and its uncertainty within climate models. Section 7.6.2 considers the critical processes determining the large-scale spatial patterns of temperature response including polar amplification, land-ocean warming contrasts, and gradients in sea-surface warming in the Pacific Ocean. Section 7.6.3 assesses what is known about these large-scale spatial patterns of temperature response within the paleoclimate record and evaluates the ability of climate models to reproduce those patterns. An overall assessment considering all the lines of evidence is in Section 7.6.4.

7.6.1 Critical processes determining global temperature response to forcing

The magnitude of long-term global temperature change in response to a given radiative forcing can be understood in terms of the factors contributing to the global atmospheric energy budget: the effective radiative forcing (ERF), which drives the global energy imbalance and associated surface temperature change; the TOA radiative response to this surface warming, as set by radiative feedbacks, which governs the rate and magnitude of warming through radiative energy loss to space; and global ocean heat uptake, which offsets some of the transient surface warming.

A variety of studies evaluate the contribution that each of these factors makes to warming within coupled GCM simulations by diagnosing so-called 'warming contributions' for each process (Crook et al., 2011; Dufresne and Bony, 2008; Feldl and Roe, 2013b; Goosse et al., 2018; Pithan and Mauritsen, 2014; Vial et al., 2013). Warming contributions (units of °C) are evaluated by calculating the global energy flux (units of W m^{-2}) that each process contributes to the atmosphere (Figure 7.26a), either at the TOA or surface, then dividing that energy flux by the global mean Planck response (about 3.2 W m^{-2} $°C^{-1}$) (see Section 7.4.2). By construction, the individual warming contributions sum to the total global warming (Figure 7.26b). For long-term warming in response to CO_2 forcing, the energy added to the climate system by radiative feedbacks is larger than the ERF of CO_2 (Figure 7.26a), implying that feedbacks more than double the magnitude of global warming (Figure 7.26b). Radiative kernel methods (see Section 7.4.1) can be used to decompose the net energy input from radiative feedbacks into its components. The water-vapour, cloud and surface-albedo feedbacks enhance global warming, while the lapse-rate feedback reduces global warming. Ocean heat uptake reduces global warming by sequestering heat at depth away from the ocean surface.

[START FIGURE 7.26 HERE]

Figure 7.26: Contributions of effective radiative forcing, ocean heat uptake and radiative feedbacks to global atmospheric energy input and near-surface air temperature change at year 100 of abrupt CO_2 quadrupling simulations of CMIP5 models. (a) The energy flux to the global atmosphere associated with the effective CO_2 forcing, global ocean heat uptake, Planck response, and radiative feedbacks, which together sum to zero; inset shows energy input from individual feedbacks, summing to the total feedback energy input. (b) Contributions to net global warming calculated by dividing the energy inputs by the global Planck response (3.2 W m-2 °C-1), with the contributions from radiative forcing, ocean heat uptake, and radiative feedbacks summing to the value of net warming; inset shows warming contributions associated with individual feedbacks, summing to the total feedback contribution. Uncertainties show 25% and 75% percentiles across models. Feedbacks are calculated using radiative kernels (Shell et al., 2008) and the analysis is based on that of Goosse et al. (2018). [SOD: redo for CMIP6 models when available.]

[END FIGURE 7.26 HERE]

Differences in projected transient global warming across GCMs are dominated by differences in their radiative feedbacks, while differences in ocean heat uptake and radiative forcing play secondary roles (Figure 7.26b) (Crook et al., 2011; Dufresne and Bony, 2008; Vial et al., 2013). The uncertainty in projected global surface temperature change associated with inter-model differences in cloud feedbacks alone is about three times larger than that associated with ocean heat uptake, radiative forcing, or the combined water-vapour–lapse-rate feedback (Dufresne and Bony, 2008). Extending this energy budget analysis to equilibrium surface warming suggests that about 70% of the inter-model differences in ECS arises from uncertainty in cloud feedbacks, with the largest contribution to that spread coming from shortwave cloud feedbacks in the tropics (Vial et al., 2013).

An important limitation of understanding global warming and its uncertainty based on energy budget diagnostics within the coupled climate system is that different feedbacks interact (Section 7.4.2). For example, water-vapour and lapse-rate feedbacks are correlated (Held and Soden, 2006) owing to their joint dependence on the spatial pattern of warming (Po-Chedley et al., 2018a). Likewise, sea ice changes and the polar lapse-rate feedback are correlated because warming from sea ice loss becomes trapped near the surface in polar regions where strong temperature inversions exist (Feldl et al., 2017; Po-Chedley et al., 2018a). Moreover, feedbacks are not independent of ocean heat uptake because the spatial pattern of heat uptake influences the SST pattern on which global feedbacks depend (Section 7.4.3) (Rose et al., 2014; Rose and Rencurrel, 2016; Rugenstein et al., 2016; Winton et al., 2010). However, alternative decompositions of warming contributions that better account for correlations between feedbacks produce similar results (Caldwell et al., 2016). The key role of radiative feedbacks in governing the magnitude of global warming is also supported by the high correlation between radiative feedbacks (or ECS) and transient warming within GCMs (Grose et al., 2018; Section 7.5.1).

Another approach to evaluating the roles of forcing, feedbacks and ocean heat uptake in projected warming employs idealized energy balance models that emulate the response of GCMs. These climate 'emulators' permit quantification of the relative importance of different processes while preserving the interactions between them, which could be missed within analyses based on energy budget diagnostics (as in Figure 7.26). One such emulator assumes that the response of the deep ocean is so slow that ocean heat uptake can be approximated as proportional to global surface temperature change (Forster et al., 2013; Gregory et al., 2015; Padilla et al., 2011; Raper et al., 2002). Another emulator resolves the heat capacity of both the surface components of the climate system and the deep ocean (Geoffroy et al., 2013b; Gregory, 2000) and has been modified to account for the inconstancy of radiative feedbacks by mimicking the effects of the pattern effect (Armour, 2017; Geoffroy et al., 2013a; Held et al., 2010; Kostov et al., 2014). Using this modified emulator, Geoffroy et al. (2012) find that: under increasing atmospheric CO_2, radiative feedbacks constitute the greatest source of uncertainty (about 60% of variance) in transient warming beyond several decades; effective radiative forcing uncertainty plays secondary but important role in warming uncertainty (about 20% of variance) that diminishes beyond several decades; and ocean heat uptake processes play a minor role in warming uncertainty (less than 10% of variance) at all timescales.

More computationally intensive approaches evaluate how the climate response depends on perturbations to key parameter or structural choices within GCMs. Large 'perturbed physics ensembles' wherein a range of parameters associated with cloud physics are explored within atmospheric GCMs reliably produces a wide range of ECS due to changes in cloud feedbacks, but often produces unrealistic climate states (Sanderson et al., 2008b). Rowlands et al. (2012) performed a multi-thousand member perturbed-physics ensemble of coupled GCMs by perturbing model parameters associated with radiative forcing, cloud feedbacks, and ocean vertical diffusivity (an important parameter for ocean heat uptake). After constraining the ensemble to have a reasonable climatology and to match the observed historical warming, they found a wide range of projected warming by the year 2050 (1.4°C to 3°C relative to the 1961–1990 average) that is dominated by differences in radiative feedbacks. By swapping out different versions of the atmospheric or oceanic components of the GFDL coupled GCM, Winton et al. (2013) found that TCR and ECS depend on which atmospheric component was used (using two versions with different atmospheric physics), but that only TCR is sensitive to which oceanic component of the model was used (using two versions with different vertical coordinate systems, among other differences); TCR and ECS changed by 0.4°C and 1.4°C, respectively, when the atmospheric model component was changed, while TCR and ECS changed by 0.3°C and < 0.05°C, respectively, when the oceanic model component was changed. However, Krasting et al. (2018) found that perturbing ocean vertical diffusivity over a wide range within the GFDL climate model changed ECS by about 0.6°C, with this difference linked to different radiative feedbacks associated with different spatial patterns of sea-surface warming (see Section 7.4.3).

There is robust evidence and high agreement across a diverse range of modelling approaches and thus *high confidence* that radiative feedbacks are the largest source of uncertainty in projected global warming out to 2100 under a given emissions scenario, and that cloud feedbacks in particular are the dominant source of that uncertainty. Uncertainty in radiative forcing plays an important but generally secondary role. Uncertainty in global ocean heat uptake plays a relatively minor role in global warming uncertainty, but ocean dynamics could play an important role on long timescales through the impact on sea-surface warming patterns which in turn project onto radiative feedbacks (Section 7.4.3), or through changes in ocean circulation (Section 7.4.4).

The spread in historical warming across GCMs shows a weak correlation with inter-model differences in radiative feedback or ocean heat uptake processes but a high correlation with inter-model differences in radiative forcing owing to large variations in aerosol forcing across models (Forster et al., 2013). Likewise, the spread in projected 21st century warming across GCMs depends strongly on emissions scenario (Hawkins and Sutton, 2012; Chapter 4, Section 4.1). Strong emissions reductions would remove aerosol forcing and this could dominate the uncertainty in near-term warming projections (Armour and Roe, 2011; Mauritsen and Pincus, 2017; Smith et al., 2019). On post 2100 timescales carbon cycle uncertainty such as the uncertainty permafrost thawing becomes increasingly important, especially under high emission scenarios (Chapter 5, Section 5.3)

In summary, cloud feedbacks are the largest dominant source of uncertainty in this century's transient global warming under increasing or stable emissions scenarios (*high confidence*). Whereas, uncertainty is dominated by aerosol ERF in strong mitigation scenarios. Global ocean heat uptake is a relatively minor source of uncertainty in long-term warming. Carbon cycle feedbacks provide an increasing fraction of uncertainty on longer timescales (*high confidence*).

7.6.2 Critical processes determining large-scale spatial patterns of warming

The large-scale patterns of surface warming in observations (Chapter 2, Section 2.3) and climate model simulations (Chapter 4, Section 4.3; Figure 7.27a) share several common features. In particular, surface warming is greater in the Arctic than in the global average or even SH high latitudes; surface warming is generally greater over land than over nearby oceans; and GCMs generally simulate a weakening of the equatorial Pacific Ocean SST gradient, with greater warming in the east on multi-decadal to centennial timescales, although this feature has not yet emerged in observations (Figure 7.19, Chapter 9, Section 9.2). This section assesses process understanding of these large-scale patterns of surface temperature response from the perspective of a regional energy budget. Chapter 4, Section 4.5 discusses patterns of surface warming for 21st century forcing scenarios. Chapter 9, Section 9.2 assesses historical SST trends and the ability of coupled GCMs to replicate observed changes.

7.6.2.1 Polar amplification

Polar amplification (Flannery, 1984) describes the phenomenon that surface temperature changes tend to be amplified at the poles relative to the global mean in response to radiative forcing of the climate system. Amplified warming in the Arctic, known as Arctic amplification, was anticipated by Arrhenius (1896) based on a hypothesized loss of high-latitude snow cover with warming and thus a positive feedback associated with changes in albedo. Arctic amplification has been a ubiquitous emergent feature of climate model simulations (Hall, 2004; Hansen et al., 1984; Holland and Bitz, 2003; Manabe and Stouffer, 1980; Manabe and Wetherald, 1975; Pithan and Mauritsen, 2014; Robock, 1983; Winton, 2006) (Section 4.5; Figure 7.27a) and is also seen in observations (Serreze and Barry, 2011) (Chapter 2, Section 2.3). However, both climate models and observations show relatively less warming of the SH high latitudes. Since AR5 there is a much-improved understanding of the processes that drive polar amplification in the NH and delay its emergence in the SH.

[START FIGURE 7.27 HERE]

Figure 7.27: Contributions of effective radiative forcing, ocean heat uptake and radiative feedbacks to regional surface temperature changes at year 100 of abrupt CO_2 quadrupling simulations of CMIP5 models. (a) Pattern of near-surface air temperature change. (b-d) Contributions to net Arctic (>60°N), tropical (30°S-30°N), and Antarctic (<60°S) warming calculated by dividing regional-average energy inputs by the regional-average Planck response, with the contributions from radiative forcing, changes in atmospheric heat transport, ocean heat uptake, and radiative feedbacks summing to the value of net warming; inset shows regional

warming contributions associated with individual feedbacks, summing to the total feedback contribution. Uncertainties show 25% and 75% percentiles across models. Feedbacks are calculated using radiative kernels (Shell et al., 2008) and the analysis is based on that of Goosse et al., (2018). [SOD: Redo for CMIP6 models when available.]

[END FIGURE 7.27 HERE]

Feedbacks associated with the loss of sea ice and snow are central to polar amplification (Dai et al., 2019; Hall, 2004; Screen and Simmonds, 2010), but a variety of other factors contribute substantially as well. Regional energy budget analyses are commonly used to diagnose the relative contributions of the different factors to regional warming as projected by climate models under increased CO_2 concentrations (Crook et al., 2011; Feldl and Roe, 2013b; Goosse et al., 2018; Pithan and Mauritsen, 2014; Stuecker et al., 2018). Since the ERF of CO_2 is simulated to be largest in the tropics and smallest at high latitudes, it is diagnosed to contribute more to tropical warming than to polar warming (Figure 7.27b-d). The net atmospheric poleward heat transport into the Arctic does not change substantially because a decrease in poleward dry-static energy (sensible + potential energy) transport compensates the increase in latent energy transport (Figure 7.5) (Armour et al., 2019; Huang and Zhang, 2014; Hwang et al., 2011; Kay et al., 2012), thus suggesting little or no role for changes in atmospheric heat transport in Arctic amplification (Figure 7.27b). Instead, the primary cause of amplified Arctic warming in climate models appears to be large and positive local radiative feedbacks in the Arctic (Pithan and Mauritsen, 2014; Stuecker et al., 2018) (Figure 7.27b).

The larger contribution of feedbacks to Arctic warming than tropical warming arises from the latitudinal structure of the surface-albedo feedback, which warms the Arctic but not the tropics, and the lapse-rate feedback, which warms the Arctic but reduces warming in the tropics (Goosse et al., 2018; Graversen et al., 2014; Pithan and Mauritsen, 2014; Winton, 2006). Latitudinal structure of the lapse-rate feedback reflects weak radiative damping to space with surface warming in polar regions, where atmospheric warming is constrained to the lower troposphere owing to stably stratified conditions, and strong radiative damping in the tropics, where warming is enhanced in the upper troposphere owing to moist convective processes. Differences in the lapse-rate feedback between the tropics and polar regions are only partially compensated by differences in the water-vapour feedback (Taylor et al., 2013) and cloud feedbacks, which both favour tropical warming (Pithan and Mauritsen, 2014). Another factor contributing to polar amplification is a weaker Planck response at high latitudes owing to less efficient radiative damping where surface and atmospheric temperatures are colder (Pithan and Mauritsen, 2014).

Regional feedbacks contribute to greater warming in the Arctic than the Antarctic owing to weaker Antarctic lapse-rate and water-vapour feedbacks and a negative shortwave cloud feedback over the Southern Ocean (Figure 7.27c) (Yoshimori et al., 2017; Section 7.4.2). However, the primary driver of reduced Antarctic warming in transient simulations is the large heat uptake in the Southern Ocean associated with the upwelling of unmodified waters from depth (Armour et al., 2016; Marshall et al., 2015) (Section 9.?). The relatively weak surface cooling arising from ocean heat uptake in the NH high latitudes (Figure 7.27b) reflects strong heat uptake in the subpolar North Atlantic Ocean (Section 9.?) being partially compensated by increased heat fluxes from the ocean to the atmosphere in the Arctic Ocean which, in turn, is associated with increased northward heat transport into the Arctic under global warming (Bitz et al., 2006; Holland and Bitz, 2003; Hwang et al., 2011; Jungclaus et al., 2014; Koenigk and Brodeau, 2014; Mahlstein and Knutti, 2011; Marshall et al., 2015; Nummelin et al., 2017; Oldenburg et al., 2018; Rugenstein et al., 2013; Singh et al., 2017) (Figure 7.5). Climate model simulations of near-equilibrium warming project polar amplification in both hemispheres, but generally with less warming in the Antarctic than the Arctic (Danabasoglu and Gent, 2009; Hall, 2004; Li et al., 2013a; Yoshimori et al., 2017).

While energy budget analyses (Figure 7.27) are useful for diagnosing contributions to regional warming, their value for assessing the underlying role of individual factors is limited by interactions inherent to the coupled climate system. Polar lapse-rate, water-vapour, and surface-albedo feedbacks are coupled and influenced by warming at lower latitudes through heat transport changes (Alexeev and Jackson, 2013; Cai, 2005; Dai et al., 2019; Dong et al., 2019; Feldl et al., 2017; Graversen et al., 2014; Graversen and Burtu, 2016; Po-Chedley et al., 2018a; Rose and Rencurrel, 2016; Screen et al., 2012; Screen and Simmonds, 2010; Singh et al., 2018; Stuecker et al., 2018; Yoshimori et al., 2017; Zhou et al., 2017a). For example, episodic increases in latent heat transport into the Arctic are thought to enhance the water-vapour feedback and drive sea-ice loss on sub-seasonal timescales (Gong et al., 2017; Lee et al., 2011, 2017; Solomon, 2006; Woods and Caballero, 2016). If Arctic warming depends on the relative partitioning of atmospheric latent and sensible heat transport, then atmospheric heat transport changes could play a more prominent role in polar amplification than implied by regional energy budget analyses (Armour et al., 2019; Graversen and Burtu, 2016; Lee, 2014; Yoshimori et al., 2017). Poleward atmospheric heat transport changes are also influenced by the latitudinal structure of regional feedbacks, radiative forcing, and ocean heat uptake (Armour et al., 2019; Feldl and Roe, 2013b; Huang and Zhang, 2014; Hwang et al., 2011; Merlis, 2014; Roe et al., 2015; Rose et al., 2014; Stuecker et al., 2018; Zelinka and Hartmann, 2011).

While these various factors are thus not cleanly separable, they appear to work in concert to favour polar amplification. That is, polar amplification still occurs within GCMs when the surface-albedo (Alexeev et al., 2005; Graversen and Wang, 2009; Hall, 2004) and lapse-rate feedbacks (Graversen et al., 2014) are suppressed. It also occurs in models without any sea ice (Feldl and Roe, 2013b; Rose et al., 2014), provided that the polar atmosphere is stably stratified (Kim et al., 2018). Moist diffusive energy balance models suggest that polar amplification would occur even in the absence of any latitudinal structure in climate feedbacks owing to increased poleward latent heat transport with warming (Alexeev et al., 2005; Alexeev and Jackson, 2013; Armour et al., 2019; Flannery, 1984; Merlis and Henry, 2018; Roe et al., 2015; Rose et al., 2014). Poleward latent heat transport changes also act to favour polar amplification and prevent tropical amplification within climate models (Armour et al., 2019), resulting in strongly polar-amplified warming in response to polar forcing and a more latitudinally-uniform warming in response to tropical forcing (Alexeev et al., 2005; Rose et al., 2014; Stuecker et al., 2018).

Because many factors contribute to polar amplification, projections of polar warming are inherently more uncertain than global mean warming (Bonan et al., 2018; Holland and Bitz, 2003; Roe et al., 2015; Stuecker et al., 2018). The magnitude of Arctic amplification (ratio of Arctic to global warming) ranges from a factor of two to four in projections of 21st century warming (Section 4.5). While uncertainty in both global and tropical warming is dominated by tropical cloud feedbacks (Vial et al., 2013), uncertainty in polar warming arises primarily from polar surface-albedo and lapse-rate feedbacks, changes in atmospheric poleward heat transport, and ocean heat uptake (Bonan et al., 2018; Pithan and Mauritsen, 2014). Increases in ocean heat transport into the Arctic, as simulated by GCMs, are also correlated with the degree of projected Arctic amplification (Holland and Bitz, 2003; Hwang et al., 2011; Mahlstein and Knutti, 2011) suggesting that ocean heat transport may influence polar feedbacks (Singh et al., 2018).

Arctic amplification has a distinct seasonality with a peak in early winter (Nov-Jan) owing to sea-ice thinning and associated increases in heat fluxes from the ocean to the atmosphere resulting in strong near-surface warming (Dai et al., 2019; Hall, 2004; Holland and Bitz, 2003; Manabe and Stouffer, 1980; Pithan and Mauritsen, 2014; Serreze and Barry, 2011). Surface warming may be further amplified by cloud and lapse-rate feedbacks in autumn and winter (Burt et al., 2016; Morrison et al., 2018). Arctic amplification is weak in summer owing to surface temperatures remaining stable as excess energy goes into sea-ice melting or into the ocean mixed layer.

Based on mature process understanding, robust evidence, and a high degree of agreement across a hierarchy of climate models, there is *very high confidence* that polar amplification will be a long-term response to greenhouse gas forcing in both hemispheres. There is *high confidence* that amplified warming of the Arctic will continue over the 21st century and that polar amplification will eventually emerge in the SH on centennial timescales as the climate equilibrates with radiative forcing and Southern Ocean heat uptake is reduced. However, the timing of the emergence of SH polar amplification remains uncertain due to insufficient knowledge of the timescales associated with Southern Ocean warming and the response to surface wind and freshwater forcing (Bintanja et al., 2013; Kostov et al., 2017, 2018; Pauling et al., 2017; Purich et al., 2018). GCM simulations indicate that large freshwater input to the Southern Ocean from melting ice shelves could substantially delay the emergence of polar amplified warming by stratifying and cooling the surface ocean around Antarctica (Bronselaer et al., 2018; Golledge et al., 2019) (*low confidence* due to medium agreement but limited evidence). However, even a large reduction in the AMOC due, for instance, to greatly increased freshwater runoff from Greenland would be insufficient to eliminate Arctic amplification (Liu et al., 2017b, 2017c; Wen et al., 2018) (*medium confidence* based on to medium agreement and medium evidence).

7.6.2.2 Land–ocean warming contrast

Greater warming over land than oceans, at equivalent latitudes, is a ubiquitous feature of both observations (Chapter 2, Section 2.3.1) (Byrne and O'Gorman, 2018) and GCMs simulations of the climate response to greenhouse gas forcing (Chapter 4, Section 4.5.1; Figure 7.27). The contrast in land versus ocean warming is not transient in nature, as it persists to equilibrium in model simulations (e.g., Danabasoglu and Gent, 2009; Li et al., 2013; Rugenstein et al., 2019). As assessed in Chapter 4, Section 4.5.1, research since AR5 provides a much-improved understanding of the processes driving amplified warming over land than oceans. There is *high confidence* that greater warming over land is a consequence of the fact that relative humidity is lower over land than over the oceans. One theory relates the land-ocean warming contrast to different lapse rate changes over land and ocean: under greenhouse gas forcing, homogeneous warming of the tropical free troposphere requires more warming of near-surface air temperatures over land, where the tropospheric lapse rate follows an approximately dry adiabat, than over the ocean surface, where the moist adiabatic lapse rate can weaken with warming (Joshi et al., 2013). A related theory relates the land-ocean warming contrast to the temperature changes required to maintain a nearly-uniform increase in moist static energy (latent plus sensible energy) of the near-surface air over land and oceans: over land, where relative humidity is low, a given increase in moist static energy requires a large sensible energy increase and thus a larger increase in temperature than over oceans, where relative humidity is high and moist static energy increase can be accomplished by latent energy (Byrne and O'Gorman, 2013, 2018). The land-ocean warming contrast causes relative humidity to decrease over land (Byrne and O'Gorman, 2016, 2018; Chadwick et al., 2016), constituting a feedback that further strengthens the land-ocean warming contrast. An idealized representation of these thermodynamic arguments is able to replicate the in land-ocean warming contrast and land relative humidity observed over recent decades and simulated by GCMs (Byrne and O'Gorman, 2013, 2018). Section 4.5.1 discusses the causes of uncertainty in land-ocean warming contrast as simulated by GCMs.

Based on mature process understanding, robust observational and modelling evidence, and a high degree of agreement across studies, there is *high confidence* that near-surface air temperature over land will, on average, increase by more than that over the oceans in both the transient and equilibrium response to greenhouse gas forcing.

7.6.2.3 Tropical sea-surface temperature gradients

A weakening of the equatorial Pacific Ocean's east-west SST gradient, with greater warming in the east than the west, is a common feature of the equilibrium climate response to CO_2 forcing as projected by GCMs (e.g., Figure 7.27). There are thought to be several factors contributing to this patter. In the absence of any changes in atmospheric or oceanic circulations, the east-west surface temperature difference is theorized to decrease owing to weaker evaporative damping, and thus greater warming in response to forcing, where climatological temperatures are colder in the eastern Pacific cold tongue (Hartmann and Michelsen, 1993; Knutson and Manabe, 1995; Luo et al., 2015; Xie et al., 2010). Within atmospheric GCMs overlying mixed-layer oceans, this gradient in damping has been linked to the rate of change with warming of the saturation specific humidity, which is set by the Clasius-Clapeyron relation (Merlis and Schneider, 2011). Gradients in low-cloud feedbacks may also favour eastern equatorial Pacific warming (DiNezio et al., 2009; Meehl and Washington, 1996).

In the coupled climate system, changes in atmospheric and oceanic circulations will influence the east-west temperature gradient as well. It is expected that as global temperature increases and as the east-west temperature gradient weakens, a weakening Walker circulation (Vecchi et al., 2006, 2008) will further weaken the east-west temperature gradient through a reduction of equatorial upwelling of cold water in the east Pacific and a reduction in the transport of warmer water to the western equatorial Pacific and Indian Ocean (Dong and McPhaden, 2017; England et al., 2014; Li et al., 2017; Maher et al., 2018).

Research since AR5 (Burls and Fedorov, 2014; Erfani and Burls, 2019; Fedorov et al., 2015) has built on an earlier theory (Barreiro and Philander, 2008; Liu and Huang, 1997) linking the east-west temperature gradient to the north-south temperature gradient. In particular, model simulations suggest that a reduction in the equator-to-pole temperature gradient (polar amplification) increases the temperature of water subducted in the extra-tropics, which in turn is upwelled in the eastern Pacific. Thus, polar amplified warming, with greater warming in the mid-latitudes and subtropics than in the deep tropics, is expected to contribute to the weakening of the east-west equatorial Pacific SST gradient on decadal to centennial timescales. For all of these reasons, GCMs generally project an El Niño–like pattern of Pacific warming on centennial timescales.

The transient adjustment of equatorial Pacific SST gradient is influenced by the fact that upwelling waters delay surface warming in the east since they have not been at the surface for years to decades to experience the greenhouse gas forcing. This 'thermostat mechanism' (Cane et al., 1997; Clement et al., 1996) is not thought to persist to equilibrium since it does not account for the eventual increase in temperatures of upwelled waters (Liu et al., 2005; Luo et al., 2017; Xie et al., 2010) which will occur as surface warming becomes polar amplified. An individual CMIP5 GCM (GFDL's ESM2M) has been found to transiently warm with a La Niña–like pattern of Pacific temperature change, more similar to the SST trends seen over the historical record (Section 9.2), owing to a weakening nonlinear ENSO amplitude (Kohyama et al., 2017), but this pattern does not appear to persist to equilibrium (Paynter et al., 2018).

Chapter 9, Section 9.2 assesses the ability of models to replicate observed Pacific warming trends over the historical record and discusses possible reasons for model deficiencies including mean state biases, a misrepresentation of radiative forcing, or a misrepresentation of the forced response due, for instance, to inadequate representation of the equatorial undercurrent (Coats and Karnauskas, 2018). Coupled GCMs are generally unable to replicate the observed strengthening of the Walker circulation that is thought to have contributed to the La Niña–like warming pattern seen over recent decades, perhaps due to biases in simulated tropical Atlantic SSTs which diminish the connection between Atlantic and Pacific basins and thus reduce multi-decadal Pacific temperature variability (Kajtar et al., 2018; Kucharski et al., 2014; Luo et al., 2018; McGregor et al., 2018). With *medium confidence*, the observed Walker circulation strengthening is thought to have resulted from a combination of transient factors including sulfate aerosol forcing (Hua et al., 2018; Takahashi and Watanabe, 2016) and multi-decadal tropical Atlantic SST trends (Chafik et al., 2016; Kajtar et al., 2017; Kucharski et al., 2011, 2014, 2015; Li et al., 2016; Sun et al., 2017). There is emerging evidence that the Walker circulation has strengthened again since around 2011, suggesting that a transition to an El Niño–like warming pattern may currently be underway (Cha et al., 2018) (*low confidence* due to limited evidence).

Based on medium evidence and a high degree of agreement, GCM simulations and process understanding provides *medium confidence* that the La Niña–like warming pattern seen over the historical record is transient in nature and that the eastern tropical Pacific Ocean will increase by more than SSTs in the western tropical Pacific Ocean on multi-centennial timescales under greenhouse gas forcing.

7.6.3 Paleoclimate constraints on patterns of warming

Paleoclimate data can provide observational evidence of patterns of surface warming during past time periods of high atmospheric CO_2 concentration [SOD: add *PlioMIP2 and DeepMIP data papers; Hollis et al, submitted*]. Furthermore, comparison of these data with paleoclimate model simulations of the same time periods allows an evaluation of modelled patterns of surface warming in response to high CO_2 and other forcings. Furthermore, paleoclimate model simulations can provide insights into the possible mechanisms

that led to these patterns of warming. In this context, there has been a focus on the mid-Pliocene warm period (MPWP, about 3 million years ago, CO_2 concentrations of 350 to 400 ppmv [*SOD: CO_2 estimates will depend on Chapter 5 assessment]*, reduced Greenland and Antarctic ice sheets, Chapter 2, Section 2.3.2.1.1; Table 2.A.1; Chapter 5, Section 5.2.2.2), and the early Eocene climatic optimum (EECO, ~50 million years ago, CO_2 concentrations of 800 to 1200 ppmv [*SOD CO_2 estimates will depend on Chapter 5 assessment]*, absence of continental ice sheets, Chapter 2, Section 2.3.2.1.1; Table 2.A.1; Chapter 5, Section 5.5.1). These time periods provide indirect observational evidence for long-term changes in meridional temperature gradients (polar amplification) and longitudinal temperature gradients in the tropics, in a world with elevated atmospheric CO_2 concentrations compared with pre-industrial.
[*For SOD this could be extended to the LGM, but for now we keep it as relevant as possible to future changes by restricting to higher-then-preindustrial CO_2. An LGM model-data comparison is due to be carried out in Chapter 3]*]

7.6.3.1 Polar amplification in past high-CO_2 climates

At the time of AR5, polar amplification was evident in estimates of paleoclimate SST and land temperature records from both the MPWP and the EECO, but uncertainties associated with proxy calibrations (MPWP and EECO) and the role of orbital forcing (MPWP) meant that the degree of polar amplification during these time periods was not accurately known. Furthermore, although some models (CCSM3; Winguth et al., 2010; Huber and Caballero, 2011) at that time were able to reproduce the strong polar amplification implied by temperature proxies of the EECO, this was achieved at CO_2 concentrations substantially higher than those indicated by CO_2 proxies (Anagnostou et al., 2016).

Since AR5 there has been progress in improving the accuracy of temperature reconstructions of the MPWP and EECO time periods (Hollis et al., submitted). In particular, reconstructions of the MPWP have been focused on a short time slice with an orbit similar to modern-day (isotopic stage KM5C; Haywood et al., 2013, 2016), and there are more robust constraints on CO_2 concentrations from both of these time periods (Martínez-Botí et al., 2015; Anagnostou et al., 2016); as such, the degree of polar amplification during these high-CO_2 time periods can now be better quantified, and the ability of models to reproduce this pattern can be better assessed.

[START FIGURE 7.28 HERE]

Figure 7.28: [N.B. that the model results in this figure are old simulations, and the data has been synthetically generated. This placeholder is just to show the style of the anticipated figure for SOD.]. Temperature changes compared with pre-industrial for the high-CO2 MPWP and EECO time periods, from proxies and models. (a) proxy reconstructions of temperature change (black circles), including published uncertainties (vertical bars), for the MPWP (Stage KM5c), as synthesized by [PlioMIP data paper]. Coloured lines show the modelled zonal mean surface air temperature difference compared with preindustrial for 4 models from the PlioMIP ensemble [(b) proxy reconstructions of temperature change (black circles), including published uncertainties (vertical bars), for the early Eocene (EECO), as synthesized by Hollis et al. (submitted). Coloured lines show the modelled zonal mean surface air temperature difference compared with preindustrial. for 4 models from the DeepMIP ensemble (c) proxy reconstructions of temperature change (coloured filled circles) for the MPWP (Stage KM5c), as synthesized by [PlioMIP data paper]. Background colours show the mean surface air temperature difference compared with preindustrial for the ensemble mean of the PlioMIP ensemble (d) proxy reconstructions of temperature change (coloured filled circles) for the early Eocene (EECO), as synthesized by Hollis et al (submitted). Background colours show the mean surface air temperature difference compared with preindustrial for the ensemble mean of the DeepMIP ensemble.

[END FIGURE 7.28 HERE]

Since AR5 there has also been a change in the degree of polar amplification predicted by paleoclimate models of the EECO and MPWP. For the EECO, initial work indicated that changes to model parameters associated with clouds could increase simulated polar amplification, and improve agreement between models and data (Kiehl and Shields, 2013; Sagoo et al., 2013), but such parameter changes were not process-based. In support of these initial findings, recent models that include a process-based representation of cloud microphysics also exhibit increased polar amplification compared to models in AR5, which agrees better with the proxy-based estimates, and which is obtained at CO_2 concentrations in agreement with the proxy records (Figure 7.28b,d).

Overall, the proxy reconstructions give *high confidence* that meridional temperature gradients were reduced in both hemispheres in the MPWP and EECO, and this is further supported by model simulations of these time periods, which are more consistent with the proxies than at the time of AR5. As such, the confidence is higher than at the time of AR5 in the ability of models to accurately simulate polar amplification.

7.6.3.2 Tropical longitudinal temperature gradients in past high-CO_2 climates

In AR5, it was stated that paleoclimate proxies indicate a reduction in the longitudinal SST gradient across the equatorial Pacific during the MPWP (Masson-Delmotte et al., 2013). This assessment was based on SST reconstructions between two sites situated very close to the equator in the heart of the western Pacific warm pool (ODP 806) and eastern Pacific cold tongue (ODP 847), respectively. SST reconstructions based on the magnesium to calcium ratio (Mg/Ca) in foraminifera and the alkenone unsaturation index ($U_{37}^{k\prime}$) generally agree that during the Pliocene the SST gradient between these two sites was reduced compared with the long-term mean of the modern (Dekens et al., 2008; Fedorov et al., 2013; Wara et al., 2005).

Since AR5, the generation of a new SST record from the ODP 806 warm pool site based on the ${TEX_{86}}^{H}$proxy (Zhang et al., 2014), the inclusion of $U_{37}^{k\prime}$ and ${TEX_{86}}^{H}$ SST reconstructions from sites in the South China Sea as warm pool estimates (O'Brien et al., 2014; Zhang et al., 2014), and the inclusion of several new sites from the eastern Pacific as cold tongue estimates (Fedorov et al., 2015; Zhang et al., 2014), has led to revised gradient estimates ranging between a about 1 and 1.5°C (Zhang et al., 2014) and about 3°C (Fedorov et al., 2015) reduction in the zonal gradient for the MPWP relative to the Late Quaternary (0-0.5Ma). While these revised estimates differ in magnitude due to differences in the sites and SST proxies used to evaluate the longitudinal SST gradient, and while there are uncertainties associated with the calibrations of the proxies, there is *medium confidence* that the average zonal gradient in the tropical Pacific was weaker during the Pliocene than during the modern.

7.6.4 Overall assessment of climate response

[Note for SOD. This overall assessment will combine the observations, model, and paleo evidence from 7.6.1-7.6.3. Given the lack of CMIP6-PMIP4 model results available at present, this is just a placeholder for now].

The paleoclimate proxy record of past warm climates, GCM simulations of those past climates, and GCM projections of climate response to CO_2 forcing provides robust evidence and a high degree of agreement and thus *very high confidence* that equilibrium warming will be polar amplified in both hemispheres. Arctic amplification has already been observed (Chapter 2, Section 2.3) and its causes are well understood. Polar amplification in the SH has yet emerged over the historical record (Chapter 2, Section 2.3) owing to delayed warming of the Southern Ocean surface and associated heat uptake.

The paleoclimate proxy record of past warm climates, GCM simulations of those past climates, and GCM projections of climate response to CO_2 forcing provides medium evidence and a medium degree of agreement and thus *medium confidence* that equilibrium warming will be characterized by a weakening of the east-west tropical Pacific SST gradient.

Overall the observed pattern of warming over the instrumental period, with minima of warming in the eastern tropical Pacific Ocean and Southern Ocean (Figure 7.27), stands in contrast to the equilibrium warming pattern either inferred from the proxy record or simulated by GCMs under CO_2 forcing. There is *medium confidence* that the observed strengthening of the east-west SST gradient, which has been associated with increased easterly winds over the tropical Pacific in recent decades, is transient in nature and will eventually give way to a weakening of the gradient on centennial timescales. There is *high confidence* that the SH high latitudes will warm by more than the tropics on centennial timescales. However, there is only *low confidence* that such a feature will emerge this century.

7.7 Metrics to evaluate emissions

7.7.1 Introduction to metrics and innovations since IPCC AR5

Emissions metrics attempt to summarise the contribution different gases and forcing agents make to some aspect of climate change. They do this by comparing the relative effects of emissions of different gases on some climate variable, according to some formula. Although absolute metrics exist, most metrics are usually relative, in the sense that they are constructed by comparing to a reference gas, which is almost always CO_2 (Myhre et al., 2013b). In effect, metrics are used as an imperfect summary of the “exchange rates” between different forcing species.

The cause-effect chain for climate forcing, climate response, and climate impacts is displayed in Figure 7.2 (Fuglestvedt et al., 2003). Each step in the causal chain requires an inference or modelling framework that maps causes to effects. Emissions metrics map from emissions of some species to somewhere further down the chain, radiative forcing (GWP) or temperature (GTP, MGTP, GWP*) or impacts (such as sea level rise or socioeconomic impacts). While items lower in the chain have greater policy relevance, they are also subject to greater uncertainty.

Metrics can facilitate the comparison of effects of forcing agents in support of policy goals. They cannot define policy goals or targets but can support the evaluation and implementation of choices within multi-component policies (i.e., they can help suggest which emissions to abate). The most appropriate metric will depend on which aspects of climate change are most important to a particular application, and different climate policy goals may lead to different conclusions about what is the most suitable metric (Myhre et al., 2013b).

While metrics can provide a useful way of comparing the effects of different gases, they may not be required if gases or forcing agents are treated separately (Harvey, 2000, p. 294-295). Alternatively, many of the most fundamental problems associated with combining short- and long-lived forcings in a single metric could be avoided via a two-basket approach, one for short-lived agents and one for long-lived (Jackson, 2009). In particular, because of the different effects of gases with a long residence time (e.g. CO_2, N_2O, SF_6) and those of forcing agents with timescales of a couple of decades or less (e.g. CH_4, black carbon) there may be reasons to compare either within a two-basket approach or a multi-basket approach. Multi-basket schemes manage different gases more directly at the level of policy design, where different approaches to regulation and price can be tailored around the specifics of different forcing agents (Daniel et al., 2012). Although there is a history of using single-basket approaches, supported by emissions metrics, in climate policy, multi-basket approaches also have many precedents in environmental management, including the Montreal Protocol.

7.7.2 Physical description of metrics

This section, being part of the WG I report, discusses metrics that relate emissions to physical changes in the climate system. One such metric, the 100-year GWP, has extensively been employed in climate policy to equate emissions of different greenhouse gases. Yet other physical metrics exist, which are discussed in this section. Further, metrics that relate emissions to more general “damage” or “cost” changes may be more of use when analysing the economics of mitigation pathways (Johansson, 2012; Sarofim and Giordano, 2018) (discussed in AR5 WG III Chapters 3 and 4).

Emission metrics are a simple way of representing the magnitude of the climate effect of a unit emission of a species. Examples of the climate effect are the radiative forcing, global average surface temperature, global precipitation and global sea level (Houghton et al., 1990; Shine et al., 2005, 2015; Sterner et al., 2014). When used to represent the climate impact the metrics are referred to as absolute metrics and expressed in units of impact per kg (e.g. AGWP or AGTP). More commonly these are compared with a standard species (almost always CO_2) to give a dimensionless factor (e.g. GWP or GTP).

Chapter 8 of WGI AR5 (Myhre et al., 2013b) comprehensively discussed different physical metrics so this section focusses on key updates since that report. Since AR5 there has been further understanding of the radiative effects of emitted species (see 7.3.2). Note that for CO_2, CH_4 and N_2O the radiative efficiencies vary with background and so have always evolved between assessment reports (see Figure 8.31 of Myhre et al. (2013)). Since AR5 metrics relating to new physical quantities (precipitation (Shine et al., 2015) and sea level (Sterner et al., 2014)) have been quantified. There have been developments in understanding how to compare short-lived species (SLCFs) to CO_2 (Allen et al., 2016; Smith et al., 2012). Understanding of the effect on metrics of the carbon-cycle response to temperature has improved. Although there has been greater understanding since AR5 of the carbon cycle responses to CO_2 emissions (Chapter 5, Section 5.5), there has been no new quantification of the response of the carbon-cycle to a pulse emission since Joos et al. (2013).

- The radiative efficiencies used in climate metrics should include rapid adjustments to the target species and CO_2 where available.
- Carbon cycle responses are sufficiently well understood that they should be included in climate metrics
- Mixed step and pulse metrics can be a useful way of comparing short-lived climate forcers with CO_2.

7.7.2.1 Radiative properties

Since AR5 there have been changes in the understanding of the radiative properties of emitted species for details on these see 7.3.1, 7.3.2, 7.3.3. For CO_2, CH_4 and N_2O better accounting of the spectral properties of these gases has led to re-evaluation of their stratospheric-temperature adjusted radiative efficiencies and their dependence on the background state (Etminan et al., 2016). For CO_2 and CH_4 the tropospheric rapid adjustments are assessed to be non-zero. The re-evaluated effective radiative efficiency forcing for CO_2 will affect all relative climate metrics.

The effective radiative efficiencies (including rapid adjustments) for 2017 conditions for CO_2, CH_4 and N_2O are assessed to be 1.37×10^{-5} (1.23×10^{-5} to 1.51×10^{-5}, 3.79×10^{-4} (3.15×10^{-4} to 4.43×10^{-4}) and 2.92×10^{-3} (2.63×10^{-3} to 3.21×10^{-3}) W m^{-2} ppb^{-1} respectively, compared to 1.37×10^{-5}, 3.63×10^{-4} and 3.00×10^{-3} W m^{-2} ppb^{-1} in Myhre et al. (2013b). For CO_2 and CH_4 increases due to the re-evaluated radiative properties and rapid adjustments more than offset the decreases due to the increasing background. For N_2O both the re-evaluated radiative properties and the increasing background act to decrease the effective radiative efficiency.

7.7.2.2 Physical quantities

All the emission metrics are related to top of atmosphere (effective) radiative forcing following a change in emission. A global temperature-change potential was introduced by Shine et al. (2005) by convolving the radiative forcing with a temperature response function $R_{\mathrm{T}}(t)$derived from a two-layer energy balance model. Sterner et al. (2014) took this further using an upwelling-diffusion energy balance model to derive sea level rise (SLR) as a SLR response function to radiative forcing or as a response function to global surface temperature $R_{\mathrm{SLR}}(t)$. Each step from radiative forcing to temperature to SLR includes longer timescales and therefore prolongs further the contribution of short-lived species. Thus, SLCFs become relatively more important for SLR than temperature or radiative forcing.

To illustrate this, the absolute global radiative forcing metric is defined:

$$A\mathrm{GRF}_X(H) = \Delta F_X(H) \qquad \textit{Equation 7.1}$$

as the forcing after time H due to a unit pulse emission of species X. This is similar to instantaneous climate impact (ICI) (Edwards and Trancik, 2014). Then the absolute global temperature-change potential:

$$A\mathrm{GTP}^X(H) = \Delta T^X(H) = \int_0^H A\mathrm{GRF}^X(t) R_{\mathrm{T}}(H - t)dt \qquad \textit{Equation 7.2}$$

is the global mean surface temperature change after time H. The absolute global sea-level rise:

$$\begin{aligned} A\mathrm{GSR}^X(H) = \Delta\mathrm{SLR}^X(H) &= \int_0^H A\mathrm{GTP}^X(t) R_{\mathrm{SLR}}(H - t)dt \\ &= \int_0^H \int_0^{t'} \mathrm{AGRF}^X(t') R_{\mathrm{T}}(t - t') R_{\mathrm{SLR}}(H - t)dt'dt \end{aligned} \qquad \textit{Equation 7.3}$$

is the global mean sea level rise after time H.

A metric for precipitation, absolute global precipitation potential AGPP (Shine et al., 2015) has two components, fast and slow. The fast component is related to the effective atmospheric forcing (not top of atmosphere forcing) and is assumed to be linearly related to the effective radiative forcing by a dimensionless factor f^X that is species dependent. The slow component is related to a change in surface temperature by a factor k (W m^{-2} $°C^{-1}$) that is species independent. The AGPP in kg s^{-1} m^{-2} is then given by:

$$\begin{aligned} A\mathrm{GPP}^X(H) = \Delta P^X(H) &= \frac{1}{L}\left(kA\mathrm{GTP}^X(H) - f^X \mathrm{AGRF}^X(H)\right) \\ &= \frac{1}{L}\left(k\int_0^H k\mathrm{AGRF}^X(t) R_{\mathrm{T}}(H - t)dt - f^X A\mathrm{GRF}^X(H)\right) \end{aligned} \qquad \textit{Equation 7.4}$$

where L is the latent heat of vaporisation of water in J kg^{-1}.

Since the AGPP is the difference of two terms and is strongly dependent on the factor f^X it is not possible to generalise as to whether this is higher or lower for SLCFs. Both f^X and k need to be derived from climate models.

It has been shown that for the physical variables discussed, metrics can be constructed that are linear functions of radiative forcing. Similar metrics could be devised for other climate variables provided they can be related by response functions to radiative forcing or temperature change. Global damage potentials have been designed (Sarofim and Giordano, 2018) that are related to powers of the surface temperature change. These can be more closely aligned with the economic and social costs of pollutant emissions but being non-linear they depend on the size of the emission and rely on the assumption of an ideal climate state from which the perturbations are measured.

The physical metrics described above are instantaneous or endpoint values defined at a time H after the emission. These are appropriate when the goal is to not exceed a fixed target such as a temperature limit or sea-level rise limit at a specific time. The above metrics can also be integrated from the time of emission, so the impact is in degree-years for temperature or metre-years for sea-level rise. These reflect that the impact depends on how long the change occurs for, not just how large the change is. The integrated version of a metric iAGxx is given by $\mathrm{iAGxx}(H) = \int_0^H \mathrm{AGxx}\,dt$. The commonly used GWP metric is the integrated form of the radiative forcing metric, i.e. GWP=iGRF. Integrated metrics include the effects of a pulse emission from the shortest timescales up to the time horizon, whereas endpoint metrics only include the effects that persist out to the time horizon. SLCFs have therefore relatively higher integrated metrics than endpoint metrics (Levasseur et al., 2016).

7.7.2.3 Carbon cycle responses and other indirect contributions

AR5 (Myhre et al., 2013) included a contribution to climate metrics from carbon-cycle responses, representing an adjustment to conventional approaches which considers more of the causal chain displayed in Figure 7.2. Any agent that warms the surface perturbs the terrestrial and oceanic carbon fluxes, typically causing a net flux of CO_2 into the atmosphere and hence further warming. This aspect is already included in the carbon cycle models that are used to generate the radiative effects of a pulse of CO_2, but was neglected for non-CO_2 species in the conventional metrics. A simplistic account of the carbon cycle response was included in AR5 based on a single study (Collins et al., 2013b). Since AR5 this understanding has been revised (Gasser et al., 2017; Sterner and Johansson, 2017) using carbon cycle models to derive the time evolution of CO_2 following a unit pulse emission $R_{\mathrm{CO2}}(t)$ and the CO_2 flux perturbation following a unit temperature pulse $R_F(t)$. In Collins et al. (2013a) $R_F(t)$ was set simply to $\Gamma \times \delta(t)$ whereas the newer studies include a more complete functional form accounting for subsequent re-uptake after the removal of the pulse. The increase in any metric (AGxx^X) due to the carbon cycle response can be derived from the convolution of the temperature response $\mathrm{AGTP}^X(t)$ with the CO_2 flux response to temperature and the equivalent metric for CO_2:

$$\Delta\mathrm{AGxx}^X = \int_0^H \int_0^t AGTP^X(t')R_F(t-t')\mathrm{AGxx}^{\mathrm{CO2}}(H-t)dt'dt \qquad \textit{Equation 7.5}$$

Including the carbon cycle response for non-CO_2 treats CO_2 and non-CO_2 species consistently. *Confidence* in the method for calculating the carbon cycle response is *high* therefore we assess that including this more accurately represents the climate effects of non-CO2 species than excluding it. The values have only been calculated in two carbon cycle models so the error is assessed to be ±100%. Carbon cycle response are included in all the metrics presented in Table 7.17 and Table 7.A.1 using the response function $R_F(t)$ of Gasser et al. (2017) (their Appendix C3).

Emissions of non-CO_2 species can affect the carbon cycle in other ways: emissions of ozone precursors can reduce the carbon uptake by plants (Collins et al., 2013b); emissions of reactive nitrogen species can fertilize the carbon cycle (Zaehle et al., 2015); and emissions of aerosols or their precursors can affect the utilisation of light by plants. There is robust evidence that these processes occur and are important, but insufficient evidence to determine the magnitude of their contributions to climate metrics.

Emissions of chemically-reactive species can lead to indirect contributions from chemical production or destruction of other greenhouse gases. For methane AR5 assessed the contributions from ozone and stratospheric water vapour add 50% and 15% respectively to its climate metrics. There have been no updates to these values yet. IPCC AR5 included a contribution to the climate metrics for ozone-depleting substances (ODSs) from the loss of stratospheric ozone. These contributions are unchanged for AR6. Oxidation of methane and other hydrocarbons leads ultimately to the production of CO_2 (Boucher et al., 2009). For hydrocarbons from fossil sources this will lead to new CO_2 in the atmosphere however this can already be included in carbon emission totals (Muñoz and Schmidt, 2016).

7.7.2.4 Comparing short-lived climate forcers (SLCFs) with CO_2

Climate metrics are often criticised for over or under stating the importance of different species on climate in terms of their role on future globally averaged surface temperature change, particularly for short-lived climate forcers (SLCFs) e.g (Pierrehumbert, 2014). They are particularly sensitive to the choice of time horizon. Global temperature-change potentials (GTP) for 50-year and 100-year time horizons for methane range from 14 to 4, see (Table 7.17 and Table 7.A.1). The time dependence occurs because the temperature changes following a pulse of CO_2 (in kg) emissions are roughly constant in time, the principle behind TCRE, (see Figure 7.29b) whereas the temperature change following a pulse of SLCF emission declines. A step change in SLCF emissions (in kg yr^{-1}) that is maintained indefinitely leads to a constant change in SLCF abundance (for timescales significantly longer than the lifetime of the SLCF). This will also cause a roughly constant change in temperature (Figure 7.29a) – and hence more similar behaviour to CO_2 (Allen et al., 2016, 2018b; Smith et al., 2012). Metrics for step emission changes can be derived by integrating the more standard pulse emission changes up to the time horizon:

$$\mathrm{AGTP}_X^S = \int_0^H \mathrm{AGTP}_X(H-t)dt \qquad \textit{Equation 7.6}$$

The ratio of the step metric for SLCFs with the pulse metric for CO_2 leads to a mixed-GTP $=$ $\mathrm{AGTP}_X^S/\mathrm{AGTP}_{\mathrm{CO2}}$. This has the units of years, (the standard GTP is dimensionless). This mixed-GTP shows much less variation with time than the standard GTP (comparing Figure 7.29c with d) and provides a scaling for comparing a change in emission rate (in kg yr^{-1}) of SLCF with a pulse emission or change in carbon budget of CO_2 (in kg). Allen et al. (2016) show that an approximation (which they designate GWP*) to the mixed-GTP metric can be derived by simply scaling the GWP by the time horizon H. While the mixed-GTP can be calculated for any species, it is most useful for short-lived species, i.e. those with lifetimes much less than the time horizon of the metric. The time variance of metrics can be accounted for exactly using the CO_2 forcing equivalent (CO_2-fe) metric (Allen et al., 2018b). Such metrics provide a way of effectively comparing emissions of short- and long-lived greenhouse gases on globally averaged surface temperature. These could be challenging to implement into single-basket policy approaches for several reasons, especially the high relative value of changes in short-lived pollutants.

[START FIGURE 7.29 HERE]

Figure 7.29: Climate metrics for two SLCFs: HFC-32 and CH4, (lifetimes of 5.2 and 12.4) years. (a) temperature response to a step change in SLCF emission. (b) temperature response to a pulse CO_2 emission. (c) conventional GTP metrics (pulse vs pulse). (d) mixed-GTP metric (step vs pulse).

[END FIGURE 7.29 HERE]

7.7.2.5 Climate metrics by species

Climate metrics for selected species are presented in Table 7.17, with further species presented in appendix Table 7.A.1. GWP(100) values are included for consistency with previous reports, but this does not imply a continued recommendation of their use. GWP values are not presented for other time horizons. Mixed metrics (MGTPs) comparing step changes in SLCFs with pulse emissions of CO_2 are presented for shorter-lived species. The decrease in radiative efficiency of CO_2 at higher concentrations is compensated by the increase due to rapid adjustments (Section 7.7.2.2) leading to no change in the denominator for the climate metrics. The climate metrics for methane have increased due to the increase in the methane radiative efficiency (Etminan et al., 2016) although much of this is offset by the rapid adjustment (Section 7.3.2) leading to an increase of 4% in the methane radiative efficiency. The radiative efficiency of N_2O is decreased following Etminan et al. (2016) leading to lower climate metrics compared to AR5. The radiative properties and lifetime of halocarbons are unchanged from AR5. The carbon cycle responses are assessed to contribute less than in AR5 so that for all species the climate metrics are slightly smaller than in AR5.

[START Table 7.17 HERE]

Table 7.17: Climate metrics for selected species. Mixed GTPs (MGTPs) are shown for species with a lifetime less than 20 years (see section 7.7.2.5). These values include carbon cycle responses as described in 7.7.2.4. The radiative efficiencies are as described in section 7.3.2 and include rapid adjustments where assessed to be non-zero in 7.3.2. The climate response function is from Geoffroy et al. (2013). Chemical effect of methane and N2O are included as in AR5. Contributions from stratospheric ozone depletion are not included.

Species	Lifetime	GWP(100)	GTP(50)	GTP(100)	MGTP(50) (years)	MGTP(100) (years)
CH4	12.4	32	14.5	6.6	3050	3750
N2O	121	271	288	242		
HFC-32	5.2	722	190	142	72500	86500
HFC-134a	13.4	1390	690	295	132000	164000
CFC-11	45	4950	5020	2590		
CF4	50000	6980	7210	8550		

[END Table 7.17 HERE]

[START BOX 7.3 HERE]

BOX 7.3: Metric types

Many single-valued emissions metrics struggle to capture aspects of the climate response under different scenarios.

Environmental science and related disciplines often draw the distinction between stock pollution, in which pollutants and damages are essentially cumulative, and flow pollution, in which pollutants are short-lived and damages follow the flow of pollution. This distinction is relevant to climate change, since some forcing agents (CO_2, N_2O and other GHGs with multidecadal or longer residence times) behave as stock pollutants, while other short lived climate pollutants (see Chapter 6) and methane) behave much more as flow pollutants. This means the impacts of CO_2, N_2O and other long-lived gases are usually functions of cumulative emissions: this is why there is a near-linear relationship between GSAT and cumulative CO_2 emissions, for instance. On the other hand, the climate effects of short lived climate pollutants and methane more closely follow the pattern of emissions themselves. The distinction is particularly important when emissions of different species are declining: as emissions decline to zero, the climate effects of CO_2 asymptote to a value implied by the total amount of anthropogenic CO_2 emissions emitted since the pre-industrial period, while the climate effects of methane decline to zero if methane emissions decline to zero. Metric choice can, and usually does, obscure this distinction.

Whether or not the distinction between stock pollution and flow pollution is relevant within a given pollution management regime depends upon the goals of the regime and the considerations (including value judgements) underpinning it. However, the distinction is important in the calculation of the warming implied by a given emissions portfolio (Allen et al., 2018a; Box 2, 2018b). It is not possible to unambiguously calculate the future warming trajectory implied by an emissions portfolio containing substantial short lived climate pollutants and long-lived gases when these are reported on a common equivalence metric, unless the metric itself preserves the distinction between stock and flow pollution.

This box compares GWP20, GWP100, GTP, GWP* and MGTP against RCP2.6, RCP4.5 and RCP6.0 for ERF and temperature over the period 2000-2150.

[Will be expanded for SOD with Figures]

It can be seen that the metrics which preserve the stock vs flow distinction – GWP* and MGTP – shadow the effects of the gases on temperature across the period plotted (and beyond). The metric which provides the poorest mapping of emissions to temperatures is GWP20, followed by the customary metric, GWP100.

[END BOX 7.3 HERE]

7.7.3 Applications of metrics

7.7.3.1 Interpretations of metrics

As discussed in 7.1 above, emissions metrics can be interpreted in several different ways. For instance, the conversion of some quantity of emissions of one gas into some "equivalent" amount of CO_2 informs something about relative contribution to climate change, and this may be more or less useful depending on the goodness of fit between the metric and the policy goals in question (Harvey, 2000). However, there are several choices that determine the numerical specifics of any emissions metric, and these choices pertain to a mix of scientific and value judgements over which reasonable minds may disagree.

The variable used to compare the effects of different emissions is a matter of choice: common choices include radiative forcing (Houghton et al., 1990) and temperature (Shine et al., 2005), but other variables have also formed the basis of comparison, including sea level rise (Sterner et al., 2014), and dollar-denominated climate change damages (Tol et al., 2012). Emissions metrics can play important roles in framing scientific information for policymakers. Metrics are also used in areas such as Life Cycle Assessments and Integrated Assessment Modelling (e.g., by IPCC WGIII).

The timescale associated with the comparison is also a choice. Partly to show the effects of timescale on metrics, previous IPCC reports reported 20 year, 100 year, and 500 year values for GWP (Forster et al., 2007), and 20-year and 100-year values for GWP and GTP, with and without the inclusion of carbon cycle feedbacks (Myhre et al., 2013b). Time-varying metrics also involve the choice of a time-horizon, though in these cases the time horizon is usually derived from a climate target (most commonly a temperature target). Time horizon is a choice that, ideally, ought to reflect decision-makers' needs, depending on the specific application and the appropriate weighting of different aspects of climate change for a given situation. The most common approach uses a 100-year timescale, but this is not universally appropriate (Myhre et al., 2013b; Chapter 8, Section 8.7). In fact, Houghton et al. (1990), specifically noted that 20, 100, and 500 year timescales they discussed were merely 'candidates for discussion [that] should not be considered as having any special significance'.

Because metrics have had a role in establishing the "exchange rate" between gases, there has been particular focus on the role of metrics in price-based comparisons between greenhouse gases. The most common economic interpretation of the role of metrics is that policy makers would like to undertake cost-effective reductions of GHG emissions by comparing the discounted marginal abatement costs and damages associated with the emission of another unit of one greenhouse gas against the emission of another unit of another greenhouse gas(Manne and Richels, 2001). Assuming a decision maker has access to the marginal abatement costs associated with their decision, they would like a signal regarding the discounted present value of the marginal impacts associated with each gas (Manne and Richels, 2001; Tol et al., 2012). However, scientists cannot directly measure or assess these marginal impacts; models that attempt to gauge the impacts from climate change report a wide range of possible responses. The observation of (Manne and

Richels, 2001), “Unfortunately, we lack at present the necessary knowledge to specify the shapes of the damage functions and to assign values to many categories of impacts” still holds and, in view of the inherent difficulty in modelling welfare impacts of climate change, will continue to be the case for the foreseeable future. Inability to access these damage functions has partly led to the deployment of simple, physically-based metrics as scientific tools for policy (Myhre et al., 2013b).

7.7.3.2 Matching metrics and policy goals

Different metrics may be more or less well-aligned with the impacts of climate change on specific variables, but no single metric captures the relative roles of different forcing agents across all potential variables of interest. No matter how it is done, the way different gases are compared is value-laden. Scientifically, values play out through the choices behind the variable(s), as well as the associated functional form and timescales. The customary – GWP(100) – rests on path dependent decisions made by climate negotiators in response to the fact that GWP(100) was the only metric discussed in the IPCC FAR (Houghton et al., 1990). Yet scientists presented GWP(100) in the FAR not as a suggestion, but as an illustration “to illustrate the difficulties inherent in the concept.” GWP(100) was developed following precedents derived from the approach taken to the ozone problem (Shine, 2009), and though scientists were clear from the outset about the matters of choice involved.

As well as the alignment between metrics and policy goals, other properties are also important, including the uncertainty associated with either the physical variable or the policy target. Often there is a trade-off between some of these properties – well-being is notoriously difficult to measure, for instance, and policy makers often resort either to well-measured variables that are only imperfectly aligned with well-being (such as financial income) or to variables that may be better aligned with the goals of policy, but are more uncertain or poorly measured (such as composite indicators of well-being). In practice, researchers have usually used a simple proxy measure to make this comparison (Myhre et al., 2013b). From a purely scientific view, the comparison between the impacts of different gases could be made in a number of ways, since there are a range of physical variables, functional forms and timescales on which basis the comparison could be made.

Though metric choice is value-laden, it is not arbitrary. Metrics can be more or less well-aligned with a policy target or goal. For instance, if a policy-maker is concerned primarily with warming decades into the future, then an integrated metric is a relatively poor choice. If the metric aligns well with global damage potential, as is the case with GWP(100) (Myhre et al., 2013b; Tol et al., 2012) then the metric would be a good fit for a cost-benefit framework. If the metric aligns well with global cost potential, as is the case with GTP(100), then the metric would be a good choice for a cost-effectiveness framework (Myhre et al., 2013b; Tol et al., 2012).

Box 7.3 shows the relative performance of a range of metrics in response to future scenarios. Within the current climate change regime, the most discussed targets are the global mean temperature targets established by Article 2 of the Paris Agreement. The Paris Agreement has no other numerical targets, but it does have two other implicit science targets in Article 4 which articulated in support of the temperature goals in Article 2: these are an early peaking target, and the aim to “achieve a balance between anthropogenic emissions by sources and removals by sinks of greenhouse gases in the second half of this century”. The Article 4 goals contain important constraints regarding international equity, sustainable development, and poverty reduction.

It is clear that the traditional metric, GWP100, gives the wrong sign of the contribution of SLCPs and methane to warming when emissions are declining. This is a general property of integrated metrics. End point metrics are less prone to this error. The least erroneous are newer metrics such as GWP* (Allen et al., 2018b) and MGTP, developed since AR5, which compare a step-change in short-lived forcing with a pulse of long-lived gases more accurately correlate with the temperature effects of emissions scenarios. In response to the fact that the “Global Warming Potential” does not, under most scenarios, do a good job of representing the temperature effects of emissions, Myhre et al. (2013) observed that “the name ‘Global

Warming Potential' may be somewhat misleading, and 'relative cumulative forcing index' would be more appropriate."

Innovations since AR5 have continued to develop longstanding critiques of the customary metric, GWP, and these critiques have been extended to include all metrics which do not preserve the distinction, important for variables such as global mean temperatures, between short- and long-lived forcing agents. Alternative methods for comparing greenhouse gases have been developed, and some of these give a more faithful simulation of the temperature effects of a portfolio of gases, especially under mitigation scenarios, such as those implied by successful attainment of the temperature goals set out in Article 2 of the Paris Agreement. (*high confidence*.) While it is reasonable to call attention to the importance of coherence between choices regarding carbon accounting or metric choice and the science goals that have been agreed, such as those in the Paris Agreement, IPCC is a non-prescriptive body, and so it cannot make specific recommendations regarding metrics (and this includes previous recommendations (made in AR4), which should not have been made). Ultimately, it is a matter for policymakers to decide which metric to use, because they have the social licence to make the normative judgments regarding timescale, variable choice and functional form that underpin metric choice. Physical science can only form a subset of the inputs to those choices.

7.8 Key Knowledge Gaps

- Observations of ocean heat imbalance over the 19th century hampers assessing longer term historical trends with precision (Section 7.2)
- The processes governing rapid adjustments that comprise a ~10% part of the effective radiative forcing need to be carefully tested with detailed numerical models and observations (Section 7.3)
- In particular, the contribution of rapid adjustments to the effective radiative forcing associated with aerosol-cloud interactions is poorly bounded. The reasons why results from different observational analyses contradict each other in this respect need to be identified, as do the sources of model disagreement (Section 7.3)
- Mixed-phase, ice and convective cloud responses to aerosol changes and climate feedbacks are poorly observed and modelled (Section 7.3, Section 7.4)
- The future possible future warming of the Eastern Pacific and its timing has important implications for projections of global warming and ECS. It is predicted by most models but is difficult to infer from paleo observations, especially with the timing of such a warming. (Section 7.4, Section 7.5)
- The high-end estimate of ECS remains relatively poorly constrained., emerging lines of evidence offer possible ways forward (Section 7.5)

Frequently Asked Questions

FAQ 7.1: Clouds --- What have we learned since IPCC AR5?

In often seems we are making little progress on understanding clouds and their role in climate change. We in fact have made a tonne of progress and can now quantify their amplifying effect on global warming from greenhouse gases, but details remain to be worked out.

Clouds cover two thirds of the Earth's surface. They generally form when the water vapour that is present in updrafts of air condenses out of the air to form water drops. We see the reflections from these little drops of water as clouds. When the drops grow large enough, they can fall to the surface as rain. If they get cold enough, they can freeze to make ice crystals that can grow and fall to the surface as snow. Clouds play a key role in the Earth's water cycle and also in the Earth's energy budget. Over the last four decades, numerous satellites have measured the role that clouds play in reflecting sunlight and trapping thermal radiation. High clouds tend to trap more radiation than they reflect, and low clouds reflect more than they trap. On average, their reflection wins out and overall clouds cool the climate.

The temperature structure as well as the moisture structure of the atmosphere controls the occurrence of clouds, and clouds themselves shape the atmospheric circulation by releasing condensation heat and altering the radiative balance. For decades it has also been known that the radiative properties of clouds depend on the abundance of aerosol particles upon which cloud droplets and ice crystals must form. Since atmospheric aerosol concentrations have increased considerably since pre-industrial times due to fossil fuel and biomass burning, today's atmosphere contains more such particles than at pre-industrial times. This has made clouds more reflective, because cloud droplets have predictably become more numerous and smaller. There is broad agreement that this cooling effect has counteracted a considerable portion of the greenhouse warming over the last century, though exact quantification has been a challenge. It has also been proposed that the more numerous but smaller droplets act to extend cloud lifetime and/or increase cloud water content by delaying rain formation, but this effect remains controversial. While some studies using satellite observations find evidence in strong support of it, others find a negligible impact. Climate models also disagree on the matter, simulating everything from negligible to very strong cooling due to aerosol effects on cloud temporal and spatial extent. On balance, the evidence points to an amplification of cloud-mediated aerosol cooling through increased cloud lifetimes and/or amounts, but the magnitude of this amplification remains poorly quantified.

When the global radiation balance is perturbed by increasing atmospheric greenhouse gases clouds also change as the climate state warms. Climate scientists often refer to the 'cloud feedback'. This feedback relates to how clouds will change in a warmer world, and how these changes will affect the radiation balance of the Earth. It is the largest component of uncertainty in global warming projections for a given emission pathway and has proved a tricky nut to crack. The problem stems from the fact that clouds can change in a myriad of ways and their processes tend to occur on much smaller scales than represented by current global climate models. The latest generation of climate models have improved their representation of clouds by both increasing their resolutions and sophisticating their representation of processes that occur at still finer scales, so-called sub-grid parameterisations (Chapter 1). Yet, this improvement is incremental, and the representation of cloud processes even in the world's best climate models remains a challenge.

Over the past decade, new detailed numerical simulation and measurement efforts have allowed us to accelerate our understanding of how the clouds interact with circulation, and how their changes affect climate. Analyses in IPCC AR5 were able to make use of cloud measurements by radar and LiDAR on a series of satellites. These active sensors gave information on vertical profiles of cloud occurrence and cloud water, overcoming earlier limitations. Increase in computer power also made very large area simulations possible at horizontal resolutions of a few kilometres where convective cloud systems could be explicitly resolved (FAQ7.1, Figure 1). Such simulations complemented large-eddy simulations that simulate particular cloud systems over a few days and have the resolutions of 100m or less.

Since IPCC AR5, these observations and modelling efforts have been further developed and integrated to

build a more complete understanding of cloud processes. For example, aerosol-cloud processes are routinely represented in fine detail. Furthermore, extensive analyses of the latest climate model simulations have enabled scientists to propose a number of constraints on the overall cloud feedback.
A coordinated set of simulations for stratocumulus and trade cumulus cloud regions has revealed how low clouds are reduced and thinned in response to increasing surface temperature, providing evidence that the cloud feedback amplifies global warming (Section 7.4.2).

[START FIGURE FAQ7.1, Figure 1 HERE]

FAQ7.1, Figure 1: Global view of infrared brightness temperature (T_{bb}) on 6 August, 2016, and monthly- and zonal-mean cross section of cloud liquid (blue) and ice (purple) contents. T_{bb} has a low value where cloud covers surface and is used as a measure of cloud distribution from space. (Top) Satellite observations and (bottom) a global cloud-resolving simulation using 3.5 km NICAM. Colours are the same between the two panels. Thin purple curves in the top panel show the satellite paths along which the zonal mean is calculated.

[END FIGURE FAQ7.1, Figure 1 HERE]

Verification of cloud vertical structure in climate models using recent satellite products identified a common error in their simulations, particularly in representing mixed-phase clouds (clouds that may contain both liquid and ice) for the present climate over the Southern Ocean. Recent studies have also revisited the problem of how deep tropical clouds will change with warming from a new perspective. If tropical high clouds, called anvil clouds, decrease in size in a warmer climate, that will have a cooling effect, reducing the amount of expected warming from greenhouse gas increases. Climate scientists now believe that a reduction of anvil cloud area will occur in association with a greater clustering of convective storms with warming. To date, observational analyses, detailed simulations, and theory have helped climate scientists understand these processes in greater detail, but they have yet to accurately determine their role in cloud feedback.

In summary, more and more cloud processes are being understood and simulated well enough to enable us to narrow the range of possible cloud feedbacks and cloud responses to aerosol changes, which will ultimately help us better constrain future projections of climate. The assessment in Section 7.4 halves the uncertainty range in cloud feedback compared to IPCC AR5 and assesses that it is now *very likely* that cloud changes will amplify the global warming effect of greenhouse gases. In contrast our emissions of polluting gases such as sulphur dioxide and particles enhance the cooling effect of cloud, and this cooling effect can now be better constrained (Section 7.3). The nut is still firmly in its shell but scientists are hungry and we have much better nutcrackers than 10 years ago so it shouldn't take long!

FAQ 7.2: Which emission metric should I use?

Emission metrics are used in climate policy to compare greenhouse gases, but there is a debate over which to use. Science can help inform appropriate metrics for specific policy targets but societal values and judgements about what is important are the deciding factor.

Emission metrics provide a summary of the comparative effects, over some time horizon, of different emissions, as assessed against some specific climate or socioeconomic measure. They provide a short-hand for comparing emissions. It has been customary to use one such metric, the global warming potential or GWP, in carbon accounting approaches. However, while they are potentially useful, metrics can be misleading if used inappropriately, and they are not essential. Gases and other forcing agents could be treated separately by a climate policy, without the need for comparison between them. The Montreal Protocol used a multi-basket approach which allowed trading within a basket of similarly behaving gases, but not between different baskets of gases. Climate policies, starting with the Kyoto Protocol, have adopted a single-basket approach based on GWP evaluated over a 100-year time horizon. However, the focus on a single metric to trade gases has received substantial criticism from the scientific and research community since Kyoto's inception. Partly in response to this criticism, a range of alternatives have been proposed. GWP100 compares the integrated radiative forcing over 100 years of a gas to carbon dioxide. Some of the alternatives have attempted to instead compare the damages from different emissions. Others have made different choices over whether to compare the effects of emissions at a point in time, integrated over time or their transient effects. Some arguments regarding metrics have focused on choosing different time-horizons or on avoiding trade-offs that are rational under GWP100 but which would leave the world warmer overall.

Because emission metrics have, so far, attempted to compare the effects of different gases against some function of a single climate or socioeconomic measure, and because policy is multi-faceted, there is no universally-applicable metric. This does not mean that all metrics are equally valuable, or evidentially supported, or intellectually defensible. Some emission metrics probably are better than others, because some choices are either better-supported, scientifically, or more compatible with widely-shared normative judgements (e.g. about time horizons).

In Box 7.3 the performance of different metrics against different climate variables is shown. Here we discuss metric performance against the scientific goals articulated in the Paris Agreement. The global climate change regime complex contains many elements, but temperature and greenhouse gas stabilization have central roles. Article 2 of the Convention states "The ultimate objective of this Convention [is] stabilization of greenhouse gas concentrations in the atmosphere at a level that would prevent dangerous anthropogenic interference with the climate system." The Paris Agreement commits countries to "holding the increase in the global average temperature to well below 2°C above pre-industrial levels and to pursue efforts to limit the temperature increase to 1.5°C above pre-industrial levels[.]" Article 4 states: "In order to achieve the long-term temperature goal set out in Article 2, Parties aim to reach global peaking of greenhouse gas emissions as soon as possible, recognizing that peaking will take longer for developing country Parties, and to undertake rapid reductions thereafter in accordance with best available science, so as to achieve a balance between anthropogenic emissions by sources and removals by sinks of greenhouse gases in the second half of this century, on the basis of equity, and in the context of sustainable development and efforts to eradicate poverty." The only explicit climate targets expressed numerically in the Paris Agreement are the temperature targets in Article 2. Neither the greenhouse gas stabilization (UNFCCC) nor the "balance between anthropogenic emissions by sources and removals by sinks of greenhouse gases" nor the early peaking targets in Article 4 are enumerated.

It has been shown repeatedly that the temperature targets (Paris Agreement) are poorly-matched with integrated metrics such as GWP100 as traditionally used. It is a general property of integrating metrics that they cannot shadow the temperature effects of a trajectory of long-lived and short-lived greenhouse gases. They are better suited for comparing other climate measures, such as sea-level rise or the accumulation of energy in the climate system.

Trajectory-based approaches to the comparison of gases and other forcing agents better capture the temperature effects of short-lived and long-lived emissions. The warming signal implied by a portfolio of gases under such metrics is much less ambiguous than that of the same portfolio of gases reported under GWP20 or GWP100. This does not mean that trajectory-based approaches have universal applicability as it is still inherent within them that short-lived greenhouse gases and long-lived gases should be treated differently: a one-off emission of a long-lived gas needs to be compared to an indefinitely sustained emission change in a short-lived gas. If policy goals are focused instead on things other than temperature targets, such as integrated measures of change, then an integrated metric would be a better choice for those goals.

As identified by previous reports, metric choice should be informed by policy goals. On the presumption that policymakers will care about many different measures over many different timescales, considering short and long-lived greenhouse gases separately may be advantageous. However, the choice of how – or whether – to compare the effects of different gases within either a single-basket approach or a two- or multi-basket approach, relies on choices that science alone cannot determine.

References

Abe-Ouchi, A., Saito, F., Kawamura, K., Raymo, M. E., Okuno, J., Takahashi, K., et al. (2013). Insolation-driven 100,000-year glacial cycles and hysteresis of ice-sheet volume. *Nature* 500, 190–193. doi:10.1038/nature12374.

Abel, S. J., Boutle, I. A., Waite, K., Fox, S., Brown, P. R. A., Cotton, R., et al. (2017). The Role of Precipitation in Controlling the Transition from Stratocumulus to Cumulus Clouds in a Northern Hemisphere Cold-Air Outbreak. *J. Atmos. Sci.* 74, 2293–2314. doi:10.1175/JAS-D-16-0362.1.

Abraham, J. P., Baringer, M., Bindoff, N. L., Boyer, T., Cheng, L. J., Church, J. A., et al. (2013). A review of global ocean temperature observations: Implications for ocean heat content estimates and climate change. *Rev. Geophys.* 51, 450–483. doi:10.1002/rog.20022.

Adam, O., Schneider, T., Brient, F., and Bischoff, T. (2016). Relation of the double-ITCZ bias to the atmospheric energy budget in climate models. *Geophys. Res. Lett.* doi:10.1002/2016GL069465.

Ainsworth, E. A., and Rogers, A. (2007). The response of photosynthesis and stomatal conductance to rising [CO 2]: Mechanisms and environmental interactions. *Plant, Cell Environ.* 30, 258–270. doi:10.1111/j.1365-3040.2007.01641.x.

Albrecht, B. A. (1989). Aerosols, cloud microphysics, and fractional cloudiness. *Science* 245, 1227–30. doi:10.1126/science.245.4923.1227.

Aldrin, M., Holden, M., Guttorp, P., Skeie, R. B., Myhre, G., and Berntsen, T. K. (2012). Bayesian estimation of climate sensitivity based on a simple climate model fitted to observations of hemispheric temperatures and global ocean heat content. *Environmetrics* 23, 253–271. doi:10.1002/env.2140.

Alexeev, V. A., and Jackson, C. H. (2013). Polar amplification: is atmospheric heat transport important? *Clim. Dyn.* 41, 533–547. doi:10.1007/s00382-012-1601-z.

Alexeev, V. A., Langen, P. L., and Bates, J. R. (2005). Polar amplification of surface warming on an aquaplanet in ``ghost forcing'' experiments without sea ice feedbacks. *Clim. Dyn.* 24, 655–666. doi:10.1007/s00382-005-0018-3.

Allan, R. P., Liu, C., Loeb, N. G., Palmer, M., Roberts, M., Smith, D., et al. (2014a). Changes in global net radiative imbalance 1985–2012. *Geophys. Res. Lett.* 41, 5588–5597. doi:10.1002/2014GL060962.

Allan, R. P., Liu, C., Zahn, M., Lavers, D. A., Koukouvagias, E., and Bodas-Salcedo, A. (2014b). Physically Consistent Responses of the Global Atmospheric Hydrological Cycle in Models and Observations. *Surv. Geophys.* 35, 533–552. doi:10.1007/s10712-012-9213-z.

Allen, M. R., Dube, O. P., Solecki, W., Aragón-Durand, F., Cramer, W., Humphreys, S., et al. (2018a). “Framing and Context,” in *Global Warming of 1.5°C. An IPCC Special Report on the impacts of global warming of 1.5°C above pre-industrial levels and related global greenhouse gas emission pathways, in the context of strengthening the global response to the threat of climate change*, eds. V. Masson-Delmotte, P. Zhai, H.-O. Pörtner, D. Roberts, J. Skea, P. R. Shukla, et al. (In Press).

Allen, M. R., Fuglestvedt, J. S., Shine, K. P., Reisinger, A., Pierrehumbert, R. T., and Forster, P. M. (2016). New use of global warming potentials to compare cumulative and short-lived climate pollutants. *Nat. Clim. Chang.* 6, 773–776. doi:10.1038/nclimate2998.

Allen, M. R., Shine, K. P., Fuglestvedt, J. S., Millar, R. J., Cain, M., Frame, D. J., et al. (2018b). A solution to the misrepresentations of CO 2 -equivalent emissions of short-lived climate pollutants under ambitious mitigation. *npj Clim. Atmos. Sci.* 1. doi:10.1038/s41612-018-0026-8.

Allen, R. J., Norris, J. R., and Wild, M. (2013). Evaluation of multidecadal variability in CMIP5 surface solar radiation and inferred underestimation of aerosol direct effects over Europe, China, Japan, and India. *J. Geophys. Res.* 118, 6311–6336. doi:Doi 10.1002/Jgrd.50426.

Allen, R. J., Sherwood, S. C., Norris, J. R., and Zender, C. S. (2012). Recent Northern Hemisphere tropical expansion primarily driven by black carbon and tropospheric ozone. *Nature* 485, 350–354. doi:https://doi.org/10.1038/nature11097.

Alo, C. A., and Anagnostou, E. N. (2017). A sensitivity study of the impact of dynamic vegetation on simulated future climate change over Southern Europe and the Mediterranean. *Int. J. Climatol.* 37, 2037–2050. doi:10.1002/joc.4833.

Anagnostou, E., John, E. H., Edgar, K. M., Foster, G. L., Ridgwell, A., Inglis, G. N., et al. (2016). Anagnostou, E., John, E. H., Edgar, K. M., Foster, G. L., Ridgwell, A., Inglis, G. N., … Pearson, P. N. (2016). Changing atmospheric CO2concentration was the primary driver of early Cenozoic climate. Nature, 533, 380–384. https://doi.org/10.1038/nature. *Nature* 533, 380–384. doi:10.1038/nature17423.

Andrews, E., Ogren, J. A., Kinne, S., and Samset, B. (2017a). Comparison of AOD, AAOD and column single scattering albedo from AERONET retrievals and in situ profiling measurements. *Atmos. Chem. Phys.* 17, 6041–6072. doi:10.5194/acp-17-6041-2017.

Andrews, T., Betts, R. A., Booth, B. B. B., Jones, C. D., and Jones, G. S. (2017b). Effective radiative forcing from historical land use change. *Clim. Dyn.* 48, 3489–3505. doi:10.1007/s00382-016-3280-7.

Andrews, T., Forster, P. M., Boucher, O., Bellouin, N., and Jones, A. (2010). Precipitation, radiative forcing and global temperature change. *Geophys. Res. Lett.* doi:10.1029/2010GL043991.
Andrews, T., Gregory, J. M., Paynter, D., Silvers, L. G., Zhou, C., Mauritsen, T., et al. (2018). Accounting for Changing Temperature Patterns Increases Historical Estimates of Climate Sensitivity. *Geophys. Res. Lett.* 45, 8490–8499. doi:10.1029/2018GL078887.
Andrews, T., Gregory, J. M., and Webb, M. J. (2015). The Dependence of Radiative Forcing and Feedback on Evolving Patterns of Surface Temperature Change in Climate Models. *J. Clim.* 28, 1630–1648. doi:10.1175/JCLI-D-14-00545.1.
Andrews, T., Gregory, J. M., Webb, M. J., and Taylor, K. E. (2012). Forcing, feedbacks and climate sensitivity in CMIP5 coupled atmosphere-ocean climate models. *Geophys. Res. Lett.* 39, L09712. doi:10.1029/2012GL051607.
Andrews, T., and Webb, M. J. (2018). The dependence of global cloud and lapse rate feedbacks on the spatial structure of tropical pacific warming. *J. Clim.* doi:10.1175/JCLI-D-17-0087.1.
Andronova, N. G., and Schlesinger, M. E. (2001). Objective estimation of the probability density function for climate sensitivity. *J. Geophys. Res. Atmos.* 106, 22605–22611. doi:10.1029/2000JD000259.
Ångström, K. (1900). Ueber die Bedeutung des Wasserdampfes und der Kohlensäure bei der Absorption der Erdatmosphäre. *Ann. Phys.* 308, 720–732. doi:10.1002/andp.19003081208.
Annan, J. D., and Hargreaves, J. C. (2006). Using multiple observationally-based constraints to estimate climate sensitivity. *Geophys. Res. Lett.* 33. doi:10.1029/2005GL025259.
Armour, K. C. (2017). Energy budget constraints on climate sensitivity in light of inconstant climate feedbacks. *Nat. Clim. Chang.* doi:10.1038/nclimate3278.
Armour, K. C., Bitz, C. M., and Roe, G. H. (2013). Time-Varying Climate Sensitivity from Regional Feedbacks. *J. Clim.* doi:10.1175/JCLI-D-12-00544.1.
Armour, K. C., Marshall, J., Scott, J. R., Donohoe, A., and Newsom, E. R. (2016). Southern Ocean warming delayed by circumpolar upwelling and equatorward transport. *Nat. Geosci.* doi:10.1038/ngeo2731.
Armour, K. C., and Roe, G. H. (2011). Climate commitment in an uncertain world. *Geophys. Res. Lett.* doi:10.1029/2010GL045850.
Armour, K. C., Siler, N., Donohoe, A., and Roe, G. H. (2019). Meridional Atmospheric Heat Transport Constrained by Energetics and Mediated by Large-Scale Diffusion. *J. Clim.*
Armstrong, E., Valdes, P., House, J., and Singarayer, J. (2019). Investigating the feedbacks between CO2, vegetation and the AMOC in a coupled climate model. *Clim. Dyn.* 0, 0. doi:10.1007/s00382-019-04634-2.
Arneth, A., Harrison, S. P., Zaehle, S., Tsigaridis, K., Menon, S., Bartlein, P. J., et al. (2010). Terrestrial biogeochemical feedbacks in the climate system. *Nat. Geosci.* 3, 525.
Arnold, N. P., and Randall, D. A. (2015). Global-scale convective aggregation: Implications for the Madden-Julian Oscillation. *J. Adv. Model. Earth Syst.* 7, 1499–1518. doi:10.1002/2015MS000498.
Arora, V. K., Boer, G. J., Friedlingstein, P., Eby, M., Jones, C. D., Christian, J. R., et al. (2013). Carbon-concentration and carbon-climate feedbacks in CMIP5 earth system models. *J. Clim.* 26, 5289–5314. doi:10.1175/JCLI-D-12-00494.1.
Arrhenius, S. (1896). On the Influence of Carbonic Acid in the Air upon the Temperature of the Ground. *Philos. Mag. J. Sci.* 41, 237–279.
Augustine, J. A., and Dutton, E. G. (2013). Variability of the surface radiation budget over the United States from 1996 through 2011 from high-quality measurements. *J. Geophys. Res.* 118, 43–53. doi:Doi 10.1029/2012jd018551.
Balkanski, Y., Schulz, M., Claquin, T., and Guibert, S. (2007). Reevaluation of Mineral aerosol radiative forcings suggests a better agreement with satellite and AERONET data. *Atmos. Chem. Phys.* 7, 81–95.
Balmaseda, M. A., Trenberth, K. E., and Källén, E. (2013). Distinctive climate signals in reanalysis of global ocean heat content. *Geophys. Res. Lett.* 40, 1754–1759. doi:10.1002/grl.50382.
Barnes, E. A., and Polvani, L. (2013). Response of the midlatitude jets, and of their variability, to increased greenhouse gases in the CMIP5 models. *J. Clim.* 26, 7117–7135. doi:10.1175/JCLI-D-12-00536.1.
Barreiro, M., and Philander, S. G. (2008). Response of the tropical Pacific to changes in extratropical clouds. *Clim. Dyn.* doi:10.1007/s00382-007-0363-5.
Bauer, S. E., Bausch, A., Nazarenko, L., Tsigaridis, K., Xu, B., Edwards, R., et al. (2013). Historical and future black carbon deposition on the three ice caps: Ice core measurements and model simulations from 1850 to 2100. *J. Geophys. Res. Atmos.* 118, 7948–7961. doi:10.1002/jgrd.50612.
Bekki, S., Rap, A., Poulain, V., Dhomse, S., Marchand, M., Lefevre, F., et al. (2013). Climate impact of stratospheric ozone recovery. *Geophys. Res. Lett.* 40, 2796–2800. doi:10.1002/grl.50358.
Bellouin, N., Boucher, O., Haywood, J., and Reddy, M. S. (2005). Global estimate of aerosol direct radiative forcing from satellite measurements. *Nature* 438, 1138–1141. doi:10.1038/nature04348.
Bellouin, N., Mann, G. W., Woodhouse, M. T., Johnson, C., Carslaw, K. S., and Dalvi, M. (2013a). Impact of the modal aerosol scheme GLOMAP-mode on aerosol forcing in the Hadley Centre Global Environmental Model. *Atmos. Chem. Phys.* 13, 3027–3044. doi:10.5194/acp-13-3027-2013.

Bellouin, N., Quaas, J., Morcrette, J.-J., and Boucher, O. (2013b). Estimates of aerosol radiative forcing from the MACC re-analysis. *Atmos. Chem. Phys.* 13, 2045–2062. doi:10.5194/acp-13-2045-2013.
Bender, F. A. M., Ekman, A. M. L., and Rodhe, H. (2010). Response to the eruption of Mount Pinatubo in relation to climate sensitivity in the CMIP3 models. *Clim. Dyn.* 35, 875–886. doi:10.1007/s00382-010-0777-3.
Bender, F. A. M., Ramanathan, V., and Tselioudis, G. (2012). Changes in extratropical storm track cloudiness 1983-2008: Observational support for a poleward shift. *Clim. Dyn.* 38, 2037–2053.
Bentamy, A., Piolle, J. F., Grouazel, A., Danielson, R., Gulev, S., Paul, F., et al. (2017). Review and assessment of latent and sensible heat flux accuracy over the global oceans. *Remote Sens. Environ.* 201, 196–218. doi:10.1016/j.rse.2017.08.016.
Bieltvedt Skeie, R., Berntsen, T., Aldrin, M., Holden, M., and Myhre, G. (2018). Climate sensitivity estimates -- sensitivity to radiative forcing time series and observational data. *Earth Syst. Dyn.* 9, 879–894. doi:10.5194/esd-9-879-2018.
Bindoff, N. L., Stott, P. A., AchutaRao, K. ., Allen, M. R., Gillett, N., Gutzler, D., et al. (2013). “Detection and Attribution of Climate Change, from Global to Regional,” in *Climate Change 2013: The Physical Science Basis. Contribution of Working Group I to the Fifth Assessment Report of the Intergovernmental Panel on Climate Change*, eds. T. F. Stocker, D. Qin, G.-K. Plattner, M. Tignor, S. K. Allen, J. Boschung, et al. (Cambridge, United Kingdom and New York, NY, USA: Cambridge University Press).
Bintanja, R., Van Oldenborgh, G. J., Drijfhout, S. S., Wouters, B., and Katsman, C. A. (2013). Important role for ocean warming and increased ice-shelf melt in Antarctic sea-ice expansion. *Nat. Geosci.* doi:10.1038/ngeo1767.
Bischoff, T., and Schneider, T. (2014). Energetic constraints on the position of the intertropical convergence zone. *J. Clim.* doi:10.1175/JCLI-D-13-00650.1.
Bisiaux, M. M., Edwards, R., McConnell, J. R., Curran, M. A. J., Van Ommen, T. D., Smith, A. M., et al. (2012). Changes in black carbon deposition to Antarctica from two high-resolution ice core records, 1850–2000 AD. *Atmos. Chem. Phys.* 12, 4107–4115. doi:10.5194/acp-12-4107-2012.
Bitz, C. M., Gent, P. R., Woodgate, R. A., Holland, M. M., and Lindsay, R. (2006). The influence of sea ice on ocean heat uptake in response to increasing CO2. *J. Clim.* doi:10.1175/JCLI3756.1.
Bloch-Johnson, J., Pierrehumbert, R. T., and Abbot, D. S. (2015). Feedback temperature dependence determines the risk of high warming. *Geophys. Res. Lett.* 42, 4973–4980. doi:10.1002/2015GL064240.
Blossey, P. N., Bretherton, C. S., Thornton, J. A., and Virts, K. S. (2018). Locally Enhanced Aerosols Over a Shipping Lane Produce Convective Invigoration but Weak Overall Indirect Effects in Cloud-Resolving Simulations. *Geophys. Res. Lett.* doi:10.1029/2018GL078682.
Bodas-Salcedo, A., Hill, P. G., Furtado, K., Williams, K. D., Field, P. R., Manners, J. C., et al. (2016). Large Contribution of Supercooled Liquid Clouds to the Solar Radiation Budget of the Southern Ocean. *J. Clim.* 29, 4213–4228. doi:10.1175/JCLI-D-15-0564.1.
Bodas-Salcedo, A., Webb, M. J., Bony, S., Chepfer, H., Dufresne, J.-L., Klein, S. A., et al. (2011). COSP: Satellite simulation software for model assessment. *Bull. Am. Meteorol. Soc.* 92, 1023–1043. doi:10.1175/2011BAMS2856.1.
Bodas-Salcedo, A., Williams, K. D., Field, P. R., and Lock, A. P. (2012). The Surface Downwelling Solar Radiation Surplus over the Southern Ocean in the Met Office Model: The Role of Midlatitude Cyclone Clouds. *J. Clim.* 25, 7467–7486. doi:10.1175/JCLI-D-11-00702.1.
Bodman, R. W., and Jones, R. N. (2016). Bayesian estimation of climate sensitivity using observationally constrained simple climate models. *Wiley Interdiscip. Rev. Clim. Chang.* 7, 461–473. doi:10.1002/wcc.397.
Boeke, R. C., and Taylor, P. C. (2016). Evaluation of the Arctic surface radiation budget in CMIP5 models. *J. Geophys. Res.* 121, 8525–8548. doi:10.1002/2016JD025099.
Boer, G. J., Stowasser, M., and Hamilton, K. (2007). Inferring climate sensitivity from volcanic events. *Clim. Dyn.* doi:10.1007/s00382-006-0193-x.
Boer, G. J., and Yu, B. (2003). Dynamical aspects of climate sensitivity. *Geophys. Res. Lett.* doi:10.1029/2002GL016549.
Bonan, D. B., Armour, K. C., Roe, G. H., Siler, N., and Feldl, N. (2018). Geophysical Research Letters Sources of Uncertainty in the Meridional Pattern of Climate Change. *Geophys. Res. Lett.* doi:10.1029/2018GL079429.
Bonan, G. B. (2008). Forests and Climate Change: Forcings, Feedbacks, and the Climate Benefits of Forests. *Science (80-.).* 320, 1444–1449. doi:10.1126/science.1155121.
Bond, T. C., Doherty, S. J., Fahey, D. W., Forster, P. M., Berntsen, T., DeAngelo, B. J., et al. (2013). Bounding the role of black carbon in the climate system: A scientific assessment. *J. Geophys. Res. Atmos.* 118, 5380–5552. doi:10.1002/jgrd.50171.
Bony, S., Colman, R., Kattsov, V. M., Allan, R. P., Bretherton, C. S., Dufresne, J.-L., et al. (2006). How Well do we Understand and Evaluate Climate Change Feedback Processes? *J. Clim.* 19, 3445–3482, doi: 10.1175/JCLI3819.1.
Bony, S., and Dufresne, J. L. (2005). Marine boundary layer clouds at the heart of tropical cloud feedback uncertainties

in climate models. *Geophys. Res. Lett.* 32, L20806. doi:10.1029/2005GL023851.
Bony, S., Stevens, B., Coppin, D., Becker, T., Reed, K. A., Voigt, A., et al. (2016). Thermodynamic control of anvil cloud amount. *Proc. Natl. Acad. Sci.* 113, 8927 LP-8932. doi:10.1073/pnas.1601472113.
Bony, S., Stevens, B., Frierson, D. M. W., Jakob, C., Kageyama, M., Pincus, R., et al. (2015). Clouds, circulation and climate sensitivity. *Nat. Geosci.* 8, 261. Available at: http://dx.doi.org/10.1038/ngeo2398.
Booth, B. B. B., Harris, G. R., Jones, A., Wilcox, L., Hawcroft, M., Carslaw, K. S., et al. (2018). Comments on "Rethinking the Lower Bound on Aerosol Radiative Forcing." *J. Clim.* 31, 9407–9412. doi:10.1175/JCLI-D-17-0369.1.
Bopp, L., Boucher, O., Aumont, O., Belviso, S., Dufresne, J.-L., Pham, M., et al. (2004). Will marine dimethylsulphide emissions alleviate global warming? A model study. *Can. J. Fish. Aquat. Sci.* 61, 826–835.
Boucher, O., Balkanski, Y., Hodnebrog, Ø., Myhre, C. L., Myhre, G., Quaas, J., et al. (2016). Jury is still out on the radiative forcing by black carbon. *Proc. Natl. Acad. Sci. U. S. A.* 113, E5092-3. doi:10.1073/pnas.1607005113.
Boucher, O., Friedlingstein, P., Collins, B., and Shine, K. P. (2009). The indirect global warming potential and global temperature change potential due to methane oxidation. *Environ. Res. Lett.* 4. doi:10.1088/1748-9326/4/4/044007.
Boucher, O., Randall, D., Artaxo, P., Bretherton, C., Feingold, G., Forster, P., et al. (2013). "Clouds and Aerosols," in *Climate Change 2013: The Physical Science Basis. Contribution of Working Group I to the Fifth Assessment Report of the Intergovernmental Panel on Climate Change*, eds. T. F. Stocker, D. Qin, G.-K. Plattner, M. Tignor, S. K. Allen, J. Boschung, et al. (Cambridge, United Kingdom and New York, NY, USA: Cambridge Univeristy Press), 571–657. doi:10.1017/CBO9781107415324.016.
Boyer, T., Domingues, C. M., Good, S. A., Johnson, G. C., Lyman, J. M., Ishii, M., et al. (2016). Sensitivity of Global Upper-Ocean Heat Content Estimates to Mapping Methods, XBT Bias Corrections, and Baseline Climatologies. *J. Clim.* 29, 4817–4842. doi:10.1175/JCLI-D-15-0801.1.
Braconnot, P., Harrison, S. P., Kageyama, M., Bartlein, P. J., Masson-Delmotte, V., Abe-Ouchi, A., et al. (2012). Evaluation of climate models using palaeoclimatic data. *Nat. Clim. Chang.* 2, 417.
Brenguier, J.-L., Pawlowska, H., Schüller, L., Preusker, R., Fischer, J., Fouquart, Y., et al. (2000). Radiative Properties of Boundary Layer Clouds: Droplet Effective Radius versus Number Concentration. *J. Atmos. Sci.* 57, 803–821. doi:10.1175/1520-0469(2000)057<0803:RPOBLC>2.0.CO;2.
Bréon, F.-M., Tanré, D., and Generoso, S. (2002). Aerosol effect on cloud droplet size monitored from satellite. *Science* 295, 834–8. doi:10.1126/science.1066434.
Bretherton, C. S. (2015). Insights into low-latitude cloud feedbacks from high-resolution models. *Philos. Trans. R. Soc. A Math. Phys. Eng. Sci.* 373. doi:10.1098/rsta.2014.0415.
Bretherton, C. S., Blossey, P. N., and Jones, C. R. (2013). Mechanisms of marine low cloud sensitivity to idealized climate perturbations: A single-LES exploration extending the CGILS cases. *J. Adv. Model. Earth Syst.* doi:10.1002/jame.20019.
Bretherton, C. S., Blossey, P. N., and Khairoutdinov, M. (2005). An Energy-Balance Analysis of Deep Convective Self-Aggregation above Uniform SST. *J. Atmos. Sci.* 62, 4273–4292. doi:10.1175/JAS3614.1.
Bretherton, C. S., Blossey, P. N., and Stan, C. (2014). Cloud feedbacks on greenhouse warming in the superparameterized climate model SP-CCSM4. *J. Adv. Model. Earth Syst.* 6, 1185–1204. doi:10.1002/2014MS000355.
Brient, F., and Schneider, T. (2016). Constraints on climate sensitivity from space-based measurements of low-cloud reflection. *J. Clim.* 29, 5821–5835. doi:10.1175/JCLI-D-15-0897.1.
Brient, F., Schneider, T., Tan, Z., Bony, S., Qu, X., and Hall, A. (2016). Shallowness of tropical low clouds as a predictor of climate models' response to warming. *Clim. Dyn.* 47, 433–449. doi:10.1007/s00382-015-2846-0.
Bronselaer, B., Stouffer, R. J., Winton, M., Griffies, S. M., Hurlin, W. J., Russell, J. L., et al. (2018). Change in future climate due to Antarctic meltwater. *Nature* 564, 53–58. doi:10.1038/s41586-018-0712-z.
Brown, P. T., and Caldeira, K. (2017). Greater future global warming inferred from Earth's recent energy budget. *Nature* 552, 45–50. doi:10.1038/nature24672.
Brown, P. T., Li, W., Li, L., and Ming, Y. (2014). Top-of-atmosphere radiative contribution to unforced decadal global temperature variability in climate models. *Geophys. Res. Lett.* 41, 5175–5183. doi:10.1002/2014GL060625.
Brown, P. T., Stolpe, M. B., and Caldeira, K. (2018). Assumptions for emergent constraints. *Nature* 563, E1–E3. doi:10.1038/s41586-018-0638-5.
Bunzel, F., and Schmidt, H. (2013). The Brewer–Dobson Circulation in a Changing Climate: Impact of the Model Configuration. *J. Atmos. Sci.* 70, 1437–1455. doi:10.1175/JAS-D-12-0215.1.
Burls, N. J., and Fedorov, A. V. (2014). What controls the mean east-west sea surface temperature gradient in the equatorial pacific: The role of cloud albedo. *J. Clim.* 27, 2757–2778. doi:10.1175/JCLI-D-13-00255.1.
Burt, M. A., Randall, D. A., and Branson, M. D. (2016). Dark warming. *J. Clim.* doi:10.1175/JCLI-D-15-0147.1.
Byrne, M. P., and O'Gorman, P. A. (2013). Link between land-ocean warming contrast and surface relative humidities in simulations with coupled climate models. *Geophys. Res. Lett.* 40, 5223–5227. doi:10.1002/grl.50971.
Byrne, M. P., and O'Gorman, P. A. (2016). Understanding decreases in land relative humidity with global warming:

Conceptual model and GCM simulations. *J. Clim.* 29, 9045–9061. doi:10.1175/JCLI-D-16-0351.1.
Byrne, M. P., and O'Gorman, P. A. (2018). Trends in continental temperature and humidity directly linked to ocean warming. *Proc. Natl. Acad. Sci.* 115, 4863–4868. doi:10.1073/pnas.1722312115.
Caballero, R., and Huber, M. (2013). State-dependent climate sensitivity in past warm climates and its implications for future climate projections. *Proc. Natl. Acad. Sci.* 110, 14162–14167. doi:10.1073/pnas.1303365110.
Cai, M. (2005). Dynamical amplification of polar warming. *Geophys. Res. Lett.* doi:10.1029/2005GL024481.
Caldwell, P. M., Zelinka, M. D., Taylor, K. E., and Marvel, K. (2016). Quantifying the sources of intermodel spread in equilibrium climate sensitivity. *J. Clim.* 29, 513–524. doi:10.1175/JCLI-D-15-0352.1.
Cane, M. A., Clement, A. C., Kaplan, A., Kushnir, Y., Pozdnyakov, D., Seager, R., et al. (1997). Twentieth-Century Sea Surface Temperature Trends. *Science (80-.).* 275, 957–960. doi:10.1126/science.275.5302.957.
Cao, L., Bala, G., Caldeira, K., Nemani, R., and Ban-Weiss, G. (2010). Importance of carbon dioxide physiological forcing to future climate change. *Proc. Natl. Acad. Sci. U. S. A.* 107. doi:10.1073/pnas.0913000107.
Cao, Y., Liang, S., Chen, X., and He, T. (2015). Assessment of Sea Ice Albedo Radiative Forcing and Feedback over the Northern Hemisphere from 1982 to 2009 Using Satellite and Reanalysis Data. *J. Clim.* 28, 1248–1259. doi:10.1175/JCLI-D-14-00389.1.
Ceppi, P., and Gregory, J. M. (2017). Relationship of tropospheric stability to climate sensitivity and Earth's observed radiation budget. *Proc. Natl. Acad. Sci.* 114, 13126–13131. doi:10.1073/pnas.1714308114.
Ceppi, P., and Hartmann, D. L. (2015). Connections between clouds, radiation, and midlatitude dynamics: A review. *Curr. Clim. Chang. Rep.* 1, 94–102.
Ceppi, P., and Shepherd, T. G. (2017). Contributions of climate feedbacks to changes in atmospheric circulation. *J. Clim.* 30, 9097–9118. doi:10.1175/JCLI-D-17-0189.1.
Cess, R. D., Potter, G. L., Blanchet, J. P., Boer, G. J., Del Genio, A. D., Deque, M., et al. (1990). Intercomparison and interpretation of climate feedback processes in 19 atmospheric general circulation models. *J. Geophys. Res.* 95, 16601–16615. doi:10.1029/JD095iD10p16601.
Cha, S. C., Moon, J. H., and Song, Y. T. (2018). A Recent Shift Toward an El Niño-Like Ocean State in the Tropical Pacific and the Resumption of Ocean Warming. *Geophys. Res. Lett.* 45, 11,885-11,894. doi:10.1029/2018GL080651.
Chadwick, R., Good, P., and Willett, K. (2016). A simple moisture advection model of specific humidity change over land in response to SST warming. *J. Clim.* 29, 7613–7632. doi:10.1175/JCLI-D-16-0241.1.
Chafik, L., Häkkinen, S., England, M. H., Carton, J. A., Nigam, S., Ruiz-Barradas, A., et al. (2016). Global linkages originating from decadal oceanic variability in the subpolar North Atlantic. *Geophys. Res. Lett.* 43, 10,909-10,919. doi:10.1002/2016GL071134.
Charlson, R. J., Lovelock, J. E., Andreae, M. O., and Warren, S. G. (1987). Oceanic phytoplankton, atmospheric sulphur, cloud albedo and climate. *Nature* 326, 655.
Charney, J. G., Arakawa, A., Baker, D. J., Bolin, B., Dickinson, R. E., Goody, R. M., et al. (1979). *Carbon Dioxide and Climate: A Scientific Assessment*. Washington, DC: The National Academies Press doi:10.17226/12181.
Checa-Garcia, R., Hegglin, M. I., Kinnison, D., Plummer, D. A., and Shine, K. P. (2018). Historical Tropospheric and Stratospheric Ozone Radiative Forcing Using the CMIP6 Database. *Geophys. Res. Lett.* 45, 3264–3273. doi:10.1002/2017GL076770.
Chen, J., Liu, Y., Zhang, M., and Peng, Y. (2016a). New understanding and quantification of the regime dependence of aerosol-cloud interaction for studying aerosol indirect effects. *Geophys. Res. Lett.* 43, 1780–1787. doi:10.1002/2016GL067683.
Chen, R., Wood, R., Li, Z., Ferraro, R., and Chang, F.-L. (2008). Studying the vertical variation of cloud droplet effective radius using ship and space-borne remote sensing data. *J. Geophys. Res.* 113, D00A02. doi:10.1029/2007JD009596.
Chen, X., Liang, S., and Cao, Y. (2016b). Satellite observed changes in the Northern Hemisphere snow cover phenology and the associated radiative forcing and feedback between 1982 and 2013. *Environ. Res. Lett.* 11, 84002. doi:10.1088/1748-9326/11/8/084002.
Chen, Y.-C., Christensen, M. W., Stephens, G. L., and Seinfeld, J. H. (2014). Satellite-based estimate of global aerosol–cloud radiative forcing by marine warm clouds. *Nat. Geosci.* 7, 643–646. doi:10.1038/ngeo2214.
Cheng, L., Abraham, J., Hausfather, Z., and Trenberth, K. E. (2019). How fast are the oceans warming? *Science (80-.).* 363, 128–129. doi:10.1126/science.aav7619.
Cheng, L., Trenberth, K. E., Fasullo, J., Boyer, T., Abraham, J., and Zhu, J. (2017). Improved estimates of ocean heat content from 1960 to 2015. *Sci. Adv.* 3. doi:10.1126/sciadv.1601545.
Cheng, L., Trenberth, K. E., Palmer, M. D., Zhu, J., and Abraham, J. P. (2016). Observed and simulated full-depth ocean heat-content changes for 1970--2005. *Ocean Sci.* 12, 925–935. doi:10.5194/os-12-925-2016.
Cheng, W., Chiang, J. C. H., and Zhang, D. (2013). Atlantic meridional overturning circulation (AMOC) in CMIP5 Models: RCP and historical simulations. *J. Clim.* doi:10.1175/JCLI-D-12-00496.1.
Chepfer, H., Noel, V., Winker, D., and Chiriaco, M. (2014). Where and when will we observe cloud changes due to

climate warming? *Geophys. Res. Lett.* 41, 8387–8395.
Cherian, R., Quaas, J., Salzmann, M., and Wild, M. (2014). Pollution trends over Europe constrain global aerosol forcing as simulated by climate models. *Geophys. Res. Lett.* doi:10.1002/2013GL058715.
Ching, J., Zaveri, R. A., Easter, R. C., Riemer, N., and Fast, J. D. (2016). A three-dimensional sectional representation of aerosol mixing state for simulating optical properties and cloud condensation nuclei. *J. Geophys. Res. Atmos.* 121, 5912–5929. doi:10.1002/2015JD024323.
Christensen, M. W., Chen, Y. C., and Stephens, G. L. (2016). Aerosol indirect effect dictated by liquid clouds. *J. Geophys. Res.* 121. doi:10.1002/2016JD025245.
Christensen, M. W., Neubauer, D., Poulsen, C. A., Thomas, G. E., McGarragh, G. R., Povey, A. C., et al. (2017). Unveiling aerosol–cloud interactions – Part 1: Cloud contamination in satellite products enhances the aerosol indirect forcing estimate. *Atmos. Chem. Phys.* 17, 13151–13164. doi:10.5194/acp-17-13151-2017.
Christensen, M. W., and Stephens, G. L. (2011). Microphysical and macrophysical responses of marine stratocumulus polluted by underlying ships: Evidence of cloud deepening. *J. Geophys. Res.* 116, D03201. doi:10.1029/2010JD014638.
Christensen, M. W., Suzuki, K., Zambri, B., and Stephens, G. L. (2014). Ship track observations of a reduced shortwave aerosol indirect effect in mixed-phase clouds. *Geophys. Res. Lett.* 41, 6970–6977. doi:10.1002/2014GL061320.
Chung, E.-S., and Soden, B. J. (2015a). An Assessment of Direct Radiative Forcing, Radiative Adjustments, and Radiative Feedbacks in Coupled Ocean–Atmosphere Models*. *J. Clim.* 28, 4152–4170. doi:10.1175/JCLI-D-14-00436.1.
Chung, E.-S., and Soden, B. J. (2015b). An assessment of methods for computing radiative forcing in climate models. *Environ. Res. Lett.* 10, 074004. doi:10.1088/1748-9326/10/7/074004.
Chung, E.-S., and Soden, B. J. (2018). On the compensation between cloud feedback and cloud adjustment in climate models. *Clim. Dyn.* 50, 1267–1276. doi:10.1007/s00382-017-3682-1.
Chung, E. S., Soden, B. J., and Sohn, B. J. (2010). Revisiting the determination of climate sensitivity from relationships between surface temperature and radiative fluxes. *Geophys. Res. Lett.* doi:10.1029/2010GL043051.
Church, J. a., Clark, P. U., Cazenave, A., Gregory, J. M., Jevrejeva, S., Levermann, A., et al. (2013). "Sea level change," in *Climate Change 2013: The Physical Science Basis. Contribution of Working Group I to the Fifth Assessment Report of the Intergovernmental Panel on Climate Change*, eds. T. F. Stocker, D. Qin, G.-K. Plattner, M. Tignor, S. K. Allen, J. Boschung, et al. (Cambridge, United Kingdom and New York, NY, USA: Cambridge University Press), 1137–1216. doi:10.1017/CB09781107415315.026.
Clement, A. C., Seager, R., Cane, M. A., and Zebiak, S. E. (1996). An ocean dynamical thermostat. *J. Clim.* doi:10.1175/1520-0442(1996)009<2190:AODT>2.0.CO;2.
Coats, S., and Karnauskas, K. B. (2018). A role for the equatorial undercurrent in the ocean dynamical thermostat. *J. Clim.* doi:10.1175/JCLI-D-17-0513.1.
Colbo, K., and Weller, R. A. (2009). Accuracy of the IMET Sensor Package in the Subtropics. *J. Atmos. Ocean. Technol.* 26, 1867–1890. doi:10.1175/2009JTECHO667.1.
Collins, M., Booth, B. B. B., Bhaskaran, B., Harris, G. R., Murphy, J. M., Sexton, D. M. H., et al. (2011a). Climate model errors, feedbacks and forcings: a comparison of perturbed physics and multi-model ensembles. *Clim. Dyn.* 36, 1737–1766. doi:10.1007/s00382-010-0808-0.
Collins, M., Knutti, R., Arblaster, J., Dufresne, J.-L. J.-L., Fichefet, T., Friedlingstein, P., et al. (2013a). "Long-term Climate Change: Projections, Commitments and Irreversibility," in *Climate Change 2013: The Physical Science Basis. Contribution of Working Group I to the Fifth Assessment Report of the Intergovernmental Panel on Climate Change*, eds. T. F. Stocker, D. Qin, G.-K. Plattner, M. Tignor, S. K. Allen, J. Boschung, et al. (Cambridge, United Kingdom and New York, NY, USA: Cambridge University Press), 1029–1136. doi:10.1017/CBO9781107415324.024.
Collins, W. D., Feldman, D. R., Kuo, C., and Nguyen, N. H. (2018). Large regional shortwave forcing by anthropogenic methane informed by Jovian observations. *Sci. Adv.* doi:10.1126/sciadv.aas9593.
Collins, W. J., Bellouin, N., Doutriaux-Boucher, M., Gedney, N., Halloran, P., Hinton, T., et al. (2011b). Development and evaluation of an Earth-System model – HadGEM2. *Geosci. Model Dev.* doi:10.5194/gmd-4-1051-2011.
Collins, W. J., Fry, M. M., Yu, H., Fuglestvedt, J. S., Shindell, D. T., and West, J. J. (2013b). Global and regional temperature-change potentials for near-term climate forcers. *Atmos. Chem. Phys.* doi:10.5194/acp-13-2471-2013.
Colman, R. (2003). A comparison of climate feedbacks in general circulation models. *Clim. Dyn.* 20, 865–873. doi:10.1007/s00382-003-0310-z.
Colman, R. A. (2015). Climate radiative feedbacks and adjustments at the Earth's surface. *J. Geophys. Res.* 120, 3173–3182. doi:10.1002/2014JD022896.
Colman, R., and Hanson, L. (2017). On the relative strength of radiative feedbacks under climate variability and change. *Clim. Dyn.* 49, 2115–2129. doi:10.1007/s00382-016-3441-8.
Colman, R., and McAvaney, B. (2009). Climate feedbacks under a very broad range of forcing. *Geophys. Res. Lett.* 36,

1–5. doi:10.1029/2008GL036268.

Comiso, J. C., Gersten, R. A., Stock, L. V, Turner, J., Perez, G. J., and Cho, K. (2017). Positive Trend in the Antarctic Sea Ice Cover and Associated Changes in Surface Temperature. *J. Clim.* 30, 2251–2267. doi:10.1175/JCLI-D-16-0408.1.

Conover, J. H. (1966). Anomalous Cloud Lines. *J. Atmos. Sci.* 23, 778–785. doi:10.1175/1520-0469(1966)023<0778:ACL>2.0.CO;2.

Coppin, D., and Bony, S. (2015). Physical mechanisms controlling the initiation of convective self-aggregation in a General Circulation Model. *J. Adv. Model. Earth Syst.* 7, 2060–2078. doi:10.1002/2015MS000571.

Covey, C., Abe-Ouchi, A., Boer, G. J., Boville, B. A., Cubasch, U., Fairhead, L., et al. (2000). The seasonal cycle in coupled ocean-atmosphere general circulation models. *Clim. Dyn.* 16, 775–787. doi:10.1007/s003820000081.

Cowtan, K., and Way, R. G. (2014). Coverage bias in the HadCRUT4 temperature series and its impact on recent temperature trends. *Q. J. R. Meteorol. Soc.* 140, 1935–1944. doi:10.1002/qj.2297.

Cox, P. M., Huntingford, C., and Williamson, M. S. (2018a). Emergent constraint on equilibrium climate sensitivity from global temperature variability. *Nature* 553, 319–322. doi:10.1038/nature25450.

Cox, P. M., Williamson, M. S., Nijsse, F. J. M. M., and Huntingford, C. (2018b). Cox et al. reply. *Nature* 563, E10–E15. doi:10.1038/s41586-018-0641-x.

Cronin, T. W., and Wing, A. A. (2017). Clouds, Circulation, and Climate Sensitivity in a Radiative-Convective Equilibrium Channel Model. *J. Adv. Model. Earth Syst.* 9, 2883–2905. doi:10.1002/2017MS001111.

Crook, J. A., and Forster, P. M. (2014). Comparison of surface albedo feedback in climate models and observations. *Geophys. Res. Lett.* 41, 1717–1723. doi:10.1002/2014GL059280.Received.

Crook, J. A., Forster, P. M., and Stuber, N. (2011). Spatial patterns of modeled climate feedback and contributions to temperature response and polar amplification. *J. Clim.* doi:10.1175/2011JCLI3863.1.

Crook, J. A., Jackson, L. S., Osprey, S. M., and Forster, P. M. (2015). A comparison of temperature and precipitation responses to different earth radiation management geoengineering schemes. *J. Geophys. Res.* 120, 9352–9373. doi:10.1002/2015JD023269.

Cui, Z., Gadian, A., Blyth, A., Crosier, J., Crawford, I., Cui, Z., et al. (2014). Observations of the Variation in Aerosol and Cloud Microphysics along the 20°S Transect on 13 November 2008 during VOCALS-REx. *J. Atmos. Sci.* 71, 2927–2943. doi:10.1175/JAS-D-13-0245.1.

Dagan, G., Koren, I., Altaratz, O., and Lehahn, Y. (2018). Shallow convective cloud field lifetime as a key factor for evaluating aerosol effects. *iScience*. doi:10.1016/J.ISCI.2018.11.032.

Dai, A., Luo, D., Song, M., and Liu, J. (2019). Arctic amplification is caused by sea-ice loss under increasing CO2. *Nat. Commun.* 10, 121. doi:10.1038/s41467-018-07954-9.

Dai, H., Yang, H., and Yin, J. (2017). Roles of energy conservation and climate feedback in Bjerknes compensation: a coupled modeling study. *Clim. Dyn.* doi:10.1007/s00382-016-3386-y.

Danabasoglu, G., and Gent, P. R. (2009). Equilibrium climate sensitivity: Is it accurate to use a slab ocean model? *J. Clim.* doi:10.1175/2008JCLI2596.1.

Daniel, J. S., Fleming, E. L., Portmann, R. W., Velders, G. J. M., Jackman, C. H., and Ravishankara, A. R. (2010). Options to accelerate ozone recovery: Ozone and climate benefits. *Atmos. Chem. Phys.* doi:10.5194/acp-10-7697-2010.

Daniel, J. S., Solomon, S., Sanford, T. J., McFarland, M., Fuglestvedt, J. S., and Friedlingstein, P. (2012). Limitations of single-basket trading: lessons from the Montreal Protocol for climate policy. *Clim. Change* 111, 241–248. doi:10.1007/s10584-011-0136-3.

Dekens, P. S., Ravelo, A. C., McCarthy, M. D., and Edwards, C. A. (2008). A 5 million year comparison of Mg/Ca and alkenone paleothermometers. *Geochemistry, Geophys. Geosystems* 9. doi:10.1029/2007GC001931.

Desbruyères, D., McDonagh, E. L., King, B. A., and Thierry, V. (2017). Global and Full-Depth Ocean Temperature Trends during the Early Twenty-First Century from Argo and Repeat Hydrography. *J. Clim.* 30, 1985–1997. doi:10.1175/JCLI-D-16-0396.1.

Deser, C., Knutti, R., Solomon, S., and Phillips, A. S. (2012). Communication of the role of natural variability in future North American climate. doi:10.1038/NCLIMATE1562.

Dessler, A. E. (2011). Cloud variations and the Earth's energy budget. *Geophys. Res. Lett.* doi:10.1029/2011GL049236.

Dessler, A. E. E. (2013). Observations of climate feedbacks over 2000-10 and comparisons to climate models. *J. Clim.* 26, 333–342. doi:10.1175/JCLI-D-11-00640.1.

Dessler, A. E., and Forster, P. M. (2018). An estimate of equilibrium climate sensitivity from interannual variability. *J. Geophys. Res. Atmos.* doi:10.1029/2018JD028481.

Dessler, A. E., Mauritsen, T., and Stevens, B. (2018). The influence of internal variability on Earth's energy balance framework and implications for estimating climate sensitivity. *Atmos. Chem. Phys.* 18, 5147–5155. doi:10.5194/acp-18-5147-2018.

Dessler, A. E., and Zelinka, M. D. (2015). "Climate Feedbacks," in *Encyclopedia of Atmospheric Sciences*, eds. G. R. North, J. Pyle, and F. Zhang, 18–25.

Dewitte, S., and Clerbaux, N. (2018). Decadal Changes of Earth's Outgoing Longwave Radiation. *Remote Sens.* 10. doi:10.3390/rs10101539.

Dietmüller, S., Ponater, M., and Sausen, R. (2014). Interactive ozone induces a negative feedback in CO2-driven climate change simulations. *J. Geophys. Res. Atmos.* 119, 1796–1805. doi:10.1002/2013JD020575.

DiNezio, P. N., Clement, A. C., Vecchi, G. A., Soden, B. J., Kirtman, B. P., and Lee, S.-K. (2009). Climate Response of the Equatorial Pacific to Global Warming. *J. Clim.* 22, 4873–4892. doi:10.1175/2009jcli2982.1.

Doherty, S. J., Grenfell, T. C., Forsstrom, S., Hegg, D. L., Brandt, R. E., and Warren, S. G. (2013). Observed vertical redistribution of black carbon and other insoluble light-absorbing particles in melting snow. *J. Geophys. Res. Atmos* 118, 5553–5569. doi:10.1002/jgrd.50235.

Dolinar, E. K., Dong, X., Xi, B., Jiang, J. H., and Su, H. (2015). Evaluation of CMIP5 simulated clouds and TOA radiation budgets using NASA satellite observations. *Clim. Dyn.* 44, 2229–2247. doi:10.1007/s00382-014-2158-9.

Dong, L., and McPhaden, M. J. (2017). The effects of external forcing and internal variability on the formation of interhemispheric sea surface temperature gradient trends in the Indian Ocean. *J. Clim.* 30, 9077–9095. doi:10.1175/JCLI-D-17-0138.1.

Dong, Y., Armour, K. C., Proistosescu, C., and Battisti, D. S. (2019). Attributing Historical and Future Evolution of Radiative Feedbacks to Regional Warming. *J. Clim.*

Donohoe, A., Armour, K. C., Pendergrass, A. G., and Battisti, D. S. (2014a). Shortwave and longwave radiative contributions to global warming under increasing CO_2. *Proc. Natl. Acad. Sci.* doi:10.1073/pnas.1412190111.

Donohoe, A., and Battisti, D. S. (2011). Atmospheric and Surface Contributions to Planetary Albedo. *J. Clim.* 24, 4402–4418. doi:10.1175/2011JCLI3946.1.

Donohoe, A., and Battisti, D. S. (2012). What determines meridional heat transport in climate models? *J. Clim.* doi:10.1175/JCLI-D-11-00257.1.

Donohoe, A., Marshall, J., Ferreira, D., Armour, K., and Mcgee, D. (2014b). The interannual variability of tropical precipitation and interhemispheric energy transport. *J. Clim.* 27, 3377–3392. doi:10.1175/JCLI-D-13-00499.1.

Donohoe, A., Marshall, J., Ferreira, D., and Mcgee, D. (2013). The relationship between ITCZ location and cross-equatorial atmospheric heat transport: From the seasonal cycle to the last glacial maximum. *J. Clim.* doi:10.1175/JCLI-D-12-00467.1.

Doutriaux-Boucher, M., Webb, M. J., Gregory, J. M., and Boucher, O. (2009). Carbon dioxide induced stomatal closure increases radiative forcing via a rapid reduction in low cloud. *Geophys. Res. Lett.* 36, 1–5. doi:10.1029/2008GL036273.

Douville, H., Ribes, A., Decharme, B., Alkama, R., and Sheffield, J. (2013). Anthropogenic influence on multidecadal changes in reconstructed global evapotranspiration. *Nat. Clim. Chang.* 3, 59–62. doi:10.1038/NCLIMATE1632.

Dowsett, H. J., and Cronin, T. M. (1990). High eustatic sea level during the middle Pliocene:Evidence from the southeastern U.S. Atlantic Coastal Plain. *Geology* 18, 435–438. doi:10.1130/0091-7613(1990)018<0435:HESLDT>2.3.CO;2.

Duan, L., Cao, L., Bala, G., and Caldeira, K. (2018). Comparison of the Fast and Slow Climate Response to Three Radiation Management Geoengineering Schemes. *J. Geophys. Res. Atmos.* 123, 11,980-12,001. doi:10.1029/2018JD029034.

Dubovik, O., Sinyuk, A., Lapyonok, T., Holben, B. N., Mishchenko, M., Yang, P., et al. (2006). Application of spheroid models to account for aerosol particle nonsphericity in remote sensing of desert dust. *J. Geophys. Res.* 111, D11208. doi:10.1029/2005JD006619.

Dufresne, J.-L., and Saint-Lu, M. (2016). Positive feedback in climate: stabilization or runaway, illustrated by a simple experiment. *Bull.~Am.~Meteorol.~Soc.* 97, 755–765. doi:10.1175/BAMS-D-14-00022.1.

Dufresne, J. L., and Bony, S. (2008). An assessment of the primary sources of spread of global warming estimates from coupled atmosphere-ocean models. *J. Clim.* doi:10.1175/2008JCLI2239.1.

Dyke, J., and Kleidon, A. (2010). The maximum entropy production principle: Its theoretical foundations and applications to the earth system. *Entropy*. doi:10.3390/e12030613.

Eastman, R., and Warren, S. G. (2013). 39Yr survey of cloud changes from land stations worldwide 1971-2009: long term trends, relation to aerosols, and expansion of the tropical belt. *J. Clim.* 26, 1286–1303.

Ebmeier, S. K., Sayer, A. M., Grainger, R. G., Mather, T. A., and Carboni, E. (2014). Systematic satellite observations of the impact of aerosols from passive volcanic degassing on local cloud properties. *Atmos. Chem. Phys.* 14, 10601–10618. doi:10.5194/acp-14-10601-2014.

Edwards, M. R., and Trancik, J. E. (2014). Climate impacts of energy technologies depend on emissions timing. *Nat. Clim. Chang.* doi:10.1038/nclimate2204.

Egorova, T., Schmutz, W., Rozanov, E., Shapiro, A. ~I., Usoskin, I., Beer, J., et al. (2018). Revised historical solar irradiance forcing. *\aap* 615, A85. doi:10.1051/0004-6361/201731199.

Elagib, N. A., and Alvi, S. H. (2013). Moderate solar dimming in an accelerating warming climate of Bahrain. *Int. J. Glob. Warm.* 5, 96–107.

Emanuel, K., Wing, A. A., and Vincent, E. M. (2014). Radiative-convective instability. *J. Adv. Model. Earth Syst.* 6, 75–90. doi:10.1002/2013MS000270.

Engel, A., Bönisch, H., Ostermöller, J., Chipperfield, M. P., Dhomse, S., and Jöckel, P. (2018). A refined method for calculating equivalent effective stratospheric chlorine. *Atmos. Chem. Phys.* doi:10.5194/acp-18-601-2018.

England, M. H., Mcgregor, S., Spence, P., Meehl, G. A., Timmermann, A., Cai, W., et al. (2014). Recent intensification of wind-driven circulation in the Pacific and the ongoing warming hiatus. *Nat. Clim. Chang.* 4, 222–227. doi:10.1038/nclimate2106.

Erfani, E., and Burls, N. J. (2019). The Strength of Low-Cloud Feedbacks and Tropical Climate: A CESM Sensitivity Study. *J. Clim.*, JCLI-D-18-0551.1. doi:10.1175/JCLI-D-18-0551.1.

Essery, R., Rutter, N., Pomeroy, J., Baxter, R., Stähli, M., Gustafsson, D., et al. (2009). SNOWMIP2: An Evaluation of Forest Snow Process Simulations. *Bull. Am. Meteorol. Soc.* 90, 1120–1136. doi:10.1175/2009BAMS2629.1.

Etminan, M., Myhre, G., Highwood, E. J., and Shine, K. P. (2016). Radiative forcing of carbon dioxide, methane, and nitrous oxide: A significant revision of the methane radiative forcing. *Geophys. Res. Lett.* doi:10.1002/2016GL071930.

Exarchou, E., Kuhlbrodt, T., Gregory, J. M., and Smith, R. S. (2014). Ocean Heat Uptake Processes: A Model Intercomparison. *J. Clim.* 28, 887–908. doi:10.1175/JCLI-D-14-00235.1.

Fan, J., Wang, Y., Rosenfeld, D., and Liu, X. (2016). Review of Aerosol–Cloud Interactions: Mechanisms, Significance, and Challenges. *J. Atmos. Sci.* 73, 4221–4252. doi:10.1175/JAS-D-16-0037.1.

Fedorov, A. V., Burls, N. J., Lawrence, K. T., and Peterson, L. C. (2015). Tightly linked zonal and meridional sea surface temperature gradients over the past five million years. *Nat. Geosci.* doi:10.1038/ngeo2577.

Fedorov, A. V, Brierley, C. M., Lawrence, K. T., Liu, Z., Dekens, P. S., and Ravelo, A. C. (2013). Patterns and mechanisms of early Pliocene warmth. *Nature* 496, 43. Available at: http://dx.doi.org/10.1038/nature12003.

Feldl, N., Anderson, B. T., and Bordoni, S. (2017). Atmospheric eddies mediate lapse rate feedback and arctic amplification. *J. Clim.* doi:10.1175/JCLI-D-16-0706.1.

Feldl, N., and Bordoni, S. (2016). Characterizing the Hadley circulation response through regional climate feedbacks. *J. Clim.* 29, 613–622. doi:10.1175/JCLI-D-15-0424.1.

Feldl, N., and Roe, G. H. (2013a). Four perspectives on climate feedbacks. *Geophys. Res. Lett.* 40, 4007–4011. doi:10.1002/grl.50711.

Feldl, N., and Roe, G. H. (2013b). The nonlinear and nonlocal nature of climate feedbacks. *J. Clim.* doi:10.1175/JCLI-D-12-00631.1.

Fels, S. B., Mahlman, J. D., Schwarzkopf, M. D., Sinclair, R. W., Fels, S. B., Mahlman, J. D., et al. (1980). Stratospheric Sensitivity to Perturbations in Ozone and Carbon Dioxide: Radiative and Dynamical Response. *J. Atmos. Sci.* 37, 2265–2297. doi:10.1175/1520-0469(1980)037<2265:SSTPIO>2.0.CO;2.

Feng, Y., and Ramanathan, V. (2010). Investigation of aerosol–cloud interactions using a chemical transport model constrained by satellite observations. *Tellus B Chem. Phys. Meteorol.* 62, 69–86. doi:10.1111/j.1600-0889.2009.00444.x.

Feng, Y., Ramanathan, V., and Kotamarthi, V. R. (2013). Brown carbon: a significant atmospheric absorber of solar radiation? *Atmos. Chem. Phys.* 13, 8607–8621. doi:10.5194/acp-13-8607-2013.

Fiedler, S., Stevens, B., Gidden, M., Smith, S. J., Riahi, K., and van Vuuren, D. (2018). First forcing estimates from the future CMIP6 scenarios of anthropogenic aerosol optical properties and an associated Twomey effect. *Geosci. Model Dev. Discuss.*, 1–26. doi:10.5194/gmd-2018-244.

Fiedler, S., Stevens, B., and Mauritsen, T. (2017). On the sensitivity of anthropogenic aerosol forcing to model-internal variability and parameterizing a Twomey effect. *J. Adv. Model. Earth Syst.* 9, 1325–1341. doi:10.1002/2017MS000932.

Fisher, J. B., Melton, F., Middleton, E., Hain, C., Anderson, M., Allen, R., et al. (2017). The future of evapotranspiration: Global requirements for ecosystem functioning, carbon and climate feedbacks, agricultural management, and water resources. *WATER Resour. Res.* 53, 2618–2626. doi:10.1002/2016WR020175.

Flanner, M. G., Shell, K. M., Barlage, M., Perovich, D. K., and Tschudi, M. A. (2011). Radiative forcing and albedo feedback from the {Northern Hemisphere} cryosphere between 1979 and 2008. *Nat. Geosci.* 4, 151–155. doi:10.1038/ngeo1062.

Flanner, M. G., and Zender, C. S. (2006). Linking snowpack microphysics and albedo evolution. *J. Geophys. Res.* 111. doi:10.1029/2005JD006834.

Flannery, B. P. (1984). Energy Balance Models Incorporating Transport of Thermal and Latent Energy. *J. Atmos. Sci.*

Flato, G., Marotzke, J., Abiodun, B., Braconnot, P., Chou, S. C. C., Collins, W., et al. (2013). “Evaluation of Climate Models,” in *Climate Change 2013: The Physical Science Basis. Contribution of Working Group I to the Fifth Assessment Report of the Intergovernmental Panel on Climate Change*, eds. T. F. Stocker, D. Qin, G.-K. Plattner, M. Tignor, S. K. Allen, J. Boschung, et al. (Cambridge University Press, Cambridge, United Kingdom and New York, NY, USA), 741–866. doi:10.1017/CBO9781107415324.020.

Folini, D., and Wild, M. (2015). The effect of aerosols and sea surface temperature on China’s climate in the late

twentieth century from ensembles of global climate simulations. *J. Geophys. Res.* 120, 2261–2279. doi:10.1002/2014JD022851.
Forest, C. E. (2002). Quantifying Uncertainties in Climate System Properties with the Use of Recent Climate Observations. *Science (80-.).* 295, 113–117. doi:10.1126/science.1064419.
Forest, C. E. (2018). Inferred Net Aerosol Forcing Based on Historical Climate Changes: a Review. *Curr. Clim. Chang. Reports* 4, 11–22. doi:10.1007/s40641-018-0085-2.
Forest, C. E., Stone, P. H., and Sokolov, A. P. (2006). Estimated PDFs of climate system properties including natural and anthropogenic forcings. *Geophys. Res. Lett.* 33. doi:10.1029/2005GL023977.
Forest, C. E., Stone, P. H., and Sokolov, A. P. (2008). Constraining climate model parameters from observed 20th century changes. *Tellus A Dyn. Meteorol. Oceanogr.* 60, 911–920. doi:10.1111/j.1600-0870.2008.00346.x.
Forster, et al. (2007). Radiative Forcing of Climate Change, in Climate Change 2007: The Physical Science Basis. Contribution of Working Group I to the Fourth Assessment Report of the Intergovernmental Panel on Climate Change, edited by S. Solomon, D. Qin, M. Manning, Z. Chen, M.
Forster, P. M. (2016). Inference of Climate Sensitivity from Analysis of Earth's Energy Budget. *Annu. Rev. Earth Planet. Sci.* 44, 85–106. doi:10.1146/annurev-earth-060614-105156.
Forster, P. M., Andrews, T., Good, P., Gregory, J. M., Jackson, L. S., and Zelinka, M. (2013). Evaluating adjusted forcing and model spread for historical and future scenarios in the CMIP5 generation of climate models. *J. Geophys. Res. Atmos.* 118, 1139–1150. doi:10.1002/jgrd.50174.
Forster, P. M. D. F., and Gregory, J. M. (2006). The climate sensitivity and its components diagnosed from earth radiation budget data. *J. Clim.* doi:10.1175/JCLI3611.1.
Forster, P. M. de F., and Taylor, K. E. (2006). Climate forcings and climate sensitivities diagnosed from coupled climate model integration. *J. Clim.* 19, 6181–6194. doi:10.1175/JCLI3974.1.
Forster, P. M., Richardson, T., Maycock, A. C., Smith, C. J., Samset, B. H., Myhre, G., et al. (2016). Recommendations for diagnosing effective radiative forcing from climate models for CMIP6. *J. Geophys. Res.* doi:10.1002/2016JD025320.
Forster, P., Ramaswamy, V., Artaxo, P., Berntsen, T., Betts, R., Fahey, D. W., et al. (2007). "Changes in Atmospheric Constituents and in Radiative Forcing," in *Climate Change 2007. The Physical Science Basis*, eds. S. Solomon, D. Qin, M. Manning, Z. Chen, M. Marquis, K. B. Averyt, et al. (United Kingdom: Cambridge University Press). Available at: http://www.ipcc.ch/pdf/assessment-report/ar4/wg1/ar4-wg1-chapter2.pdf.
Foster, G. L., and Rae, J. W. B. (2016). Reconstructing Ocean pH with Boron Isotopes in Foraminifera. *Annu. Rev. Earth Planet. Sci.* 44, 207–237. doi:10.1146/annurev-earth-060115-012226.
Frame, D. J., Booth, B. B. B., Kettleborough, J. A., Stainforth, D. A., Gregory, J. M., Collins, M., et al. (2005). Constraining climate forecasts: The role of prior assumptions. *Geophys. Res. Lett.* 32. doi:10.1029/2004GL022241.
Frame, D. J., Stone, D. A., Stott, P. A., and Allen, M. R. (2006). Alternatives to stabilization scenarios. *Geophys. Res. Lett.* doi:10.1029/2006GL025801.
Fransworth, A., Lunt, D. J., O'Brian, C., Inglis, G. N., Foster, G. L., Markwick, P., et al. Climate sensitivity on geological timescales controlled by non-linear feedbacks and ocean circulation. submitted.
Freud, E., and Rosenfeld, D. (2012). Linear relation between convective cloud drop number concentration and depth for rain initiation. *J. Geophys. Res. Atmos.* 117. doi:10.1029/2011JD016457.
Friedrich, T., Timmermann, A., Tigchelaar, M., Timm, O. E., and Ganopolski, A. (2016). Nonlinear climate sensitivity and its implications for future greenhouse warming. *Sci. Adv.* 2. doi:10.1126/sciadv.1501923.
Frierson, D. M. W., and Hwang, Y. T. (2012). Extratropical influence on ITCZ shifts in slab ocean simulations of global warming. *J. Clim.* doi:10.1175/JCLI-D-11-00116.1.
Frierson, D. M. W., Hwang, Y. T., Fučkar, N. S., Seager, R., Kang, S. M., Donohoe, A., et al. (2013). Contribution of ocean overturning circulation to tropical rainfall peak in the Northern Hemisphere. *Nat. Geosci.* 6, 940–944. doi:10.1038/ngeo1987.
Froelicher, T. L., Sarmiento, J. L., Paynter, D. J., Dunne, J. P., Krasting, J. P., and Winton, M. (2015). Dominance of the Southern Ocean in anthropogenic carbon and heat uptake in CMIP5 models. *J. Clim.* doi:10.1175/JCLI-D-14-00117.1.
Fuglestvedt, J. S., Berntsen, T. K., Godal, O., Sausen, R., Shine, K. P., and Skodvin, T. (2003). Metrics of climate change: Assessing radiative forcing and emission indices. *Clim. Change* 58, 267–331. doi:10.1023/A:1023905326842.
Fyke, J., Sergienko, O., Löfverström, M., Price, S., and Lenaerts, J. T. M. (2018). An Overview of Interactions and Feedbacks Between Ice Sheets and the Earth System. *Rev. Geophys.* 56, 361–408. doi:10.1029/2018RG000600.
Gabric, A. J., Qu, B., Rotstayn, L., and Shephard, J. M. (2013). Global simulations of the impact on contemporary climate of a perturbation to the sea-to-air flux of dimethylsulfide. *Aust. Meteorol. Oceanogr. J.* 63, 365–376.
Gan, C. M., Pleim, J., Mathur, R., Hogrefe, C., Long, C. N., Xing, J., et al. (2014). Assessment of the effect of air pollution controls on trends in shortwave radiation over the United States from 1995 through 2010 from multiple

observation networks. *Atmos. Chem. Phys.* 14, 1701–1715. doi:Doi 10.5194/Acp-14-1701-2014.

Gao, S., Chiu, L. S., and Shie, C.-L. (2013). Trends and variations of ocean surface latent heat flux: Results from GSSTF2c data set. *Geophys. Res. Lett.* 40, 380–385. doi:10.1029/2012GL054620.

Garcia, R. D., Cuevas, E., Garcia, O. E., Cachorro, V. E., Palle, P., Bustos, J. J., et al. (2014). Reconstruction of global solar radiation time series from 1933 to 2013 at the Izana Atmospheric Observatory. *Atmos. Meas. Tech.* 7, 3139–3150. doi:Doi 10.5194/Amt-7-3139-2014.

Gasser, T., Peters, G. P., Fuglestvedt, J. S., Collins, W. J., Shindell, D. T., and Ciais, P. (2017). Accounting for the climate- carbon feedback in emission metrics. *Earth Syst. Dyn.* doi:10.5194/esd-8-235-2017.

Gassó, S. (2008). Satellite observations of the impact of weak volcanic activity on marine clouds. *J. Geophys. Res.* 113, D14S19. doi:10.1029/2007JD009106.

Gebbie, G., and Huybers, P. (2019). The Little Ice Age and 20th Century Deep Pacific Cooling. *Science (80-.).* 363, 70–74. doi:10.1126/science.aar8413.

Geoffroy, O., Saint-Martin, D., Bellon, G., Voldoire, A., Olivié, D. J. L. L., and Tytéca, S. (2013a). Transient Climate Response in a Two-Layer Energy-Balance Model. Part II: Representation of the Efficacy of Deep-Ocean Heat Uptake and Validation for CMIP5 AOGCMs. *J. Clim.* 26, 1859–1876. doi:10.1175/JCLI-D-12-00196.1.

Geoffroy, O., Saint-martin, D., Olivié, D. J. L., Voldoire, A., Bellon, G., and Tytéca, S. (2013b). Transient climate response in a two-layer energy-balance model. Part I: Analytical solution and parameter calibration using CMIP5 AOGCM experiments. *J. Clim.* 26, 1841–1857. doi:10.1175/JCLI-D-12-00195.1.

Geoffroy, O., Saint-Martin, D., and Ribes, A. (2012). Quantifying the sources of spread in climate change experiments. *Geophys. Res. Lett.* 39. doi:10.1029/2012GL054172.

George, R. C., and Wood, R. (2010). Subseasonal variability of low cloud radiative properties over the southeast Pacific Ocean. *Atmos. Chem. Phys.* 10, 4047–4063. doi:10.5194/acp-10-4047-2010.

Gerber, H., and Gerber, H. (1996). Microphysics of Marine Stratocumulus Clouds with Two Drizzle Modes. *J. Atmos. Sci.* 53, 1649–1662. doi:10.1175/1520-0469(1996)053<1649:MOMSCW>2.0.CO;2.

Gettelman, A., Kay, J. E., and Shell, K. M. (2012). The evolution of climate sensitivity and climate feedbacks in the Community Atmosphere Model. *J. Clim.* 25, 1453–1469. doi:10.1175/JCLI-D-11-00197.1.

Ghan, S., Wang, M., Zhang, S., Ferrachat, S., Gettelman, A., Griesfeller, J., et al. (2016). Challenges in constraining anthropogenic aerosol effects on cloud radiative forcing using present-day spatiotemporal variability. *Proc. Natl. Acad. Sci. U. S. A.* 113, 5804–11. doi:10.1073/pnas.1514036113.

Ghimire, B., Williams, C. A., Masek, J., Gao, F., Wang, Z., Schaaf, C., et al. (2014). Global albedo change and radiative cooling from anthropogenic land cover change, 1700 to 2005 based on MODIS, land use harmonization, radiative kernels, and reanalysis. *Geophys. Res. Lett.* doi:10.1002/2014GL061671.

Gillett, N. P., Arora, V. K., Flato, G. M., Scinocca, J. F., and Von Salzen, K. (2012). Improved constraints on 21st-century warming derived using 160 years of temperature observations. *Geophys. Res. Lett.* 39, 1–5. doi:10.1029/2011GL050226.

Gillett, N. P., Arora, V. K., Matthews, D., and Allen, M. R. (2013). Constraining the ratio of global warming to cumulative CO2 emissions using CMIP5 simulations. *J. Clim.* 26, 6844–6858. doi:10.1175/JCLI-D-12-00476.1.

Giorgetta, M. A., Jungclaus, J., Reick, C. H., Legutke, S., Bader, J., Böttinger, M., et al. (2013). Climate and carbon cycle changes from 1850 to 2100 in MPI-ESM simulations for the Coupled Model Intercomparison Project phase 5. *J. Adv. Model. Earth Syst.* 5, 572–597. doi:10.1002/jame.20038.

Gleckler, P. J., Durack, P. J., Stouffer, R. J., Johnson, G. C., and Forest, C. E. (2016). Industrial-era global ocean heat uptake doubles in recent decades. *Nat. Clim. Chang.* 6, 394. Available at: http://dx.doi.org/10.1038/nclimate2915.

Goelzer, H., Huybrechts, P., Loutre, M. F., Goosse, H., Fichefet, T., and Mouchet, A. (2011). Impact of Greenland and Antarctic ice sheet interactions on climate sensitivity. *Clim. Dyn.* 37, 1005–1018. doi:10.1007/s00382-010-0885-0.

Goelzer, H., Nowicki, S., Edwards, T., Beckley, M., Abe-Ouchi, A., Aschwanden, A., et al. (2018). Design and results of the ice sheet model initialisation initMIP-Greenland: An ISMIP6 intercomparison. *Cryosphere* 12, 1433–1460. doi:10.5194/tc-12-1433-2018.

Golaz, J. C., Golaz, J. C., and Levy, H. (2013). Cloud tuning in a coupled climate model: Impact on 20th century warming. *Geophys. Res. Lett.* 40, 2246–2251. doi:10.1002/grl.50232.

Goldner, A., Herold, N., and Huber, M. (2014). Antarctic glaciation caused ocean circulation changes at the Eocene-Oligocene transition. *Nature* 511, 574–577. doi:10.1038/nature13597.

Golledge, N. R., Keller, E. D., Gomez, N., Naughten, K. A., Bernales, J., Trusel, L. D., et al. (2019). Global environmental consequences of twenty-first-century ice-sheet melt. *Nature* 566, 65–72. doi:10.1038/s41586-019-0889-9.

Gong, T., Feldstein, S., and Lee, S. (2017). The role of downward infrared radiation in the recent arctic winter warming trend. *J. Clim.* doi:10.1175/JCLI-D-16-0180.1.

Good, P., Andrews, T., Chadwick, R., Dufresne, J. L., Gregory, J. M., Lowe, J. A., et al. (2016). NonlinMIP contribution to CMIP6: Model intercomparison project for non-linear mechanisms: Physical basis, experimental design and analysis principles (v1.0). *Geosci. Model Dev.* 9, 4019–4028. doi:10.5194/gmd-9-4019-2016.

Good, P., Lowe, J. A., Andrews, T., Wiltshire, A., Chadwick, R., Ridley, J. K., et al. (2015). Nonlinear regional warming with increasing CO2concentrations. *Nat. Clim. Chang.* 5, 138–142. doi:10.1038/nclimate2498.

Goosse, H., Kay, J. E., Armour, K. C., Bodas-Salcedo, A., Chepfer, H., Docquier, D., et al. (2018). Quantifying climate feedbacks in polar regions. *Nat. Commun.* doi:10.1038/s41467-018-04173-0.

Goren, T., and Rosenfeld, D. (2012). Satellite observations of ship emission induced transitions from broken to closed cell marine stratocumulus over large areas. *J. Geophys. Res. Atmos.* 117. doi:10.1029/2012JD017981.

Goren, T., and Rosenfeld, D. (2014). Decomposing aerosol cloud radiative effects into cloud cover, liquid water path and Twomey components in marine stratocumulus. *Atmos. Res.* 138, 378–393. doi:10.1016/J.ATMOSRES.2013.12.008.

Goren, T., and Rosenfeld, D. (2015). Extensive closed cell marine stratocumulus downwind of Europe-A large aerosol cloud mediated radiative effect or forcing? *J. Geophys. Res. Atmos.* 120, 6098–6116. doi:10.1002/2015JD023176.

Grandey, B. S., Rothenberg, D., Avramov, A., Jin, Q., Lee, H. H., Liu, X., et al. (2018). Effective radiative forcing in the aerosol-climate model CAM5.3-MARC-ARG. *Atmos. Chem. Phys.* 18, 15783–15810. doi:10.5194/acp-18-15783-2018.

Grandey, B. S., Stier, P., and Wagner, T. M. (2013). Investigating relationships between aerosol optical depth and cloud fraction using satellite, aerosol reanalysis and general circulation model data. *Atmos. Chem. Phys.* 13, 3177–3184. doi:10.5194/acp-13-3177-2013.

Graversen, R. G., and Burtu, M. (2016). Arctic amplification enhanced by latent energy transport of atmospheric planetary waves. *Q. J. R. Meteorol. Soc.* 142, 2046–2054. doi:10.1002/qj.2802.

Graversen, R. G., Langen, P. L., and Mauritsen, T. (2014). Polar Amplification in CCSM4: Contributions from the Lapse Rate and Surface Albedo Feedbacks. *J. Clim.* 27, 4433–4450. doi:10.1175/JCLI-D-13-00551.1.

Graversen, R. G., and Wang, M. (2009). Polar amplification in a coupled climate model with locked albedo. *Clim. Dyn.* doi:10.1007/s00382-009-0535-6.

Gray, L. J., Rumbold, S. T., and Shine, K. P. (2009). Stratospheric Temperature and Radiative Forcing Response to 11-Year Solar Cycle Changes in Irradiance and Ozone. *J. Atmos. Sci.* doi:10.1175/2009jas2866.1.

Gregory, J. M. (2000). Vertical heat transports in the ocean and their effect on time-dependent climate change. *Clim. Dyn.* doi:10.1007/s003820000059.

Gregory, J. M., and Andrews, T. (2016). Variation in climate sensitivity and feedback parameters during the historical period. *Geophys. Res. Lett.* doi:10.1002/2016GL068406.

Gregory, J. M., Andrews, T., Ceppi, P., Mauritsen, T., and Webb, M. J. How accurately can the climate sensitivity to CO_2 be estimated from historical climate change? submitted.

Gregory, J. M., Andrews, T., and Good, P. (2015). The inconstancy of the transient climate response parameter under increasing CO2. *Philos. Trans. R. Soc. A Math. Phys. Eng. Sci.* 373. doi:10.1098/rsta.2014.0417.

Gregory, J. M., Andrews, T., Good, P., Mauritsen, T., and Forster, P. M. (2016). Small global-mean cooling due to volcanic radiative forcing. *Clim. Dyn.* 47, 3979–3991. doi:10.1007/s00382-016-3055-1.

Gregory, J. M., Dixon, K. W., Stouffer, R. J., Weaver, A. J., Driesschaert, E., Eby, M., et al. (2005). A model intercomparison of changes in the Atlantic thermohaline circulation in response to increasing atmospheric CO2 concentration. *Geophys. Res. Lett.* doi:10.1029/2005GL023209.

Gregory, J. M., Ingram, W. J., Palmer, M. A., Jones, G. S., Stott, P. A., Thorpe, R. B., et al. (2004). A new method for diagnosing radiative forcing and climate sensitivity. *Geophys. Res. Lett.* 31, L03205. doi:10.1029/2003GL018747.

Gregory, J. M., Jones, C. D., Cadule, P., and Friedlingstein, P. (2009). Quantifying carbon cycle feedbacks. *J. Clim.* doi:10.1175/2009JCLI2949.1.

Gregory, J. M., Stouffer, R. J., Raper, S. C. B., Stott, P. A., and Rayner, N. A. (2002). An observationally based estimate of the climate sensitivity. *J. Clim.* 15, 3117–3121. doi:10.1175/1520-0442(2002)015<3117:AOBEOT>2.0.CO;2.

Greve, P., Orlowsky, B., Mueller, B., Sheffield, J., Reichstein, M., and Seneviratne, S. I. (2014). Global assessment of trends in wetting and drying over land (vol 7, pg 716, 2014). *Nat. Geosci.* 7. doi:10.1038/NGEO2274.

Grise, K. M., Polvani, L. M., Tselioudis, G., Wu, Y., and Zelinka, M. D. (2013). The ozone hole indirect effect: Cloud-radiative anomalies accompanying the poleward shift of the eddy-driven jet in the Southern Hemisphere. *Geophys. Res. Lett.* doi:10.1002/grl.50675.

Grise, K. M., Son, S. W., Correa, G. J. P., and Polvani, L. M. (2014). The response of extratropical cyclones in the Southern Hemisphere to stratospheric ozone depletion in the 20th century. *Atmos. Sci. Lett.* doi:10.1002/asl2.458.

Groebner, J., Reda, I., Wacker, S., Nyeki, S., Behrens, K., and Gorman, J. (2014). A new absolute reference for atmospheric longwave irradiance measurements with traceability to SI units. *J. Geophys. Res.* 119, 7083–7090. doi:10.1002/2014JD021630.

Grose, M. R., Gregory, J., Colman, R., and Andrews, T. (2018). What Climate Sensitivity Index Is Most Useful for Projections? *Geophys. Res. Lett.* 45, 1559–1566. doi:10.1002/2017GL075742.

Grosvenor, D. P., Sourdeval, O., Zuidema, P., Ackerman, A., Alexandrov, M. D., Bennartz, R., et al. (2018). Remote Sensing of Droplet Number Concentration in Warm Clouds: A Review of the Current State of Knowledge and Perspectives. *Rev. Geophys.* 56, 409–453. doi:10.1029/2017RG000593.

Gryspeerdt, E., Goren, T., Sourdeval, O., Quaas, J., Mülmenstädt, J., Dipu, S., et al. (2018a). Constraining the aerosol influence on cloud liquid water path. *Atmos. Chem. Phys. Discuss.*, 1–25. doi:10.5194/acp-2018-885.

Gryspeerdt, E., Quaas, J., and Bellouin, N. (2016). Constraining the aerosol influence on cloud fraction. *J. Geophys. Res. Atmos.* 121, 3566–3583. doi:10.1002/2015JD023744.

Gryspeerdt, E., Quaas, J., Ferrachat, S., Gettelman, A., Ghan, S., Lohmann, U., et al. (2017). Constraining the instantaneous aerosol influence on cloud albedo. *Proc. Natl. Acad. Sci. U. S. A.* 114, 4899–4904. doi:10.1073/pnas.1617765114.

Gryspeerdt, E., Sourdeval, O., Quaas, J., Delanoë, J., Krämer, M., and Kühne, P. (2018b). Ice crystal number concentration estimates from lidar–radar satellite remote sensing – Part 2: Controls on the ice crystal number concentration. *Atmos. Chem. Phys.* 18, 14351–14370. doi:10.5194/acp-18-14351-2018.

Gryspeerdt, E., Stier, P., and Grandey, B. S. (2014a). Cloud fraction mediates the aerosol optical depth-cloud top height relationship. *Geophys. Res. Lett.* 41, 3622–3627. doi:10.1002/2014GL059524.

Gryspeerdt, E., Stier, P., and Partridge, D. G. (2014b). Satellite observations of cloud regime development: the role of aerosol processes. *Atmos. Chem. Phys.* 14, 1141–1158. doi:10.5194/acp-14-1141-2014.

Gulev, S. K., and Belyaev, K. (2012). Probability Distribution Characteristics for Surface Air-Sea Turbulent Heat Fluxes over the Global Ocean. *J. Clim.* 25, 184–206. doi:10.1175/2011JCLI4211.1.

Gustafsson, Ö., and Ramanathan, V. (2016). Convergence on climate warming by black carbon aerosols. *Proc. Natl. Acad. Sci.* 113, 4243–4245. doi:10.1073/PNAS.1603570113.

Hall, A. (2004). The role of surface albedo feedback in climate. *J. Clim.* 17, 1550–1568. doi:10.1175/1520-0442(2004)017<1550:TROSAF>2.0.CO;2.

Hall, A., and Qu, X. (2006). Using the current seasonal cycle to constrain snow albedo feedback in future climate change. *Geophys. Res. Lett.* 33, 1–4. doi:10.1029/2005GL025127.

Hansen, J., Lacis, A., Rind, D., Russell, G., Stone, P., Fung, I., et al. (1984). "Climate sensitivity: Analysis of feedback mechanisms," in *AGU Geophysical Monograph*, eds. J. E. Hansen and T. Takahashi (Washington, D. C., D. C.: AGU), 130–163.

Hansen, J., Russell, G., Lacis, A., Fung, I., Rind, D., and Stone, P. (1985). Climate Response Times: Dependence on Climate Sensitivity and Ocean Mixing. *Science (80-.).* 229, 857–859. doi:10.1126/science.229.4716.857.

Hansen, J., Sato, M., Ruedy, R., Nazarenko, L., Lacis, A., Schmidt, G. a., et al. (2005). Efficacy of climate forcings. *J. Geophys. Res.* 110, 1–45. doi:10.1029/2005JD005776.

Hansen, J., Sato, M., Russell, G., Kharecha, P., and A, P. T. R. S. (2013). Climate sensitivity , sea level and atmospheric carbon dioxide Climate sensitivity , sea level and atmospheric carbon dioxide Author for correspondence :

Hargreaves, J. C., and Annan, J. D. (2016). Could the Pliocene constrain the equilibrium climate sensitivity? *Clim. Past* 12, 1591–1599. doi:10.5194/cp-12-1591-2016.

Hargreaves, J. C., Annan, J. D., Yoshimori, M., and Abe-Ouchi, A. (2012). Can the Last Glacial Maximum constrain climate sensitivity? *Geophys. Res. Lett.* 39, 1–5. doi:10.1029/2012GL053872.

Harper, A. B., Wiltshire, A. J., Cox, P. M., Friedlingstein, P., Jones, C. D., Mercado, L. M., et al. (2018). Vegetation distribution and terrestrial carbon cycle in a carbon cycle configuration of JULES4.6 with new plant functional types. *Geosci. Model Dev.* 11, 2857–2873. doi:10.5194/gmd-11-2857-2018.

Harrison, S. P., Bartlein, P. J., Brewer, S., Prentice, I. C., Boyd, M., Hessler, I., et al. (2014). Climate model benchmarking with glacial and mid-Holocene climates. *Clim. Dyn.* 43, 671–688. doi:10.1007/s00382-013-1922-6.

Harrison, S. P., Bartlein, P. J., Izumi, K., Li, G., Annan, J., Hargreaves, J., et al. (2015). Evaluation of CMIP5 palaeo-simulations to improve climate projections. *Nat. Clim. Chang.* 5, 735–743. doi:10.1038/nclimate2649.

Hartmann, D. J., Klein Tank, A. M. G., Rusticucci, M., Alexander, L. V, Brönnimann, S., Charabi, Y. A.-R., et al. (2013). "Observations: Atmosphere and Surface," in *Climate Change 2013: The Physical Science Basis. Contribution of Working Group I to the Fifth Assessment Report of the Intergovernmental Panel on Climate Change*, eds. T. F. Stocker, D. Qin, G.-K. Plattner, M. Tignor, S. K. Allen, J. Boschung, et al. (Cambridge, United Kingdom and New York, NY, USA: Cambridge University Press), 159–254. doi:10.1017/CBO9781107415324.008.

Hartmann, D. L., and Larson, K. (2002). An important constraint on tropical cloud - climate feedback. *Geophys. Res. Lett.* 29, 1951. doi:10.1029/2002GL015835.

Hartmann, D. L., and Michelsen, M. L. (1993). Large-scale effects on regulation of tropical sea surface temperature. *J. Clim.*

Harvey, L. D. D. (2000). *Global warming : the hard science*. Prentice Hall.

Hasselmann, K. (1976). Stochastic climate models Part I. Theory. *Tellus* 28, 473–485. doi:10.1111/j.2153-3490.1976.tb00696.x.

Hassler, B., Young, P. J., Portmann, R. W., Bodeker, G. E., Daniel, J. S., Rosenlof, K. H., et al. (2013). Comparison of three vertically resolved ozone data sets: Climatology, trends and radiative forcings. *Atmos. Chem. Phys.* doi:10.5194/acp-13-5533-2013.

Hawkins, E., and Sutton, R. (2012). Time of emergence of climate signals. *Geophys. Res. Lett.* 39. doi:10.1029/2011GL050087.

Haywood, A. M., Dolan, A. M., Pickering, S. J., Dowsett, H. J., McClymont, E. L., Prescott, C. L., et al. (2013a). On the identification of a Pliocene time slice for data model comparison. *Philos. Trans. R. Soc. London A Math. Phys. Eng. Sci.* 371. doi:10.1098/rsta.2012.0515.

Haywood, A. M., Dowsett, H. J., Dolan, A. M., Rowley, D., Abe-Ouchi, A., Otto-Bliesner, B., et al. (2016). The Pliocene Model Intercomparison Project (PlioMIP) Phase 2: scientific objectives and experimental design. *Clim. Past* 12, 663–675. doi:10.5194/cp-12-663-2016.

Haywood, A. M., Hill, D. J., Dolan, A. M., Otto-Bliesner, B. L., Bragg, F., Chan, W.-L., et al. (2013b). Large-scale features of Pliocene climate: results from the Pliocene Model Intercomparison Project. *Clim. Past* 9, 191–209. doi:10.5194/cp-9-191-2013.

Haywood, J., and Boucher, O. (2000). Estimates of the direct and indirect radiative forcing due to tropospheric aerosols: A review. *Rev. Geophys.* 38, 513. doi:10.1029/1999RG000078.

He, C., Liu, Z., and Hu, A. (2019). The transient response of atmospheric and oceanic heat transports to anthropogenic warming. *Nat. Clim. Chang.* doi:10.1038/s41558-018-0387-3.

He, Y., Wang, K., Zhou, C., and Wild, M. (2018). A Revisit of Global Dimming and Brightening Based on the Sunshine Duration. *Geophys. Res. Lett.* 45, 4281–4289. doi:10.1029/2018GL077424.

Hegerl, G. C., Crowley, T. J., Hyde, W. T., and Frame, D. J. (2006). Climate sensitivity constrained by temperature reconstructions over the past seven centuries. *Nature* 440, 1029. Available at: https://doi.org/10.1038/nature04679.

Hegerl, G. C., and Zwiers, F. (2011). Use of models in detection and attribution of climate change. *WIREs Clim Chang.* 2, 570–591. doi:10.1002/wcc.121.

Heinemann, M., Jungclaus, J. H., and Marotzke, J. (2009). Warm Paleocene/Eocene climate as simulated in ECHAM5/MPI-OM. *Clim. Past* 5, 785–802. doi:10.5194/cp-5-785-2009.

Heinze, C., Eyring, V., Friedlingstein, P., Jones, C., Balkanski, Y., Collins, W., et al. (2018). Climate feedbacks in the Earth system and prospects for their evaluation. *Earth Syst. Dyn. Discuss.* 2018, 1–94. doi:10.5194/esd-2018-84.

Held, I. M., Hemler, R. S., and Ramaswamy, V. (1993). Radiative-Convective Equilibrium with Explicit Two-Dimensional Moist Convection. *J. Atmos. Sci.* 50, 3909–3927. doi:10.1175/1520-0469(1993)050<3909:RCEWET>2.0.CO;2.

Held, I. M., and Shell, K. M. (2012). Using Relative Humidity as a State Variable in Climate Feedback Analysis. 25, 2578–2582. doi:10.1175/JCLI-D-11-00721.1.

Held, I. M., and Soden, B. J. (2006). Robust Responses of the Hydrological Cycle to Global Warming. *J. Clim.* 19, 5686–5699. doi:10.1175/JCLI3990.1.

Held, I. M., Winton, M., Takahashi, K., Delworth, T., Zeng, F., and Vallis, G. K. (2010). Probing the Fast and Slow Components of Global Warming by Returning Abruptly to Preindustrial Forcing. *J. Clim.* 23, 2418–2427. doi:10.1175/2009JCLI3466.1.

Held, I. M., Zhao, M., and Wyman, B. (2007). Dynamic Radiative–Convective Equilibria Using GCM Column Physics. *J. Atmos. Sci.* 64, 228–238. doi:10.1175/JAS3825.11.

Heymsfield, A. J., Kennedy, P. C., Massie, S., Schmitt, C., Wang, Z., Haimov, S., et al. (2010). Aircraft-Induced Hole Punch and Canal Clouds. *Bull. Am. Meteorol. Soc.* 91, 753–766. doi:10.1175/2009BAMS2905.1.

Heyn, I., Block, K., Mülmenstädt, J., Gryspeerdt, E., Kühne, P., Salzmann, M., et al. (2017). Assessment of simulated aerosol effective radiative forcings in the terrestrial spectrum. *Geophys. Res. Lett.* doi:10.1002/2016GL071975.

Hodnebrog, Ø., Etminan, M., Fuglestvedt, J. S., Marston, G., Myhre, G., Nielsen, C. J., et al. (2013). Global warming potentials and radiative efficiencies of halocarbons and related compounds: A comprehensive review. *Rev. Geophys.* doi:10.1002/rog.20013.

Hodnebrog, Ø., Myhre, G., and Samset, B. H. (2014). How shorter black carbon lifetime alters its climate effect. *Nat. Commun.* 5, 5065. doi:10.1038/ncomms6065.

Hoesly, R. M., Smith, S. J., Feng, L., Klimont, Z., Janssens-Maenhout, G., Pitkanen, T., et al. (2018). Historical (1750–2014) anthropogenic emissions of reactive gases and aerosols from the Community Emissions Data System (CEDS). *Geosci. Model Dev.* 11, 369–408. doi:10.5194/gmd-11-369-2018.

Holland, M. M., and Bitz, C. M. (2003). Polar amplification of climate change in coupled models. *Clim. Dyn.* doi:10.1007/s00382-003-0332-6.

Hollis, C. J., and et al. The DeepMIP contribution to PMIP4: methodologies for selection, compilation and analysis of latest Paleocene and early Eocene climate proxy data, incorporating version 0.1 of the DeepMIP database. submitted.

Holloway, C. E., Wing, A. A., Bony, S., Muller, C., Masunaga, H., L'Ecuyer, T. S., et al. (2017). Observing Convective

Aggregation. *Surv. Geophys.* 38, 1199–1236. doi:10.1007/s10712-017-9419-1.
Hopcroft, P. O., and Valdes, P. J. (2015). How well do simulated last glacial maximum tropical temperatures constrain equilibrium climate sensitivity? *Geophys. Res. Lett.* 42, 5533–5539. doi:10.1002/2015GL064903.
Houghton, J. T., Jenkins, G. J., and Ephraums, J. J. (1990). *Climate Change The IPCC Scientific Assessment*. doi:10.1097/MOP.0b013e3283444c89.
Hourdin, F., Mauritsen, T., Gettelman, A., Golaz, J.-C., Balaji, V., Duan, Q., et al. (2017). The Art and Science of Climate Model Tuning. *Bull. Am. Meteorol. Soc.* 98, 589–602. doi:10.1175/BAMS-D-15-00135.1.
Hsu, N. C., Lee, J., Sayer, A. M., Carletta, N., Chen, S.-H., Tucker, C. J., et al. (2017). Retrieving near-global aerosol loading over land and ocean from AVHRR. *J. Geophys. Res. Atmos.* 122, 9968–9989. doi:10.1002/2017JD026932.
Hua, W., Dai, A., and Qin, M. (2018). Contributions of Internal Variability and External Forcing to the Recent Pacific Decadal Variations. *Geophys. Res. Lett.* 45, 7084–7092. doi:10.1029/2018GL079033.
Huang, P., Xie, S. P., Hu, K., Huang, G., and Huang, R. (2013). Patterns of the seasonal response of tropical rainfall to global warming. *Nat. Geosci.* 6, 357–361. doi:10.1038/ngeo1792.
Huang, Y., Xia, Y., and Tan, X. (2017). On the pattern of CO_2 radiative forcing and poleward energy transport. *J. Geophys. Res. Atmos.* doi:10.1002/2017JD027221.
Huang, Y., and Zhang, M. (2014). The implication of radiative forcing and feedback for meridional energy transport. *Geophys. Res. Lett.* doi:10.1002/2013GL059079.
Huber, M., Beyerle, U., and Knutti, R. (2014). Estimating climate sensitivity and future temperature in the presence of natural climate variability. *Geophys. Res. Lett.* 41, 2086–2092. doi:10.1002/2013GL058532.
Huber, M., and Caballero, R. (2011). The early Eocene equable climate problem revisited. *Clim. Past* 7, 603–633. doi:10.5194/cp-7-603-2011.
Huber, M., Mahlstein, I., Wild, M., Fasullo, J., and Knutti, R. (2010). Constraints on Climate Sensitivity from Radiation Patterns in Climate Models. *J. Clim.* 24, 1034–1052. doi:10.1175/2010JCLI3403.1.
Hurtt, G. C., Chini, L. P., Frolking, S., Betts, R. A., Feddema, J., Fischer, G., et al. (2011). Harmonization of land-use scenarios for the period 1500-2100: 600 years of global gridded annual land-use transitions, wood harvest, and resulting secondary lands. *Clim. Change*. doi:10.1007/s10584-011-0153-2.
Huybers, P. (2010). Compensation between Model Feedbacks and Curtailment of Climate Sensitivity. *J. Clim.* 23, 3009–3018. doi:10.1175/2010JCLI3380.1.
Hwang, Y.-T., and Frierson, D. M. W. (2013). Link between the double-Intertropical Convergence Zone problem and cloud biases over the Southern Ocean. *Proc. Natl. Acad. Sci.* doi:10.1073/pnas.1213302110.
Hwang, Y. T., and Frierson, D. M. W. (2010). Increasing atmospheric poleward energy transport with global warming. *Geophys. Res. Lett.* doi:10.1029/2010GL045440.
Hwang, Y. T., Frierson, D. M. W., and Kay, J. E. (2011). Coupling between Arctic feedbacks and changes in poleward energy transport. *Geophys. Res. Lett.* doi:10.1029/2011GL048546.
Imamovic, A., Tanaka, K., Folini, D., and Wild, M. (2016). Global dimming and urbanization: did stronger negative SSR trends collocate with regions of population growth? *Atmos. Chem. Phys.* 16, 2719–2725. doi:10.5194/acp-16-2719-2016.
Ingram, W. (2013). A new way of quantifying GCM water vapour feedback. *Clim. Dyn.* 40, 913–924. doi:10.1007/s00382-012-1294-3.
Jackson, S. C. (2009). Parallel Pursuit of Near-Term and Long-Term Climate Mitigation. *Science (80-.).* 326, 526–527. doi:DOI: 10.1126/science.1177042.
Jahani, B., Dinpashoh, Y., and Wild, M. (2018). Dimming in Iran since the 2000s and the potential underlying causes. *Int. J. Climatol.* 38, 1543–1559. doi:10.1002/joc.5265.
Jethva, H., Torres, O., Waquet, F., Chand, D., and Hu, Y. (2013). How do A-train sensors intercompare in the retrieval of above-cloud aerosol optical depth? A case study-based assessment. *Geophys. Res. Lett.* 41, 186–192. doi:10.1002/2013GL058405.
Jiang, J. H., Su, H., Huang, L., Wang, Y., Massie, S., Zhao, B., et al. (2018). Contrasting effects on deep convective clouds by different types of aerosols. *Nat. Commun.* 9, 3874. doi:10.1038/s41467-018-06280-4.
Jiang, J. H., Su, H., Zhai, C., Perun, V. S., Del Genio, A., Nazarenko, L. S., et al. (2012). Evaluation of cloud and water vapor simulations in CMIP5 climate models using NASA "A-Train" satellite observations. *J. Geophys. Res. Atmos.* 117. doi:10.1029/2011JD017237.
Jiao, C., Flanner, M. G., Balkanski, Y., Bauer, S. E., Bellouin, N., Berntsen, T. K., et al. (2014). An AeroCom assessment of black carbon in Arctic snow and sea ice. *Atmos. Chem. Phys.* 14, 2399–2417. doi:10.5194/acp-14-2399-2014.
Jiménez-de-la-Cuesta, D., and Mauritsen, T. Emergent constraints on Earth's transient- and equilibrium response to doubled CO2 by post-1970s global warming. submitted.
Jing, X., and Suzuki, K. (2018). The Impact of Process-Based Warm Rain Constraints on the Aerosol Indirect Effect. *Geophys. Res. Lett.* 45, 10,729-10,737. doi:10.1029/2018GL079956.

Jo, D. S., Park, R. J., Lee, S., Kim, S.-W., and Zhang, X. (2016). A global simulation of brown carbon: implications for photochemistry and direct radiative effect. *Atmos. Chem. Phys.* 16, 3413–3432. doi:10.5194/acp-16-3413-2016.
Johansson, D. J. A. (2012). Economics- and physical-based metrics for comparing greenhouse gases. *Clim. Change*. doi:10.1007/s10584-011-0072-2.
Johansson, D. J. A., O'Neill, B. C., Tebaldi, C., and Häggström, O. (2015). Equilibrium climate sensitivity in light of observations over the warming hiatus. *Nat. Clim. Chang.* 5, 449. Available at: https://doi.org/10.1038/nclimate2573.
Johnson, G. C., Lyman, J. M., and Loeb, N. G. (2016). Improving estimates of Earth's energy imbalance. *Nat. Clim. Chang.* 6, 639–640. doi:10.1038/nclimate3043.
Johnson, J. S., Regayre, L. A., Yoshioka, M., Pringle, K. J., Lee, L. A., Sexton, D. M. H., et al. (2018). The importance of comprehensive parameter sampling and multiple observations for robust constraint of aerosol radiative forcing. *Atmos. Chem. Phys.* 18, 13031–13053. doi:10.5194/acp-18-13031-2018.
Jonko, A. K., Shell, K. M., Sanderson, B. M., and Danabasoglu, G. (2013). Climate Feedbacks in CCSM3 under Changing CO2 Forcing. Part II: Variation of Climate Feedbacks and Sensitivity with Forcing. *J. Clim.* 26, 2784–2795. doi:10.1175/JCLI-D-12-00479.1.
Joos, F., Roth, R., Fuglestvedt, J. S., Peters, G. P., Enting, I. G., Von Bloh, W., et al. (2013). Carbon dioxide and climate impulse response functions for the computation of greenhouse gas metrics: A multi-model analysis. *Atmos. Chem. Phys.* 13, 2793–2825. doi:10.5194/acp-13-2793-2013.
Joshi, M. M., Lambert, F. H., and Webb, M. J. (2013). An explanation for the difference between twentieth and twenty-first century land-sea warming ratio in climate models. *Clim. Dyn.* 41, 1853–1869. doi:10.1007/s00382-013-1664-5.
Jungclaus, J. H., Bard, E., Baroni, M., Braconnot, P., Cao, J., Chini, L. P., et al. (2017). The PMIP4 contribution to CMIP6 -- Part 3: The last millennium, scientific objective, and experimental design for \hack{\newline} the PMIP4 \textit{past1000} simulations. *Geosci. Model Dev.* 10, 4005–4033. doi:10.5194/gmd-10-4005-2017.
Jungclaus, J. H., Lohmann, K., and Zanchettin, D. (2014). Enhanced 20th century heat transfer to the Arctic simulated in the context of climate variations over the last millennium. *Clim. Past Discuss.* doi:10.5194/cpd-10-2895-2014.
Kablick, G., Fromm, M., Miller, S., Partain, P., Peterson, D., Lee, S., et al. (2018). The Great Slave Lake PyroCb of 5 August 2014: Observations, Simulations, Comparisons With Regular Convection, and Impact on UTLS Water Vapor. *J. Geophys. Res. Atmos.* 123, 12,332-12,352. doi:10.1029/2018JD028965.
Kaercher, B. (2018). Formation and radiative forcing of contrail cirrus. *Nat. Commun.* doi:10.1038/s41467-018-04068-0.
Kahn, R. A., Berkoff, T. A., Brock, C., Chen, G., Ferrare, R. A., Ghan, S., et al. (2017). SAM-CAAM: A Concept for Acquiring Systematic Aircraft Measurements to Characterize Aerosol Air Masses. *Bull. Am. Meteorol. Soc.* 98, 2215–2228. doi:10.1175/BAMS-D-16-0003.1.
Kahnert, M., and Kylling, A. (2004). Radiance and flux simulations for mineral dust aerosols: Assessing the error due to using spherical or spheroidal model particles. *J. Geophys. Res.* 109, D09203. doi:10.1029/2003JD004318.
Kajtar, J. B., Santoso, A., England, M. H., and Cai, W. (2017). Tropical climate variability: interactions across the Pacific, Indian, and Atlantic Oceans. *Clim. Dyn.* 48, 2173–2190. doi:10.1007/s00382-016-3199-z.
Kajtar, J. B., Santoso, A., McGregor, S., England, M. H., and Baillie, Z. (2018). Model under-representation of decadal Pacific trade wind trends and its link to tropical Atlantic bias. *Clim. Dyn.* 50, 1471–1484. doi:10.1007/s00382-017-3699-5.
Kamae, Y., Ogura, T., Watanabe, T., Xie, S. P., and Ueda, H. (2016). Robust cloud feedback over tropical land in a warming climate. *J. Geophys. Res.* 121, 2593–2609. doi:https://doi.org/10.1002/2015JD024525.
Kamae, Y., and Watanabe, M. (2012). On the robustness of tropospheric adjustment in CMIP5 models. *Geophys. Res. Lett.* 39. doi:10.1029/2012GL054275.
Kang, S. M., Held, I. M., Frierson, D. M. W., and Zhao, M. (2008). The response of the ITCZ to extratropical thermal forcing: Idealized slab-ocean experiments with a GCM. *J. Clim.* doi:10.1175/2007JCLI2146.1.
Kang, S. M., and Xie, S. P. (2014). Dependence of climate response on meridional structure of external thermal forcing. *J. Clim.* 27, 5593–5600. doi:10.1175/JCLI-D-13-00622.1.
Kanji, Z. A., Ladino, L. A., Wex, H., Boose, Y., Burkert-Kohn, M., Cziczo, D. J., et al. (2017). Overview of Ice Nucleating Particles. *Meteorol. Monogr.* 58, 1.1-1.33. doi:10.1175/AMSMONOGRAPHS-D-16-0006.1.
Kärcher, B. (2017). Cirrus Clouds and Their Response to Anthropogenic Activities. *Curr. Clim. Chang. Reports* 3, 45–57. doi:10.1007/s40641-017-0060-3.
Karset, I. H. H., Berntsen, T. K., Storelvmo, T., Alterskjær, K., Grini, A., Olivié, D., et al. (2018). Strong impacts on aerosol indirect effects from historical oxidant changes. *Atmos. Chem. Phys.* 18, 7669–7690. doi:10.5194/acp-18-7669-2018.
Kato, S., Rose, F. G., Rutan, D. A., Thorsen, T. J., Loeb, N. G., Doelling, D. R., et al. (2018). Surface Irradiances of Edition 4.0 Clouds and the Earth's Radiant Energy System (CERES) Energy Balanced and Filled (EBAF) Data Product. *J. Clim.* in press.

Kato, S., Xu, K.-M., Wong, T., Loeb, N. G., Rose, F. G., Trenberth, K. E., et al. (2016). Investigation of the Residual in Column-Integrated Atmospheric Energy Balance Using Cloud Objects. *J. Clim.* 29, 7435–7452. doi:10.1175/JCLI-D-15-0782.1.

Kaufman, Y. J., and Koren, I. (2006). Smoke and pollution aerosol effect on cloud cover. *Science* 313, 655–8. doi:10.1126/science.1126232.

Kaufman, Y. J., Koren, I., Remer, L. A., Rosenfeld, D., and Rudich, Y. (2005). The effect of smoke, dust, and pollution aerosol on shallow cloud development over the Atlantic Ocean. *Proc. Natl. Acad. Sci. U. S. A.* 102. doi:10.1073/pnas.0505191102.

Kay, J. E., Holland, M. M., Bitz, C. M., Blanchard-Wrigglesworth, E., Gettelman, A., Conley, A., et al. (2012). The Influence of Local Feedbacks and Northward Heat Transport on the Equilibrium Arctic Climate Response to Increased Greenhouse Gas Forcing. *J. Clim.* 25, 5433–5450. doi:10.1175/JCLI-D-11-00622.1.

Kay, J. E., Medeiros, B., Hwang, Y. T., Gettelman, A., Perket, J., and Flanner, M. G. (2014). Processes controlling Southern Ocean shortwave climate feedbacks in CESM. *Geophys. Res. Lett.* 41, 616–622.

Kennedy-Asser, A. T., Lunt, D. J., Farnsworth, A., and Valdes, P. J. (2019). Assessing Mechanisms and Uncertainty in Modeled Climatic Change at the Eocene-Oligocene Transition. *Paleoceanogr. Paleoclimatology*. doi:10.1029/2018PA003380.

Khairoutdinov, M., and Emanuel, K. (2013). Rotating radiativeconvective equilibrium simulated by a cloudresolving model. *J. Adv. Model. Earth Syst.* 5, 816–825.

Kiehl, J. T., and Shields, C. A. (2013). Sensitivity of the Palaeocene-Eocene Thermal Maximum climate to cloud properties. *Philos. Trans. R. Soc. London A Math. Phys. Eng. Sci.* 371. doi:10.1098/rsta.2013.0093.

Kim, D., Kang, S. M., Shin, Y., and Feldl, N. (2018). Sensitivity of Polar Amplification to Varying Insolation Conditions. *J. Clim.* 31, 4933–4947. doi:10.1175/JCLI-D-17.

Kinne, S. (2019). Aerosol radiative effects with MACv2. *Atmos. Chem. Phys. Discuss.*, 1–50. doi:10.5194/acp-2018-949.

Kirk-Davidoff, D. B. (2009). On the diagnosis of climate sensitivity using observations of fluctuations. Available at: www.atmos-chem-phys.net/9/813/2009/.

Klein, S. A., and Hall, A. (2015). Emergent Constraints for Cloud Feedbacks. *Curr. Clim. Chang. Reports* 1, 276–287. doi:10.1007/s40641-015-0027-1.

Klein, S. A., Hall, A., Norris, J. R., and Pincus, R. (2017). Low-cloud feedbacks from cloud-controlling factors: A review. *Surv. Geophys.* 38, 1307–1329. doi:https://doi.org/10.1007/s10712-017-9433-3.

Klein, S. A., Zhang, Y., Zelinka, M. D., Pincus, R., Boyle, J., and Gleckler, P. J. (2013). Are climate model simulations of clouds improving? An evaluation using the ISCCP simulator. *J. Geophys. Res. Atmos.* 118, 1329–1342. doi:10.1002/jgrd.50141.

Klocke, D., Pincus, R., and Quaas, J. (2011). On constraining estimates of climate sensitivity with present-day observations through model weighting. *J. Clim.* 24, 6092–6099. doi:10.1175/2011JCLI4193.1.

Knutson, T. R., and Manabe, S. (1995). Time-mean response over the tropical Pacific to increased CO_2 in a coupled ocean atmosphere model. *J. Clim.* doi:10.1175/1520-0442(1995)008<2181:TMROTT>2.0.CO;2.

Knutti, R., and Hegerl, G. C. (2008). The equilibrium sensitivity of the Earth's temperature to radiation changes. *Nat. Geosci.* 1, 735. doi:10.1038/ngeo337.

Knutti, R., Joos, F., Müller, S. A., Plattner, G. K., and Stocker, T. F. (2005). Probabilistic climate change projections for CO_2 stabilization profiles. *Geophys. Res. Lett.* 32, 1–4. doi:10.1029/2005GL023294.

Knutti, R., Masson, D., and Gettelman, A. (2013). Climate model genealogy: Generation CMIP5 and how we got there. *Geophys. Res. Lett.* 40, 1194–1199. doi:10.1002/grl.50256.

Knutti, R., Meehl, G. A., Allen, M. R., and Stainforth, D. A. (2006). Constraining Climate Sensitivity from the Seasonal Cycle in Surface Temperature. *J. Clim.* 19, 4224–4233. doi:10.1175/JCLI3865.1.

Knutti, R., and Rugenstein, M. A. A. (2015). Feedbacks, climate sensitivity and the limits of linear models. *Philos. Trans. R. Soc. A Math. Phys. Eng. Sci.* 373, 20150146. doi:10.1098/rsta.2015.0146.

Knutti, R., Rugenstein, M. A. A., and Hegerl, G. C. (2017). Beyond equilibrium climate sensitivity. *Nat. Geosci.* 10, 727–736. doi:10.1038/NGEO3017.

Knutti, R., Stocker, T. F., Joos, F., and Plattner, G.-K. (2002). Constraints on radiative forcing and future climate change from observations and climate model ensembles. *Nature* 416, 719–723. doi:10.1038/416719a.

Koenigk, T., and Brodeau, L. (2014). Ocean heat transport into the Arctic in the twentieth and twenty-first century in EC-Earth. *Clim. Dyn.* doi:10.1007/s00382-013-1821-x.

Köhler, P., De Boer, B., Von Der Heydt, A. S., Stap, L. B., and Van De Wal, R. S. W. (2015). On the state dependency of the equilibrium climate sensitivity during the last 5 million years. *Clim. Past* 11, 1801–1823. doi:10.5194/cp-11-1801-2015.

Köhler, P., Knorr, G., Stap, L. B., Ganopolski, A., De Boer, B., Van De Wal, R. S. W., et al. (2018). The Effect of Obliquity-Driven Changes on Paleoclimate Sensitivity During the Late Pleistocene. *Geophys. Res. Lett.* 45. doi:10.1029/2018GL077717.

Köhler, P., Stap, L. B., von der Heydt, A. S., de Boer, B., Van De Wal, R. S. W., and Bloch-Johnson, J. (2017). A state-dependent quantification of climate sensitivity based on paleo data of the last 2.1 million years. *Paleoceanography*, 1–13. doi:10.1002/2017PA003190.
Kohyama, T., Hartmann, D. L., and Battisti, D. S. (2017). La Niña-like mean-state response to global warming and potential oceanic roles. *J. Clim.* 30, 4207–4225. doi:10.1175/JCLI-D-16-0441.1.
Kok, J. F., Ridley, D. A., Zhou, Q., Miller, R. L., Zhao, C., Heald, C. L., et al. (2017). Smaller desert dust cooling effect estimated from analysis of dust size and abundance. *Nat. Geosci.* 10, 274–278. doi:10.1038/ngeo2912.
Kok, J. F., Ward, D. S., Mahowald, N. M., and Evan, A. T. (2018). Global and regional importance of the direct dust-climate feedback. *Nat. Commun.* 9, 241.
Konsta, D., Dufresne, J.-L., Chepfer, H., Idelkadi, A., and Cesana, G. (2015). Use of A-train satellite observations (CALIPSO–PARASOL) to evaluate tropical cloud properties in the LMDZ5 GCM. *Clim. Dyn.* 47, 1263–1284. doi:10.1007/s00382-016-3050-6.
Konwar, M., Maheskumar, R. S., Kulkarni, J. R., Freud, E., Goswami, B. N., and Rosenfeld, D. (2012). Aerosol control on depth of warm rain in convective clouds. *J. Geophys. Res. Atmos.* 117, n/a-n/a. doi:10.1029/2012JD017585.
Köppen, W., and Geiger, R. (1936). Das Geographische System der Klimate. *Handb. der Klimatologie*, 7–30. doi:10.3354/cr01204.
Koren, I., Feingold, G., and Remer, L. A. (2010). The invigoration of deep convective clouds over the Atlantic: aerosol effect, meteorology or retrieval artifact? *Atmos. Chem. Phys.* 10, 8855–8872. doi:10.5194/acp-10-8855-2010.
Koren, I., Kaufman, Y. J., Rosenfeld, D., Remer, L. A., and Rudich, Y. (2005). Aerosol invigoration and restructuring of Atlantic convective clouds. *Geophys. Res. Lett.* 32, n/a-n/a. doi:10.1029/2005GL023187.
Kostov, Y., Armour, K. C., and Marshall, J. (2014). Impact of the Atlantic meridional overturning circulation on ocean heat storage and transient climate change. *Geophys. Res. Lett.* doi:10.1002/2013GL058998.
Kostov, Y., Ferreira, D., Armour, K. C., and Marshall, J. (2018). Contributions of Greenhouse Gas Forcing and the Southern Annular Mode to Historical Southern Ocean Surface Temperature Trends. *Geophys. Res. Lett.* doi:10.1002/2017GL074964.
Kostov, Y., Marshall, J., Hausmann, U., Armour, K. C., Ferreira, D., and Holland, M. M. (2017). Fast and slow responses of Southern Ocean sea surface temperature to SAM in coupled climate models. *Clim. Dyn.* doi:10.1007/s00382-016-3162-z.
Krasting, J. P., Stouffer, R. J., Griffies, S. M., Hallberg, R. W., Malyshev, S. L., Samuels, B. L., et al. (2018). Role of Ocean Model Formulation in Climate Response Uncertainty. *J. Clim.* doi:10.1175/JCLI-D-18-0035.1.
Kretzschmar, J., Salzmann, M., Mülmenstädt, J., Boucher, O., and Quaas, J. (2017). Comment on "Rethinking the Lower Bound on Aerosol Radiative Forcing." *J. Clim.* 30, 6579–6584. doi:10.1175/JCLI-D-16-0668.1.
Kubota, M., Iwabe, N., Cronin, M. F., and Tomita, H. (2008). Surface heat fluxes from the NCEP/NCAR and NCEP/DOE reanalyses at the Kuroshio Extension Observatory buoy site. *J. Geophys. Res.* 113. doi:10.1029/2007JC004338.
Kucharski, F., Kang, I.-S. S., Farneti, R., and Feudale, L. (2011). Tropical Pacific response to 20th century Atlantic warming. *Geophys. Res. Lett.* 38, n/a-n/a. doi:10.1029/2010GL046248.
Kucharski, F., No, H.-H., King, M. P., Ikram, F., Mogensen, K., Molteni, F., et al. (2015). Atlantic forcing of Pacific decadal variability. *Clim. Dyn.* 46, 2337–2351. doi:10.1007/s00382-015-2705-z.
Kucharski, F., Syed, F. S., Burhan, A., Farah, I., and Gohar, A. (2014). Tropical Atlantic influence on Pacific variability and mean state in the twentieth century in observations and CMIP5. *Clim. Dyn.* 44, 881–896. doi:10.1007/s00382-014-2228-z.
Kuhlbrodt, T., Gregory, J. M., and Shaffrey, L. C. (2015). A process-based analysis of ocean heat uptake in an AOGCM with an eddy-permitting ocean component. *Clim. Dyn.* 45, 3205–3226. doi:10.1007/s00382-015-2534-0.
Kulmala, M., Suni, T., Lehtinen, K. E. J., Dal Maso, M., Boy, M., Reissell, A., et al. (2004). A new feedback mechanism linking forests, aerosols, and climate. *Atmos. Chem. Phys.* 4, 557–562. doi:10.5194/acp-4-557-2004.
Kummer, J. R., and Dessler, A. E. (2014). The impact of forcing efficacy on the equilibrium climate sensitivity. *Geophys. Res. Lett.* 41, 3565–3568. doi:10.1002/2014GL060046.
Kutzbach, J. E., He, F., Vavrus, S. J., and Ruddiman, W. F. (2013). The dependence of equilibrium climate sensitivity on climate state: Applications to studies of climates colder than present. *Geophys. Res. Lett.* 40, 3721–3726. doi:10.1002/grl.50724.
L'Ecuyer, T. S., Beaudoing, H. K., Rodell, M., Olson, W., Lin, B., Kato, S., et al. (2015). The Observed State of the Energy Budget in the Early Twenty-First Century. *J. Clim.* 28, 8319–8346. doi:10.1175/Jcli-D-14-00556.1.
Lacagnina, C., Hasekamp, O. P., and Torres, O. (2017). Direct radiative effect of aerosols based on PARASOL and OMI satellite observations. *J. Geophys. Res. Atmos.* 122, 2366–2388. doi:10.1002/2016JD025706.
Larson, E. J. L., and Portmann, R. W. (2016). A temporal kernel method to compute effective radiative forcing in CMIP5 transient simulations. *J. Clim.* doi:10.1175/JCLI-D-15-0577.1.
Le Bris, K., DeZeeuw, J., Godin, P. J., and Strong, K. (2018). Infrared absorption cross-sections, radiative efficiency and global warming potential of HFC-43-10mee. *J. Mol. Spectrosc.* doi:10.1016/j.jms.2017.06.004.

Le Bris, K., and Graham, L. (2014). Quantitative comparisons of absorption cross-section spectra and integrated intensities of HFC-143a. *J. Quant. Spectrosc. Radiat. Transf.* doi:10.1016/j.jqsrt.2014.09.005.

Lean, J. L. (2018). Estimating Solar Irradiance Since 850 CE. *Earth Sp. Sci.* 5, 133–149. doi:10.1002/2017EA000357.

Lean, J. L., Rottman, G. J., Kyle, H. L., Woods, T. N., Hickey, J. R., and Puga, L. C. (1997). Detection and parameterization of variations in solar mid- and near-ultraviolet radiation (200-400 nm). *J. Geophys. Res. Atmos.* doi:10.1029/97JD02092.

Lean, J., Rottman, G., Harder, J., and Kopp, G. (2005). "SORCE contributions to new understanding of global change and solar variability," in *The Solar Radiation and Climate Experiment (SORCE): Mission Description and Early Results* doi:10.1007/0-387-37625-9_3.

Lebo, Z. J., and Feingold, G. (2014). On the relationship between responses in cloud water and precipitation to changes in aerosol. *Atmos. Chem. Phys.* 14, 11817–11831. doi:10.5194/acp-14-11817-2014.

Lebsock, M. D., Stephens, G. L., and Kummerow, C. (2008). Multisensor satellite observations of aerosol effects on warm clouds. *J. Geophys. Res.* 113, D15205. doi:10.1029/2008JD009876.

Lee, S.-S., Feingold, G., Chuang, P. Y., Lee, S.-S., Feingold, G., and Chuang, P. Y. (2012). Effect of Aerosol on Cloud–Environment Interactions in Trade Cumulus. *J. Atmos. Sci.* 69, 3607–3632. doi:10.1175/JAS-D-12-026.1.

Lee, S. (2014). A theory for polar amplification from a general circulation perspective. *Asia-Pacific J. Atmos. Sci.* doi:10.1007/s13143-014-0024-7.

Lee, S., Gong, T., Feldstein, S. B., Screen, J. A., and Simmonds, I. (2017). Revisiting the Cause of the 1989–2009 Arctic Surface Warming Using the Surface Energy Budget: Downward Infrared Radiation Dominates the Surface Fluxes. *Geophys. Res. Lett.* doi:10.1002/2017GL075375.

Lee, S., Gong, T., Johnson, N., Feldstein, S. B., and Pollard, D. (2011). On the possible link between tropical convection and the northern hemisphere arctic surface air temperature change between 1958 and 2001. *J. Clim.* doi:10.1175/2011JCLI4003.1.

Lembo, V., Folini, D., Wild, M., and Lionello, P. (2019). Inter-hemispheric differences in energy budgets and cross-equatorial transport anomalies during the 20th century. *Clim. Dyn.* doi:10.1007/s00382-018-4572-x.

Levasseur, A., Cavalett, O., Fuglestvedt, J. S., Gasser, T., Johansson, D. J. A., Jørgensen, S. V., et al. (2016). Enhancing life cycle impact assessment from climate science: Review of recent findings and recommendations for application to LCA. *Ecol. Indic.* doi:10.1016/j.ecolind.2016.06.049.

Lewis, N., and Curry, J. A. (2015). The implications for climate sensitivity of AR5 forcing and heat uptake estimates. *Clim. Dyn.* 45, 1009–1023. doi:10.1007/s00382-014-2342-y.

Lewis, N., Curry, J., Lewis, N., and Curry, J. (2018). The impact of recent forcing and ocean heat uptake data on estimates of climate sensitivity. *J. Clim.*, JCLI-D-17-0667.1. doi:10.1175/JCLI-D-17-0667.1.

Li, C., von Storch, J. S., and Marotzke, J. (2013a). Deep-ocean heat uptake and equilibrium climate response. *Clim. Dyn.* 40, 1071–1086. doi:10.1007/s00382-012-1350-z.

Li, J.-L. F., Waliser, D. E., Stephens, G., Lee, S., L'Ecuyer, T., Kato, S., et al. (2013b). Characterizing and understanding radiation budget biases in CMIP3/CMIP5 GCMs, contemporary GCM, and reanalysis. *J. Geophys. Res.* 118, 8166–8184. doi:10.1002/jgrd.50378.

Li, J., Jian, B., Huang, J., Hu, Y., Zhao, C., Kawamoto, K., et al. (2018a). Long-term variation of cloud droplet number concentrations from space-based Lidar. *Remote Sens. Environ.* 213, 144–161. doi:10.1016/J.RSE.2018.05.011.

Li, X., Xie, S.-P. P., Gille, S. T., and Yoo, C. (2016). Atlantic-induced pan-tropical climate change over the past three decades. *Nat. Clim. Chang.* 6, 275–279. doi:10.1038/nclimate2840.

Li, Y., Han, W., and Zhang, L. (2017). Enhanced Decadal Warming of the Southeast Indian Ocean During the Recent Global Surface Warming Slowdown. *Geophys. Res. Lett.* 44, 9876–9884. doi:10.1002/2017GL075050.

Li, Y., Thompson, D. W. J., Bony, S., and Merlis, T. M. (2018b). Thermodynamic Control on the Poleward Shift of the Extratropical Jet in Climate Change Simulations: The Role of Rising High Clouds and Their Radiative Effects. *J. Clim.* 32, 917–934. doi:10.1175/JCLI-D-18-0417.1.

Libardoni, A. G., and Forest, C. E. (2011). Sensitivity of distributions of climate system properties to the surface temperature dataset. *Geophys. Res. Lett.* 38. doi:10.1029/2011GL049431.

Lin, G., Penner, J. E., Flanner, M. G., Sillman, S., Xu, L., and Zhou, C. (2014). Radiative forcing of organic aerosol in the atmosphere and on snow: Effects of SOA and brown carbon. *J. Geophys. Res. Atmos.* 119, 7453–7476. doi:10.1002/2013JD021186.

Lindzen, R. S., Chou, M. D., and Hou, A. Y. (2001). Does the Earth Have an Adaptive Infrared Iris? *Bull. Am. Meteorol. Soc.* 82, 417–432. doi:10.1175/1520-0477(2001)082<0417:DTEHAA>2.3.CO;2.

Liu, C., Allan, R. P., Berrisford, P., Mayer, M., Hyder, P., Loeb, N., et al. (2015). Combining satellite observations and reanalysis energy transports to estimate global net surface energy fluxes 1985-2012. *J. Geophys. Res.* 120, 9374–9389. doi:10.1002/2015JD023264.

Liu, C., Allan, R. P., Mayer, M., Hyder, P., Loeb, N. G., Roberts, C. D., et al. (2017a). Evaluation of satellite and reanalysis-based global net surface energy flux and uncertainty estimates. *J. Geophys. Res.* 122, 6250–6272. doi:10.1002/2017JD026616.

Liu, C., and Barnes, E. A. (2015). Extrememoisture transport into the Arctic linked to Rossby wave breaking. *J. Geophys. Res.* 120, 3774–3788. doi:10.1002/2014JD022796.

Liu, W., Lu, J., Xie, S. P., and Fedorov, A. (2018). Southern Ocean Heat Uptake, redistribution, and storage in a warming climate: The role of meridional overturning circulation. *J. Clim.* doi:10.1175/JCLI-D-17-0761.1.

Liu, W., Xie, S. P., Liu, Z., and Zhu, J. (2017b). Overlooked possibility of a collapsed atlantic meridional overturning circulation in warming climate. *Sci. Adv.* doi:10.1126/sciadv.1601666.

Liu, Y., Hallberg, R., Sergienko, O., Samuels, B. L., Harrison, M., and Oppenheimer, M. (2017c). Climate response to the meltwater runoff from Greenland ice sheet: evolving sensitivity to discharging locations. *Clim. Dyn.* doi:10.1007/s00382-017-3980-7.

Liu, Z., and Huang, B. (1997). A coupled theory of tropical climatology: Warm pool, cold tongue, and walker circulation. *J. Clim.* 10, 1662–1679. doi:10.1175/1520-0442(1997)010<1662:ACTOTC>2.0.CO;2.

Liu, Z., Vavrus, S., He, F., Wen, N., and Zhong, Y. (2005). Rethinking Tropical Ocean Response to Global Warming: The Enhanced Equatorial Warming*. *J. Clim.* 18, 4684–4700. doi:10.1175/jcli3579.1.

Lloyd, G., Choularton, T. W., Bower, K. N., Gallagher, M. W., Crosier, J., O'Shea, S., et al. (2018). In situ measurements of cloud microphysical and aerosol properties during the break-up of stratocumulus cloud layers in cold air outbreaks over the North Atlantic. *Atmos. Chem. Phys.* 18, 17191–17206. doi:10.5194/acp-18-17191-2018.

Loeb, N. G., Doelling, D. R., Wang, H. L., Su, W. Y., Nguyen, C., Corbett, J. G., et al. (2018a). Clouds and the Earth's Radiant Energy System (CERES) Energy Balanced and Filled (EBAF) Top-of-Atmosphere (TOA) Edition-4.0 Data Product. *J. Clim.* 31, 895–918. doi:10.1175/Jcli-D-17-0208.1.

Loeb, N. G., Doelling, D. R., Wang, H., Su, W., and Kato, S. (2018b). Surface irradiances of edition 4.0 Clouds and the Earth's Radiant Energy System (CERES) Energy Balanced and Filled (EBAF) data product. *J. Clim.* 31, 4501–4527. doi:10.1175/JCLI-D-17-0523.1.

Loeb, N. G., Lyman, J. M., Johnson, G. C., Allan, R. P., Doelling, D. R., Wong, T., et al. (2012). Observed changes in top-of-the-atmosphere radiation and upper-ocean heating consistent within uncertainty. *Nat. Geosci.* doi:10.1038/ngeo1375.

Loeb, N. G., Rutan, D. A., Kato, S., and Wang, W. (2014). Observing Interannual Variations in Hadley Circulation Atmospheric Diabatic Heating and Circulation Strength. *J. Clim.* 27, 4139–4158. doi:10.1175/JCLI-D-13-00656.1.

Loeb, N. G., Thorsen, T. J., Norris, J. R., Wang, H., and Su, W. (2018c). Changes in Earth's Energy Budget during and after the "Pause" in Global Warming: An Observational Perspective. doi:10.3390/cli6030062.

Loeb, N. G., Wang, H., Cheng, A., Kato, S., Fasullo, J. T., Xu, K.-M., et al. (2016). Observational constraints on atmospheric and oceanic cross-equatorial heat transports: revisiting the precipitation asymmetry problem in climate models. *Clim. Dyn.* 46, 3239–3257. doi:10.1007/s00382-015-2766-z.

Longman, R. J., Giambelluca, T. W., Alliss, R. J., and Barnes, M. L. (2014). Temporal solar radiation change at high elevations in Hawai'i. *J. Geophys. Res.* 119, 6022–6033. doi:Doi 10.1002/2013jd021322.

Lu, J., Vecchi, G. A., and Reichler, T. (2007). Expansion of the Hadley cell under global warming. *Geophys. Res. Lett.* 34. doi:10.1029/2006GL028443.

Lu, P., Zhang, H., and Wu, J. (2017). Inhomogeneous radiative forcing of NF3. *Atmosphere (Basel).* 8. doi:10.3390/atmos8010017.

Lund, M. T., Myhre, G., Haslerud, A. S., Skeie, R. B., Griesfeller, J., Platt, S. M., et al. (2018a). Concentrations and radiative forcing of anthropogenic aerosols from 1750 to 2014 simulated with the Oslo CTM3 and CEDS emission inventory. *Geosci. Model Dev.* 11, 4909–4931. doi:10.5194/gmd-11-4909-2018.

Lund, M. T., Samset, B. H., Skeie, R. B., Watson-Parris, D., Katich, J. M., Schwarz, J. P., et al. (2018b). Short Black Carbon lifetime inferred from a global set of aircraft observations. *npj Clim. Atmos. Sci.* 1, 31. doi:10.1038/s41612-018-0040-x.

Lunt, D. J., Haywood, A. M., Schmidt, G. A., Salzmann, U., Valdes, P. J., and Dowsett, H. J. (2009). Earth system sensitivity inferred from Pliocene modelling and data. *Nat. Geosci.* 3, 60.

Luo, J. J., Wang, G., and Dommenget, D. (2018). May common model biases reduce CMIP5's ability to simulate the recent Pacific La Niña-like cooling? *Clim. Dyn.* 50, 1335–1351. doi:10.1007/s00382-017-3688-8.

Luo, Y., Lu, J., Liu, F., and Garuba, O. (2017). The role of ocean dynamical thermostat in delaying the El Niño-Like response over the equatorial Pacific to climate warming. *J. Clim.* 30, 2811–2827. doi:10.1175/JCLI-D-16-0454.1.

Luo, Y., Lu, J., Liu, F., and Liu, W. (2015). Understanding the El Niño-like oceanic response in the tropical Pacific to global warming. *Clim. Dyn.* doi:10.1007/s00382-014-2448-2.

Lutsko, N. J., and Takahashi, K. (2018). What Can the Internal Variability of CMIP5 Models Tell Us about Their Climate Sensitivity? *J. Clim.* 31, 5051–5069. doi:10.1175/JCLI-D-17-0736.1.

Luyssaert, S., Jammet, M., Stoy, P. C., Estel, S., Pongratz, J., Ceschia, E., et al. (2014). Land management and land-cover change have impacts of similar magnitude on surface temperature. *Nat. Clim. Chang.* doi:10.1038/nclimate2196.

Lyman, J. M., Good, S. A., Gouretski, V. V., Ishii, M., Johnson, G. C., Palmer, M. D., et al. (2010). Robust warming of the global upper ocean. *Nature* 465, 334–337. doi:10.1038/nature09043.
Lyman, J. M., and Johnson, G. C. (2008). Estimating Annual Global Upper-Ocean Heat Content Anomalies despite Irregular In Situ Ocean Sampling. *J. Clim.* 21, 5629–5641. doi:10.1175/2008JCLI2259.1.
Ma, X., Yu, F., and Quaas, J. (2014). Reassessment of satellite-based estimate of aerosol climate forcing. *J. Geophys. Res. Atmos.* 119, 10,310-394,409. doi:10.1002/2014JD021670.
MacIntosh, C. R. R., Allan, R. P. P., Baker, L. H. H., Bellouin, N., Collins, W., Mousavi, Z., et al. (2016). Contrasting fast precipitation responses to tropospheric and stratospheric ozone forcing. *Geophys. Res. Lett.* 43, 1263–1271. doi:10.1002/2015GL067231.
Maher, N., England, M. H., Gupta, A. Sen, and Spence, P. (2018). Role of Pacific trade winds in driving ocean temperatures during the recent slowdown and projections under a wind trend reversal. *Clim. Dyn.* 51, 321–336. doi:10.1007/s00382-017-3923-3.
Mahlstein, I., and Knutti, R. (2011). Ocean heat transport as a cause for model uncertainty in projected arctic warming. *J. Clim.* doi:10.1175/2010JCLI3713.1.
Mahowald, N. M., and Luo, C. (2003). A less dusty future? *Geophys. Res. Lett.* 30. doi:10.1029/2003GL017880.
Malavelle, F. F., Haywood, J. M., Jones, A., Gettelman, A., Clarisse, L., Bauduin, S., et al. (2017). Strong constraints on aerosol-cloud interactions from volcanic eruptions. *Nature* 546, 485–491. doi:10.1038/nature22974.
Mallick, K., Trebs, I., Boegh, E., Giustarini, L., Schlerf, M., Drewry, D. T., et al. (2016). Canopy-scale biophysical controls of transpiration and evaporation in the Amazon Basin. *Hydrol. EARTH Syst. Sci.* 20, 4237–4264. doi:10.5194/hess-20-4237-2016.
Manabe, S., and Bryan, K. (1985). CO2-induced change in a coupled ocean-atmosphere model and its paleoclimatic implications. *J. Geophys. Res.* 90, 11,611-689,707. doi:10.1029/JC090iC06p11689.
Manabe, S., and Stouffer, R. J. (1980). Sensitivity of a global climate model to an increase of CO2 concentration in the atmosphere. *J. Geophys. Res. Ocean.* 85, 5529–5554. doi:10.1029/JC085iC10p05529.
Manabe, S., and Wetherald, R. T. (1975). The Effects of Doubling the CO2 Concentration on the climate of a General Circulation Model. *J. Atmos. Sci.* 32, 3–15. doi:10.1175/1520-0469(1975)032<0003:TEODTC>2.0.CO;2.
Manara, V., Beltrano, M. C., Brunetti, M., Maugeri, M., Sanchez-Lorenzo, A., Simolo, C., et al. (2015). Sunshine duration variability and trends in Italy from homogenized instrumental time series (1936-2013). *J. Geophys. Res.* 120, 3622–3641. doi:Doi 10.1002/2014jd022560.
Manara, V., Brunetti, M., Celozzi, A., Maugeri, M., Sanchez-Lorenzo, A., and Wild, M. (2016). Detection of dimming/brightening in Italy from homogenized all-sky and clear-sky surface solar radiation records and underlying causes (1959-2013). *Atmos. Chem. Phys.* 16, 11145–11161. doi:10.5194/acp-16-11145-2016.
Manne, A. S., and Richels, R. G. (2001). An alternative approach to establishing trade-offs among greenhouse gases. *Nature* 410, 675. Available at: http://dx.doi.org/10.1038/35070541.
Marsh, D. R., Lamarque, J.-F., Conley, A. J., and Polvani, L. M. (2016). Stratospheric ozone chemistry feedbacks are not critical for the determination of climate sensitivity in CESM1(WACCM). *Geophys. Res. Lett.* 43, 3928–3934. doi:10.1002/2016GL068344.
Marshall, J., Donohoe, A., Ferreira, D., and McGee, D. (2014). The ocean’s role in setting the mean position of the Inter-Tropical Convergence Zone. *Clim. Dyn.* 42, 1967–1979. doi:10.1007/s00382-013-1767-z.
Marshall, J., Scott, J. R., Armour, K. C., Campin, J. M., Kelley, M., and Romanou, A. (2015). The ocean’s role in the transient response of climate to abrupt greenhouse gas forcing. *Clim. Dyn.* doi:10.1007/s00382-014-2308-0.
Martínez-Botí, M. A., Foster, G. L., Chalk, T. B., Rohling, E. J., Sexton, P. F., Lunt, D. J., et al. (2015). Plio-Pleistocene climate sensitivity evaluated using high-resolution CO2 records. *Nature* 518, 49–54. doi:10.1038/nature14145.
Marvel, K., Pincus, R., Schmidt, G. A., and Miller, R. L. (2018). Internal Variability and Disequilibrium Confound Estimates of Climate Sensitivity From Observations. *Geophys. Res. Lett.* 45, 1595–1601. doi:10.1002/2017GL076468.
Marvel, K., Schmidt, G. a., Miller, R. L., and Nazarenko, L. S. (2016). Implications for climate sensitivity from the response to individual forcings. *Nat. Clim. Chang.* 6, 386–389. doi:10.1038/nclimate2888.
Masson-Delmotte, V., Schulz, M., Abe-Ouchi, A., Beer, J., Ganopolski, A., González Rouco, J. F., et al. (2013). “Information from Paleoclimate Archives,” in *Climate Change 2013: The Physical Science Basis. Contribution of Working Group I to the Fifth Assessment Report of the Intergovernmental Panel on Climate Change*, eds. T. F. Stocker, D. Qin, G.-K. Plattner, M. Tignor, S. K. Allen, J. Boschung, et al. (Cambridge, United Kingdom and New York, NY, USA: Cambridge University Press), 383–464. doi:10.1017/CBO9781107415324.013.
Matsui, H., Hamilton, D. S., and Mahowald, N. M. (2018). Black carbon radiative effects highly sensitive to emitted particle size when resolving mixing-state diversity. *Nat. Commun.* 9, 3446. doi:10.1038/s41467-018-05635-1.
Mauritsen, T. (2016). Global warming: Clouds cooled the Earth. *Nat. Geosci.* 9, 865–867. doi:10.1038/ngeo2838.
Mauritsen, T., Bader, J., Becker, T., Behrens, J., Bittner, M., Brokopf, R., et al. (2019). Developments in the MPI-M Earth System Model version 1.2 (MPI-ESM 1.2) and its response to increasing CO2. *J. Adv. Model. Earth Syst.* 0.

doi:10.1029/2018MS001400.
Mauritsen, T., Graversen, R. G., Klocke, D., Langen, P. L., Stevens, B., and Tomassini, L. (2013). Climate feedback efficiency and synergy. *Clim. Dyn.* 41, 2539–2554. doi:10.1007/s00382-013-1808-7.
Mauritsen, T., and Pincus, R. (2017). Committed warming inferred from observations. *Nat. Clim. Chang.* 7, 652–655. doi:10.1038/nclimate3357.
Mauritsen, T., and Stevens, B. (2015). Missing iris effect as a possible cause of muted hydrological change and high climate sensitivity in models. *Nat. Geosci.* 8, 346–351. doi:10.1038/ngeo2414.
Maycock, A. C. (2016). The contribution of ozone to future stratospheric temperature trends. *Geophys. Res. Lett.* 43, 4609–4616. doi:10.1002/2016GL068511.
Mbengue, C., and Schneider, T. (2018). Linking Hadley Circulation and Storm Tracks in a Conceptual Model of the Atmospheric Energy Balance. *J. Atmos. Sci.* 75, 841–856. doi:10.1175/jas-d-17-0098.1.
McCabe, M. F., Aragon, B., Houborg, R., and Mascaro, J. (2017a). CubeSats in Hydrology: Ultrahigh-Resolution Insights Into Vegetation Dynamics and Terrestrial Evaporation. *WATER Resour. Res.* 53, 10017–10024. doi:10.1002/2017WR022240.
McCabe, M. F., Rodell, M., Alsdorf, D. E., Miralles, D. G., Uijlenhoet, R., Wagner, W., et al. (2017b). The future of Earth observation in hydrology. *Hydrol. EARTH Syst. Sci.* 21, 3879–3914. doi:10.5194/hess-21-3879-2017.
McComiskey, A., and Feingold, G. (2012). The scale problem in quantifying aerosol indirect effects. *Atmos. Chem. Phys.* 12, 1031–1049. doi:10.5194/acp-12-1031-2012.
McCoy, D. T., Bender, F. A.-M., Mohrmann, J. K. C., Hartmann, D. L., Wood, R., and Grosvenor, D. P. (2017a). The global aerosol-cloud first indirect effect estimated using MODIS, MERRA, and AeroCom. *J. Geophys. Res. Atmos.* 122, 1779–1796. doi:10.1002/2016JD026141.
McCoy, D. T., Eastman, R., Hartmann, D. L., and Wood, R. (2017b). The Change in Low Cloud Cover in a Warmed Climate Inferred from AIRS, MODIS, and ERA-Interim. *J. Clim.* 30, 3609–3620. doi:10.1175/JCLI-D-15-0734.1.
McCoy, D. T., Field, P. R., Elsaesser, G. S., Bodas-Salcedo, A., Kahn, B. H., Zelinka, M. D., et al. (2019). Cloud feedbacks in extratropical cyclones: Insight from long-term satellite data and high-resolution global simulations. *Atmos. Chem. Phys.* doi:10.5194/acp-19-1147-2019.
McCoy, D. T., Field, P. R., Schmidt, A., Grosvenor, D. P., Bender, F. A.-M., Shipway, B. J., et al. (2018). Aerosol midlatitude cyclone indirect effects in observations and high-resolution simulations. *Atmos. Chem. Phys.* 18, 5821–5846. doi:10.5194/acp-18-5821-2018.
McCoy, D. T., Hartmann, D. L., and Grosvenor, D. P. (2014a). Observed Southern Ocean Cloud Properties and Shortwave Reflection. Part I: Calculation of SW Flux from Observed Cloud Properties. *J. Clim.* 27, 8836–8857. doi:10.1175/JCLI-D-14-00287.1.
McCoy, D. T., Hartmann, D. L., and Grosvenor, D. P. (2014b). Observed Southern Ocean Cloud Properties and Shortwave Reflection. Part II: Phase Changes and Low Cloud Feedback. *J. Clim.* 27, 8858–8868. doi:10.1175/JCLI-D-14-00288.1.
McCoy, D. T., Tan, I., Hartmann, D. L., Zelinka, M. D., and Storelvmo, T. (2016). On the relationships among cloud cover, mixed-phase partitioning, and planetary albedo in GCMs. *J. Adv. Model. Earth Syst.* 8, 650–668.
McGregor, S., Stuecker, M. F., Kajtar, J. B., England, M. H., and Collins, M. (2018). Model tropical Atlantic biases underpin diminished Pacific decadal variability. *Nat. Clim. Chang.* 8, 493–498. doi:10.1038/s41558-018-0163-4.
Meehl, G. A., and Washington, W. M. (1996). El Nino-like climate change in a model with increased atmospheric CO2 concentrations. *Nature*. doi:10.1038/382056a0.
Meinshausen, M., Raper, S. C. B., and Wigley, T. M. L. (2011). Emulating coupled atmosphere-ocean and carbon cycle models with a simpler model, MAGICC6 – Part 1: Model description and calibration. *Atmos. Chem. Phys.* 11, 1417–1456. doi:10.5194/acp-11-1417-2011.
Meraner, K., Mauritsen, T., and Voigt, A. (2013). Robust increase in equilibrium climate sensitivity under global warming. *Geophys. Res. Lett.* 40, 5944–5948. doi:10.1002/2013GL058118.
Merlis, T. M. (2014). Interacting components of the top-of-atmosphere energy balance affect changes in regional surface temperature. *Geophys. Res. Lett.* 41, 7291–7297. doi:10.1002/2014GL061700.
Merlis, T. M. (2015). Direct weakening of tropical circulations from masked CO 2 radiative forcing . *Proc. Natl. Acad. Sci.* 112, 13167–13171. doi:10.1073/pnas.1508268112.
Merlis, T. M., Held, I. M., Stenchikov, G. L., Zeng, F., and Horowitz, L. W. (2014). Constraining transient climate sensitivity using coupled climate model simulations of volcanic eruptions. *J. Clim.* doi:10.1175/JCLI-D-14-00214.1.
Merlis, T. M., and Henry, M. (2018). Simple estimates of polar amplification in moist diffusive energy balance models. *J. Clim.* doi:10.1175/JCLI-D-17-0578.1.
Merlis, T. M., and Schneider, T. (2011). Changes in zonal surface temperature gradients and Walker circulations in a wide range of climates. *J. Clim.* 24, 4757–4768. doi:10.1175/2011JCLI4042.1.
Michalsky, J., Dutton, E., Rubes, M., Nelson, D., Stoffel, T., Wesley, M., et al. (1999). Optimal measurement of surface shortwave irradiance using current instrumentation. *J. Atmos. Ocean. Technol.* 16, 55–69. doi:10.1175/1520-

0426(1999)016<0055:OMOSSI>2.0.CO;2.
Michalsky, J. J., Dolce, R., Dutton, E. G., Haeffelin, M., Major, G., Schlemmer, J. A., et al. (2003). Results from the first ARM diffuse horizontal shortwave irradiance comparison. *J. Geophys. Res.* 108. doi:10.1029/2002JD002825.
Michibata, T., Suzuki, K., Sato, Y., and Takemura, T. (2016). The source of discrepancies in aerosol–cloud–precipitation interactions between GCM and A-Train retrievals. *Atmos. Chem. Phys.* 16, 15413–15424. doi:10.5194/acp-16-15413-2016.
Millar, R. J., Otto, A., Forster, P. M., Lowe, J. A., Ingram, W. J., and Allen, M. R. (2015). Model structure in observational constraints on transient climate response. *Clim. Change* 131, 199–211. doi:10.1007/s10584-015-1384-4.
Mishchenko, M. I., Geogdzhayev, I. V, Liu, L., Ogren, J. A., Lacis, A. A., Rossow, W. B., et al. (2003). Aerosol retrievals from AVHRR radiances: effects of particle nonsphericity and absorption and an updated long-term global climatology of aerosol properties. *J. Quant. Spectrosc. Radiat. Transf.* 79–80, 953–972. doi:10.1016/S0022-4073(02)00331-X.
Mlynczak, M. G., Daniels, T. S., Kratz, D. P., Feldman, D. R., Collins, W. D., Mlawer, E. J., et al. (2016). The spectroscopic foundation of radiative forcing of climate by carbon dioxide. *Geophys. Res. Lett.* doi:10.1002/2016GL068837.
Modak, A., Bala, G., Caldeira, K., and Cao, L. (2018). Does shortwave absorption by methane influence its effectiveness? *Clim. Dyn.*, 1–20. doi:10.1007/s00382-018-4102-x.
Modak, A., Bala, G., Cao, L., and Caldeira, K. (2016). Why must a solar forcing be larger than a CO<inf>2</inf>forcing to cause the same global mean surface temperature change? *Environ. Res. Lett.* 11. doi:10.1088/1748-9326/11/4/044013.
Morgenstern, O., Hegglin, M., Rozanov, E., O'Connor, F., Luke Abraham, N., Akiyoshi, H., et al. (2017). Review of the global models used within phase 1 of the Chemistry-Climate Model Initiative (CCMI). *Geosci. Model Dev.* doi:10.5194/gmd-10-639-2017.
Morrison, A. K., Griffies, S. M., Winton, M., Anderson, W. G., and Sarmiento, J. L. (2016). Mechanisms of Southern Ocean heat uptake and transport in a global eddying climate model. *J. Clim.* doi:10.1175/JCLI-D-15-0579.1.
Morrison, A. L., Kay, J. E., Frey, W. R., Chepfer, H., and Guzman, R. (2018). Cloud Response to Arctic Sea Ice Loss and Implications for Future Feedbacks in the CESM1 Climate Model. *J. Geophys. Res. Atmos.* doi:10.1029/2018jd029142.
Mueller, B., Hirschi, M., Jimenez, C., Ciais, P., Dirmeyer, P. A., Dolman, A. J., et al. (2013). Benchmark products for land evapotranspiration: LandFlux-EVAL multi-data set synthesis. *Hydrol. EARTH Syst. Sci.* 17, 3707–3720. doi:10.5194/hess-17-3707-2013.
Muhlbauer, A., McCoy, I. L., and Wood, R. (2014). Climatology of stratocumulus cloud morphologies: microphysical properties and radiative effects. *Atmos. Chem. Phys.* 14, 6695–6716. doi:10.5194/acp-14-6695-2014.
Muller, C. J., and Held, I. M. (2012). Detailed Investigation of the Self-Aggregation of Convection in Cloud-Resolving Simulations. *J. Atmos. Sci.* 69, 2551–2565. doi:10.1175/JAS-D-11-0257.1.
Mülmenstädt, J., Sourdeval, O., Delanoë, J., and Quaas, J. (2015). Frequency of occurrence of rain from liquid-, mixed-, and ice-phase clouds derived from A-Train satellite retrievals. *Geophys. Res. Lett.* 42, 6502–6509. doi:10.1002/2015GL064604.
Muñoz, I., and Schmidt, J. H. (2016). Methane oxidation, biogenic carbon, and the IPCC's emission metrics. Proposal for a consistent greenhouse-gas accounting. *Int. J. Life Cycle Assess.* doi:10.1007/s11367-016-1091-z.
Murphy, D. M., and Forster, P. M. (2010). On the accuracy of deriving climate feedback parameters from correlations between surface temperature and outgoing radiation. *J. Clim.* doi:10.1175/2010JCLI3657.1.
Murphy, D. M., Solomon, S., Portmann, R. W., Rosenlof, K. H., Forster, P. M., and Wong, T. (2009). An observationally based energy balance for the Earth since 1950. *J. Geophys. Res. Atmos.* doi:10.1029/2009JD012105.
Murphy, J. M. (1995). Transient Response of the Hadley Centre Coupled Ocean-Atmosphere Model to Increasing Carbon Dioxide. Part III: Analysis of Global-Mean Response Using Simple Models. *J. Clim.* doi:10.1175/1520-0442(1995)008<0496:TROTHC>2.0.CO;2.
Muscheler, R., Adolphi, F., Herbst, K., and Nilsson, A. (2016). The Revised Sunspot Record in Comparison to Cosmogenic Radionuclide-Based Solar Activity Reconstructions. *Sol. Phys.* 291, 3025–3043. doi:10.1007/s11207-016-0969-z.
Myers, T. A., and Norris, J. R. (2016). Reducing the uncertainty in subtropical cloud feedback. *Geophys. Res. Lett.* 43, 2144–2148. doi:10.1002/2015GL067416.
Myhre, G., Aas, W., Cherian, R., Collins, W., Faluvegi, G., Flanner, M., et al. (2017). Multi-model simulations of aerosol and ozone radiative forcing due to anthropogenic emission changes during the period 1990–2015. *Atmos. Chem. Phys.* doi:10.5194/acp-17-2709-2017.
Myhre, G., Highwood, E. J., Shine, K. P., and Stordal, F. (1998). New estimates of radiative forcing due to well mixed

greenhouse gases. *Geophys. Res. Lett.* doi:10.1029/98GL01908.
Myhre, G., Nilsen, J. S., Gulstad, L., Shine, K. P., Rognerud, B., and Isaksen, I. S. A. (2007). Radiative forcing due to stratospheric water vapour from CH4 oxidation. *Geophys. Res. Lett.* doi:10.1029/2006GL027472.
Myhre, G., and Samset, B. H. (2015). Standard climate models radiation codes underestimate black carbon radiative forcing. *Atmos. Chem. Phys.* 15, 2883–2888. doi:10.5194/acp-15-2883-2015.
Myhre, G., Samset, B. H., Hodnebrog, Ø., Andrews, T., Boucher, O., Faluvegi, G., et al. (2018). Sensible heat has significantly affected the global hydrological cycle over the historical period. *Nat. Commun.* 9, 1922. doi:10.1038/s41467-018-04307-4.
Myhre, G., Samset, B. H., Schulz, M., Balkanski, Y., Bauer, S., Berntsen, T. K., et al. (2013a). Radiative forcing of the direct aerosol effect from AeroCom Phase II simulations. *Atmos. Chem. Phys.* 13, 1853–1877. doi:10.5194/acp-13-1853-2013.
Myhre, G., Shindell, D., Bréon, F.-M., Collins, W., Fuglestvedt, J., Huang, J., et al. (2013b). "Anthropogenic and Natural Radiative Forcing," in *Climate Change 2013: The Physical Science Basis. Contribution of Working Group I to the Fifth Assessment Report of the Intergovernmental Panel on Climate Change*, eds. T. F. Stocker, D. Qin, G.-K. Plattner, M. Tignor, S. K. Allen, J. Boschung, et al. (Cambridge, United Kingdom and New York, NY, USA, United Kingdom and New York, NY, USA: Cambridge University Press), 659–740. doi:10.1017/CBO9781107415324.018.
Nabat, P., Somot, S., Mallet, M., Sanchez-Lorenzo, A., and Wild, M. (2014). Contribution of anthropogenic sulfate aerosols to the changing Euro-Mediterranean climate since 1980. *Geophys. Res. Lett.* 41, 5605–5611. doi:Doi 10.1002/2014gl060798.
Nakajima, T., Higurashi, A., Kawamoto, K., and Penner, J. E. (2001). A possible correlation between satellite-derived cloud and aerosol microphysical parameters. *Geophys. Res. Lett.* 28, 1171–1174. doi:10.1029/2000GL012186.
Nam, C., Bony, S., Dufresne, J. L., and Chepfer, H. (2012). The too few, too bright tropical low-cloud problem in CMIP5 models. *Geophys. Res. Lett.* 39, L21801. doi:10.1029/2012GL053421.
Nam, C. C. W., and Quaas, J. (2012). Evaluation of Clouds and Precipitation in the ECHAM5 General Circulation Model Using CALIPSO and CloudSat Satellite Data. *J. Clim.* 25, 4975–4992. doi:10.1175/JCLI-D-11-00347.1.
Namazi, M., von Salzen, K., and Cole, J. N. S. (2015). Simulation of black carbon in snow and its climate impact in the Canadian Global Climate Model. *Atmos. Chem. Phys.* 15, 10887–10904. doi:10.5194/acp-15-10887-2015.
Narenpitak, P., Bretherton, C. S., and Khairoutdinov, M. F. (2017). Cloud and circulation feedbacks in a nearglobal aquaplanet cloudresolving model. *J. Adv. Model. Earth Syst.* 9, 1069–1090.
Nauels, A., Meinshausen, M., Mengel, M., Lorbacher, K., and Wigley, T. M. L. (2017). Synthesizing long-term sea level rise projections -- the MAGICC sea level model v2.0. *Geosci. Model Dev.* 10, 2495–2524. doi:10.5194/gmd-10-2495-2017.
Neelin, J. D., Chou, C., and Su, H. (2003). Tropical drought regions in global warming and El Niño teleconnections. *Geophys. Res. Lett.* 30. doi:10.1029/2003GL018625.
Neubauer, D., Christensen, M. W., Poulsen, C. A., and Lohmann, U. (2017). Unveiling aerosol–cloud interactions – Part 2: Minimising the effects of aerosol swelling and wet scavenging in ECHAM6-HAM2 for comparison to satellite data. *Atmos. Chem. Phys.* 17, 13165–13185. doi:10.5194/acp-17-13165-2017.
Norris, J. R., Allen, R. J., Evan, A. T., Zelinka, M. D., O'Dell, C. W., and Klein, S. A. (2016). Evidence for climate change in the satellite cloud record. *Nature* 536, 72. doi:10.1038/nature18273.
Notaro, M., Vavrus, S., and Liu, Z. (2007). Global vegetation and climate change due to future increases in CO2 as projected by a fully coupled model with dynamic vegetation. *J. Clim.* 20, 70–90. doi:10.1175/JCLI3989.1.
Nowack, P. J., Luke Abraham, N., Maycock, A. C., Braesicke, P., Gregory, J. M., Joshi, M. M., et al. (2015). A large ozone-circulation feedback and its implications for global warming assessments. *Nat. Clim. Chang.* 5, 41–45. doi:10.1038/nclimate2451.
Nowicki, S. M. J., Payne, A., Larour, E., Seroussi, H., Goelzer, H., Lipscomb, W., et al. (2016). Ice Sheet Model Intercomparison Project (ISMIP6) contribution to CMIP6. *Geosci. Model Dev.* 9, 4521–4545. doi:10.5194/gmd-9-4521-2016.
Nummelin, A., Li, C., and Hezel, P. J. (2017). Connecting ocean heat transport changes from the midlatitudes to the Arctic Ocean. *Geophys. Res. Lett.* doi:10.1002/2016GL071333.
O'Brien, C. L., Foster, G. L., Martínez-Botí, M. A., Abell, R., Rae, J. W. B., and Pancost, R. D. (2014). High sea surface temperatures in tropical warm pools during the Pliocene. *Nat. Geosci.* 7, 606. Available at: http://dx.doi.org/10.1038/ngeo2194.
O'Gorman, P. A., and Muller, C. J. (2010). How closely do changes in surface and column water vapor follow Clausius-Clapeyron scaling in climate change simulations? *Environ. Res. Lett.* 5, 25207. doi:10.1088/1748-9326/5/2/025207.
O'Gorman, P. A., and Singh, M. S. (2013). Vertical structure of warming consistent with an upward shift in the middle and upper troposphere. *Geophys. Res. Lett.* 40, 1838–1842. doi:10.1002/grl.50328.
O'ishi, R., Abe-Ouchi, A., Prentice, I. C., and Sitch, S. (2009). Vegetation dynamics and plant CO2responses as

positive feedbacks in a greenhouse world. *Geophys. Res. Lett.* 36, 1–5. doi:10.1029/2009GL038217.

Ohmura, A., Dutton, E. G., Forgan, B., Frohlich, C., Gilgen, H., Hegner, H., et al. (1998). Baseline Surface Radiation Network (BSRN/WCRP): New precision radiometry for climate research. *Bull. Am. Meteorol. Soc.* 79, 2115–2136. doi:10.1175/1520-0477(1998)079<2115:BSRNBW>2.0.CO;2.

Oikawa, E., Nakajima, T., and Winker, D. (2018). An Evaluation of the Shortwave Direct Aerosol Radiative Forcing Using CALIOP and MODIS Observations. *J. Geophys. Res. Atmos.* 123, 1211–1233. doi:10.1002/2017JD027247.

Oldenburg, D., Armour, K. C., Thompson, L., and Bitz, C. M. (2018). Distinct mechanisms of ocean heat transport into the Arctic under internal variability and climate change. *Geophys. Res. Lett.* doi:10.1029/2018GL078719.

Oliveira, P. J. C., Davin, E. L., Levis, S., and Seneviratne, S. I. (2011). Vegetation-mediated impacts of trends in global radiation on land hydrology: a global sensitivity study. *Glob. Chang. Biol.* 17, 3453–3467. doi:10.1111/j.1365-2486.2011.02506.x.

Olson, R., Sriver, R., Chang, W., Haran, M., Urban, N. M., and Keller, K. (2013). What is the effect of unresolved internal climate variability on climate sensitivity estimates? *J. Geophys. Res. Atmos.* 118, 4348–4358. doi:10.1002/jgrd.50390.

Otto, A., Otto, F. E. L., Boucher, O., Church, J., Hegerl, G., Forster, P. M., et al. (2013). Energy budget constraints on climate response. *Nat. Geosci.* 6, 415–416. doi:10.1038/ngeo1836.

Ozawa, H., Ohmura, A., Lorenz, R. D., and Pujol, T. (2003). The second law of thermodynamics and the global climate system: A review of the maximum entropy production principle. *Rev. Geophys.* doi:10.1029/2002RG000113.

Paasonen, P., Asmi, A., Petaja, T., Kajos, M. K., Aijala, M., Junninen, H., et al. (2013). Warming-induced increase in aerosol number concentration likely to moderate climate change. *Nat. Geosci.* 6, 438–442. doi:10.1038/NGEO1800.

Padilla, L. E., Vallis, G. K., and Rowley, C. W. (2011). Probabilistic estimates of transient climate sensitivity subject to uncertainty in forcing and natural variability. *J. Clim.* doi:10.1175/2011JCLI3989.1.

Palmer, M. D. (2017). Reconciling Estimates of Ocean Heating and Earth's Radiation Budget. *Curr. Clim. Chang. Reports* 3, 78–86. doi:10.1007/s40641-016-0053-7.

Palmer, M. D., Harris, G. R., and Gregory, J. M. (2018). Extending CMIP5 projections of global mean temperature change and sea level rise due to thermal expansion using a physically-based emulator. *Environ. Res. Lett.* 13, 84003. Available at: http://stacks.iop.org/1748-9326/13/i=8/a=084003.

Palmer, M. D., and McNeall, D. J. (2014). Internal variability of Earth's energy budget simulated by CMIP5 climate models. *Environ. Res. Lett.* 9, 34016. Available at: http://stacks.iop.org/1748-9326/9/i=3/a=034016.

Palmer, M. D., McNeall, D. J., and Dunstone, N. J. (2011). Importance of the deep ocean for estimating decadal changes in Earth's radiation balance. *Geophys. Res. Lett.* 38. doi:10.1029/2011GL047835.

Palmer, M. D., Roberts, C. D., Balmaseda, M., Chang, Y. S., Chepurin, G., Ferry, N., et al. (2017). Ocean heat content variability and change in an ensemble of ocean reanalyses. *Clim. Dyn.* 49, 909–930. doi:10.1007/s00382-015-2801-0.

Papanastasiou, D. K., Beltrone, A., Marshall, P., and Burkholder, J. B. (2018). Global warming potential estimates for the C1-C3hydrochlorofluorocarbons (HCFCs) included in the Kigali Amendment to the Montreal Protocol. *Atmos. Chem. Phys.* doi:10.5194/acp-18-6317-2018.

Parding, K., Olseth, J. A., Dagestad, K. F., and Liepert, B. G. (2014). Decadal variability of clouds, solar radiation and temperature at a high-latitude coastal site in Norway. *Tellus Ser. B-Chemical Phys. Meteorol.* 66. doi:Artn 25897 Doi 10.3402/Tellusb.V66.25897.

Pascale, S., Gregory, J. M., Ambaum, M. H. P., Tailleux, R., and Lucarini, V. (2012). Vertical and horizontal processes in the global atmosphere and the maximum entropy production conjecture. *Earth Syst. Dyn.* doi:10.5194/esd-3-19-2012.

Pauling, A. G., Smith, I. J., Langhorne, P. J., and Bitz, C. M. (2017). Time-Dependent Freshwater Input From Ice Shelves: Impacts on Antarctic Sea Ice and the Southern Ocean in an Earth System Model. *Geophys. Res. Lett.* doi:10.1002/2017GL075017.

Payne, A. E., Jansen, M. F., and Cronin, T. W. (2015). Conceptual model analysis of the influence of temperature feedbacks on polar amplification. *Geophys. Res. Lett.* 42, 9561–9570. doi:10.1002/2015GL065889.

Paynter, D., Frölicher, T. L., Horowitz, L. W., and Silvers, L. G. (2018). Equilibrium Climate Sensitivity Obtained From Multimillennial Runs of Two GFDL Climate Models. *J. Geophys. Res. Atmos.* 123, 1921–1941. doi:10.1002/2017JD027885.

Peng, J., Hu, M., Guo, S., Du, Z., Zheng, J. J., Shang, D., et al. (2016). Markedly enhanced absorption and direct radiative forcing of black carbon under polluted urban environments. *Proc. Natl. Acad. Sci. U. S. A.* 113, 4266–71. doi:10.1073/pnas.1602310113.

Penner, J. E., Andreae, M., Annegarn, K. H., Barrie, L., Feichter, J., Hegg, D., et al. (2001). Aerosols, their direct and indirect effects. In: Climate Change 2001: The Scientific Basis. Contribution of Working Group I to the Third Assessment Report of the Intergovernmental Panel on Climate Change [Houghton, J.T., et al. (eds.)]. Cambridge

Universi.
Penner, J. E., Xu, L., and Wang, M. (2011). Satellite methods underestimate indirect climate forcing by aerosols. *Proc. Natl. Acad. Sci. U. S. A.* 108, 13404–8. doi:10.1073/pnas.1018526108.
Persad, G. G., Ming, Y., and Ramaswamy, V. (2014). The role of aerosol absorption in driving clear-sky solar dimming over East Asia. *J. Geophys. Res.* 119, 10,410–10,424. doi:Doi 10.1002/2014jd021577.
Petersik, P., Salzmann, M., Kretzschmar, J., Cherian, R., Mewes, D., and Quaas, J. (2018). Subgrid-scale variability in clear-sky relative humidity and forcing by aerosol–radiation interactions in an atmosphere model. *Atmos. Chem. Phys.* 18, 8589–8599. doi:10.5194/acp-18-8589-2018.
Pfeifroth, U., Sanchez-Lorenzo, A., Manara, V., Trentmann, J., and Hollmann, R. (2018). Trends and Variability of Surface Solar Radiation in Europe Based On Surface- and Satellite-Based Data Records. *J. Geophys. Res.* 123, 1735–1754. doi:10.1002/2017JD027418.
Pfister, P. L., and Stocker, T. F. (2017). State-Dependence of the Climate Sensitivity in Earth System Models of Intermediate Complexity. *Geophys. Res. Lett.* 44, 10,643-10,653. doi:10.1002/2017GL075457.
Pierrehumbert, R. T. (2014). *Short-lived climate pollution.* doi:10.1146/annurev-earth-060313-054843.
Pincus, R., Forster, P. M., and Stevens, B. (2016). The Radiative Forcing Model Intercomparison Project (RFMIP): Experimental protocol for CMIP6. *Geosci. Model Dev.* 9, 3447–3460. doi:10.5194/gmd-9-3447-2016.
Pincus, R., Mlawer, E. J., Oreopoulos, L., Ackerman, A. S., Baek, S., Brath, M., et al. (2015). Radiative flux and forcing parameterization error in aerosol-free clear skies. *Geophys. Res. Lett.* 42, 5485–5492. doi:10.1002/2015GL064291.
Pinsky, M. B., and Khain, A. P. (2002). Effects of in-cloud nucleation and turbulence on droplet spectrum formation in cumulus clouds. *Q. J. R. Meteorol. Soc.* 128, 501–533. doi:10.1256/003590002321042072.
Pistone, K., Eisenman, I., and Ramanathan, V. (2014). Observational determination of albedo decrease caused by vanishing Arctic sea ice. *Proc. Natl. Acad. Sci.* 111, 3322–3326. doi:10.1073/pnas.1318201111.
Pithan, F., and Mauritsen, T. (2014). Arctic amplification dominated by temperature feedbacks in contemporary climate models. *Nat. Geosci.* 7, 181–184. doi:10.1038/ngeo2071.
Po-Chedley, S., Armour, K. C., Bitz, C. M., Zelinka, M. D., and Santer, B. D. (2018a). Sources of intermodel spread in the lapse rate and water vapor feedbacks. *J. Clim.* doi:10.1175/JCLI-D-17-0674.1.
Po-Chedley, S., Proistosescu, C., Armour, K. C., and Santer, B. D. (2018b). Climate constraint reflects forced signal. *Nature* 563, E6–E9. doi:10.1038/s41586-018-0640-y.
Popke, D., Stevens, B., and Voigt, A. (2013). Climate and climate change in a radiative-convective equilibrium version of ECHAM6. *J. Adv. Model. Earth Syst.* 5, 1–14. doi:10.1029/2012MS000191.
Popp, M., Schmidt, H., and Marotzke, J. (2016). Transition to a Moist Greenhouse with CO2 and solar forcing. *Nat. Commun.* 7, 10627. Available at: https://doi.org/10.1038/ncomms10627.
Port, U., Brovkin, V., and Claussen, M. (2012). The influence of vegetation dynamics on anthropogenic climate change. *Earth Syst. Dyn.* 3, 233–243. doi:10.5194/esd-3-233-2012.
Posselt, R., Mueller, R., Trentrnann, J., Stockli, R., and Liniger, M. A. (2014). A surface radiation climatology across two Meteosat satellite generations. *Remote Sens. Environ.* 142, 103–110. doi:Doi 10.1016/J.Rse.2013.11.007.
Prabha, T. V., Khain, A., Maheshkumar, R. S., Pandithurai, G., Kulkarni, J. R., Konwar, M., et al. (2011). Microphysics of Premonsoon and Monsoon Clouds as Seen from In Situ Measurements during the Cloud Aerosol Interaction and Precipitation Enhancement Experiment (CAIPEEX). *J. Atmos. Sci.* 68, 1882–1901. doi:10.1175/2011JAS3707.1.
Prentice, I. C., Cramer, W., Harrison, S. P., Leemans, R., Monserud, R. A., and Solomon, A. M. (1992). A global biome model based on plant physiology and dominance, soil properties and climate. *J. Biogeogr.* 19, 117–134.
Previdi, M., Smith, K. L., and Polvani, L. M. (2015). How Well Do the CMIP5 Models Simulate the Antarctic Atmospheric Energy Budget? *J. Clim.* 28, 7933–7942. doi:10.1175/JCLI-D-15-0027.1.
Proistosescu, C., Donohoe, A., Armour, K. C., Roe, G. H., Stuecker, M. F., and Bitz, C. M. (2018). Radiative Feedbacks From Stochastic Variability in Surface Temperature and Radiative Imbalance. *Geophys. Res. Lett.* doi:10.1029/2018GL077678.
Proistosescu, C., and Huybers, P. J. (2017). Slow climate mode reconciles historical and model-based estimates of climate sensitivity. *Sci. Adv.* 3, 1–7. doi:10.1126/sciadv.1602821.
Purich, A., England, M. H., Cai, W., Sullivan, A., and Durack, P. J. (2018). Impacts of broad-scale surface freshening of the Southern Ocean in a coupled climate model. *J. Clim.* doi:10.1175/JCLI-D-17-0092.1.
Purkey, S. G., and Johnson, G. C. (2010). Warming of Global Abyssal and Deep Southern Ocean Waters between the 1990s and 2000s: Contributions to Global Heat and Sea Level Rise Budgets. *J. Clim.* 23, 6336–6351. doi:10.1175/2010JCLI3682.1.
Purkey, S. G., and Johnson, G. C. (2013). Antarctic Bottom Water Warming and Freshening: Contributions to Sea Level Rise, Ocean Freshwater Budgets, and Global Heat Gain. *J. Clim.* 26, 6105–6122. doi:10.1175/JCLI-D-12-00834.1.
Qu, X. ., Hall, A., Klein, S. A., and DeAngelis, A. M. (2015). Positive tropical marine lowcloud cover feedback inferred

from cloudcontrolling factors. *Geophys. Res. Lett.* 42, 7767–7775. doi:10.1002/2015GL065627.
Qu, X., and Hall, A. (2007). What controls the strength of snow-albedo feedback? *J. Clim.* 20, 3971–3981.
Qu, X., and Hall, A. (2014). On the persistent spread in snow-albedo feedback. *Clim. Dyn.* 42, 69–81. doi:10.1007/s00382-013-1774-0.
Qu, X., Hall, A., Klein, S. A., and Caldwell, P. M. (2014). On the spread of changes in marine low cloud cover in climate model simulations of the 21st century. *Clim. Dyn.* doi:10.1007/s00382-013-1945-z.
Quaas, J., Boucher, O., Bellouin, N., and Kinne, S. (2008). Satellite-based estimate of the direct and indirect aerosol climate forcing. *J. Geophys. Res. Atmos.* 113, n/a-n/a. doi:10.1029/2007JD008962.
Quaas, J., Boucher, O., Jones, A., Weedon, G. P., Kieser, J., and Joos, H. (2009a). Exploiting the weekly cycle as observed over Europe to analyse aerosol indirect effects in two climate models. *Atmos. Chem. Phys.* 9, 8493–8501. doi:10.5194/acp-9-8493-2009.
Quaas, J., Ming, Y., Menon, S., Takemura, T., Wang, M., Penner, J. E., et al. (2009b). Aerosol indirect effects – general circulation model intercomparison and evaluation with satellite data. *Atmos. Chem. Phys.* 9, 8697–8717. doi:10.5194/acp-9-8697-2009.
Randall, D. A., Wood, R. A., Bony, S., Colman, R., Fichefet, T., Fyfe, J., et al. (2007). “Climate Models and Their Evaluation,” in *{C}limate Change 2007: The Scientific Basis. {C}ontribution of Working Group {I} to the Fourth Assessment Report of the {I}ntergovernmental {P}anel on {C}limate {C}hange*, eds. S. Solomon, D. Qin, M. Manning, Z. Chen, M. Marquis, K. B. Averyt, et al. (Cambridge University Press, {C}ambridge, {U}nited {K}ingdom and {N}ew {Y}ork, {NY}, {USA}), 589–662.
Randles, C. A., da Silva, A. M., Buchard, V., Colarco, P. R., Darmenov, A., Govindaraju, R., et al. (2017). The MERRA-2 Aerosol Reanalysis, 1980 Onward. Part I: System Description and Data Assimilation Evaluation. *J. Clim.* 30, 6823–6850. doi:10.1175/JCLI-D-16-0609.1.
Raper, S. C. B., Gregory, J. M., and Stouffer, R. J. (2002). The Role of Climate Sensitivity and Ocean Heat Uptake on AOGCM Transient Temperature Response. Available at: http://www-pcmdi.llnl.gov/.
Raschke, E., Kinne, S., Rossow, W. B., Stackhouse, P. W., and Wild, M. (2016). Comparison of Radiative Energy Flows in Observational Datasets and Climate Modeling. *J. Appl. Meteorol. Climatol.* 55, 93–117. doi:10.1175/Jamc-D-14-0281.1.
Rayner, N. A., Parker, D. E., Horton, E. B., Folland, C. K., Alexander, L. V., Rowell, D. P., et al. (2003). Global analyses of sea surface temperature, sea ice, and night marine air temperature since the late nineteenth century. *J. Geophys. Res.* 108, 4407. doi:10.1029/2002JD002670.
Regayre, L. A., Johnson, J. S., Yoshioka, M., Pringle, K. J., Sexton, D. M. H., Booth, B. B. B., et al. (2018). Aerosol and physical atmosphere model parameters are both important sources of uncertainty in aerosol ERF. *Atmos. Chem. Phys.* 18, 9975–10006. doi:10.5194/acp-18-9975-2018.
Rémy, S., Bellouin, N., Benedetti, A., and Boucher, O. (2018). Aerosols [in “State of the Climate in 2017”]. *Bull. Amer. Meteor. Soc.*, 99, S49–S51. doi:doi:10.1175/2018BAMSStateoftheClimate.1.
Resplandy, L., Keeling, R. F., Eddebbar, Y., Brooks, M. K., Wang, R., Bopp, L., et al. (2018). Quantification of ocean heat uptake from changes in atmospheric O2 and CO2 composition. *Nature* 563, 105–108. doi:10.1038/s41586-018-0651-8.
Rhein, M., Rintoul, S. R., Aoki, S., Campos, E., Chambers, D., Feely, R. A., et al. (2013). “Observations: Ocean,” in *Climate Change 2013: The Physical Science Basis. Contribution of Working Group I to the Fifth Assessment Report of the Intergovernmental Panel on Climate Change*, eds. T. F. Stocker, D. Qin, G.-K. Plattner, M. Tignor, S. K. Allen, J. Boschung, et al. (Cambridge, United Kingdom and New York, NY, USA: Cambridge University Press), 255�316. doi:10.1017/CBO9781107415324.010.
Richardson, M., Cowtan, K., Hawkins, E., and Stolpe, M. B. (2016). Reconciled climate response estimates from climate models and the energy budget of Earth. *Nat. Clim. Chang.* 6, 931–935. doi:10.1038/nclimate3066.
Richardson, M., Cowtan, K., and Millar, R. J. (2018a). Global temperature definition affects achievement of long-term climate goals. *Environ. Res. Lett.* 13, 054004. doi:10.1088/1748-9326/aab305.
Richardson, T. B., Forster, P., Andrews, T., Boucher, O., Faluvegi, G., Fläschner, D., et al. Drivers of precipitation change: An energetic understanding.
Richardson, T. B., Forster, P. M., Andrews, T., Boucher, O., Faluvegi, G., Fläschner, D., et al. (2018b). Carbon Dioxide Physiological Forcing Dominates Projected Eastern Amazonian Drying. *Geophys. Res. Lett.* doi:10.1002/2017GL076520.
Richardson, T. B., Forster, P. M., Smith, C. J., Maycock, A. C., Wood, T., Andrews, T., et al. Efficacy of climate forcings in PDRMIP models.
Rienecker, M. M., Suarez, M. J., Gelaro, R., Todling, R., Bacmeister, J., Liu, E., et al. (2011). MERRA: NASA’s Modern-Era Retrospective Analysis for Research and Applications. *J. Clim.* 24, 3624–3648. doi:10.1175/JCLI-D-11-00015.1.
Ringer, M. A., Andrews, T., and Webb, M. J. (2014). Global-mean radiative feedbacks and forcing in atmosphere-only and coupled atmosphereocean climate change experiments. *Geophys. Res. Lett.* 41, 4035–4042. doi:10.1002/

2014GL060347.
Riser, S. C., Freeland, H. J., Roemmich, D., Wijffels, S., Troisi, A., Belbéoch, M., et al. (2016). Fifteen years of ocean observations with the global Argo array. *Nat. Clim. Chang.* 6, 145–153. doi:10.1038/nclimate2872.
Robock, A. (1983). Ice and Snow Feedbacks and the Latitudinal and Seasonal Distribution of Climate Sensitivity. *J. Atmos. Sci.* 40, 986–997.
Rodell, M., Famiglietti, J. S., Wiese, D. N., Reager, J. T., Beaudoing, H. K., Landerer, F. W., et al. (2018). Emerging trends in global freshwater availability. *Nature* 557, 650+. doi:10.1038/s41586-018-0123-1.
Roe, G. H., and Armour, K. C. (2011). How sensitive is climate sensitivity? *Geophys. Res. Lett.* doi:10.1029/2011GL047913.
Roe, G. H., and Baker, M. B. (2007). Why Is Climate Sensitivity So Unpredictable? *Science (80-.).* 318, 629–632. doi:10.1126/science.1144735.
Roe, G. H., Feldl, N., Armour, K. C., Hwang, Y. T., and Frierson, D. M. W. (2015). The remote impacts of climate feedbacks on regional climate predictability. *Nat. Geosci.* doi:10.1038/ngeo2346.
Roemmich, D., Church, J., Gilson, J., Monselesan, D., Sutton, P., and Wijffels, S. (2015). Unabated planetary warming and its ocean structure since 2006. *Nat. Clim. Chang.* 5, 240. Available at: http://dx.doi.org/10.1038/nclimate2513.
Roemmich, D., John Gould, W., and Gilson, J. (2012). 135 years of global ocean warming between the Challenger expedition and the Argo Programme. *Nat. Clim. Chang.* 2, 425–428. doi:10.1038/nclimate1461.
Rohling, E. J., Sluijs, A., Dijkstra, H. A., Köhler, P., Van De Wal, R. S. W., Von Der Heydt, A. S., et al. (2012). Making sense of palaeoclimate sensitivity. *Nature* 491, 683–691. doi:10.1038/nature11574.
Rohrschneider, T., Stevens, B., and Mauritsen, T. (2019). On simple representations of the climate response to external radiative forcing. *Clim. Dyn.* doi:10.1007/s00382-019-04686-4.
Rose, B. E. J., Armour, K. C., Battisti, D. S., Feldl, N., and Koll, D. D. B. (2014). The dependence of transient climate sensitivity and radiative feedbacks on the spatial pattern of ocean heat uptake. *Geophys. Res. Lett.* doi:10.1002/2013GL058955.
Rose, B. E. J., and Ferreira, D. (2013). Ocean heat transport and water vapor greenhouse in a warm equable climate: A new look at the low gradient paradox. *J. Clim.* doi:10.1175/JCLI-D-11-00547.1.
Rose, B. E. J., and Rayborn, L. (2016). The Effects of Ocean Heat Uptake on Transient Climate Sensitivity. *Curr. Clim. Chang. Reports*. doi:10.1007/s40641-016-0048-4.
Rose, B. E. J., and Rencurrel, M. C. (2016). The Vertical Structure of Tropospheric Water Vapor: Comparing Radiative and Ocean-Driven Climate Changes. *J. Clim.* 29, 4251–4268. doi:10.1175/JCLI-D-15-0482.1.
Rosenfeld, D., and Gutman, G. (1994). Retrieving microphysical properties near the tops of potential rain clouds by multispectral analysis of AVHRR data. *Atmos. Res.* 34, 259–283. doi:10.1016/0169-8095(94)90096-5.
Rosenfeld, D., Kaufman, Y. J., and Koren, I. (2006). Switching cloud cover and dynamical regimes from open to closed Benard cells in response to the suppression of precipitation by aerosols. *Atmos. Chem. Phys.* 6. doi:10.5194/acp-6-2503-2006.
Rosenfeld, D., Yu, X., Liu, G., Xu, X., Zhu, Y., Yue, Z., et al. (2011). Glaciation temperatures of convective clouds ingesting desert dust, air pollution and smoke from forest fires. *Geophys. Res. Lett.* 38, n/a-n/a. doi:10.1029/2011GL049423.
Rosenfeld, D., Zhu, Y., Wang, M., Zheng, Y., Goren, T., and Yu, S. (2019). Aerosol-driven droplet concentrations dominate coverage and water of oceanic low level clouds. *Science*, eaav0566. doi:10.1126/science.aav0566.
Rotstayn, L. D., Collier, M. A., Shindell, D. T., and Boucher, O. (2015). Why does aerosol forcing control historical global-mean surface temperature change in CMIP5 models? *J. Clim.* 28, 6608–6625. doi:10.1175/JCLI-D-14-00712.1.
Rowlands, D. J., Frame, D. J., Ackerley, D., Aina, T., Booth, B. B. B., Christensen, C., et al. (2012). Broad range of 2050 warming from an observationally constrained large climate model ensemble. *Nat. Geosci.* doi:10.1038/ngeo1430.
Royer, D. L. (2016). Climate Sensitivity in the Geologic Past. *Annu. Rev. Earth Planet. Sci.* 44, 277–293. doi:10.1146/annurev-earth-100815-024150.
Rugenstein, M. A. A., Caldeira, K., and Knutti, R. (2016). Dependence of global radiative feedbacks on evolving patterns of surface heat fluxes. *Geophys. Res. Lett.* doi:10.1002/2016GL070907.
Rugenstein, M. A. A., Winton, M., Stouffer, R. J., Griffies, S. M., and Hallberg, R. (2013). Northern High-Latitude Heat Budget Decomposition and Transient Warming. *J. Clim.* 26, 609–621. doi:10.1175/JCLI-D-11-00695.1.
Rugenstein, M., Bloch-Johnson, J., Gregory, J., Mauritsen, T., Li, C., Frölicher, T., et al. (2019). Equilibrium climate sensitivity estimated by equilibrating climate models 2. *Submitted*.
Rypdal, M., Fredriksen, H.-B., Rypdal, K., and Steene, R. J. (2018). Emergent constraints on climate sensitivity. *Nature* 563, E4–E5. doi:10.1038/s41586-018-0639-4.
Sagoo, N., Valdes, P., Flecker, R., Gregoire, L. J., and A, P. T. R. S. (2013). The Early Eocene equable climate problem: can perturbations of climate model parameters identify possible solutions? *Philos. Trans. R. Soc.*

London A Math. Phys. Eng. Sci. 371. doi:10.1098/rsta.2013.0123.
Salzmann, M., Ming, Y., Golaz, J. C., Ginoux, P. A., Morrison, H., Gettelman, A., et al. (2010). Two-moment bulk stratiform cloud microphysics in the GFDL AM3 GCM: Description, evaluation, and sensitivity tests. *Atmos. Chem. Phys.* doi:10.5194/acp-10-8037-2010.
Salzmann, U., Dolan, A. M., Haywood, A. M., Chan, W. Le, Voss, J., Hill, D. J., et al. (2013). Challenges in quantifying Pliocene terrestrial warming revealed by data-model discord. *Nat. Clim. Chang.* 3, 969–974. doi:10.1038/nclimate2008.
Samset, B. H., and Myhre, G. (2015). Climate response to externally mixed black carbon as a function of altitude. *J. Geophys. Res. Atmos.* 120, 2913–2927. doi:10.1002/2014JD022849.
Samset, B. H., Stjern, C. W., Andrews, E., Kahn, R. A., Myhre, G., Schulz, M., et al. (2018). Aerosol Absorption: Progress Towards Global and Regional Constraints. *Curr. Clim. Chang. Reports* 4, 65–83. doi:10.1007/s40641-018-0091-4.
Sanchez-Lorenzo, A., Calbo, J., and Wild, M. (2013). Global and diffuse solar radiation in Spain: Building a homogeneous dataset and assessing their trends. *Glob. Planet. Change* 100, 343–352. doi:Doi 10.1016/J.Gloplacha.2012.11.010.
Sanchez-Lorenzo, A., Wild, M., Brunetti, M., Guijarro, J. A., Hakuba, M. Z., Calbo, J., et al. (2015). Reassessment and update of long-term trends in downward surface shortwave radiation over Europe (1939-2012). *J. Geophys. Res.* 120, 9555–9569. doi:10.1002/2015jd023321.
Sanderson, B. M., Knutti, R., Aina, T., Christensen, C., Faull, N., Frame, D. J., et al. (2008a). Constraints on model response to greenhouse gas forcing and the role of subgrid-scale processes. *J. Clim.* 21. doi:10.1175/2008JCLI1869.1.
Sanderson, B. M., Piani, C., Ingram, W. J., Stone, D. A., and Allen, M. R. (2008b). Towards constraining climate sensitivity by linear analysis of feedback patterns in thousands of perturbed-physics GCM simulations. *Clim. Dyn.* doi:10.1007/s00382-007-0280-7.
Santer, B. D., Wigley, T. M. L., Mears, C., Wentz, F. J., Klein, S. A., Seidel, D. J., et al. (2005). Amplification of Surface Temperature Trends and Variability in the Tropical Atmosphere. *Science (80-.).* 309, 1551–1556. doi:10.1126/science.1114867.
Sarofim, M. C., and Giordano, M. R. (2018). A quantitative approach to evaluating the GWP timescale through implicit discount rates. *Earth Syst. Dyn.* 9, 1013–1024. doi:10.5194/esd-9-1013-2018.
Sato, Y., Goto, D., Michibata, T., Suzuki, K., Takemura, T., Tomita, H., et al. (2018). Aerosol effects on cloud water amounts were successfully simulated by a global cloud-system resolving model. *Nat. Commun.* 9, 985. doi:10.1038/s41467-018-03379-6.
Sato, Y., and Suzuki, K. (2019). How do aerosols affect cloudiness? *Science (80-.).* 363, 580–581. doi:10.1126/science.aaw3720.
Schmidt, A., Mills, M. J., Ghan, S., Gregory, J. M., Allan, R. P., Andrews, T., et al. (2018). Volcanic Radiative Forcing From 1979 to 2015. *J. Geophys. Res. Atmos.* doi:10.1029/2018JD028776.
Schmidt, G. A., Annan, J. D., Bartlein, P. J., Cook, B. I., Guilyardi, E., Hargreaves, J. C., et al. (2014). Using palaeo-climate comparisons to constrain future projections in CMIP5. *Clim. Past* 10, 221–250. doi:10.5194/cp-10-221-2014.
Schmidt, G. A., Bader, D., Donner, L. J., Elsaesser, G. S., Golaz, J. C., Hannay, C., et al. (2017a). Practice and philosophy of climate model tuning across six US modeling centers. *Geosci. Model Dev.* 10, 3207–3223. doi:10.5194/gmd-10-3207-2017.
Schmidt, G. A., Severinghaus, J., Abe-Ouchi, A., Alley, R. B., Broecker, W., Brook, E., et al. (2017b). Overestimate of committed warming. *Nature* 547, E16–E17. doi:10.1038/nature22803.
Schneider, A., Flanner, M., and Perket, J. (2018). Multidecadal Variability in Surface Albedo Feedback Across {CMIP5} Models. *Geophys. Res. Lett.* 45, 1972–1980. doi:10.1002/2017GL076293.
Schulz, M., Textor, C., Kinne, S., Balkanski, Y., Bauer, S., Berntsen, T., et al. (2006). Radiative forcing by aerosols as derived from the AeroCom present-day and pre-industrial simulations. *Atmos. Chem. Phys.* 6, 5225–5246. doi:10.5194/acp-6-5225-2006.
Schwartz, S. E. (2007). Heat capacity, time constant, and sensitivity of Earth's climate system. *J. Geophys. Res. Atmos.* 112, 1–12. doi:10.1029/2007JD008746.
Schwartz, S. E. (2012). Determination of Earth's Transient and Equilibrium Climate Sensitivities from Observations Over the Twentieth Century: Strong Dependence on Assumed Forcing. *Surv. Geophys.* 33, 745–777. doi:10.1007/s10712-012-9180-4.
Schwinger, J., Tjiputra, J., Goris, N., Six, K. D., Kirkevag, A., Seland, O., et al. (2017). Amplification of global warming through pH dependence of DMS production simulated with a fully coupled Earth system model. *Biogeosciences* 14, 3633–3648.
Scott, C. E., Arnold, S. R., Monks, S. A., Asmi, A., Paasonen, P., and Spracklen, D. V (2018). Substantial large-scale feedbacks between natural aerosols and climate. *Nat. Geosci.* 11, 44+. doi:10.1038/s41561-017-0020-5.

Scott, C. E., Monks, S. A., Spracklen, D. V., Arnold, S. R., Forster, P. M., Rap, A., et al. (2017). Impact on short-lived climate forcers (SLCFs) from a realistic land-use change scenario: Via changes in biogenic emissions. *Faraday Discuss.* doi:10.1039/c7fd00028f.
Screen, J. A., Deser, C., and Simmonds, I. (2012). Local and remote controls on observed Arctic warming. *Geophys. Res. Lett.* 39. doi:10.1029/2012GL051598.
Screen, J. A., and Simmonds, I. (2010). The central role of diminishing sea ice in recent Arctic temperature amplification. *Nature* 464, 1334. Available at: https://doi.org/10.1038/nature09051.
Seifert, A., Heus, T., Pincus, R., and Stevens, B. (2015). Large-eddy simulation of the transient and near-equilibrium behavior of precipitating shallow convection. *J. Adv. Model. Earth Syst.* 7, 1918–1937. doi:10.1002/2015MS000489.
Seinfeld, J. H., Bretherton, C., Carslaw, K. S., Coe, H., DeMott, P. J., Dunlea, E. J., et al. (2016). Improving our fundamental understanding of the role of aerosol-cloud interactions in the climate system. *Proc. Natl. Acad. Sci. U. S. A.* 113, 5781–90. doi:10.1073/pnas.1514043113.
Seneviratne, S. I., Donat, M. G., Pitman, A. J., Knutti, R., and Wilby, R. L. (2016). Allowable CO2emissions based on regional and impact-related climate targets. *Nature*. doi:10.1038/nature16542.
Senior, C. A., and Mitchell, J. F. B. (2000). The time-dependence of climate sensitivity.
Serreze, M. C., and Barry, R. G. (2011). Processes and impacts of Arctic amplification: A research synthesis. *Glob. Planet. Change* 77, 85–96. doi:https://doi.org/10.1016/j.gloplacha.2011.03.004.
Shaffer, G., Huber, M., Rondanelli, R., Olaf, J., and Pedersen, P. (2016). Deep time evidence for climate sensitivity increase with warming. doi:10.1002/2016GL069243.Received.
Shapiro, A. I., Schmutz, W., Rozanov, E., Schoell, M., Haberreiter, M., Shapiro, A. V., et al. (2011). A new approach to the long-term reconstruction of the solar irradiance leads to large historical solar forcing. *Astron. Astrophys.* 529, A67. doi:10.1051/0004-6361/201016173.
Shell, K. M., Kiehl, J. T., and Shields, C. A. (2008). Using the Radiative Kernel Technique to Calculate Climate Feedbacks in NCAR's Community Atmospheric Model. *J. Clim.* 21, 2269–2282. doi:10.1175/2007JCLI2044.1.
Sherwood, S. C., Bony, S., Boucher, O., Bretherton, C., Forster, P. M., Gregory, J. M., et al. (2015). Adjustments in the forcing-feedback framework for understanding climate change. *Bull. Am. Meteorol. Soc.* 96, 217–228. doi:10.1175/BAMS-D-13-00167.1.
Sherwood, S. C., Bony, S., and Dufresne, J.-L. (2014). Spread in model climate sensitivity traced to atmospheric convective mixing. *Nature* 505, 37. doi:10.1038/nature12829.
Shi, J.-R., Xie, S.-P., and Talley, L. D. (2018). Evolving Relative Importance of the Southern Ocean and North Atlantic in Anthropogenic Ocean Heat Uptake. *J. Clim.* doi:10.1175/JCLI-D-18-0170.1.
Shindell, D. T. (2014). Inhomogeneous forcing and transient climate sensitivity. *Nat. Clim. Chang.* doi:10.1038/nclimate2136.
Shindell, D. T. D. T., Faluvegi, G., Rotstayn, L., and Milly, G. (2015). Spatial patterns of radiative forcing and surface temperature response. *J. Geophys. Res. Atmos.* 120, 1–19. doi:10.1002/2014JD022752.Received.
Shindell, D. T., Lamarque, J. F., Schulz, M., Flanner, M., Jiao, C., Chin, M., et al. (2013). Radiative forcing in the ACCMIP historical and future climate simulations. *Atmos. Chem. Phys.* 13, 2939–2974. doi:10.5194/acp-13-2939-2013.
Shine, K. P. (2009). The global warming potential-the need for an interdisciplinary retrial. *Clim. Change*. doi:10.1007/s10584-009-9647-6.
Shine, K. P., Fuglestvedt, J. S., Hailemariam, K., and Stuber, N. (2005). Alternatives to the Global Warming Potential for comparing climate impacts of emissions of greenhouse gases. *Clim. Change* 68, 281–302. doi:10.1007/s10584-005-1146-9.
Shine, K. P. P., Allan, R. P. P., Collins, W. J. J., and Fuglestvedt, J. S. S. (2015). Metrics for linking emissions of gases and aerosols to global precipitation changes. *Earth Syst. Dyn.* 6, 525–540. doi:10.5194/esd-6-525-2015.
Shiogama, H., Watanabe, M., Yoshimori, M., Yokohata, T., Ogura, T., Annan, J. D., et al. (2012). Perturbed physics ensemble using the MIROC5 coupled atmosphere–ocean GCM without flux corrections: experimental design and results. *Clim. Dyn.* 39, 3041–3056. doi:10.1007/s00382-012-1441-x.
Siemann, A. L., Chaney, N., and Wood, E. F. (2018). Development and Validation of a Long-Term, Global, Terrestrial Sensible Heat Flux Dataset. *J. Clim.* 31, 6073–6095. doi:10.1175/JCLI-D-17-0732.1.
Siler, N., Po-Chedley, S., and Bretherton, C. S. (2018a). Variability in modeled cloud feedback tied to differences in the climatological spatial pattern of clouds. *Clim. Dyn.* 50, 1209–1220. doi:10.1007/s00382-017-3673-2.
Siler, N., Roe, G. H., and Armour, K. C. (2018b). Insights into the zonal-mean response of the hydrologic cycle to global warming from a diffusive energy balance model. *J. Clim.* doi:10.1175/JCLI-D-18-0081.1.
Silvers, L. G., Paynter, D., and Zhao, M. (2018). The Diversity of Cloud Responses to Twentieth Century Sea Surface Temperatures. *Geophys. Res. Lett.* 45, 391–400. doi:10.1002/2017GL075583.
Singarayer, J. S., and Valdes, P. J. (2010). High-latitude climate sensitivity to ice-sheet forcing over the last 120 kyr. *Quat. Sci. Rev.* 29, 43–55. doi:10.1016/j.quascirev.2009.10.011.

Singh, H. A., Garuba, O. A., and Rasch, P. J. (2018). How Asymmetries Between Arctic and Antarctic Climate Sensitivity Are Modified by the Ocean. *Geophys. Res. Lett.* doi:10.1029/2018GL079023.

Singh, H. A., Rasch, P. J., and Rose, B. E. J. (2017). Increased Ocean Heat Convergence Into the High Latitudes With CO2 Doubling Enhances Polar-Amplified Warming. *Geophys. Res. Lett.* doi:10.1002/2017GL074561.

Sitch, S., Huntingford, C., Gedney, N., Levy, P. E., Lomas, M., Piao, S. L., et al. (2008). Evaluation of the terrestrial carbon cycle, future plant geography and climate-carbon cycle feedbacks using five Dynamic Global Vegetation Models (DGVMs). *Glob. Chang. Biol.* 14, 2015–2039. doi:10.1111/j.1365-2486.2008.01626.x.

Six, K. D., Kloster, S., Ilyina, T., Archer, S. D., Zhang, K., and Maier-Reimer, E. (2013). Global warming amplified by reduced sulphur fluxes as a result of ocean acidification. *Nat. Clim. Chang.* 3, 975.

Skeie, R. B., Berntsen, T., Aldrin, M., Holden, M., and Myhre, G. (2014). A lower and more constrained estimate of climate sensitivity using updated observations and detailed radiative forcing time series. *Earth Syst. Dyn.* 5, 139–175. doi:10.5194/esd-5-139-2014.

Skeie, R. B., Berntsen, T. K., Myhre, G., Tanaka, K., Kvalevåg, M. M., and Hoyle, C. R. (2011). Anthropogenic radiative forcing time series from pre-industrial times until 2010. *Atmos. Chem. Phys.* doi:10.5194/acp-11-11827-2011.

Skiles, S. M., Flanner, M., Cook, J. M., Dumont, M., and Painter, T. H. (2018). Radiative forcing by light-absorbing particles in snow. *Nat. Clim. Chang.* 8, 964–971. doi:10.1038/s41558-018-0296-5.

Skinner, L. (2012). A Long View on Climate Sensitivity. *Science (80-.).* 337, 917–919. doi:10.1126/science.1224011.

Smith, C. J., Forster, P. M., Allen, M., Fuglestvedt, J., Millar, R. J., Rogelj, J., et al. (2019). Current fossil fuel infrastructure does not yet commit us to 1.5 °C warming. *Nat. Commun.* doi:10.1038/s41467-018-07999-w.

Smith, C. J., Forster, P. M., Allen, M., Leach, N., Millar, R. J., Passerello, G. A., et al. (2018a). FAIR v1.3: A simple emissions-based impulse response and carbon cycle model. *Geosci. Model Dev.* doi:10.5194/gmd-11-2273-2018.

Smith, C. J., Kramer, R. J., Myhre, G., Forster, P. M., Soden, B. J., Andrews, T., et al. (2018b). Understanding Rapid Adjustments to Diverse Forcing Agents. *Geophys. Res. Lett.* 45. doi:10.1029/2018GL079826.

Smith, D. M., Allan, R. P., Coward, A. C., Eade, R., Hyder, P., Liu, C., et al. (2015). Earth's energy imbalance since 1960 in observations and CMIP5 models. *Geophys. Res. Lett.* 42, 1205–1213. doi:10.1002/2014GL062669.

Smith, S. M., Lowe, J. A., Bowerman, N. H. A., Gohar, L. K., Huntingford, C., and Allen, M. R. (2012). Equivalence of greenhouse-gas emissions for peak temperature limits. *Nat. Clim. Chang.* 2, 535–538. doi:10.1038/nclimate1496.

Snyder, C. W. (2016). Evolution of global temperature over the past two million years. *Nature* 538, 226–228. doi:10.1038/nature19798.

Soden, B. J., and Held, I. M. (2006). An Assessment of Climate Feedbacks in Coupled Ocean–Atmosphere Models. *J. Clim.* 19, 3354–3360. doi:10.1175/JCLI3799.1.

Soden, B. J. J., Collins, W. D. D., and Feldman, D. R. R. (2018). Reducing uncertainties in climate models. *Science (80-.).* 361, 326–327. doi:10.1126/science.aau1864.

Soden, B. J. J., Held, I. . M. M., Coleman, R., Shell, K. M. M., Kiehl, J. T. T., Shields, C. A. A., et al. (2008). Quantifying Climate Feedbacks Using Radiative Kernels. *J. Clim.* 21, 3504–3520. doi:10.1175/2007JCLI2110.1.

Solomon, A. (2006). Impact of latent heat release on polar climate. *Geophys. Res. Lett.* doi:10.1029/2005GL025607.

Soni, V. K., Pandithurai, G., and Pai, D. S. (2016). Is there a transition of solar radiation from dimming to brightening over India? *Atmos. Res.* 169, 209–224. doi:10.1016/j.atmosres.2015.10.010.

Spencer, R. W., and Braswell, W. D. (2010). On the diagnosis of radiative feedback in the presence of unknown radiative forcing. *J. Geophys. Res. Atmos.* doi:10.1029/2009JD013371.

Spencer, R. W., and Braswell, W. D. (2011). On the misdiagnosis of surface temperature feedbacks from variations in Earth's radiant energy balance. *Remote Sens.* doi:10.3390/rs3081603.

Stainforth, D. A., Aina, T., Christensen, C., Collins, M., Faull, N., Frame, D. J., et al. (2005). Uncertainty in predictions of the climate response to rising levels of greenhouse gases. *Nature* 433, 403–406. doi:10.1038/nature03301.

Stanhill, G., Achiman, O., Rosa, R., and Cohen, S. (2014). The cause of solar dimming and brightening at the Earth's surface during the last half century: Evidence from measurements of sunshine duration. *J. Geophys. Res.* 119, 10902–10911. doi:10.1002/2013JD021308.

Steffen, W., Rockström, J., Richardson, K., Lenton, T. M., Folke, C., Liverman, D., et al. (2018). Trajectories of the Earth System in the Anthropocene. *Proc. Natl. Acad. Sci.* 115, 8252–8259. doi:10.1073/pnas.1810141115.

Stein, T. H. M., Holloway, C. E., Tobin, I., and Bony, S. (2016). Observed Relationships between Cloud Vertical Structure and Convective Aggregation over Tropical Ocean. *J. Clim.* 30, 2187–2207. doi:10.1175/JCLI-D-16-0125.1.

Steinhilber, F., Abreu, J. A., Beer, J., Brunner, I., Christl, M., Fischer, H., et al. (2012). 9,400 years of cosmic radiation and solar activity from ice cores and tree rings. *Proc. Natl. Acad. Sci.* 109, 5967–5971. doi:10.1073/pnas.1118965109.

Stephens, G. L., Hakuba, M. Z., Hawcroft, M., Haywood, J. M., Behrangi, A., Kay, J. E., et al. (2016). The Curious Nature of the Hemispheric Symmetry of the Earth's Water and Energy Balances. *Curr. Clim. Chang. Reports* 2, 135–147. doi:10.1007/s40641-016-0043-9.

Stephens, G. L., O'Brien, D., Webster, P. J., Pilewski, P., Kato, S., and Li, J. (2015). The albedo of Earth. *Rev. Geophys.* 53, 141–163. doi:10.1002/2014RG000449.

Stephens, G. L., Vane, D. G., Boain, R. J., Mace, G. G., Sassen, K., Wang, Z., et al. (2002). THE CLOUDSAT MISSION AND THE A-TRAIN. *Bull. Am. Meteorol. Soc.* 83, 1771–1790. doi:10.1175/BAMS-83-12-1771.

Sterner, E., Johansson, D. J. A., and Azar, C. (2014). Emission metrics and sea level rise. *Clim. Change*. doi:10.1007/s10584-014-1258-1.

Sterner, E. O., and Johansson, D. J. A. (2017). The effect of climate-carbon cycle feedbacks on emission metrics. *Environ. Res. Lett.* doi:10.1088/1748-9326/aa61dc.

Stevens, B. (2015). Rethinking the lower bound on aerosol radiative forcing. *J. Clim.* 28, 4794–4819. doi:10.1175/JCLI-D-14-00656.1.

Stevens, B., and Feingold, G. (2009). Untangling aerosol effects on clouds and precipitation in a buffered system. *Nature* 461, 607.

Stevens, B., Fiedler, S., Kinne, S., Peters, K., Rast, S., Müsse, J., et al. (2017). MACv2-SP: a parameterization of anthropogenic aerosol optical properties and an associated Twomey effect for use in CMIP6. *Geosci. Model Dev.* 10, 433–452. doi:10.5194/gmd-10-433-2017.

Stevens, B., Sherwood, S. C., Bony, S., and Webb, M. J. (2016). Earth ' s Future Prospects for narrowing bounds on Earth ' s equilibrium climate sensitivity Earth ' s Future. 1–11. doi:10.1002/2016EF000376.Received.

Stevens, B., Vali, G., Comstock, K., Wood, R., van Zanten, M. C., Austin, P. H., et al. (2005). POCKETS OF OPEN CELLS AND DRIZZLE IN MARINE STRATOCUMULUS. *Bull. Am. Meteorol. Soc.* 86, 51–58. doi:10.1175/BAMS-86-1-51.

Stevenson, D. S., Young, P. J., Naik, V., Lamarque, J.-F., Shindell, D. T., Voulgarakis, A., et al. (2013). Tropospheric ozone changes, radiative forcing and attribution to emissions in the Atmospheric Chemistry and Climate Model Intercomparison Project (ACCMIP). *Atmos. Chem. Phys.* 13, 3063–3085. doi:10.5194/acp-13-3063-2013.

Stier, P. (2016). Limitations of passive remote sensing to constrain global cloud condensation nuclei. *Atmos. Chem. Phys.* 16, 6595–6607. doi:10.5194/acp-16-6595-2016.

Stjern, C. W., Samset, B. H., Myhre, G., Forster, P. M., Hodnebrog, Ø., Andrews, T., et al. (2017). Rapid Adjustments Cause Weak Surface Temperature Response to Increased Black Carbon Concentrations. *J. Geophys. Res. Atmos.* doi:10.1002/2017JD027326.

Stolarski, R. S., and Frith, S. M. (2006). Search for evidence of trend slow-down in the long-term TOMS/SBUV total ozone data record: The importance of instrument drift uncertainty. *Atmos. Chem. Phys.* doi:10.5194/acp-6-4057-2006.

Storelvmo, T. (2017). Aerosol Effects on Climate via Mixed-Phase and Ice Clouds. *Annu. Rev. Earth Planet. Sci.* doi:10.1146/annurev-earth-060115-012240.

Storelvmo, T., Heede, U. K., Leirvik, T., Phillips, P. C. B., Arndt, P., and Wild, M. (2018). Lethargic response to aerosol emissions in current climate models. *Geophys. Res. Lett.* in press.

Storelvmo, T., Leirvik, T., Lohmann, U., Phillips, P. C. B., and Wild, M. (2016). Disentangling greenhouse warming and aerosol cooling to reveal Earth's climate sensitivity. *Nat. Geosci.* 9, 286–289. doi:10.1038/ngeo2670.

Storelvmo, T., Tan, I., and Korolev, A. V. (2015). Cloud phase changes induced by CO2 warming—A powerful yet poorly constrained cloud-climate feedback. *Curr. Clim. Chang. Rep.* 1, 288–296.

Stouffer, R. J. (2004). Time scales of climate response. *J. Clim.* 17, 209–217. doi:10.1175/1520-0442(2004)017<0209:TSOCR>2.0.CO;2.

Stouffer, R. J., and Manabe, S. (2003). Equilibrium response of thermohaline circulation to large changes in atmospheric CO2 concentration. *Clim. Dyn.* 20, 759–773. doi:10.1007/s00382-002-0302-4.

Stouffer, R. J., Russell, J., and Spelman, M. J. (2006). Importance of oceanic heat uptake in transient climate change. *Geophys. Res. Lett.* doi:10.1029/2006GL027242.

Stroeve, J. C., Kattsov, V., Barrett, A., Serreze, M., Pavlova, T., Holland, M., et al. (2012). Trends in Arctic sea ice extent from CMIP5, CMIP3 and observations. *Geophys. Res. Lett.* 39. doi:10.1029/2012GL052676.

Stuecker, M. F., Bitz, C. M., Armour, K. C., Proistosescu, C., Kang, S. M., Xie, S.-P., et al. (2018). Polar amplification dominated by local forcing and feedbacks. *Submitt. to Nat. Clim. Chang.*

Sun, C., Kucharski, F., Li, J., Jin, F. F., Kang, I. S., and Ding, R. (2017). Western tropical Pacific multidecadal variability forced by the Atlantic multidecadal oscillation. *Nat. Commun.* 8. doi:10.1038/ncomms15998.

Suzuki, K., Golaz, J.-C., and Stephens, G. L. (2013). Evaluating cloud tuning in a climate model with satellite observations. *Geophys. Res. Lett.* 40, 4464–4468. doi:10.1002/grl.50874.

Suzuki, K., Stephens, G., Bodas-Salcedo, A., Wang, M., Golaz, J.-C., Yokohata, T., et al. (2015). Evaluation of the Warm Rain Formation Process in Global Models with Satellite Observations. *J. Atmos. Sci.* 72, 3996–4014. doi:10.1175/JAS-D-14-0265.1.

Svensmark, H. (1998). Influence of Cosmic Rays on Earth's Climate. *Phys. Rev. Lett.* 81, 5027–5030. doi:10.1103/PhysRevLett.81.5027.

Swingedouw, D., Fichefet, T., Huybrechts, P., Goosse, H., Driesschaert, E., and Loutre, M.-F. (2008). Antarctic ice-

sheet melting provides negative feedbacks on future climate warming. *Geophys. Res. Lett.* 35. doi:10.1029/2008GL034410.
Takahashi, C., and Watanabe, M. (2016). Pacific trade winds accelerated by aerosol forcing over the past two decades. *Nat. Clim. Chang.* 6, 768. Available at: http://dx.doi.org/10.1038/nclimate2996.
Tan, I., Storelvmo, T., and Zelinka, M. D. (2016). Observational constraints on mixed-phase clouds imply higher climate sensitivity. *Science (80-.).* 352, 224 LP-227. Available at: http://science.sciencemag.org/content/352/6282/224.abstract.
Tanaka, K., Ohmura, A., Folini, D., Wild, M., and Ohkawara, N. (2016). Is global dimming and brightening in Japan limited to urban areas? *Atmos. Chem. Phys.* 16, 13969–14001. doi:10.5194/acp-16-13969-2016.
Tang, T., Shindell, D. T., Faluvegi, G., Myhre, G., Olivié, D., Voulgarakis, A., et al. Comparison of Effective Radiative Forcing Calculations using Multiple Methods, Drivers, and Models.
Tao, W. K., Chen, J. P., Li, Z., Wang, C., and Zhang, C. (2012). Impact of aerosols on convective clouds and precipitation. *Rev. Geophys.* doi:10.1029/2011RG000369.
Taylor, P. C., Cai, M., Hu, A., Meehl, J., Washington, W., and Zhang, G. J. (2013). A Decomposition of Feedback Contributions to Polar Warming Amplification. *J. Clim.* 26, 7023–7043. doi:10.1175/JCLI-D-12-00696.1.
Tebaldi, C., and Arblaster, J. M. (2014). Pattern scaling: Its strengths and limitations, and an update on the latest model simulations. *Clim. Change*. doi:10.1007/s10584-013-1032-9.
Tebaldi, C., and Knutti, R. (2018). Evaluating the accuracy of climate change pattern emulation for low warming targets. *Environ. Res. Lett.* 13, 55006. doi:10.1088/1748-9326/aabef2.
Tegen, I., Werner, M., Harrison, S. P., and Kohfeld, K. E. (2004). Relative importance of climate and land use in determining present and future global soil dust emission. *Geophys. Res. Lett.* 31.
Terai, C. R., Bretherton, C. S., Wood, R., and Painter, G. (2014). Aircraft observations of aerosol, cloud, precipitation, and boundary layer properties in pockets of open cells over the southeast Pacific. *Atmos. Chem. Phys.* 14, 8071–8088. doi:10.5194/acp-14-8071-2014.
Terai, C. R., Klein, S. A., and Zelinka, M. D. (2016). Constraining the lowcloud optical depth feedback at middle and high latitudes using satellite observations. *J. Geophys. Res.* 121, 9696–9716. doi:10.1002/2016JD025233.
Tobin, I., Bony, S., Holloway, C. E., Grandpeix, J.-Y., Sèze, G., Coppin, D., et al. (2013). Does convective aggregation need to be represented in cumulus parameterizations? *J. Adv. Model. Earth Syst.* 5, 692–703. doi:10.1002/jame.20047.
Tobin, I., Bony, S., and Roca, R. (2012). Observational evidence for relationships between the degree of aggregation of deep convection, water vapor, surface fluxes, and radiation. *J. Clim.* 25, 6885–6904. doi:10.1175/JCLI-D-11-00258.1.
Tol, R. S. J., Berntsen, T. K., O'Neill, B. C., Fuglestvedt, J. S., and Shine, K. P. (2012). A unifying framework for metrics for aggregating the climate effect of different emissions. *Environ. Res. Lett.* 7, 044006. doi:10.1088/1748-9326/7/4/044006.
Toll, V., Christensen, M., Gassó, S., and Bellouin, N. (2017). Volcano and Ship Tracks Indicate Excessive Aerosol-Induced Cloud Water Increases in a Climate Model. *Geophys. Res. Lett.* 44, 12,492-12,500. doi:10.1002/2017GL075280.
Tomassini, L., Reichert, P., Knutti, R., Stocker, T. F., and Borsuk, M. E. (2007). Robust Bayesian Uncertainty Analysis of Climate System Properties Using Markov Chain Monte Carlo Methods. *J. Clim.* 20, 1239–1254. doi:10.1175/JCLI4064.1.
Totterdill, A., Kovács, T., Feng, W., Dhomse, S., Smith, C., Carlos Gómez-Martín, J., et al. (2016). Atmospheric lifetimes, infrared absorption spectra, radiative forcings and global warming potentials of NF3 and CF3CF2Cl (CFC-115). *Atmos. Chem. Phys.* 16, 11451–11463. doi:10.5194/acp-16-11451-2016.
Trenberth, K. E., and Fasullo, J. T. (2009). Global warming due to increasing absorbed solar radiation. *Geophys. Res. Lett.* 36. doi:10.1029/2009GL037527.
Trenberth, K. E., and Fasullo, J. T. (2010). Simulation of Present-Day and Twenty-First-Century Energy Budgets of the Southern Oceans. *J. Clim.* 23, 440–454. doi:10.1175/2009JCLI3152.1.
Trenberth, K. E., Fasullo, J. T., and Balmaseda, M. A. (2014). Earth's Energy Imbalance. *J. Clim.* 27, 3129–3144. doi:10.1175/JCLI-D-13-00294.1.
Trenberth, K. E., and Stepaniak, D. P. (2003). Seamless poleward atmospheric energy transports and implications for the Hadley circulation. *J. Clim.* doi:10.1175/1520-0442(2003)016<3706:SPAETA>2.0.CO;2.
Trenberth, K. E., Zhang, Y., Fasullo, J. T., and Taguchi, S. (2015). Climate variability and relationships between top-of-atmosphere radiation and temperatures on Earth. *J. Geophys. Res. Atmos.* 120, 3642–3659. doi:10.1002/2014JD022887.
Tsushima, Y., Brient, F., Klein, S. A., Konsta, D., Nam, C. C., Qu, X., et al. (2017). The Cloud Feedback Model Intercomparison Project (CFMIP) Diagnostic Codes Catalogue – metrics, diagnostics and methodologies to evaluate, understand and improve the representation of clouds and cloud feedbacks in climate models. *Geosci. Model Dev.* 10, 4285–4305. doi:10.5194/gmd-10-4285-2017.

Tsushima, Y., Iga, S. I., Tomita, H., Satoh, M., Noda, A. T., and Webb, M. J. (2014). High cloud increase in a perturbed SST experiment with a global nonhydrostatic model including explicit convective processes. *J. Adv. Model. Earth Syst.* 6, 571–585. doi:https://doi.org/10.1002/2013MS000301.

Tsushima, Y., and Manabe, S. (2013). Assessment of radiative feedback in climate models using satellite observations of annual flux variation. *Proc. Natl. Acad. Sci.* doi:10.1073/pnas.1216174110.

Tsushima, Y., Ringer, M. A., Webb, M. J., and Williams, K. D. (2013). Quantitative evaluation of the seasonal variations in climate model cloud regimes. *Clim. Dyn.* 41, 2679–2696. doi:10.1007/s00382-012-1609-4.

Turnock, S. T., Spracklen, D. V, Carslaw, K. S., Mann, G. W., Woodhouse, M. T., Forster, P. M., et al. (2015). Modelled and observed changes in aerosols and surface solar radiation over Europe between 1960 and 2009. *Atmos. Chem. Phys.* 15, 9477–9500. doi:10.5194/acp-15-9477-2015.

Tuzet, F., Dumont, M., Lafaysse, M., Picard, G., Arnaud, L., Voisin, D., et al. (2017). A multilayer physically based snowpack model simulating direct and indirect radiative impacts of light-absorbing impurities in snow. *Cryosph.* 11, 2633–2653. doi:10.5194/tc-11-2633-2017.

Twomey, S. (1959). The nuclei of natural cloud formation part II: The supersaturation in natural clouds and the variation of cloud droplet concentration. *Geofis. Pura e Appl.* 43, 243–249. doi:10.1007/BF01993560.

Twomey, S. (1977). The Influence of Pollution on the Shortwave Albedo of Clouds. *J. Atmos. Sci.* 34, 1149–1152. doi:10.1175/1520-0469(1977)034<1149:TIOPOT>2.0.CO;2.

Unger, N. (2014). Human land-use-driven reduction of forest volatiles cools global climate. *Nat. Clim. Chang.* doi:10.1038/nclimate2347.

vanZanten, M. C., Stevens, B., Vali, G., Lenschow, D. H., vanZanten, M. C., Stevens, B., et al. (2005). Observations of Drizzle in Nocturnal Marine Stratocumulus. *J. Atmos. Sci.* 62, 88–106. doi:10.1175/JAS-3355.1.

Várnai, T., and Marshak, A. (2015). Effect of Cloud Fraction on Near-Cloud Aerosol Behavior in the MODIS Atmospheric Correction Ocean Color Product. *Remote Sens.* 7, 5283–5299. doi:10.3390/rs70505283.

Vecchi, G. A., Soden, B. J., Wittenberg, A. T., Held, I. M., Leetmaa, A., and Harrison, M. J. (2006). Weakening of tropical Pacific atmospheric circulation due to anthropogenic forcing. *Nature* 441, 73–76. doi:10.1038/nature04744.

Vecchi, G., Clement, A., and Soden, B. J. (2008). Examining the Tropical Pacific's Response to Global Warming. *Eos (Washington. DC).*

Vergara-Temprado, J., Holden, M. A., Orton, T. R., O'Sullivan, D., Umo, N. S., Browse, J., et al. (2018). Is Black Carbon an Unimportant Ice-Nucleating Particle in Mixed-Phase Clouds? *J. Geophys. Res. Atmos.* doi:10.1002/2017JD027831.

Vial, J., Dufresne, J.-L. L., and Bony, S. (2013). On the interpretation of inter-model spread in CMIP5 climate sensitivity estimates. *Clim. Dyn.* 41, 3339–3362. doi:10.1007/s00382-013-1725-.

Vieira, L. E. A., Solanki, S. K., Krivova, N. A., and Usoskin, I. (2011). Evolution of the solar irradiance during the Holocene. *Astron. Astrophys.* 531, A6. doi:10.1051/0004-6361/201015843.

Vizcaíno, M., Mikolajewicz, U., Jungclaus, J., and Schurgers, G. (2010). Climate modification by future ice sheet changes and consequences for ice sheet mass balance. *Clim. Dyn.* 34, 301–324. doi:10.1007/s00382-009-0591-y.

Voigt, A., and Shaw, T. A. (2015). Circulation response to warming shaped by radiative changes of clouds and water vapour. *Nat. Geosci.* 8, 102. doi:10.1038/ngeo2345.

Voigt, A., and Shaw, T. A. (2016). Impact of regional atmospheric cloud radiative changes on shifts of the extratropical jet stream in response to global warming. *J. Clim.* 29, 8399–8421. doi:10.1175/JCLI-D-16-0140.1.

Voigt, A., Stevens, B., Bader, J., and Mauritsen, T. (2013). The observed hemispheric symmetry in reflected shortwave irradiance. *J. Clim.* 26, 468–477. doi:10.1175/JCLI-D-12-00132.1.

Volodin, E. M. (2008). Relation between temperature sensitivity to doubled carbon dioxide and the distribution of clouds in current climate models. *Izv. Atmos. Ocean. Phys.* 44, 288–299. doi:10.1134/S0001433808030043.

von der Heydt, A. S., and Ashwin, P. (2016). State-dependence of climate sensitivity: attractor constraints and palaeoclimate regimes. 1–21. doi:10.1093/climsys/dzx001.

von der Heydt, A. S., Dijkstra, H. A., Köhler, P., and Wal, R. Van De (2014). On the background state dependency of (palaeo) climate sensitivity. *Geophys. Res. Lett.* 41, 6484–6492. doi:doi:10.1002/2014GL061121.

von der Heydt, A. S., Dijkstra, H. A., van de Wal, R. S. W., Caballero, R., Crucifix, M., Foster, G. L., et al. (2016). Lessons on Climate Sensitivity From Past Climate Changes. *Curr. Clim. Chang. Reports* 2, 148–158. doi:10.1007/s40641-016-0049-3.

Von Schuckmann, K., Palmer, M. D., Trenberth, K. E., Cazenave, A., Chambers, D., Champollion, N., et al. (2016). An imperative to monitor Earth's energy imbalance. *Nat. Clim. Chang.* 6, 138–144. doi:10.1038/nclimate2876.

Voss, R., and Mikolajewicz, U. (2001). Long-term climate changes due to increased CO2 concentration in the coupled atmosphere-ocean general circulation model ECHAM3/LSG. *Clim. Dyn.* 17, 45–60. doi:10.1007/pl00007925.

Wang, K. C., Ma, Q., Wang, X. Y., and Wild, M. (2014). Urban impacts on mean and trend of surface incident solar radiation. *Geophys. Res. Lett.* 41, 4664–4668. doi:Doi 10.1002/2014gl060201.

Wang, M., Xu, B., Cao, J., Tie, X., Wang, H., Zhang, R., et al. (2015). Carbonaceous aerosols recorded in a

southeastern Tibetan glacier: analysis of temporal variations and model estimates of sources and radiative forcing. *Atmos. Chem. Phys.* 15, 1191–1204. doi:10.5194/acp-15-1191-2015.
Wang, R., Andrews, E., Balkanski, Y., Boucher, O., Myhre, G., Samset, B. H., et al. (2018). Spatial Representativeness Error in the Ground-Level Observation Networks for Black Carbon Radiation Absorption. *Geophys. Res. Lett.* 45, 2106–2114. doi:10.1002/2017GL076817.
Wang, R., Balkanski, Y., Boucher, O., Ciais, P., Schuster, G. L., Chevallier, F., et al. (2016). Estimation of global black carbon direct radiative forcing and its uncertainty constrained by observations. *J. Geophys. Res. Atmos.* 121, 5948–5971. doi:10.1002/2015JD024326.
Wang, Y., and Wild, M. (2016). A new look at solar dimming and brightening in China. *Geophys. Res. Lett.* 43, 11777–11785. doi:10.1002/2016GL071009.
Wang, Z., Zhang, H., Jing, X., and Wei, X. (2013). Effect of non-spherical dust aerosol on its direct radiative forcing. *Atmos. Res.* 120–121, 112–126. doi:10.1016/j.atmosres.2012.08.006.
Waquet, F., Péré, J.-C., Peers, F., Goloub, P., Ducos, F., Thieuleux, F., et al. (2016). Global detection of absorbing aerosols over the ocean in the red and near-infrared spectral region. *J. Geophys. Res. Atmos.* 121, 10,902-10,918. doi:10.1002/2016JD025163.
Wara, M. W., Ravelo, A. C., and Delaney, M. L. (2005). Permanent El Niño-Like Conditions During the Pliocene Warm Period. *Science (80-.).* 309, 758 LP-761. Available at: http://science.sciencemag.org/content/309/5735/758.abstract.
Ward, D. S., Mahowald, N. M., and Kloster, S. (2014). Potential climate forcing of land use and land cover change. *Atmos. Chem. Phys.* doi:10.5194/acp-14-12701-2014.
Warren, S. G. (2013). Can black carbon in snow be detected by remote sensing? *J. Geophys. Res. Atmos.* 118, 779–786. doi:10.1029/2012JD018476.
Watanabe, M., Shiogama, H., Yokohata, T., Kamae, Y., Yoshimori, M., Ogura, T., et al. (2012). Using a multiphysics ensemble for exploring diversity in cloud-shortwave feedback in GCMs. *J. Clim.* 25, 5416–5431.
Weaver, A. J., Eby, M., Kienast, M., and Saenko, O. A. (2007). Response of the Atlantic meridional overturning circulation to increasing atmospheric CO2: Sensitivity to mean climate state. *Geophys. Res. Lett.* doi:10.1029/2006GL028756.
Webb, M. J., Lambert, F. H., and Gregory, J. M. (2013). Origins of differences in climate sensitivity, forcing and feedback in climate models. *Clim. Dyn.* 40, 677–707. doi:10.1007/s00382-012-1336-x.
Webb, M. J., Lock, A. P., Bretherton, C. S., Bony, S., Cole, J. N. S., Idelkadi, A., et al. (2015). The impact of parametrized convection on cloud feedback. *Philos. Trans. R. Soc. A Math. Phys. Eng. Sci.* 373. doi:10.1098/rsta.2014.0414.
Wen, Q., Yao, J., Döös, K., and Yang, H. (2018). Decoding hosing and heating effects on global temperature and meridional circulations in a warming climate. *J. Clim.* doi:10.1175/JCLI-D-18-0297.1.
Wetherald, R. T., and Manabe, S. (1988). Cloud Feedback Processes in a General Circulation Model. *J. Atmos. Sci.* 45, 1397–1416.
Wigley, T. M. L., Ammann, C. M., Santer, B. D., and Raper, S. C. B. (2005). Effect of climate sensitivity on the response to volcanic forcing. *J. Geophys. Res. D Atmos.* doi:10.1029/2004JD005557.
Wijffels, S., Roemmich, D., Monselesan, D., Church, J., and Gilson, J. (2016). Ocean temperatures chronicle the ongoing warming of Earth. *Nat. Clim. Chang.* 6, 116–118. doi:10.1038/nclimate2924.
Wild, M. (2016). Decadal changes in radiative fluxes at land and ocean surfaces and their relevance for global warming. *Wiley Interdiscip. Rev. Chang.* 7, 91–107. doi:10.1002/wcc.372.
Wild, M. (2017). Towards Global Estimates of the Surface Energy Budget. *Curr. Clim. Chang. Reports* 3, 87–97. doi:10.1007/s40641-017-0058-x.
Wild, M., Folini, D., Hakuba, M. Z., Schär, C., Seneviratne, S. I., Kato, S., et al. (2015). The energy balance over land and oceans: an assessment based on direct observations and CMIP5 climate models. *Clim. Dyn.* 44, 3393–3429. doi:10.1007/s00382-014-2430-z.
Wild, M., Folini, D., Schar, C., Loeb, N., Dutton, E. G., and König-Langlo, G. (2013). The global energy balance from a surface perspective. *Clim. Dyn.* 40, 3107–3134. doi:10.1007/S00382-012-1569-8.
Wild, M., Hakuba, M. Z., Folini, D., Dörig-Ott, P., Schär, C., Kato, S., et al. (2019). The cloud-free global energy balance and inferred cloud radiative effects: an assessment based on direct observations and climate models. *Clim. Dyn.* doi:https://doi.org/10.1007/s00382-018-4413-y.
Wild, M., and Schmucki, E. (2011). Assessment of global dimming and brightening in IPCC-AR4/CMIP3 models and ERA40. *Clim. Dyn.* 37, 1671–1688. doi:Doi 10.1007/S00382-010-0939-3.
Willeit, M., Ganopolski, A., and Feulner, G. (2014). Asymmetry and uncertainties in biogeophysical climate-vegetation feedback over a range of CO2 forcings. *Biogeosciences* 11, 17–32. doi:10.5194/bg-11-17-2014.
Williams, I. N., and Pierrehumbert, R. T. (2017). Observational evidence against strongly stabilizing tropical cloud feedbacks. *Geophys. Res. Lett.* 44, 1503–1510. doi:10.1002/2016GL072202.
Williams, K. D., Ingram, W. J., and Gregory, J. M. (2008). Time variation of effective climate sensitivity in GCMs. *J.*

Clim. doi:10.1175/2008JCLI2371.1.
Wing, A. A., and Emanuel, K. A. (2014). Physical mechanisms controlling self-aggregation of convection in idealized numerical modeling simulations. *J. Adv. Model. Earth Syst.* 6, 59–74. doi:10.1002/2013MS000269.
Wing, A. A., Emanuel, K., Holloway, C. E., and Muller, C. (2017). Convective Self-Aggregation in Numerical Simulations: A Review. *Surv. Geophys.* 38, 1173–1197. doi:10.1007/s10712-017-9408-4.
Winguth, A., Shellito, C., Shields, C., and Winguth, C. (2010). Climate Response at the Paleocene–Eocene Thermal Maximum to Greenhouse Gas Forcing—A Model Study with CCSM3. *J. Clim.* 23, 2562–2584. doi:10.1175/2009JCLI3113.1.
Winnick, M. J., and Caves, J. K. (2015). Oxygen isotope mass-balance constraints on Pliocene sea level and East Antarctic Ice Sheet stability. *Geology* 43, 879–882. doi:10.1130/G36999.1.
Winton, M. (2006). Amplified Arctic climate change: What does surface albedo feedback have to do with it? *Geophys. Res. Lett.* 33. doi:10.1029/2005GL025244.
Winton, M., Adcroft, A., Griffies, S. M., Hallberg, R. W., Horowitz, L. W., and Stouffer, R. J. (2013a). Influence of ocean and atmosphere components on simulated climate sensitivities. *J. Clim.* doi:10.1175/JCLI-D-12-00121.1.
Winton, M., Griffies, S. M., Samuels, B. L., Sarmiento, J. L., and Licher, T. L. F. (2013b). Connecting changing ocean circulation with changing climate. *J. Clim.* doi:10.1175/JCLI-D-12-00296.1.
Winton, M., Takahashi, K., and Held, I. M. (2010). Importance of Ocean Heat Uptake Efficacy to Transient Climate Change. *J. Clim.* 23, 2333–2344. doi:10.1175/2009JCLI3139.1.
Wong, A., Keeley, R., and Carval, T. (2018). Argo Quality Control Manual For CTD and Trajectory Data. USA, FRANCE doi:10.13155/33951.
Wood, R., and Bretherton, C. S. (2006). On the relationship between stratiform low cloud cover and lower-tropospheric stability. *J. Clim.* doi:10.1175/JCLI3988.1.
Wood, R., Bretherton, C. S., Leon, D., Clarke, A. D., Zuidema, P., Allen, G., et al. (2011). An aircraft case study of the spatial transition from closed to open mesoscale cellular convection over the Southeast Pacific. *Atmos. Chem. Phys.* 11, 2341–2370. doi:10.5194/acp-11-2341-2011.
Woods, C., and Caballero, R. (2016). The role of moist intrusions in winter arctic warming and sea ice decline. *J. Clim.* doi:10.1175/JCLI-D-15-0773.1.
Wu, C.-J., Krivova, N. A., Solanki, S. K., and Usoskin, I. G. (2018). Solar total and spectral irradiance reconstruction over the last 9000 years. *Astron. Astrophys.* 620, A120. doi:10.1051/0004-6361/201832956.
Wyant, M. C., Bretherton, C. S., Bacmeister, J. T., Kiehl, J. T., Held, I. M., Zhao, M., et al. (2006). A comparison of low-latitude cloud properties and their response to climate change in three {AGCMs} sorted into regimes using mid-tropospheric vertical velocity. 27, 261–279, doi: 10.1007/s00382-006-0138-4.
Xie, B., Zhang, H., Wang, Z., Zhao, S., and Fu, Q. (2016). A Modeling Study of E ff ective Radiative Forcing and Climate Response Due to Tropospheric Ozone. 33, 819–828.
Xie, S. P., Deser, C., Vecchi, G. A., Ma, J., Teng, H., and Wittenberg, A. T. (2010). Global warming pattern formation: Sea surface temperature and rainfall. *J. Clim.* doi:10.1175/2009JCLI3329.1.
Yan, H., Li, Z., Huang, J., Cribb, M., and Liu, J. (2014). Long-term aerosol-mediated changes in cloud radiative forcing of deep clouds at the top and bottom of the atmosphere over the Southern Great Plains. *Atmos. Chem. Phys.* 14, 7113–7124. doi:10.5194/acp-14-7113-2014.
Yang, H., Wen, Q., Yao, J., and Wang, Y. (2017). Bjerknes compensation in meridional heat transport under freshwater forcing and the role of climate feedback. *J. Clim.* doi:10.1175/JCLI-D-16-0824.1.
Yang, J., Wang, Z., and Heymsfield, A. (2018a). On the freezing time of supercooled drops in developing convective clouds over tropical ocean. *Atmos. Res.* 211, 30–37. doi:10.1016/J.ATMOSRES.2018.04.023.
Yang, P., Feng, Q., Hong, G., Kattawar, G. W., Wiscombe, W. J., Mishchenko, M. I., et al. (2007). Modeling of the scattering and radiative properties of nonspherical dust-like aerosols. *J. Aerosol Sci.* 38, 995–1014. doi:10.1016/J.JAEROSCI.2007.07.001.
Yang, S., Wang, X. L., and Wild, M. (2018b). Homogenization and Trend Analysis of the 1958-2016 In Situ Surface Solar Radiation Records in China. *J. Clim.* 31, 4529–4541. doi:10.1175/JCLI-D-17-0891.1.
Yi, B., Hsu, C. N., Yang, P., and Tsay, S.-C. (2011). Radiative transfer simulation of dust-like aerosols: Uncertainties from particle shape and refractive index. *J. Aerosol Sci.* 42, 631–644. doi:10.1016/J.JAEROSCI.2011.06.008.
Yin, J. H. (2005). A consistent poleward shift of the storm tracks in simulations of 21st century climate. *Geophys. Res. Lett.* 32, 1–4. doi:10.1029/2005GL023684.
Yoshimori, M., Abe-Ouchi, A., and Laîné, A. (2017). The role of atmospheric heat transport and regional feedbacks in the Arctic warming at equilibrium. *Clim. Dyn.* doi:10.1007/s00382-017-3523-2.
Yoshimori, M., Hargreaves, J. C., Annan, J. D., Yokohata, T., and Abe-Ouchi, A. (2011). Dependency of feedbacks on forcing and climate state in physics parameter ensembles. *J. Clim.* 24, 6440–6455. doi:10.1175/2011JCLI3954.1.
You, Q. L., Sanchez-Lorenzo, A., Wild, M., Folini, D., Fraedrich, K., Ren, G. Y., et al. (2013). Decadal variation of surface solar radiation in the Tibetan Plateau from observations, reanalysis and model simulations. *Clim. Dyn.* 40, 2073–2086. doi:Doi 10.1007/S00382-012-1383-3.

Yu, L. (2019). “Global Air-Sea Fluxes of Heat, Fresh Water, and Momentum: Energy Budget Closure and Unanswered Questions,” in *ANNUAL REVIEW OF MARINE SCIENCE, VOL 11* Annual Review of Marine Science., ed. Carlson, CA and Giovannoni, SJ (4139 EL CAMINO WAY, PO BOX 10139, PALO ALTO, CA 94303-0897 USA: ANNUAL REVIEWS), 227–248. doi:10.1146/annurev-marine-010816-060704.

Yuan, T., Remer, L. A., and Yu, H. (2011). Microphysical, macrophysical and radiative signatures of volcanic aerosols in trade wind cumulus observed by the A-Train. *Atmos. Chem. Phys.* 11, 7119–7132. doi:10.5194/acp-11-7119-2011.

Zaehle, S., Jones, C. D., Houlton, B., Lamarque, J. F., and Robertson, E. (2015). Nitrogen availability reduces CMIP5 projections of twenty-first-century land carbon uptake. *J. Clim.* doi:10.1175/JCLI-D-13-00776.1.

Zaliapin, I., and Ghil, M. (2010). Nonlinear Processes in Geophysics Another look at climate sensitivity. *Nonlin. Process. Geophys* 17, 113–122. doi:10.5194/npg-17-113-2010.

Zanatta, M., Gysel, M., Bukowiecki, N., Müller, T., Weingartner, E., Areskoug, H., et al. (2016). A European aerosol phenomenology-5: Climatology of black carbon optical properties at 9 regional background sites across Europe. *Atmos. Environ.* 145, 346–364. doi:10.1016/J.ATMOSENV.2016.09.035.

Zanna, L., Khatiwala, S., Gregory, J. M., Ison, J., and Heimbach, P. (2019). Global reconstruction of historical ocean heat storage and transport. *Proc. Natl. Acad. Sci.* 116, 1126–1131. doi:10.1073/pnas.1808838115.

Zelinka, M. D., Andrews, T., Forster, P. M., and Taylor, K. E. (2014). Quantifying components of aerosol-cloud-radiation interactions in climate models. *J. Geophys. Res. Atmos.* 119, 7599–7615. doi:10.1002/2014JD021710.

Zelinka, M. D., and Hartmann, D. L. (2010). Why is longwave cloud feedback positive? *J. Geophys. Res.* 115, D16117. doi:10.1029/2010JD013817.

Zelinka, M. D., and Hartmann, D. L. (2011). The observed sensitivity of high clouds to mean surface temperature anomalies in the tropics. *J. Geophys. Res. Atmos.* 116, 1–16. doi:10.1029/2011JD016459.

Zelinka, M. D., and Hartmann, D. L. (2012). Climate feedbacks and their implications for poleward energy flux changes in a warming climate. *J. Clim.* doi:10.1175/JCLI-D-11-00096.1.

Zelinka, M. D., Zhou, C., and Klein, S. A. (2016). Insights from a refined decomposition of cloud feedbacks. *Geophys. Res. Lett.* 43, 9259–9269. doi:10.1002/2016GL069917.

Zhai, C., Jiang, J. H., and Su, H. (2015). Long-term cloud change imprinted in seasonal cloud variation: More evidence of high climate sensitivity. *Geophys. Res. Lett.* 42, 8729–8737. doi:10.1002/2015GL065911.

Zhang, C., Xie, S., Klein, S. A., Ma, H., Tang, S., Van Weverberg, K., et al. (2018a). CAUSES: Diagnosis of the Summertime Warm Bias in CMIP5 Climate Models at the ARM Southern Great Plains Site. *J. Geophys. Res.* 123, 2968–2992. doi:10.1002/2017JD027200.

Zhang, H., Zhao, S., Wang, Z., Zhang, X., and Song, L. (2016). The updated effective radiative forcing of major anthropogenic aerosols and their effects on global climate at present and in the future. *Int. J. Climatol.* 36, 4029–4044. doi:10.1002/joc.4613.

Zhang, H., Zhou, C., and Zhao, S. (2018b). Influences of the Internal Mixing of Anthropogenic Aerosols on Global Aridity Change. *J. Meteorol. Res.* 32, 723–733. doi:10.1007/s13351-018-7155-1.

Zhang, M., and Huang, Y. (2014). Radiative Forcing of Quadrupling CO2. *J. Clim.* 27, 2496–2508. doi:10.1175/JCLI-D-13-00535.1.

Zhang, W., Miller, P. A., Jansson, C., Samuelsson, P., Mao, J., and Smith, B. (2018c). Self-Amplifying Feedbacks Accelerate Greening and Warming of the Arctic. *Geophys. Res. Lett.* 45, 7102–7111. doi:10.1029/2018GL077830.

Zhang, X. T., Liang, S. L., Wild, M., and Jiang, B. (2015). Analysis of surface incident shortwave radiation from four satellite products. *Remote Sens. Environ.* 165, 186–202. doi:10.1016/j.rse2015.05.015.

Zhang, Y., Forrister, H., Liu, J., Dibb, J., Anderson, B., Schwarz, J. P., et al. (2017). Top-of-atmosphere radiative forcing affected by brown carbon in the upper troposphere. *Nat. Geosci.* 10, 486–489. doi:10.1038/ngeo2960.

Zhang, Y. G., Pagani, M., and Liu, Z. (2014). A 12-Million-Year Temperature History of the Tropical Pacific Ocean. *Science (80-.).* 344, 84 LP-87. doi:10.1126/science.1246172.

Zhao, B., Liou, K.-N., Gu, Y., Jiang, J. H., Li, Q., Fu, R., et al. (2018). Impact of aerosols on ice crystal size. *Atmos. Chem. Phys.* 18, 1065–1078. doi:10.5194/acp-18-1065-2018.

Zhao, S., and Suzuki, K. Differing impacts of black carbon and sulfate aerosols on global precipitation and the ITCZ location via atmosphere and ocean energy perturbations. *J. Clim.* submitted.

Zhao, T. X.-P., Laszlo, I., Dubovik, O., Holben, B. N., Sapper, J., Tanré, D., et al. (2003). A study of the effect of non-spherical dust particles on the AVHRR aerosol optical thickness retrievals. *Geophys. Res. Lett.* 30. doi:10.1029/2002GL016379.

Zhou, C., Zelinka, M. D., Dessler, A. E., and Klein, S. A. (2015). The relationship between interannual and long-term cloud feedbacks. *Geophys. Res. Lett.* doi:10.1002/2015GL066698.

Zhou, C., Zelinka, M. D., and Klein, S. A. (2016). Impact of decadal cloud variations on the Earth’s energy budget. *Nat. Geosci.* 9, 871–874. doi:10.1038/ngeo2828.

Zhou, C., Zelinka, M. D., and Klein, S. A. (2017a). Analyzing the dependence of global cloud feedback on the spatial pattern of sea surface temperature change with a Green's function approach. *J. Adv. Model. Earth Syst.* 9, 2174–2189. doi:10.1002/2017MS001096.

Zhou, C., Zhang, H., Zhao, S., and Li, J. (2017b). Simulated effects of internal mixing of anthropogenic aerosols on the aerosol–radiation interaction and global temperature. *Int. J. Climatol.* 37, 972–986. doi:10.1002/joc.5050.

Zhou, C., Zhang, H., Zhao, S., and Li, J. (2018). On Effective Radiative Forcing of Partial Internally and Externally Mixed Aerosols and Their Effects on Global Climate. *J. Geophys. Res. Atmos.* 123, 401–423. doi:10.1002/2017JD027603.

Zhu, Y., Rosenfeld, D., and Li, Z. (2018). Under What Conditions Can We Trust Retrieved Cloud Drop Concentrations in Broken Marine Stratocumulus? *J. Geophys. Res. Atmos.* 123, 8754–8767. doi:10.1029/2017JD028083.

Zickfeld, K., Solomon, S., and Gilford, D. M. (2017). Centuries of thermal sea-level rise due to anthropogenic emissions of short-lived greenhouse gases. *Proc. Natl. Acad. Sci. U. S. A.* 114, 657–662. doi:10.1073/pnas.1612066114.

Appendix 7.A:

[START TABLE 7.A.1 HERE]

Table 7.A.1: Radiative efficiencies, lifetimes, AGWP and GWP values for 100 years. AGTP, GTP, iAGTP and MGTP values for 50 and 100 years (see 7.7.2 for definitions). Carbon cycle responses are included for all species. Radiative efficiencies and lifetimes of halogenated species are from Hodnebrog et al. (2013)

Species		Lifetime yr	Radiative Efficiency W $m^{-2}ppb^{-1}$	AGWP 100 W $m^{-2}yr$ kg^{-1}	GWP 100	AGTP 50 K kg^{-1}	GTP 50	AGTP 100 K kg^{-1}	GTP 100	iAGTP 50 K yr kg^{-1}	MGTP 50 yr	iAGTP 100 K yr kg^{-1}	MGTP 100 yr
CO2			1.37E-05	9.20E-14	1	5.24E-16	1	4.86E-16	1	2.78E-14	53	5.28E-14	109
CH4		12.4	3.79E-04	2.91E-12	32	7.62E-15	15	3.23E-15	7	1.60E-12	3048	1.82E-12	3750
N2O		121	2.92E-03	2.49E-11	271	1.51E-13	288	1.17E-13	242	7.67E-12	14637	1.44E-11	29524
CFC-11		45	2.60E-01	4.56E-07	4954268	2.63E-09	5019926	1.26E-09	2590162	1.80E-07	3.43E+08	2.72E-07	5.59E+08
CFC-12		100	3.18E-01	9.94E-07	10805581	6.03E-09	11511359	4.38E-09	9014812	3.18E-07	6.07E+08	5.76E-07	1.19E+09
CFC-13		640	2.55E-01	1.35E-06	14641035	8.00E-09	15260722	8.23E-09	16923247	3.54E-07	6.75E+08	7.61E-07	1.56E+09
CFC-113		85	3.02E-01	5.67E-07	6162404	3.44E-09	6554303	2.33E-09	4797607	1.88E-07	3.59E+08	3.30E-07	6.79E+08
CFC-114		190	3.07E-01	8.33E-07	9061019	5.03E-09	9594424	4.42E-09	9092699	2.40E-07	4.58E+08	4.76E-07	9.8E+08
CFC-115		1020	2.02E-01	7.42E-07	8067808	4.39E-09	8380913	4.63E-09	9531719	1.92E-07	3.66E+08	4.18E-07	8.6E+08
HCFC-21		1.7	1.45E-01	1.45E-08	157233	2.05E-11	39078	1.48E-11	30451	8.36E-09	15940980	9.21E-09	18950765
HCFC-22		11.9	2.08E-01	1.73E-07	1877204	4.33E-	825769	1.90E-	390377	9.51E-	1.81E+08	1.08E-	2.22E+08

						10		10		08		07	
HCFC-122		0.97	1.68E-01	5.81E-09	63162	8.17E-12	15582	5.93E-12	12190	3.36E-09	6415062	3.71E-09	7621491
HCFC-122a		3.4	2.09E-01	2.53E-08	275391	3.66E-11	69808	2.61E-11	53780	1.46E-08	27801948	1.61E-08	33102825
HCFC-123		1.3	1.52E-01	7.80E-09	84826	1.10E-11	20996	7.97E-12	16397	4.51E-09	8608420	4.97E-09	10230211
HCFC-123a		4	2.30E-01	3.63E-08	394882	5.29E-11	101013	3.76E-11	77348	2.09E-08	39802717	2.31E-08	47420389
HCFC-124		5.9	1.98E-01	5.17E-08	561781	7.96E-11	151859	5.40E-11	111145	2.95E-08	56311433	3.27E-08	67255616
HCFC-132c		4.3	1.73E-01	3.33E-08	361858	4.88E-11	93078	3.45E-11	70989	1.91E-08	36444707	2.11E-08	43433680
HCFC-141b		9.2	1.62E-01	7.69E-08	836169	1.51E-10	287341	8.21E-11	168922	4.33E-08	82530384	4.84E-08	99556576
HCFC-142b		17.2	1.89E-01	1.94E-07	2113593	7.03E-10	1341810	2.41E-10	495725	1.01E-07	1.93E+08	1.21E-07	2.48E+08
HCFC-225ca		1.9	2.21E-01	1.25E-08	135831	1.77E-11	33831	1.28E-11	26331	7.21E-09	13764450	7.96E-09	16366166
HCFC-225cb		5.9	2.93E-01	5.14E-08	559076	7.92E-11	151127	5.38E-11	110610	2.94E-08	56040289	3.25E-08	66931775
trans-CF3C		0.071	4.40E-02	1.45E-10	1576	2.02E-13	385	1.47E-13	303	8.41E-11	160418	9.26E-11	190444
HFC-23		222	1.75E-01	1.20E-06	13051373	7.23E-09	13786181	6.56E-09	13485873	3.40E-07	6.48E+08	6.85E-07	1.41E+09
HFC-32		5.2	1.10E-01	6.64E-08	721576	9.95E-11	189900	6.91E-11	142223	3.80E-08	72488638	4.20E-08	86484542
HFC-41		2.8	2.30E-02	1.14E-08	124193	1.64E-11	31244	1.18E-11	24181	6.58E-09	12556977	7.26E-09	14942637
HFC-125		28.2	2.26E-01	3.10E-07	3372397	1.56E-09	2980016	5.64E-10	1159782	1.42E-07	2.71E+08	1.89E-07	3.89E+08
HFC-134		9.7	1.91E-01	1.10E-07	1191235	2.25E-10	428687	1.18E-10	241655	6.14E-08	1.17E+08	6.89E-08	1.42E+08

HFC-134a		13.4	1.61E-01	1.27E-07	1385744	3.61E-10	689601	1.44E-10	295446	6.92E-08	1.32E+08	7.96E-08	1.64E+08
HFC-143		3.5	1.28E-01	3.22E-08	349885	4.66E-11	88814	3.32E-11	68362	1.85E-08	35313286	2.04E-08	42050435
HFC-143a		47.1	1.58E-01	4.67E-07	5083399	2.72E-09	5188006	1.34E-09	2755301	1.82E-07	3.47E+08	2.78E-07	5.73E+08
HFC-152		0.4	4.40E-02	1.61E-09	17491	2.25E-12	4291	1.64E-12	3367	9.32E-10	1778932	1.03E-09	2112475
HFC-152a		1.5	9.80E-02	1.34E-08	146086	1.90E-11	36232	1.37E-11	28265	7.77E-09	14818110	8.56E-09	17612820
HFC-161		0.181	1.60E-02	3.63E-10	3951	5.07E-13	967	3.69E-13	760	2.11E-10	402031	2.32E-10	477324
HFC-227ca		28.2	2.67E-01	2.59E-07	2812421	1.30E-09	2485193	4.70E-10	967203	1.18E-07	2.26E+08	1.58E-07	3.24E+08
HFC-227ea		38.9	2.58E-01	3.27E-07	3558610	1.84E-09	3502301	8.00E-10	1645927	1.35E-07	2.58E+08	1.97E-07	4.04E+08
HFC-236cb		13.1	2.28E-01	1.18E-07	1287660	3.28E-10	625929	1.33E-10	273008	6.45E-08	1.23E+08	7.40E-08	1.52E+08
HFC-236ea		11	3.00E-01	1.31E-07	1423613	3.03E-10	577896	1.42E-10	292626	7.27E-08	1.39E+08	8.21E-08	1.69E+08
HFC-236fa		242	2.43E-01	7.81E-07	8489842	4.69E-09	8955812	4.33E-09	8898926	2.19E-07	4.18E+08	4.45E-07	9.15E+08
HFC-245ca		6.5	2.40E-01	7.02E-08	763705	1.12E-10	212820	7.37E-11	151597	4.00E-08	76389767	4.44E-08	91339699
HFC-245cb		47.1	2.43E-01	4.51E-07	4901646	2.62E-09	5002513	1.29E-09	2656787	1.76E-07	3.35E+08	2.68E-07	5.52E+08
HFC-245ea		3.2	1.60E-01	2.31E-08	250705	3.32E-11	63383	2.38E-11	48910	1.33E-08	25322705	1.47E-08	30145053
HFC-245eb		3.1	2.04E-01	2.85E-08	309661	4.10E-11	78189	2.94E-11	60382	1.64E-08	31285632	1.81E-08	37239983
HFC-245fa		7.7	2.43E-01	8.42E-08	915917	1.45E-10	276790	8.90E-11	183105	4.78E-08	91151564	5.31E-08	1.09E+08
HFC-263fb		1.2	1.00E-01	7.39E-09	80322	1.04E-11	19861	7.54E-12	15519	4.27E-09	8153371	4.71E-09	9688602

HFC-272ca		2.6	7.20E-02	1.41E-08	153438	2.02E-11	38512	1.45E-11	29846	8.14E-09	15521687	8.98E-09	18467189
HFC-329p		28.4	3.06E-01	2.31E-07	2506382	1.16E-09	2221763	4.22E-10	867659	1.05E-07	2.01E+08	1.40E-07	2.89E+08
HFC-365mfc		8.7	2.23E-01	7.91E-08	859636	1.48E-10	282400	8.41E-11	173008	4.46E-08	85102447	4.98E-08	1.02E+08
HFC-43-10m		16.1	4.20E-01	1.61E-07	1754942	5.50E-10	1048529	1.94E-10	398644	8.51E-08	1.62E+08	1.00E-07	2.06E+08
HFC-1132a		0.011	4.00E-03	4.15E-12	45	5.77E-15	11	4.21E-15	9	2.41E-12	4592	2.65E-12	5451
HFC-1141		0.006	2.00E-03	1.52E-12	17	2.12E-15	4	1.54E-15	3	8.82E-13	1684	9.72E-13	1999
(Z)-HFC-12		0.023	2.10E-02	2.24E-11	243	3.11E-14	59	2.27E-14	47	1.30E-11	24766	1.43E-11	29400
(E)-HFC-12		0.013	1.30E-02	7.96E-12	87	1.11E-14	21	8.09E-15	17	4.62E-12	8817	5.09E-12	10467
(Z)-HFC-12		0.027	1.90E-02	2.76E-11	300	3.84E-14	73	2.80E-14	58	1.60E-11	30506	1.76E-11	36215
HFC-1234yf		0.029	2.30E-02	3.51E-11	381	4.88E-14	93	3.56E-14	73	2.03E-11	38815	2.24E-11	46079
(E)-HFC-12		0.045	3.90E-02	9.27E-11	1008	1.29E-13	246	9.42E-14	194	5.38E-11	102606	5.92E-11	121809
(Z)-HFC-13		0.06	7.40E-02	1.64E-10	1785	2.29E-13	436	1.67E-13	343	9.53E-11	181755	1.05E-10	215774
HFC-1243zf		0.019	1.20E-02	1.45E-11	157	2.02E-14	38	1.47E-14	30	8.40E-12	16030	9.25E-12	19029
HFC-1345zf		0.021	1.40E-02	1.20E-11	131	1.68E-14	32	1.22E-14	25	6.98E-12	13323	7.69E-12	15816
C4F9CH=CH2		0.021	2.60E-02	1.33E-11	144	1.85E-14	35	1.35E-14	28	7.70E-12	14687	8.48E-12	17435
C6F13CH=CH		0.021	2.90E-02	1.05E-11	114	1.47E-14	28	1.07E-14	22	6.11E-12	11647	6.72E-12	13827
C8F17CH=CH		0.021	3.20E-02	9.00E-12	98	1.25E-14	24	9.15E-15	19	5.23E-12	9971	5.75E-12	11837

Methyl_chl		5	6.90E-02	1.56E-08	169750	2.33E-11	44403	1.63E-11	33423	8.94E-09	17062901	9.89E-09	20351953
Carbon_tet		26	1.70E-01	1.69E-07	1840001	8.19E-10	1563388	2.85E-10	587122	7.94E-08	1.51E+08	1.03E-07	2.13E+08
Methyl_chl		1	1.00E-02	1.20E-09	13003	1.68E-12	3209	1.22E-12	2510	6.92E-10	1320519	7.63E-10	1568898
Methylene_		0.395	3.10E-02	8.69E-10	9453	1.22E-12	2319	8.85E-13	1820	5.04E-10	961476	5.55E-10	1141744
Chloroform		0.408	7.80E-02	1.61E-09	17511	2.25E-12	4296	1.64E-12	3371	9.33E-10	1780939	1.03E-09	2114873
CH2ClCH2Cl		0.178	8.00E-03	8.69E-11	945	1.21E-13	231	8.84E-14	182	5.04E-11	96186	5.55E-11	114200
Methyl bromide		0.8	5.00E-03	2.54E-10	2766	3.57E-13	681	2.59E-13	533	1.47E-10	281043	1.62E-10	333849
Methylene_		0.337	9.00E-03	1.05E-10	1145	1.47E-13	281	1.07E-13	220	6.11E-11	116520	6.73E-11	138359
Halon-1201		5.2	1.54E-01	3.69E-08	401474	5.54E-11	105658	3.85E-11	79131	2.11E-08	40331633	2.34E-08	48118752
Halon-1202		2.9	2.72E-01	2.27E-08	246797	3.26E-11	62163	2.34E-11	48076	1.31E-08	24946965	1.44E-08	29689328
Halon-1211		16	2.94E-01	1.71E-07	1861172	5.79E-10	1105469	2.05E-10	421614	9.04E-08	1.72E+08	1.06E-07	2.19E+08
Halon-1301		65	2.98E-01	6.12E-07	6651008	3.67E-09	7006772	2.19E-09	4496652	2.17E-07	4.14E+08	3.60E-07	7.4E+08
Halon-2301		3.4	1.35E-01	1.70E-08	184915	2.46E-11	46873	1.76E-11	36111	9.78E-09	18667971	1.08E-08	22227313
Halon-2311		1	1.32E-01	4.04E-09	43905	5.68E-12	10834	4.12E-12	8475	2.34E-09	4458829	2.58E-09	5297499
Halon-2401		2.9	1.86E-01	1.80E-08	195704	2.58E-11	49293	1.85E-11	38123	1.04E-08	19782326	1.14E-08	23542902
Halon-2402		20	3.13E-01	1.44E-07	1567586	5.91E-10	1127285	1.96E-10	403349	7.26E-08	1.38E+08	8.90E-08	1.83E+08
NF3		500	2.05E-01	1.56E-06	16954171	9.28E-09	17713820	9.37E-09	19275919	4.14E-07	7.9E+08	8.82E-07	1.81E+09

SF6		3200	5.67E-01	2.28E-06	24745411	1.34E-08	25598479	1.46E-08	29974695	5.78E-07	1.1E+09	1.28E-06	2.63E+09
SF5CF3		800	5.92E-01	1.69E-06	18384008	1.00E-08	19127977	1.05E-08	21501068	4.41E-07	8.41E+08	9.54E-07	1.96E+09
SO2F2		36	2.01E-01	3.99E-07	4343208	2.20E-09	4190325	9.11E-10	1874658	1.69E-07	3.23E+08	2.41E-07	4.95E+08
PFC-14		50000	9.50E-02	6.42E-07	6981426	3.78E-09	7208145	4.16E-09	8549339	1.62E-07	3.09E+08	3.61E-07	7.42E+08
PFC-116		10000	2.51E-01	1.08E-06	11715575	6.34E-09	12102511	6.95E-09	14304086	2.72E-07	5.2E+08	6.06E-07	1.25E+09
PFC-c216		3000	2.28E-01	8.90E-07	9677948	5.25E-09	10012939	5.69E-09	11714024	2.26E-07	4.32E+08	5.01E-07	1.03E+09
PFC-218		2600	2.77E-01	8.61E-07	9357971	5.08E-09	9685100	5.50E-09	11305090	2.19E-07	4.18E+08	4.84E-07	9.96E+08
PFC-318		3200	3.15E-01	9.23E-07	10038443	5.44E-09	10384506	5.91E-09	12159801	2.35E-07	4.48E+08	5.19E-07	1.07E+09
PFC-31-10		2600	3.63E-01	8.91E-07	9686921	5.26E-09	10025549	5.69E-09	11702485	2.27E-07	4.33E+08	5.01E-07	1.03E+09
c-C5F8		0.085	7.60E-02	1.84E-10	1998	2.56E-13	488	1.87E-13	384	1.07E-10	203329	1.17E-10	241390
PFC-41-12		4100	4.05E-01	8.27E-07	8993522	4.87E-09	9299395	5.31E-09	10921944	2.10E-07	4E+08	4.65E-07	9.57E+08
PFC-51-14		3100	4.42E-01	7.66E-07	8330772	4.52E-09	8618530	4.90E-09	10087468	1.95E-07	3.72E+08	4.31E-07	8.87E+08
PFC-61-16		3000	5.02E-01	7.58E-07	8237969	4.47E-09	8523117	4.85E-09	9971099	1.93E-07	3.68E+08	4.26E-07	8.77E+08
PFC-71-18		3000	5.52E-01	7.38E-07	8024393	4.35E-09	8302148	4.72E-09	9712589	1.88E-07	3.58E+08	4.15E-07	8.54E+08
PFC-91-18		2000	5.53E-01	6.95E-07	7558792	4.10E-09	7828816	4.42E-09	9092320	1.78E-07	3.39E+08	3.91E-07	8.05E+08
Z-C10F18		2000	5.57E-01	7.00E-07	7613467	4.13E-09	7885444	4.45E-09	9158088	1.79E-07	3.41E+08	3.94E-07	8.11E+08
E-C10F18		2000	4.84E-01	6.08E-07	6615651	3.59E-09	6851984	3.87E-09	7957836	1.55E-07	2.97E+08	3.42E-07	7.04E+08

PFC-1114		0.003	2.00E-03	3.62E-13	4	5.04E-16	1	3.68E-16	1	2.10E-13	401	2.31E-13	476
PFC-1216		0.013	1.30E-02	7.01E-12	76	9.76E-15	19	7.12E-15	15	4.07E-12	7760	4.48E-12	9212
CF2=CFCF=C		0.003	3.00E-03	3.35E-13	4	4.67E-16	1	3.41E-16	1	1.95E-13	371	2.14E-13	441
CF3CF2CF=C		0.016	1.80E-02	8.91E-12	97	1.24E-14	24	9.05E-15	19	5.17E-12	9862	5.69E-12	11708
CF3CF=CFCF		0.085	6.80E-02	1.74E-10	1895	2.43E-13	463	1.77E-13	364	1.01E-10	192848	1.11E-10	228947
HFE-125		119	4.05E-01	1.20E-06	13083203	7.30E-09	13933229	5.65E-09	11619111	3.72E-07	7.1E+08	6.94E-07	1.43E+09
HFE-134 (H		24.4	4.45E-01	5.44E-07	5920792	2.55E-09	4859604	8.68E-10	1785076	2.60E-07	4.96E+08	3.34E-07	6.86E+08
HFE-143a		4.8	1.77E-01	5.13E-08	557432	7.60E-11	145019	5.33E-11	109640	2.94E-08	56064230	3.25E-08	66854371
HFE-227ea		51.6	4.42E-01	6.29E-07	6840954	3.70E-09	7066705	1.93E-09	3971403	2.38E-07	4.55E+08	3.73E-07	7.68E+08
HCFE-235ca		4.3	4.07E-01	5.73E-08	622665	8.39E-11	160163	5.94E-11	122153	3.29E-08	62711999	3.63E-08	74738230
HCFE-235da		3.5	4.21E-01	4.82E-08	524278	6.98E-11	133081	4.98E-11	102435	2.77E-08	52914554	3.06E-08	63009714
HFE-236ca		20.8	5.62E-01	4.16E-07	4518807	1.75E-09	3345212	5.81E-10	1196149	2.07E-07	3.95E+08	2.56E-07	5.27E+08
HFE-236ea2		10.8	4.53E-01	1.76E-07	1909817	3.99E-10	761190	1.90E-10	391670	9.77E-08	1.86E+08	1.10E-07	2.27E+08
HFE-236fa		7.5	3.57E-01	9.62E-08	1045641	1.63E-10	311228	1.02E-10	208780	5.46E-08	1.04E+08	6.07E-08	1.25E+08
HFE-245cb2		4.9	3.26E-01	6.43E-08	698756	9.55E-11	182269	6.68E-11	137508	3.68E-08	70257995	4.07E-08	83790278
HFE-245fa1		6.6	3.06E-01	8.12E-08	883337	1.30E-10	247579	8.53E-11	175444	4.63E-08	88322648	5.13E-08	1.06E+08
HFE-245fa2		5.5	3.60E-01	7.96E-08	866084	1.21E-10	230309	8.31E-11	170979	4.56E-08	86926114	5.04E-08	1.04E+08

CF3CF2CH2O		0.33	1.39E-01	1.85E-09	20069	2.58E-12	4920	1.88E-12	3862	1.07E-09	2041510	1.18E-09	2424146
HFE-254cb1		2.5	2.58E-01	2.95E-08	320624	4.21E-11	80383	3.03E-11	62335	1.70E-08	32442221	1.88E-08	38595146
HFE-263fb1		0.063	3.90E-02	1.30E-10	1414	1.81E-13	346	1.32E-13	272	7.54E-11	143937	8.31E-11	170877
HFE-263m1		0.43	1.27E-01	2.89E-09	31430	4.04E-12	7712	2.94E-12	6051	1.68E-09	3196350	1.85E-09	3795749
CF3CH2CH2O		0.033	2.20E-02	3.84E-11	418	5.35E-14	102	3.90E-14	80	2.23E-11	42534	2.45E-11	50494
HFE-329mcc		22.5	5.29E-01	3.00E-07	3262689	1.34E-09	2548712	4.46E-10	918331	1.47E-07	2.8E+08	1.84E-07	3.79E+08
HFE-338mmz		21.2	4.42E-01	2.57E-07	2789107	1.10E-09	2092939	3.64E-10	748956	1.27E-07	2.43E+08	1.58E-07	3.25E+08
HFE-338mcf		7.5	4.39E-01	9.11E-08	990913	1.55E-10	294939	9.62E-11	197853	5.17E-08	98707137	5.75E-08	1.18E+08
Sevofluran		2.2	3.20E-01	2.12E-08	231008	3.03E-11	57722	2.18E-11	44847	1.23E-08	23391878	1.35E-08	27820777
HFE-347mcc		5	3.45E-01	5.20E-08	565945	7.76E-11	148040	5.42E-11	111431	2.98E-08	56887708	3.30E-08	67853407
HFE-347mcf		6.6	4.21E-01	8.38E-08	911513	1.34E-10	255476	8.80E-11	181040	4.78E-08	91139887	5.30E-08	1.09E+08
HFE-347pcf		6	4.82E-01	8.72E-08	948755	1.35E-10	257641	9.13E-11	187808	4.98E-08	95068594	5.52E-08	1.14E+08
HFE-347mmy		3.7	3.19E-01	3.56E-08	387268	5.17E-11	98589	3.68E-11	75742	2.05E-08	39066072	2.26E-08	46528442
HFE-356mec		3.8	3.01E-01	3.79E-08	412372	5.51E-11	105141	3.92E-11	80692	2.18E-08	41587547	2.41E-08	49536580
HFE-356mff		0.288	1.72E-01	1.64E-09	17843	2.29E-12	4372	1.67E-12	3433	9.51E-10	1815236	1.05E-09	2155387
HFE-356pcf		5.7	3.73E-01	7.05E-08	766426	1.08E-10	205408	7.36E-11	151468	4.03E-08	76874933	4.46E-08	91785391
HFE-356pcf		3.5	3.77E-01	4.37E-08	475724	6.33E-11	120756	4.52E-11	92949	2.52E-08	48014105	2.78E-08	57174346

HFE-356pcc		3.8	3.22E-01	4.06E-08	441142	5.90E-11	112477	4.20E-11	86322	2.33E-08	44489003	2.58E-08	52992621
HFE-356mmz		0.266	1.51E-01	1.33E-09	14483	1.86E-12	3548	1.35E-12	2786	7.72E-10	1473486	8.50E-10	1749567
HFE-365mcf		0.053	4.70E-02	9.16E-11	997	1.28E-13	244	9.31E-14	192	5.32E-11	101453	5.85E-11	120441
HFE-365mcf		0.59	2.64E-01	5.73E-09	62322	8.03E-12	15317	5.84E-12	12007	3.32E-09	6335564	3.66E-09	7524644
HFE-374pc2		5	2.98E-01	6.16E-08	669439	9.18E-11	175112	6.41E-11	131808	3.53E-08	67290751	3.90E-08	80261746
CF3(CH2)2C		0.011	5.00E-03	1.79E-12	19	2.50E-15	5	1.82E-15	4	1.04E-12	1986	1.15E-12	2357
-(CF2)4CH		0.3	1.60E-01	1.26E-09	13698	1.76E-12	3357	1.28E-12	2635	7.30E-10	1393447	8.04E-10	1654577
HFE-43-10p		13.5	1.02E+00	2.76E-07	3001958	7.89E-10	1505413	3.12E-10	641261	1.50E-07	2.86E+08	1.72E-07	3.55E+08
HFE-449s1		4.7	3.64E-01	4.13E-08	449046	6.11E-11	116528	4.29E-11	88276	2.37E-08	45176049	2.62E-08	53864121
n-HFE-7100		4.7	4.20E-01	4.76E-08	518130	7.05E-11	134455	4.95E-11	101856	2.73E-08	52126211	3.02E-08	62150908
i-HFE-7100		4.7	3.52E-01	3.99E-08	434243	5.91E-11	112686	4.15E-11	85365	2.29E-08	43686729	2.53E-08	52088380
HFE-569sf2		0.8	3.05E-01	5.58E-09	60654	7.83E-12	14938	5.69E-12	11697	3.23E-09	6162886	3.56E-09	7320841
n-HFE-7200		0.8	3.47E-01	6.35E-09	69007	8.91E-12	16995	6.47E-12	13308	3.68E-09	7011546	4.05E-09	8328957
i-HFE-7200		0.8	2.38E-01	4.35E-09	47330	6.11E-12	11656	4.44E-12	9127	2.52E-09	4809072	2.78E-09	5712656
HFE-236ca1		25	6.53E-01	5.24E-07	5698730	2.49E-09	4741652	8.53E-10	1755372	2.49E-07	4.74E+08	3.21E-07	6.6E+08
HFE-338pcc		12.9	8.58E-01	2.85E-07	3100304	7.77E-10	1483146	3.18E-10	654996	1.56E-07	2.97E+08	1.78E-07	3.67E+08
(CF3)2CHOH		1.9	2.61E-01	1.78E-08	193733	2.53E-11	48252	1.83E-11	37556	1.03E-08	19631888	1.14E-08	23342651

HG-02		26	1.15E+00	4.86E-07	5287752	2.36E-09	4492829	8.20E-10	1687257	2.28E-07	4.35E+08	2.97E-07	6.11E+08
HG-03		26	1.43E+00	4.46E-07	4854215	2.16E-09	4124467	7.53E-10	1548921	2.09E-07	3.99E+08	2.73E-07	5.61E+08
HG-20		25	9.20E-01	5.19E-07	5638632	2.46E-09	4691647	8.44E-10	1736860	2.46E-07	4.69E+08	3.17E-07	6.53E+08
HG-21		13.5	1.72E+00	3.81E-07	4145449	1.09E-09	2078848	4.30E-10	885527	2.07E-07	3.95E+08	2.38E-07	4.9E+08
HG-30		25	1.65E+00	7.18E-07	7802266	3.40E-09	6491908	1.17E-09	2403321	3.40E-07	6.49E+08	4.39E-07	9.04E+08
CF3CF2CF2O		0.75	2.81E-01	5.94E-09	64627	8.34E-12	15908	6.06E-12	12460	3.44E-09	6567301	3.79E-09	7800915
Fluoroxene		0.01	1.10E-02	5.26E-12	57	7.33E-15	14	5.35E-15	11	3.06E-12	5831	3.37E-12	6922
CH2FOCF2CF		6.2	3.43E-01	8.55E-08	930164	1.34E-10	255067	8.96E-11	184331	4.88E-08	93141232	5.41E-08	1.11E+08
C12H5F19O2		1	4.89E-01	5.45E-09	59214	7.66E-12	14612	5.56E-12	11430	3.15E-09	6013668	3.47E-09	7144791
CH3OCH2F		0.2	6.50E-02	1.23E-09	13323	1.71E-12	3262	1.25E-12	2562	7.11E-10	1355662	7.82E-10	1609580
CH3OCHF2		1.1	1.74E-01	1.41E-08	153144	1.98E-11	37829	1.44E-11	29575	8.15E-09	15549151	8.98E-09	18475390
CH2FOCH2F		0.9	1.93E-01	1.28E-08	138983	1.80E-11	34262	1.30E-11	26815	7.40E-09	14118148	8.15E-09	16772241
CH2FOCHF2		3.3	3.04E-01	6.05E-08	658269	8.73E-11	166639	6.25E-11	128486	3.48E-08	66472163	3.85E-08	79138448
CH2FOCF3		4.4	3.28E-01	7.38E-08	802594	1.08E-10	206865	7.66E-11	157532	4.24E-08	80811633	4.68E-08	96319521
HG'-01		2	2.92E-01	2.18E-08	236539	3.09E-11	58976	2.23E-11	45876	1.26E-08	23963763	1.39E-08	28495850
HG'-02		2	5.64E-01	2.32E-08	251804	3.29E-11	62782	2.37E-11	48837	1.34E-08	25510279	1.47E-08	30334847
HG'-03		2	7.65E-01	2.17E-08	235732	3.08E-11	58775	2.22E-11	45720	1.25E-08	23882065	1.38E-08	28398701

HFE-329me3		40	4.76E-01	4.44E-07	4833187	2.51E-09	4787070	1.11E-09	2290343	1.82E-07	3.48E+08	2.67E-07	5.48E+08
HFE-338mec		0.055	6.10E-02	9.25E-11	1006	1.29E-13	246	9.40E-14	193	5.37E-11	102447	5.91E-11	121622
CF3(CF2)6C		0.055	6.80E-02	3.22E-11	350	4.48E-14	86	3.27E-14	67	1.87E-11	35619	2.06E-11	42285
CF3(CF2)8C		0.055	5.10E-02	1.85E-11	201	2.57E-14	49	1.88E-14	39	1.07E-11	20453	1.18E-11	24281
CH3OCF2CHF		1.4	2.11E-01	1.20E-08	130583	1.70E-11	32354	1.23E-11	25254	6.94E-09	13248800	7.65E-09	15746175
PFPMIE (pe		800	6.48E-01	9.40E-07	10221291	5.57E-09	10634929	5.81E-09	11954339	2.45E-07	4.67E+08	5.30E-07	1.09E+09
HFE-216		0.023	2.50E-02	2.09E-11	227	2.91E-14	56	2.12E-14	44	1.21E-11	23147	1.34E-11	27478
HCOOCF3		3.5	3.11E-01	5.76E-08	626715	8.34E-11	159083	5.95E-11	122450	3.32E-08	63253319	3.66E-08	75320932
HCOOCF2CF3		3.5	4.42E-01	5.69E-08	619124	8.24E-11	157157	5.88E-11	120966	3.28E-08	62487240	3.62E-08	74408698
HCOOCF2CF2		2.6	5.03E-01	3.69E-08	401118	5.28E-11	100678	3.79E-11	78023	2.13E-08	40576824	2.35E-08	48276960
HCOOCF2CF2		3	5.61E-01	3.85E-08	418419	5.53E-11	105519	3.96E-11	81549	2.22E-08	42284308	2.45E-08	50327189
HCOOCH2CF3		0.44	1.58E-01	3.28E-09	35646	4.59E-12	8748	3.34E-12	6863	1.90E-09	3624993	2.09E-09	4304809
HCOOCH2CH2		0.3	1.34E-01	1.71E-09	18577	2.39E-12	4553	1.74E-12	3574	9.91E-10	1889792	1.09E-09	2243936
HCOOCHFCF3		3.2	3.49E-01	4.62E-08	502025	6.65E-11	126921	4.76E-11	97940	2.66E-08	50707555	2.93E-08	60364085
HCOOCH(CF3		3.2	3.33E-01	3.26E-08	354985	4.70E-11	89747	3.37E-11	69254	1.88E-08	35855610	2.08E-08	42683800
CH3COOCF2C		0.06	1.25E-01	1.63E-10	1770	2.27E-13	433	1.65E-13	340	9.45E-11	180239	1.04E-10	213974
CH3COOCF2C		0.06	1.07E-01	1.70E-10	1848	2.37E-13	452	1.73E-13	355	9.86E-11	188117	1.09E-10	223326

CH3COOCF2C		0.06	9.90E-02	2.01E-10	2190	2.81E-13	535	2.05E-13	421	1.17E-10	222939	1.29E-10	264666
CH3COOCF3		0.06	7.20E-02	2.04E-10	2215	2.84E-13	541	2.07E-13	426	1.18E-10	225465	1.30E-10	267665
FCOOCH3		1.8	6.70E-02	9.33E-09	101463	1.32E-11	25244	9.56E-12	19660	5.39E-09	10284308	5.94E-09	12227141
FCOOCF2CH3		0.33	1.69E-01	2.63E-09	28596	3.67E-12	7010	2.68E-12	5502	1.53E-09	2908799	1.68E-09	3453990
CF3COOCF2C		0.33	2.70E-01	3.02E-09	32853	4.22E-12	8054	3.07E-12	6322	1.75E-09	3341908	1.93E-09	3968275
CF3COOCH2C		0.06	5.30E-02	1.35E-10	1469	1.88E-13	359	1.37E-13	282	7.84E-11	149577	8.63E-11	177573
CF3COOCH2C		0.15	1.45E-01	6.70E-10	7284	9.34E-13	1782	6.81E-13	1400	3.89E-10	741245	4.28E-10	880046
CF3COOCH3		0.61	1.79E-01	5.15E-09	55986	7.21E-12	13762	5.24E-12	10787	2.98E-09	5691163	3.29E-09	6759412
HCF2COOCH3		0.11	5.30E-02	3.20E-10	3478	4.46E-13	851	3.25E-13	669	1.86E-10	353971	2.04E-10	420239
CF3COOCHF2		0.3	2.41E-01	2.66E-09	28939	3.72E-12	7092	2.71E-12	5568	1.54E-09	2943959	1.70E-09	3495653
CHF2CHFOCF		9.834	3.45E-01	1.22E-07	1324619	2.53E-10	482666	1.31E-10	269034	6.82E-08	1.3E+08	7.66E-08	1.58E+08
CF3CHFCF2O		0.389	1.91E-01	2.29E-09	24874	3.20E-12	6101	2.33E-12	4788	1.33E-09	2529893	1.46E-09	3004212
CF3CF2CF2O		67	5.81E-01	6.32E-07	6867726	3.80E-09	7247104	2.30E-09	4726507	2.22E-07	4.24E+08	3.71E-07	7.63E+08
CHF2CF2CH2		0.25	1.12E-01	1.28E-09	13920	1.79E-12	3410	1.30E-12	2677	7.42E-10	1416216	8.17E-10	1681544
CF3CHFCF2C		0.26	1.94E-01	1.67E-09	18188	2.34E-12	4456	1.70E-12	3499	9.70E-10	1850414	1.07E-09	2197107
CF3CF2CF2C		0.55	1.98E-01	3.29E-09	35736	4.60E-12	8779	3.35E-12	6884	1.90E-09	3633246	2.10E-09	4315002
CHF2CF2CH2		0.039	3.20E-02	5.16E-11	561	7.18E-14	137	5.24E-14	108	2.99E-11	57090	3.29E-11	67774

perfluoro-		0.019	2.80E-02	9.68E-12	105	1.35E-14	26	9.84E-15	20	5.62E-12	10723	6.19E-12	12730
CF3CH2CHO		0.005	4.00E-03	1.19E-12	13	1.65E-15	3	1.20E-15	2	6.88E-13	1312	7.57E-13	1558
CH2FCH2OH		0.056	1.60E-02	8.41E-11	915	1.17E-13	224	8.55E-14	176	4.88E-11	93135	5.37E-11	110566
CHF2CH2OH		0.11	3.70E-02	2.98E-10	3245	4.16E-13	794	3.03E-13	624	1.73E-10	330235	1.91E-10	392060
CF3CH2OH		0.321	1.01E-01	1.95E-09	21243	2.73E-12	5207	1.99E-12	4088	1.13E-09	2160949	1.25E-09	2565951
HCF2O(CF2C		26	1.46E+00	3.55E-07	3860431	1.72E-09	3280082	5.99E-10	1231817	1.67E-07	3.18E+08	2.17E-07	4.46E+08

[END TABLE 7.A.1 HERE]

Figures:

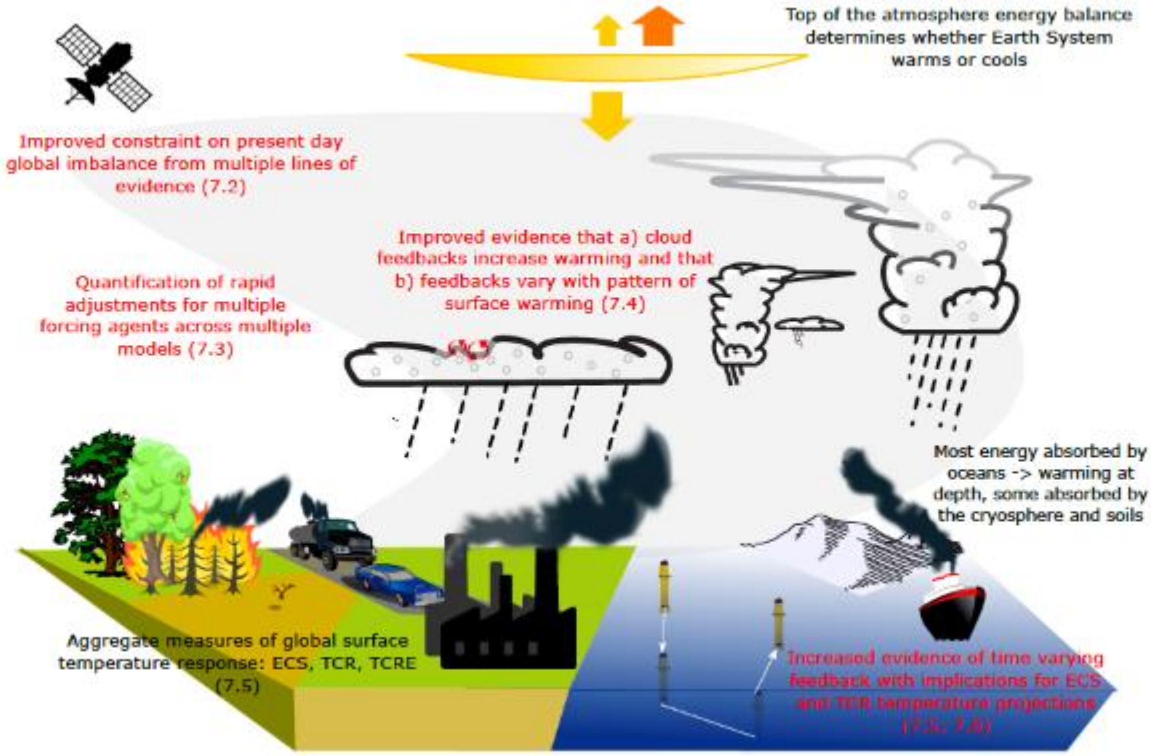

Figure 7.1: A conceptual energy budget framework to describe the state-of-the-art understanding of Earth's energy budget, climate feedbacks and the policy implications. The new elements relative to IPCC AR5 are highlighted in red.

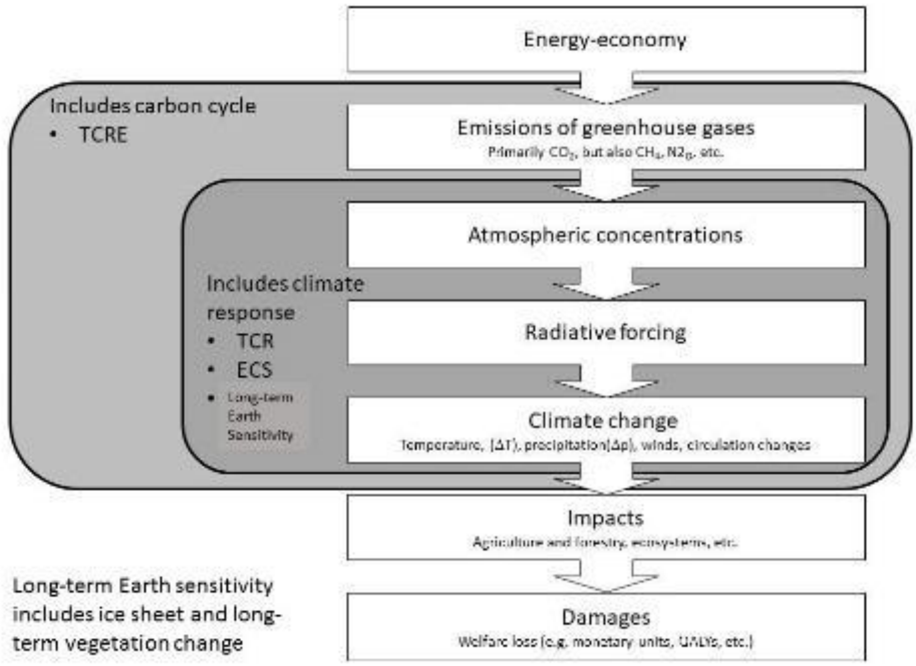

Figure 7.2: A conceptual chain of processes linking human activity to climate impacts, showing where the climate indicators and emission metrics assessed in this chapter fit within the chain and how they associate with other Working Groups.

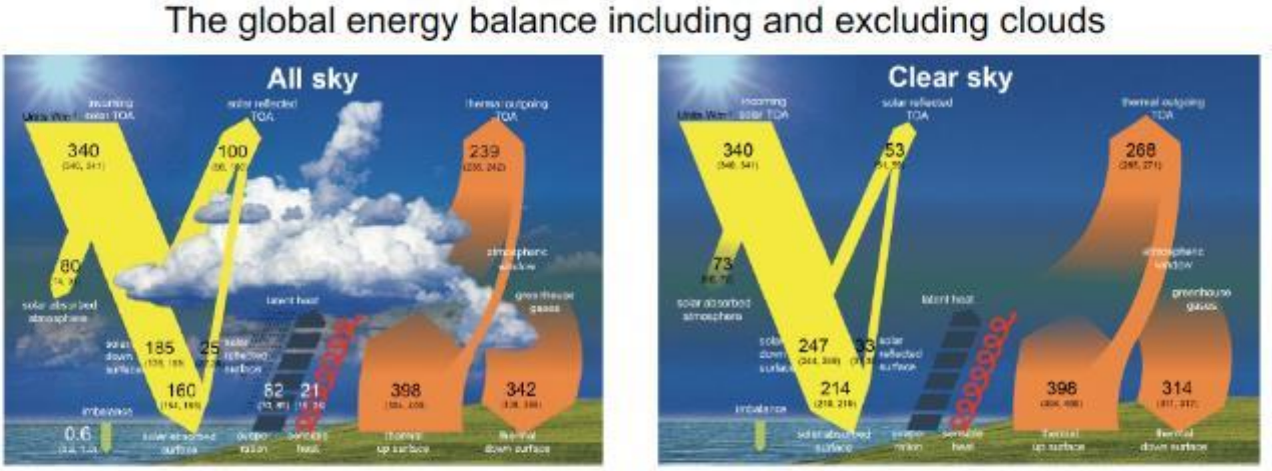

Figure 7.3: Schematic representation of the global mean energy budget of the Earth (left), and its equivalent without considerations of cloud effects (right). Numbers indicate best estimates for the magnitudes of the globally averaged energy balance components in Wm^{-2} together with their uncertainty ranges in parentheses (95% confidence range), representing present day climate conditions at the beginning of the 21[th] century. Adapted from (Wild et al., 2015, 2019). *[placeholder: change to 90% confidence range for SOD]*

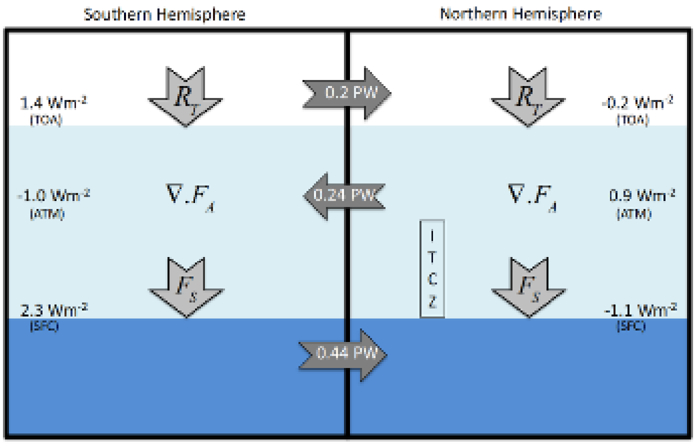

Figure 7.4: Implied cross-equatorial energy transports in the atmosphere and ocean inferred from hemispheric asymmetries in CERES TOA and surface energy budgets and mass corrected divergence in ERAinterim atmospheric total energy transport. From (Loeb et al., 2016).

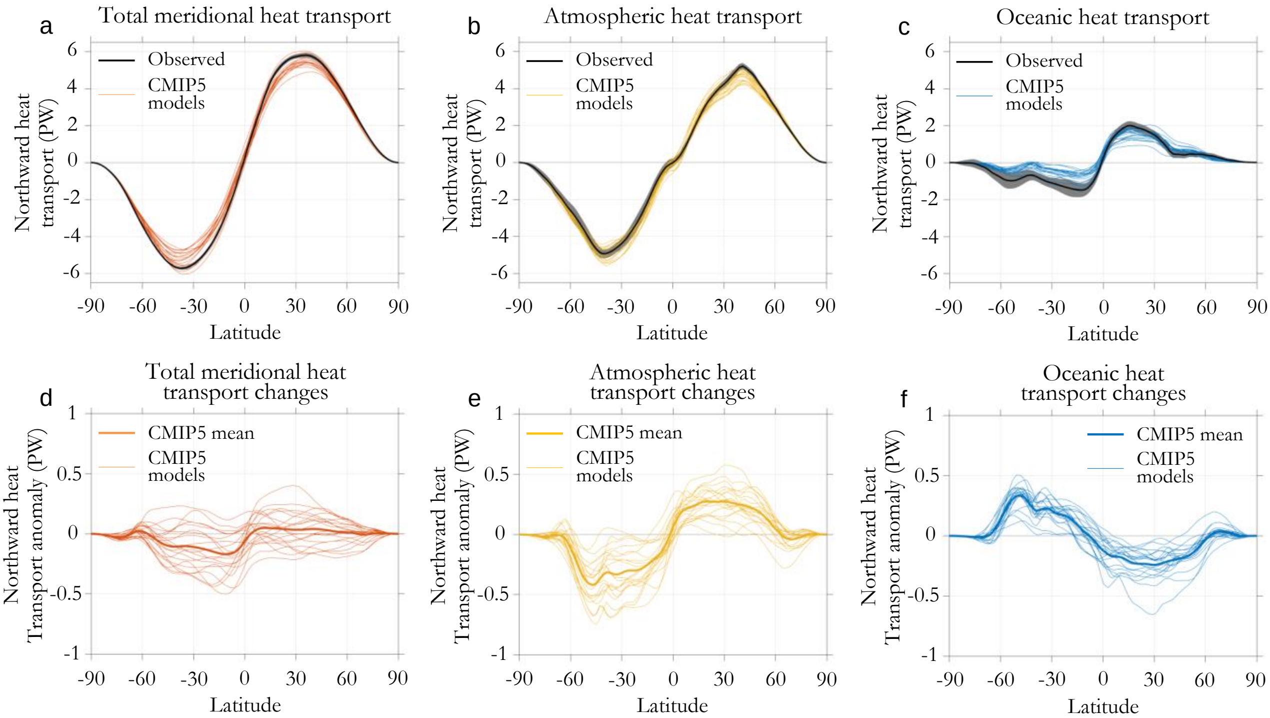

Figure 7.5: Observed and CMIP5 climatological energy transports in the atmosphere and ocean (top) and projected heat transport changes at year 100 following CO2 quadrupling (bottom). (a) Climatological total heat transport inferred from CERES TOA (Armour et al., 2019) and simulated by CMIP5 models. (b) Climatological atmospheric heat transport calculated from the NCEP Reanalysis (Trenberth and Stepaniak, 2003) and simulated by CMIP5 models. (c) Climatological oceanic heat transport inferred from surface energy budgets (calculated as a residual between atmospheric heat transport divergence and TOA radiation fluxes). Grey shading shows 5-95% range on observational estimates. For total meridional heat transport the range is estimated from inter-annual variability and total CERES calibration error added in quadrature at each latitude. For atmospheric heat transport the range is estimated from inter-annual variability and for oceanic heat transport the range is estimated as a residual from the total and atmospheric heat transports with errors propagated in quadrature. (d-f) Anomalies in total, atmospheric, and implied oceanic heat transports simulated by CMIP5 models under abrupt CO2 quadrupling relative to pre-industrial control simulations which define their climatologies in (a)-(c) (following Armour et al., 2019). Implied ocean heat transport changes shown are those derived by net sea-surface heat fluxes and thus do not account for the pattern of ocean heat storage. [placeholder redo for CMIP6 once available and update to new analyses.]

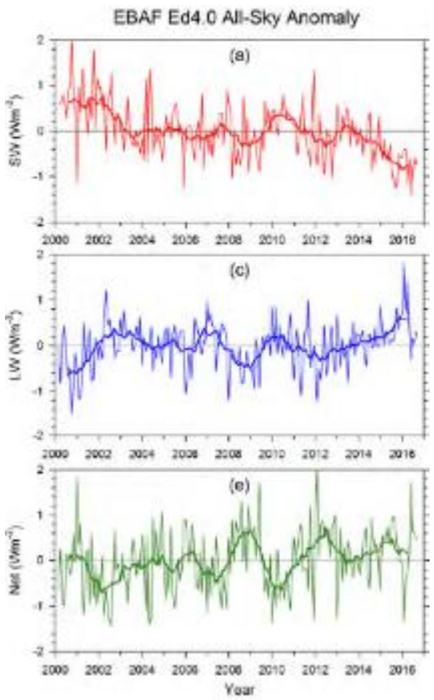

Figure 7.6: Anomalies in global mean all-sky TOA fluxes from EBAF Ed4.0 in terms of reflected shortwave (upper panel), emitted longwave (middle panel) and net TOA flux (lower panel). Thin lines are monthly anomalies. The thick line through monthly anomalies is the 12-month running mean. Larger reflected shortwave and emitted longwave flux anomalies are defined as positive in upper and middle panels. Net TOA flux is defined as incoming shortwave flux minus reflected and emitted fluxes (i.e. downward positive). Adapted from (Loeb et al., 2018).

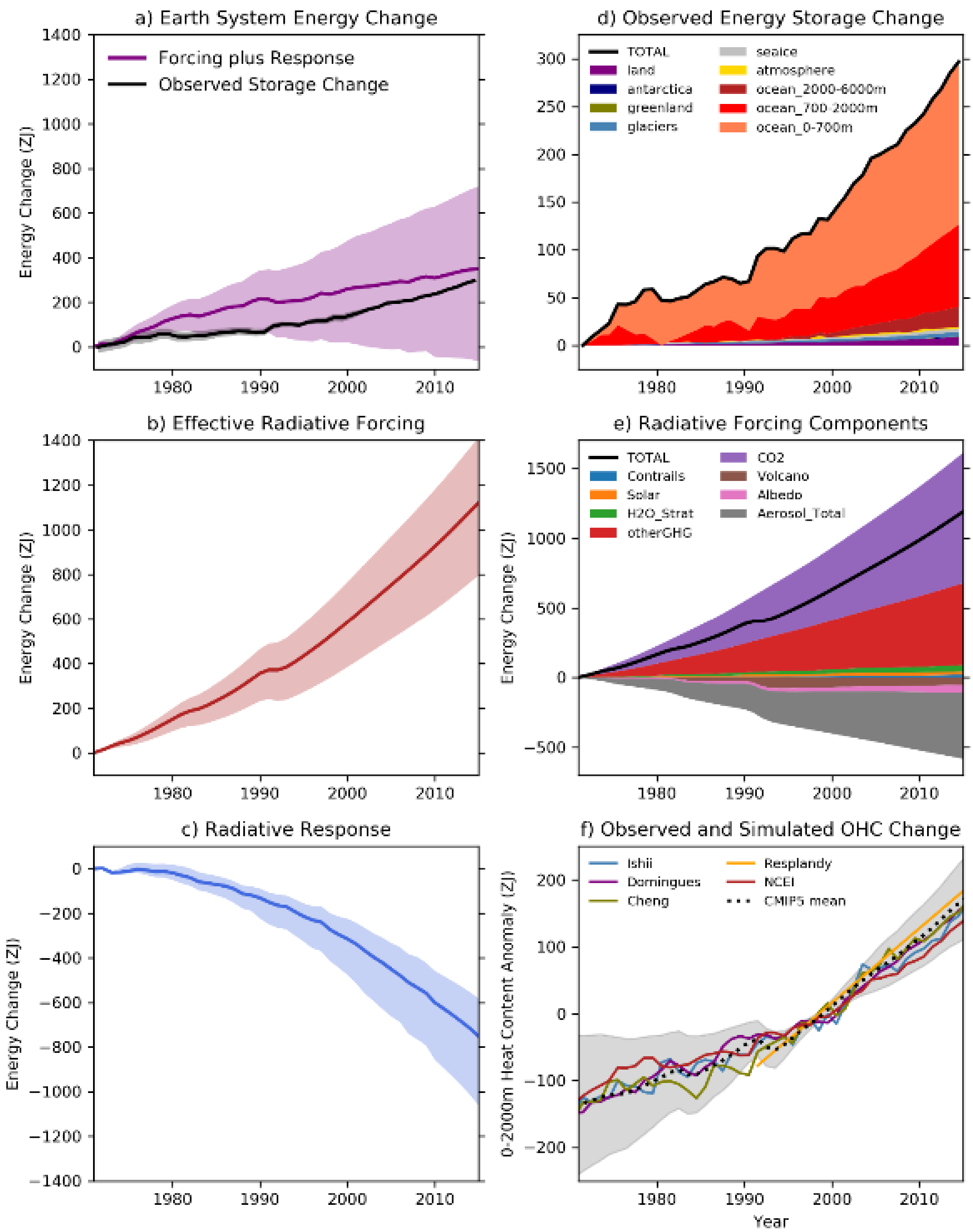

Box 7.2, Figure 1: Estimates of the net cumulative energy change (ZJ = 10^{21} Joules) for the period 1971-2015 associated with: (a) Earth System Energy Change; (b) Effective Radiative Forcing; (c) Earth System Radiative Response. Shaded regions indicate the 5th to 95th percentile uncertainty range. Panels (d) and (e) show the breakdown of components for energy storage and effective radiative forcings, respectively. Panel (f) shows the comparison of CMIP5 model simulations of 0-2000m heat content change with several observation-based estimates, following Cheng et al. (2019). The shaded regions indicate the 5th to 95th percentile range of model simulations, assuming a normal distribution. [placeholder: Observed Storage Change to be properly assessed for SOD].

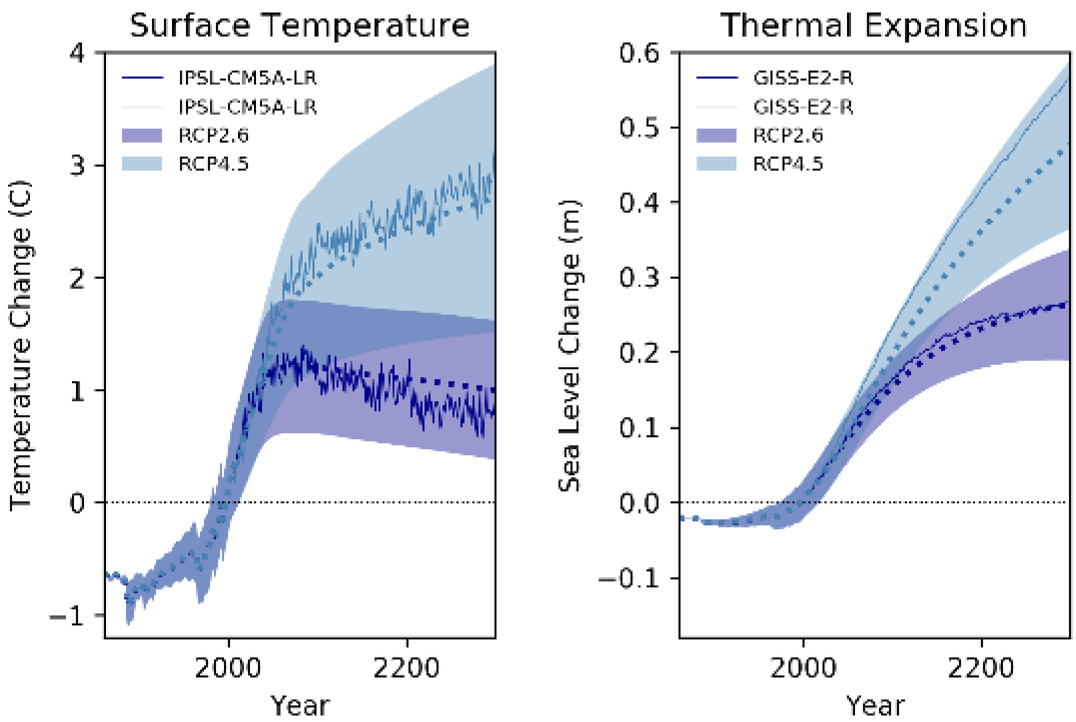

Box 7.2, Figure 2: Two-layer model simulations of global mean surface temperature (left) and ocean thermal expansion (right) under the RCP2.6 and RCP4.5 scenarios, following Palmer et al (2018). Shaded regions indicate the 90% confidence interval based on the ensemble standard deviation. Dotted lines indicate the ensemble mean response. Solid lines show a single CMIP5 model simulation to illustrate the characteristics of variability in each variable. Projections are shown relative to a 1986-2005 baseline period. [placeholder: baseline to be changed inline with AR6 standard period of 1995-2014 at SOD].

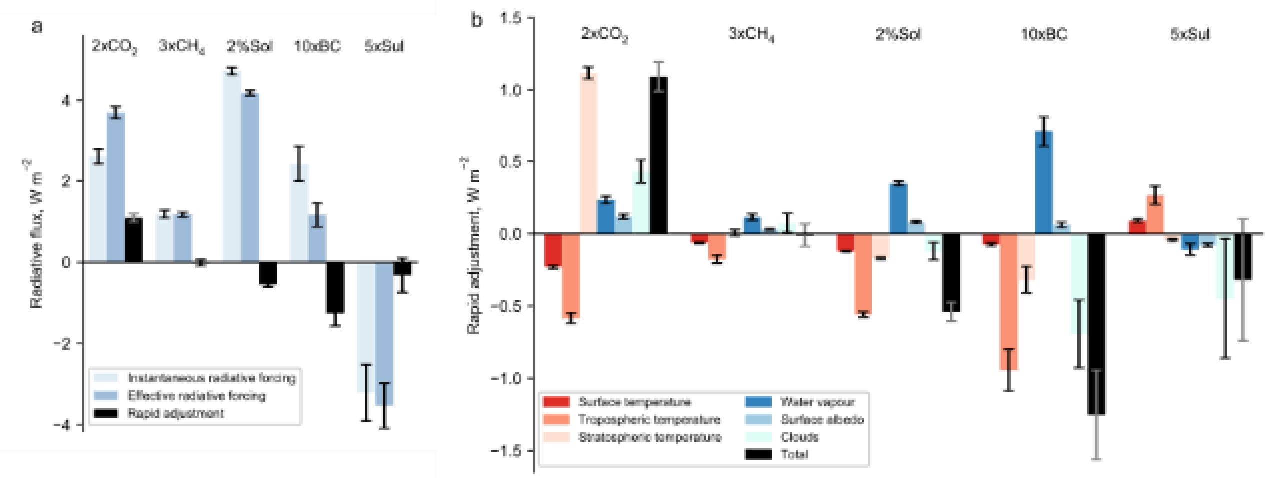

Figure 7.7: The ERF, IRF and rapid adjustment (a) and breakdown of the rapid adjustment using radiative kernels (b) for five idealised forcing experiments across nine models. The 95% confidence range is shown. Note that the land-surface response is included in ERF as an adjustment. Data modified from Smith et al. (2018). The results are computed from idealized single forcing experiments with the following abrupt perturbations from present day conditions; doubling CO_2 concentration ($2xCO_2$), tripling methane concentration ($3xCH_4$), two percent increase in insolation (2%Sol), ten times black carbon concentrations or emissions (10xBC), five times sulphate concentrations or emissions (5xSul). [*For SOD land response will be removed from the ERF in the figure.]*

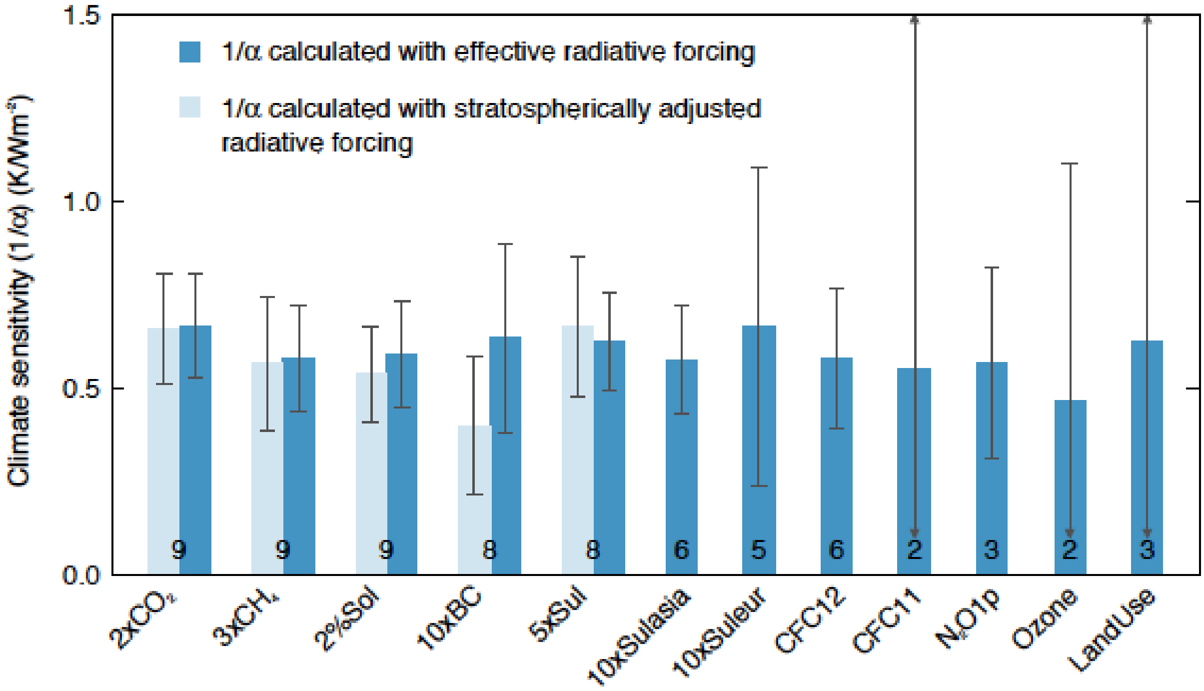

Figure 7.8: Values of climate feedback parameter (α) derived from ERF and SARF for twelve forcing experiments. Multi-model means and full model ranges are shown. ERF is derived from prescribed SST and sea-ice experiments. The number of models analysed differs between experiments as indicated on the bars. Data from Richardson et al. (Submitted). The results are computed from idealized single forcing experiments with the following abrupt perturbations from present day conditions; doubling CO_2 concentration ($2xCO_2$), tripling methane concentration ($3xCH_4$), two percent increase in insolation (2%Sol), ten times black carbon concentrations or emissions (10xBC), five times sulphate concentrations or emissions (5xSul), ten times sulphate concentrations or emissions over Asia only (10xSulasia), ten times sulphate concentrations or emissions over Europe only (10xSuleur), change in CFC-12 mixing ratio to 5ppb (CFC-12), change in CFC-11 mixing to 5ppb (CFC-11), change in N2O mixing ratio to 1ppm (N2O1p), five times tropospheric ozone concentration (Ozone), change in vegetation to pre-industrial conditions (LandUse).

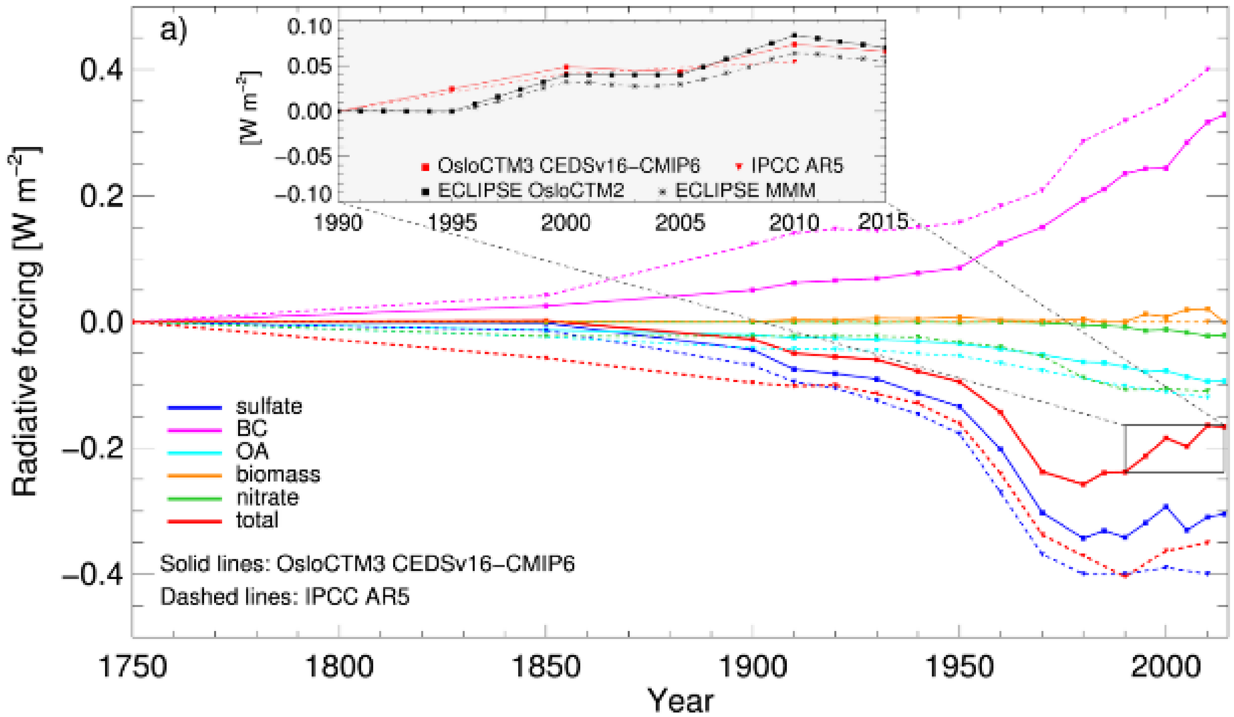

Figure 7.9: (placeholder) Radiative forcing time series for the major anthropogenic aerosol species (1750-2014), based on CEDS emissions. From Lund et al. (2018). [To be replaced by AeroCom Phsse III and/or AerChemMIP results.]

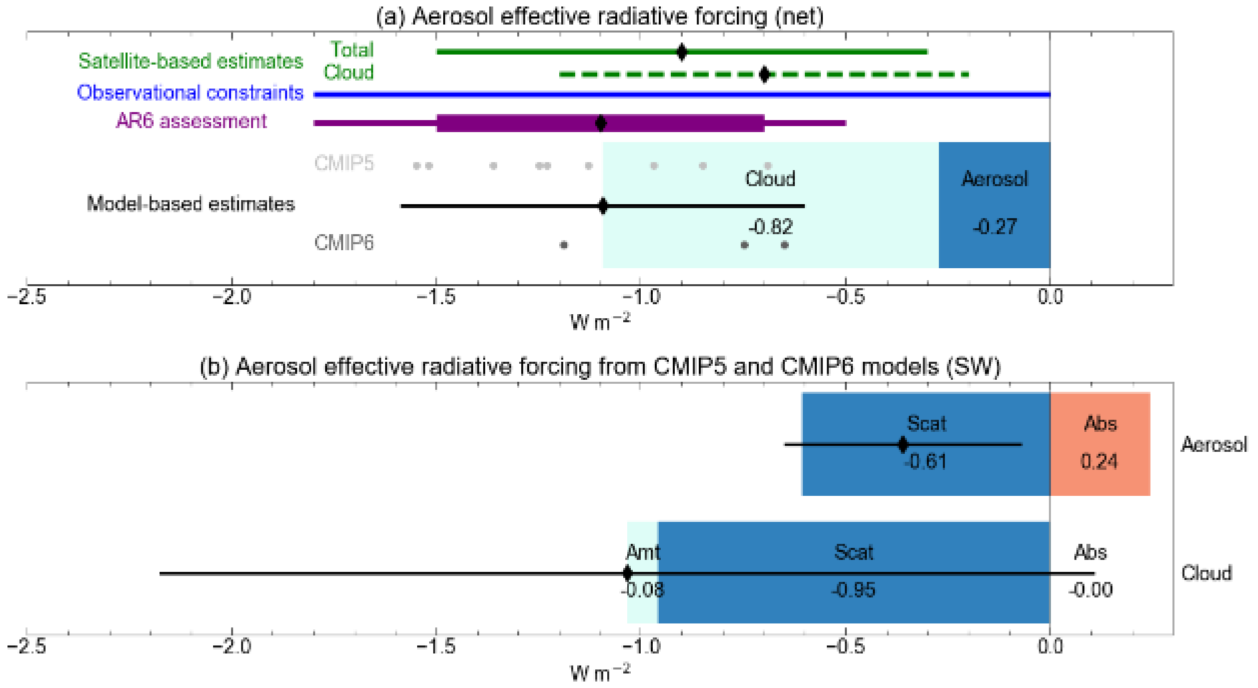

Figure 7.10: (a) Net aerosol ERFari+aci from different lines of evidence. Green lines show the *very likely* range based on satellite observations (solid bar ERFari+aci, dashed bar ERFaci). Blue line shows the *very likely* range based on observational constraints. Purple bars show the assessed *very likely* range (thin), *likely* range (thick), and best estimate (black diamond). Bars show climate model estimates, subdivided into CMIP5 models (Zelinka et al., 2014) and CMIP6 models with individual models depicted by grey dots, and multi-model mean ERFari ("Aerosol") and ERFaci ("Cloud"). Overlaid black diamond and black line shows the multi-model mean and *very likely* range of model-derived ERFari+aci. (b) Contributions to the shortwave components of model-derived ERFari and ERFaci in (a) from scattering ("Scat"), absorption ("Abs") and cloud amount ("Amt"), with total ERFari and ERFaci best estimates and *very likely* ranges overlaid as black diamonds and lines.

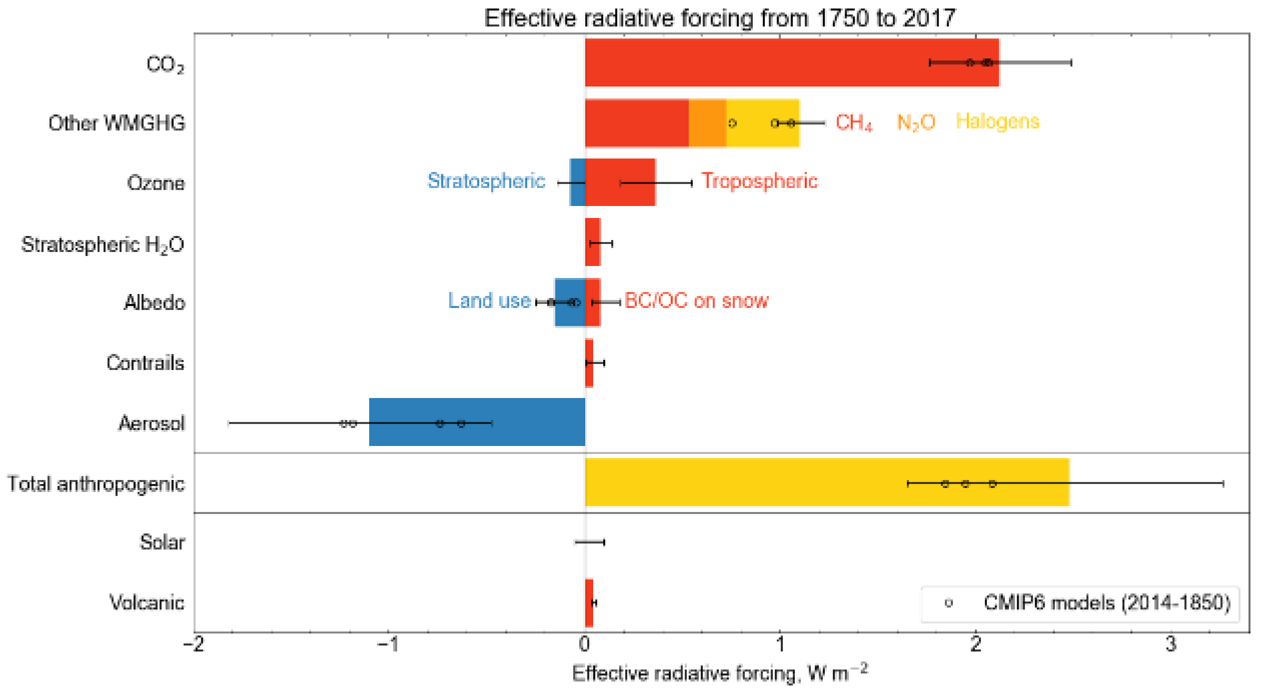

Figure 7.11: Effective radiative forcing from 1750 to 2017 by contributing forcing agents. CMIP6 model estimates for 1850-2014 are shown as circles where known.

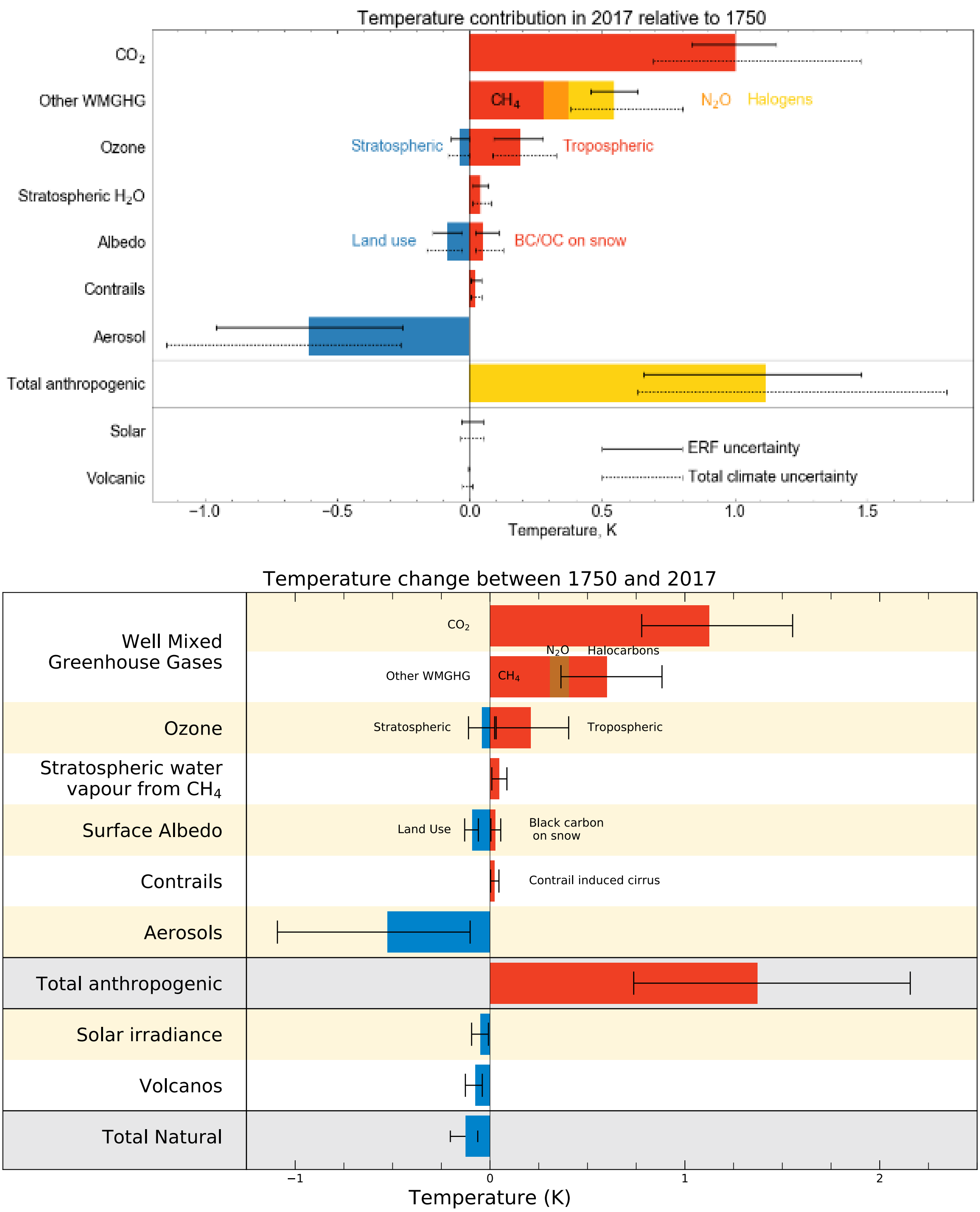

Figure 7.12: The contribution of forcing agents to 2017 temperature change relative to 1750. (top) These estimates were produced using the FaIR simple climate model emulator (Smith et al., 2018a) where ranges for ERF were taken from Section 7.3 and ranges for ECS and TCR were taken from Section 7.5. Error bars show the contribution of forcing uncertainty with best estimates of ECS and TCR (solid lines) and total response uncertainty. (bottom) the temperature changes simulated by the MAGICC simple climate model (Meinshausen et al., 2011; Nauels et al., 2017), using its own distribution of ECS and TCR, only the effect of forcing error is shown. [*Preliminary results from MAGICC based on earlier forcing estimates, will be updated for SOD]*.

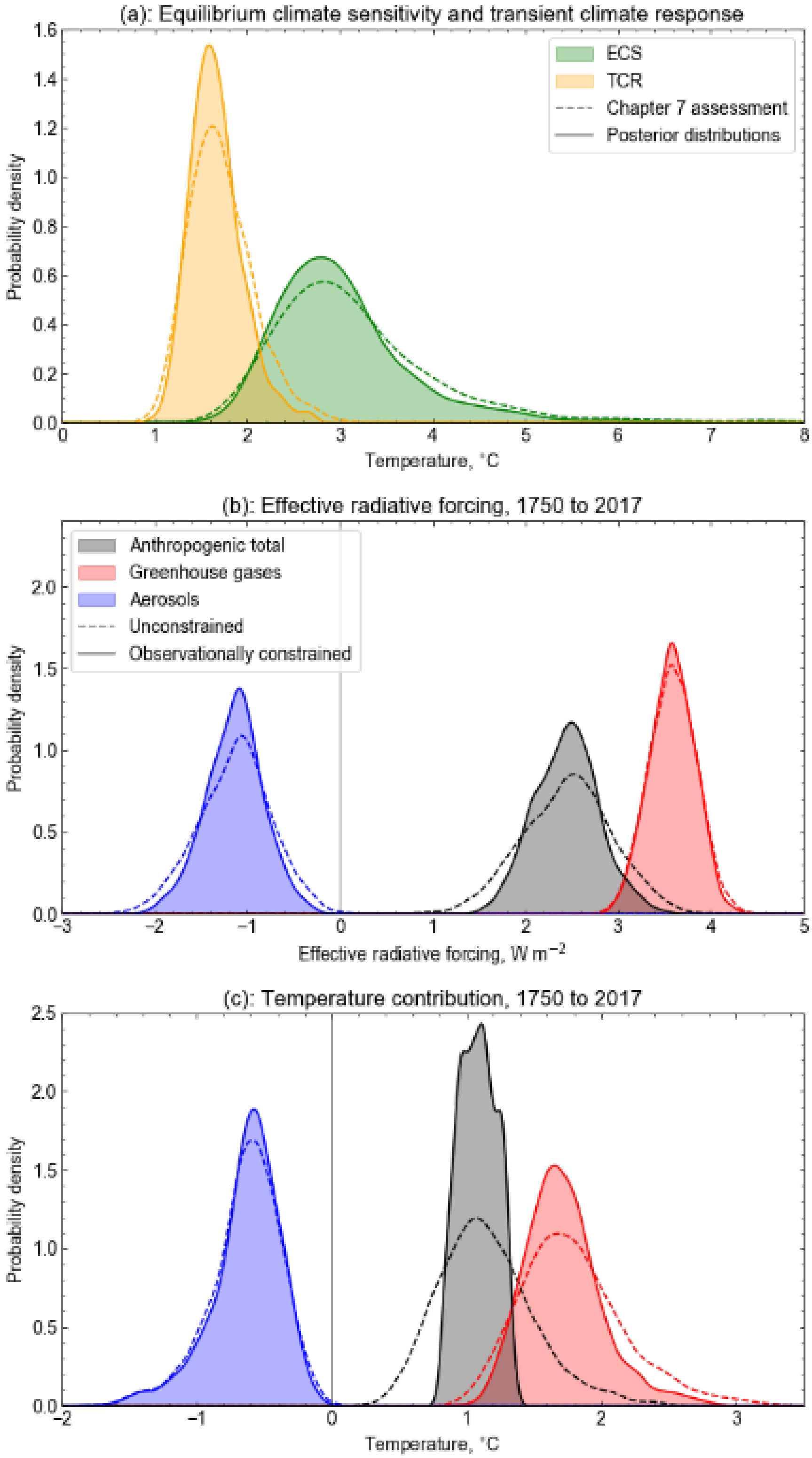

Figure 7.13: (a) Probability density functions (PDFs) of ECS and TCR; (b) Distributions of effective radiative forcing and (c) distributions of contribution to anthropogenic temperature change from 1750 to 2017. Ranges for ERF were taken from Section 7.3 and ranges for ECS and TCR were taken from Section 7.5. PDFs combine the contribution of forcing uncertainty with ranges of ECS and TCR. In each panel, the solid filled curves show the constrained (posterior) distributions after matching historical temperatures to the surface air temperature from Cowtan and Way (2014) using the FaIR simple climate model emulator (Smith et al., 2018a). In (a), dashed curves show the prior distributions as assessed in this chapter, whereas in (b) and (c) dashed curves represent distributions before constraint to historical temperature observations.

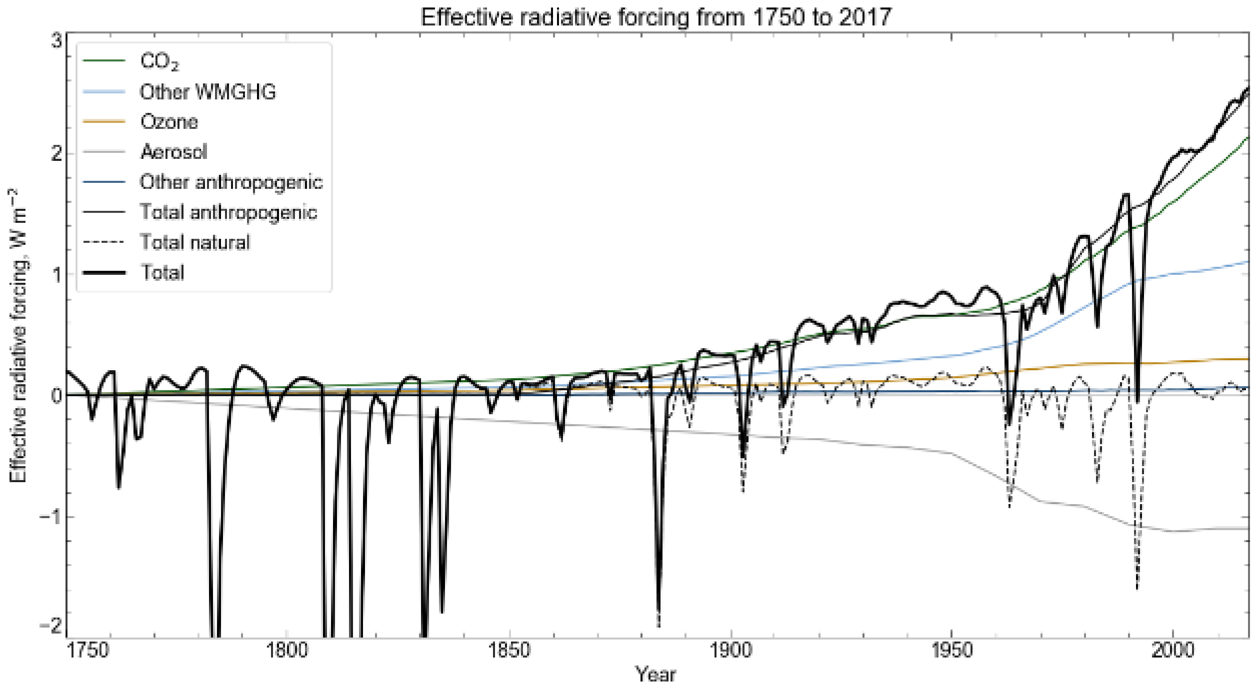

Figure 7.14: Timeseries of total (thick dashed line) and individual components (thin solid lines) of ERF from 1750 to 2017 assessed in this chapter. Some small individual components are grouped for clarity.

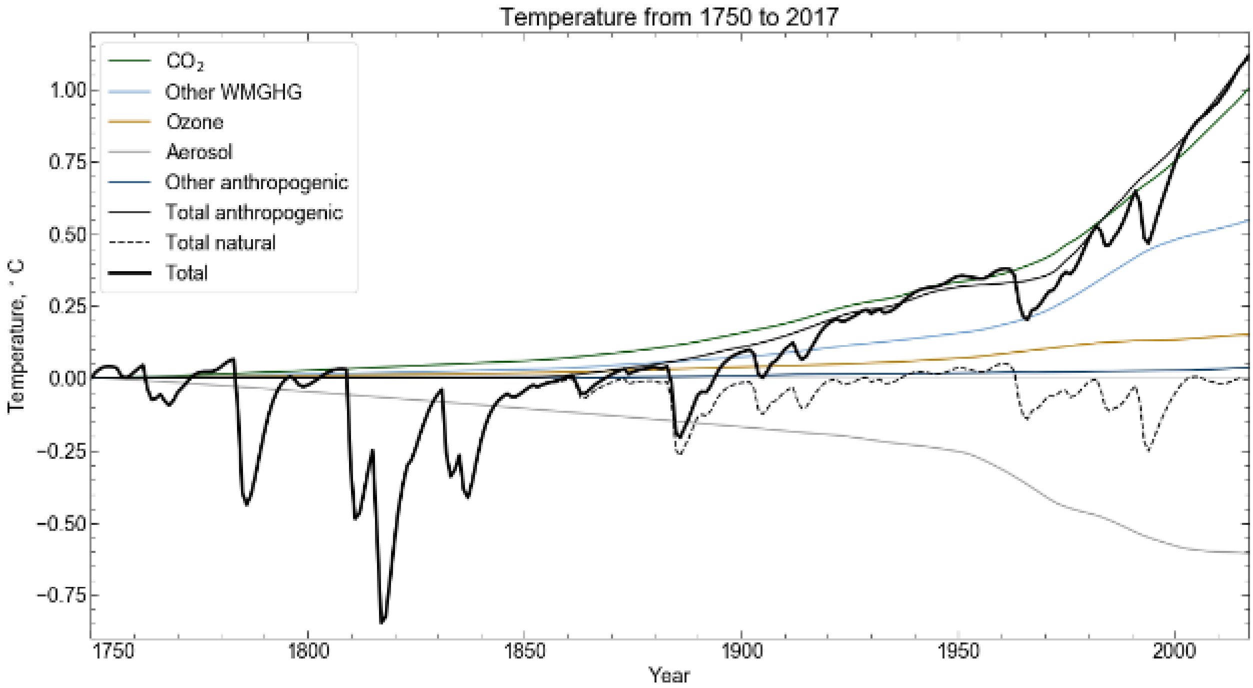

Figure 7.15: Timeseries of near surface global temperature changes, using the time series of ERFs assessed in this section (Figure 7.14) and calculated using the FaIR simple climate model emulator (Smith et al., 2018a) using the distribution of ECS and TCR assessed in section 7.5 and Section 7.3.5.3. The median of a 2000-member Monte Carlo ensemble is shown for the total temperature and the contribution from each component.

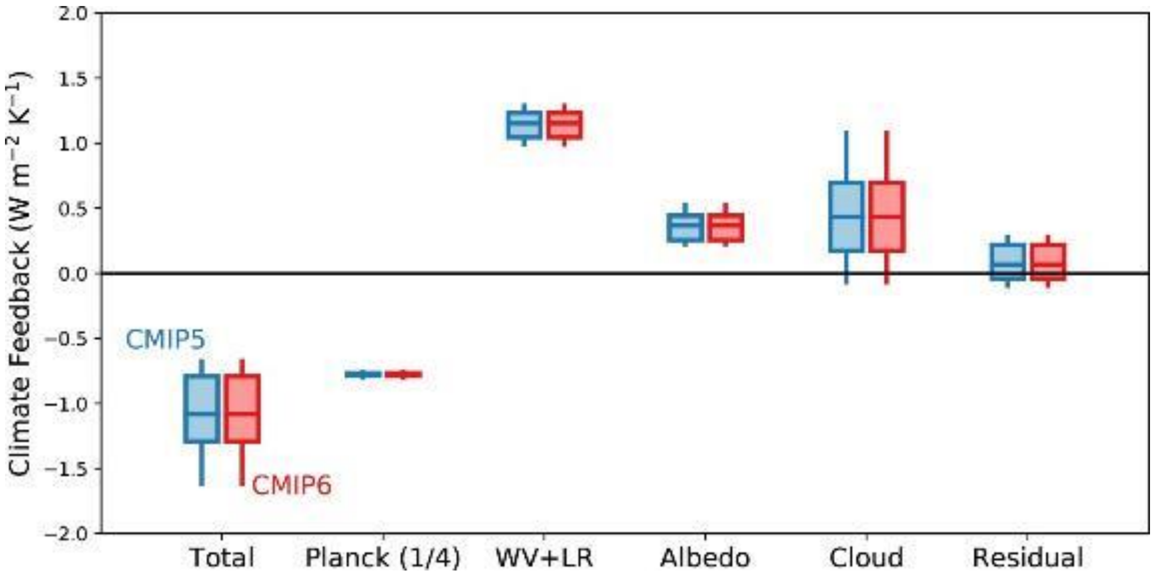

Figure 7.16: Estimates of global mean climate feedbacks in CMIP5 and CMIP6 abrupt4xCO_2 simulations. The box-whisker plot indicates the multi-model mean (horizontal lines), *likely* range (boxes) and *very likely* range (whiskers). Individual feedback terms are computed using a radiative kernel by multiplying temperature-mediated changes in the respective field. A residual between the summed feedback and the total climate feedback, the latter directly derived from the models, is shown at the right. The CMIP5 data are adopted from Caldwell et al. (2016). [*Note that the CMIP6 values are not yet available, so plotted using the CMIP5 values tentatively.*]

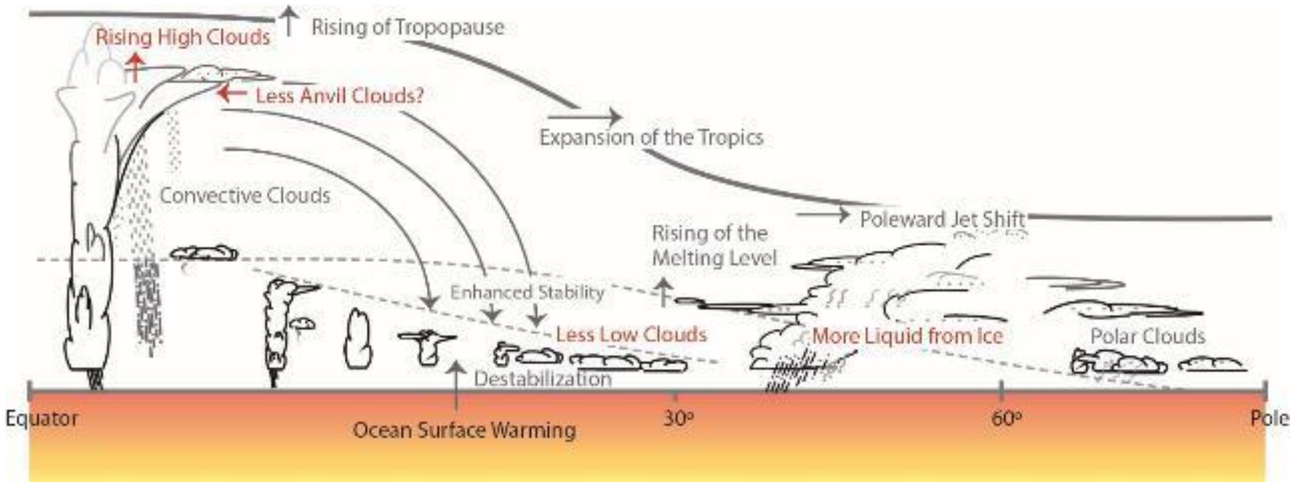

Figure 7.17: Schematic cross section of diverse cloud regimes between the tropics and Polar Regions. Thick solid and dashed curves indicate the tropopause, melting level, and the subtropical inversion layer in the current climate. Thin grey arrows represent robust responses in the large-scale circulation to greenhouse warming, supported by independent lines of evidence. Text and arrows in red show the robust part of cloud responses to the surface warming.

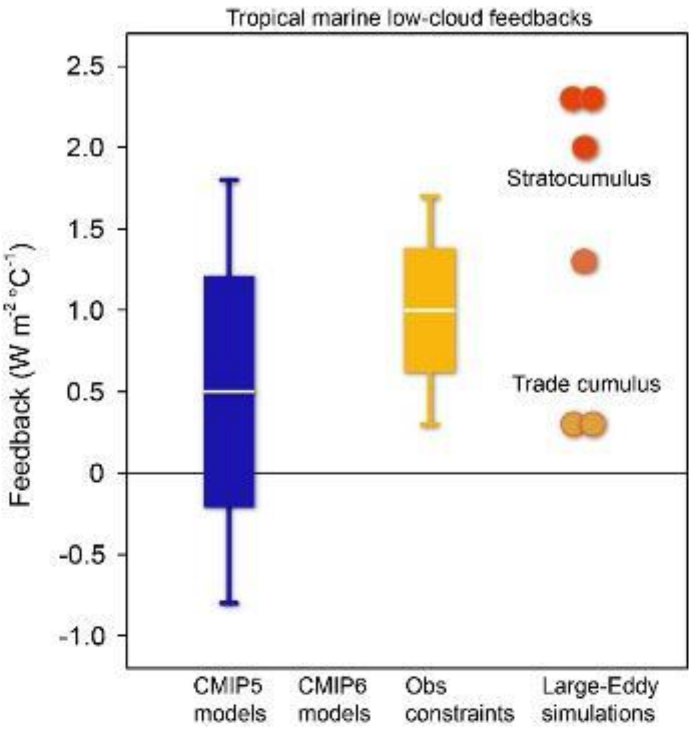

Figure 7.18: A synthetic evaluation of the tropical low-cloud feedback, derived from GCMs (blue), observed cloud controlling factors (yellow), and LES (dots). Central estimates are shown by white lines. Boxes and the error bars indicate the *likely* (66 %) and *very likely* (90 %) confidence intervals, respectively. The feedbacks are shown as local values but not the global mean. LES results are derived from six simulations for different cloud regimes over the tropical subsidence region. Data obtained from (Klein et al., 2017). [*Note that results from CMIP6 models will be added when available.*]

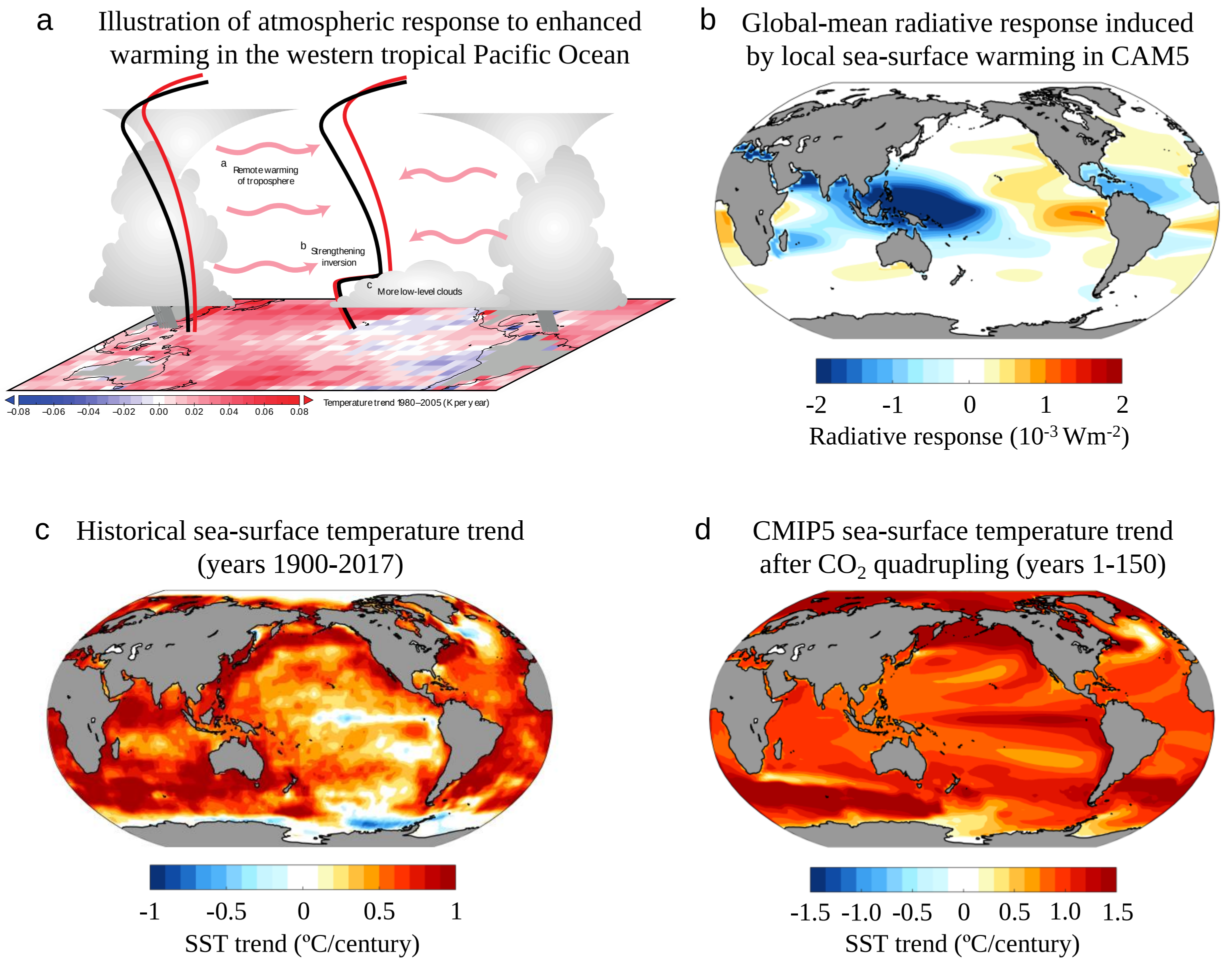

Figure 7.19: (a) Illustration of tropospheric temperature and cloud response to enhanced warming in the west Pacific Ocean relative to the east; adapted from (Mauritsen, 2016) based on results from (Zhou et al., 2016). (b) Global TOA radiative response to sea-surface warming at each location while SSTs are held fixed elsewhere in NCAR's Community Atmosphere Model version 5 (CAM5); adapted from (Zhou et al., 2017). (c) Observed sea-surface temperature linear trend over 1900-2017 (HadISST dataset; Rayner et al., 2003). (d) Sea-surface temperature linear trend over 150 years following abrupt CO_2 quadrupling simulations of CMIP5 GCMs (average of 17 models). *[Note SOD will update to show observed 1900-2018 SST trend. For SOD: show (a) as a separate figure and update. In its place add the pattern of warming under 1pctCO2 or historical for CMIP5/6]*

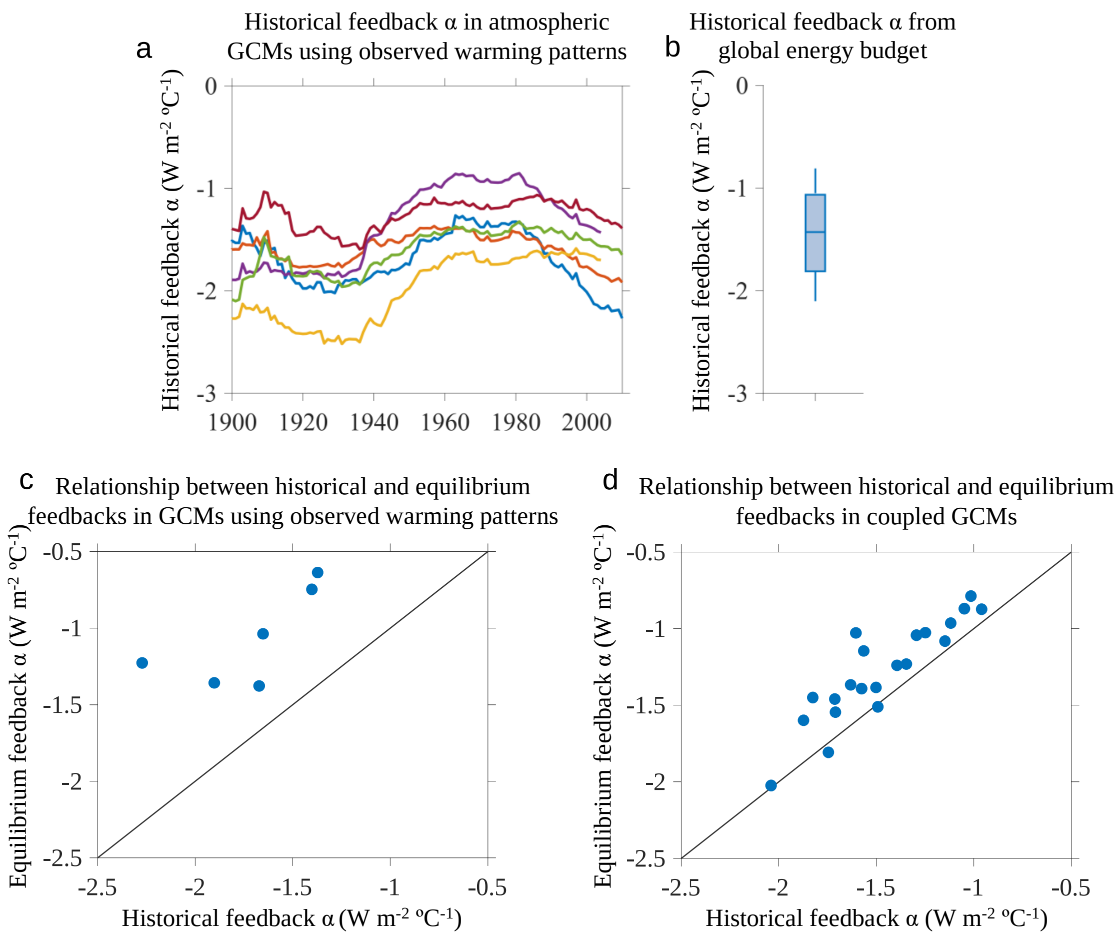

Figure 7.20: **(a)** Radiative feedback (α) over the historical record derived from atmospheric GCMs with prescribed observed SSTs and sea-ice concentration changes (modified from Andrews et al., 2018). Historical feedback is derived from linear regression of global TOA radiation against global near-surface air temperature over the simulations, with regression starting in year 1870 and ending in the year shown. **(b)** Radiative feedback derived from historical energy budget constraints (Section 7.5.3). **(c)** Relationship between historical net feedback in atmospheric GCMs constrained to match the observed pattern of warming over the over the historical record (Figure 7.19c) and the net feedback under abrupt CO_2 quadrupling within coupled versions of the same GCMs (average warming pattern shown in Figure 7.19d). Equilibrium feedback is estimated based on regression of global TOA radiation against global near-surface air temperature over years 1-150 of *abrupt4xCO*$_2$ simulations, but similar results are found if the feedback magnitude is estimated as CO_2 ERF divided by ECS. **(d)** Relationship between historical net feedback and equilibrium net feedback in fully-coupled CMIP5 models. Historical feedback is estimated at year 100 of 1%/yr CO_2 ramping simulations based on the change in global TOA radiation divided by the change in global near-surface air temperature where changes are taken with respect to pre-industrial (Armour, 2017). The equilibrium feedback magnitude is estimated as CO_2 ERF divided by ECS where ECS is derived from linear regression over years 1-150 of *abrupt4xCO*$_2$ simulations (Box 7.1). *[SOD will add additional CMIP6 models to all panels when available. Calculate feedback changes over historical simulations when forcing become available (RFMIP).]*

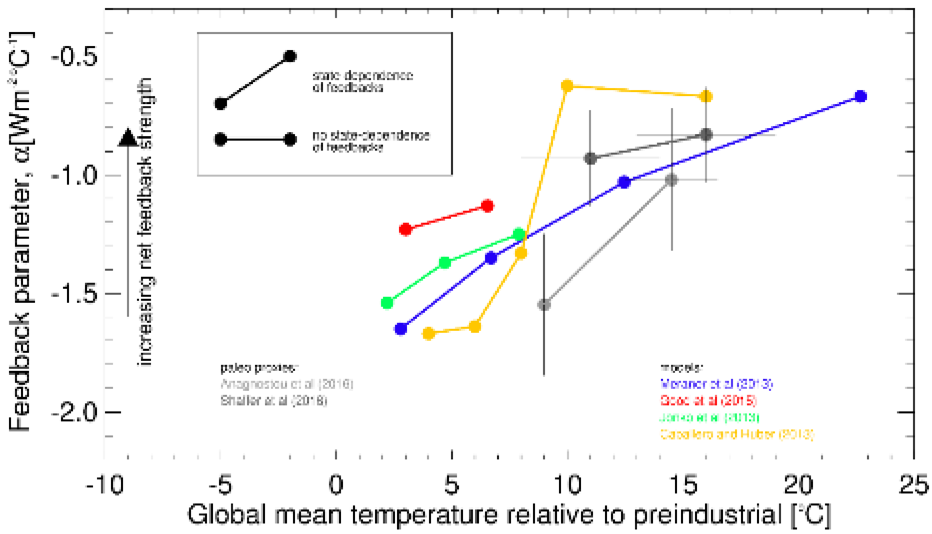

Figure 7.21: Feedback parameter, α (Wm^{-2} $°C^{-1}$), as a function of global mean surface air temperature relative to preindustrial, for model simulations (coloured circles and lines), and from paleoclimate data (grey circles and associated uncertainties). *[N.B. that some of these values will need checking with the original authors, as they are not all clear from the publications. Additionally, in some cases I have had to make assumptions about the forcing from CO_2 doubling, or the ECS, or the LGM temperature].*

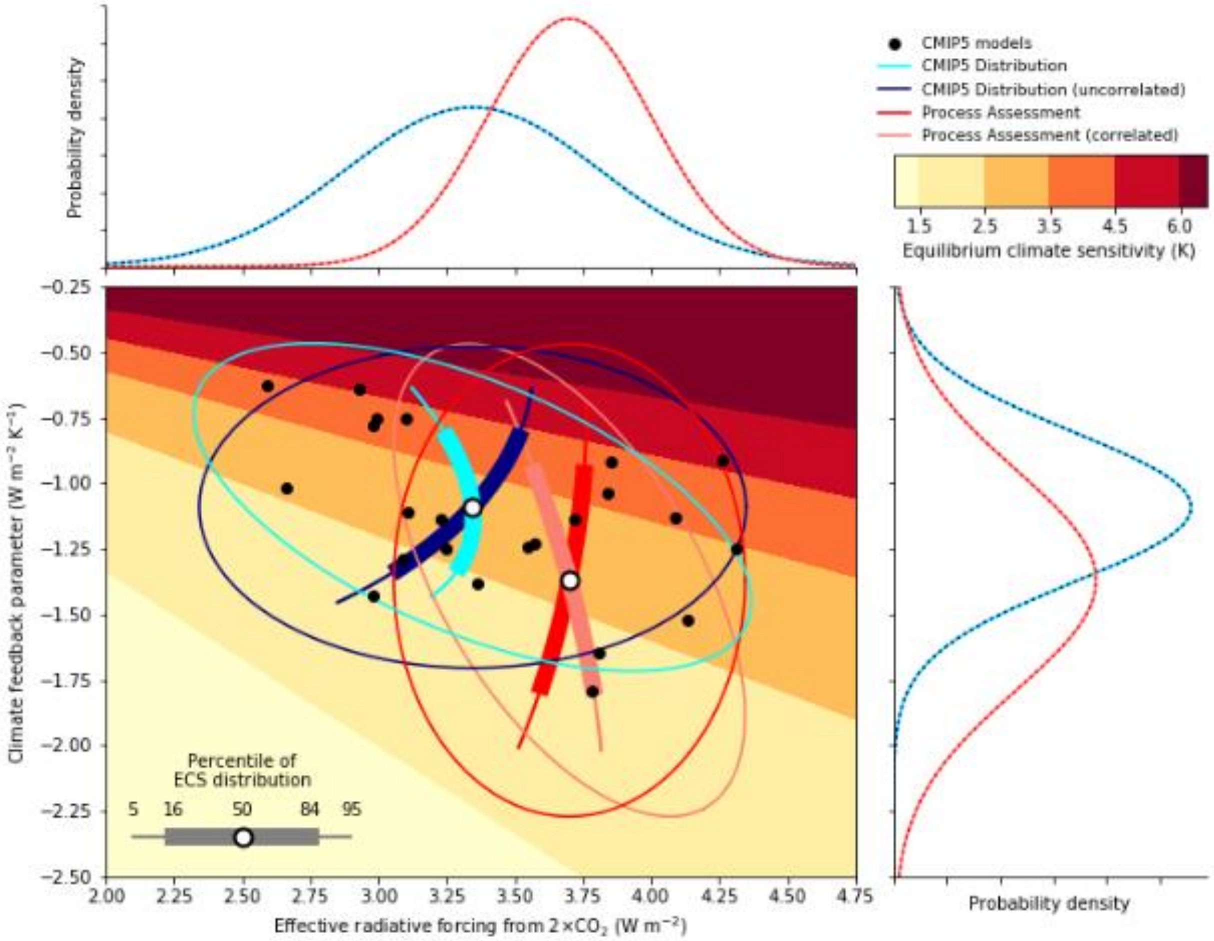

Figure 7.22: Probability distributions of ERF to CO_2 doubling ($\Delta F_{2\times CO2}$, top) and the total climate feedback (α, right), derived from CMIP5 *abrupt4xCO₂* simulations (blue) and process-based assessments in Sections 7.3.2 and 7.4.2 (red). The joint PDF is calculated on a two-dimensional plane of $\Delta F_{2\times CO2}$ and α (middle), on which the 90% range shown by an ellipse is imposed to the background theoretical values of ECS (color shading). The white dot, thick and thin curves in the ellipse represent the mean, *likely* and *very likely* range of ECS. For each set of PDFs of $\Delta F_{2\times CO2}$ and α, two different estimations of the ECS range are presented; one assuming that $\Delta F_{2\times CO2}$ and α are independent (red and blue) and the other assuming that they have a covariance seen in the CMIP5 *abrupt4xCO_2* simulations (pink and cyan). The assumption about the co-dependence between $\Delta F_{2\times CO2}$ and α does not alter the mean estimate of ECS but affects its *likely* range. Data for *abrupt4xCO_2* simulations are taken from Caldwell et al. (2016).

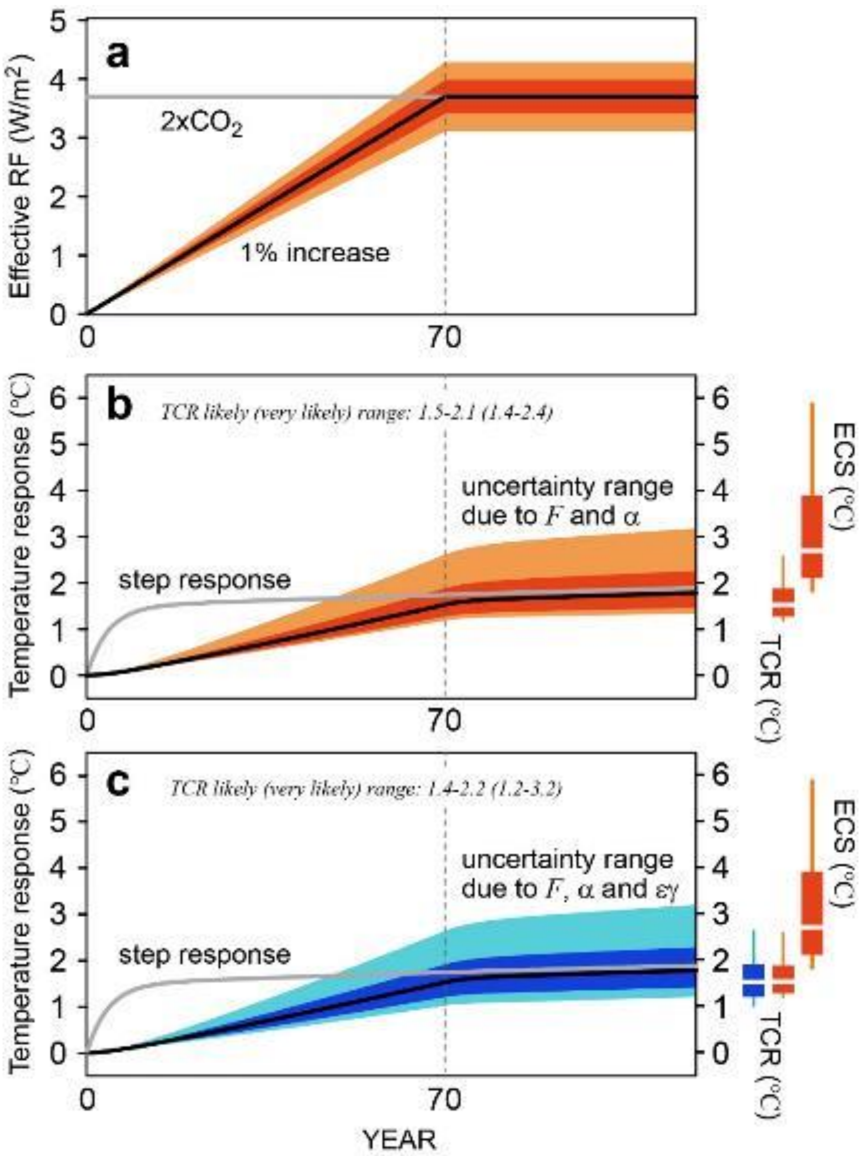

Figure 7.23: (a) Time evolution of the effective radiative forcing (ERF) to the CO_2 concentration increased by 1% per year until the year 70 (equal to the doubling, grey line) and kept fixed afterword. The range of ERF has been assessed in Section 7.3. (b)-(c) Range of surface ocean temperature response (assumed to be equivalent to the surface air temperature response) to the CO2 forcing in the two-layer EBM calculated with a given range of ECS, considering uncertainty only in ΔF2×CO2 and α (b, shading by red and orange colours) and additionally in two parameters associated with the ocean heat uptake (c, shading by blue and cyan colours). The mean estimate of the response (black curve) is identical in (b) and (c). For comparison, the step response to abrupt doubling of the CO2 concentration is displayed by grey curves. The mean and ranges of ECS and TCR are shown at the right (the values also presented in the panel).

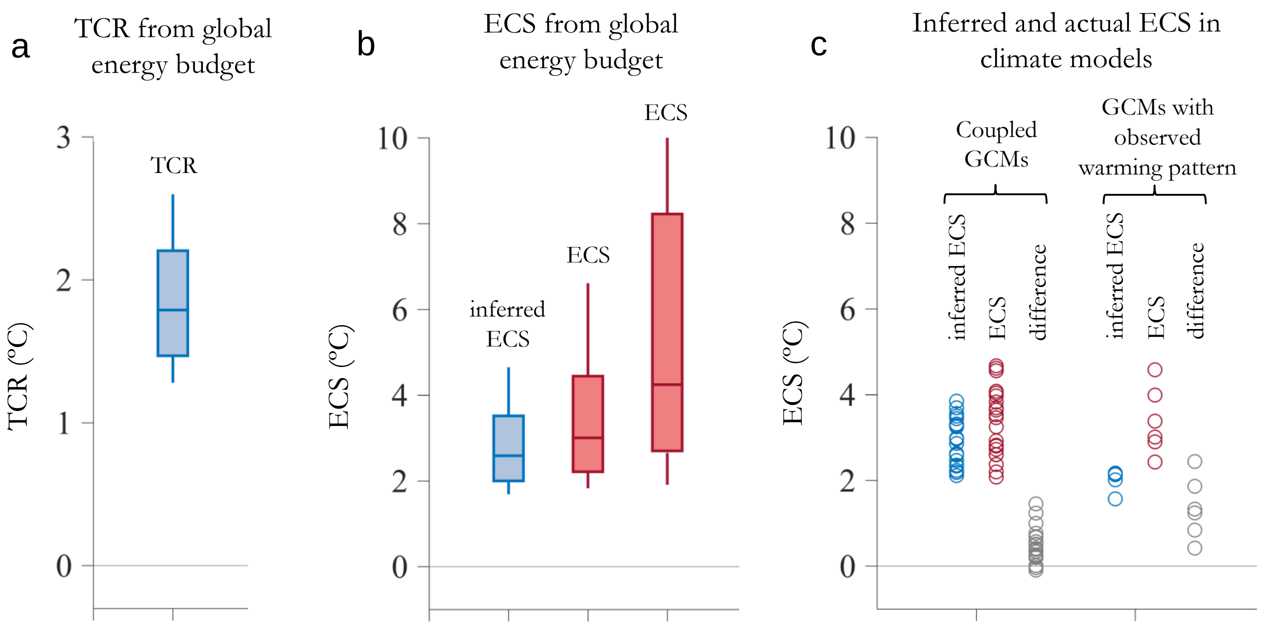

Figure 7.24: (a) TCR inferred from global energy budget constraints for the period 2002-2018 relative to 1850-1900; horizontal bar shows median value, box shows 17% to 83% range, and vertical line shows 5% to 95% range. (b) ECS inferred from global energy budget constraints for the period 2002-2018 relative to 1850-1900 (blue) and ECS accounting for the pattern effect (red) (Section 7.4.3) based on feedback changes derived from coupled GCM simulations (Armour, 2017) (middle) or from GCM simulations with prescribed historical sea-surface temperature and sea-ice concentrations (Andrews et al., 2018) (right). (c) Relationship between inferred ECS (blue) and actual ECS (red) in GCMs where the inferred ECS is derived from coupled GCM simulations (Armour, 2017) (left) or from GCM simulations with prescribed historical sea-surface temperature and sea-ice concentrations (Andrews et al., 2018) (right); actual ECS is derived from abrupt4xCO2 simulations and differences between the two are shown in grey. [Eventually redo this with using historical simulations and RFMIP forcings for CMIP6 models rather than 1pctCO2 runs.]

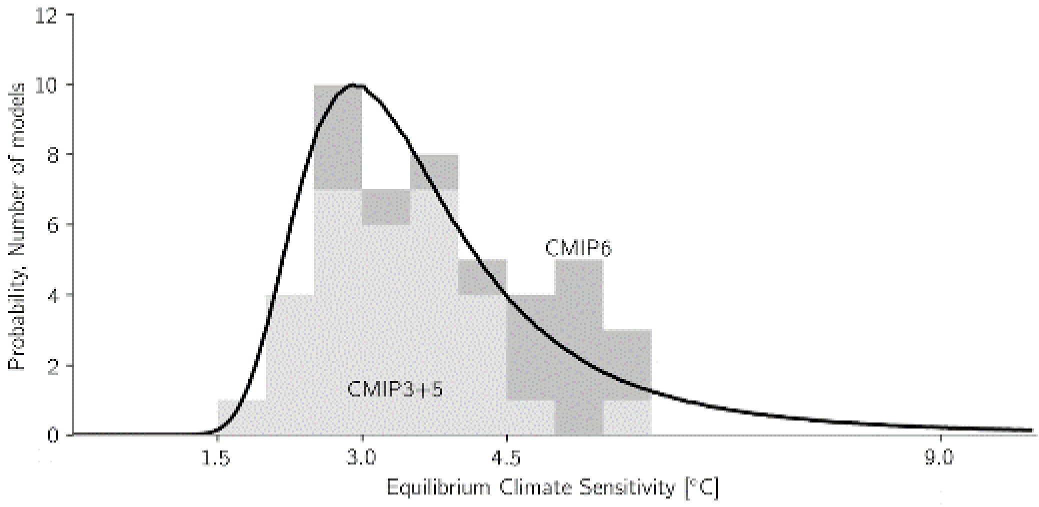

Figure 7.25: Distribution of ECS from CMIP3 and CMIP5 (light gray) and CMIP6 models (dark gray). The black line is the distribution obtained by Monte-Carlo sampling feedback parameters estimated from CMIP5 models by Caldwell et al. (2016). *[This is a preliminary analysis based partly on an informal survey]*

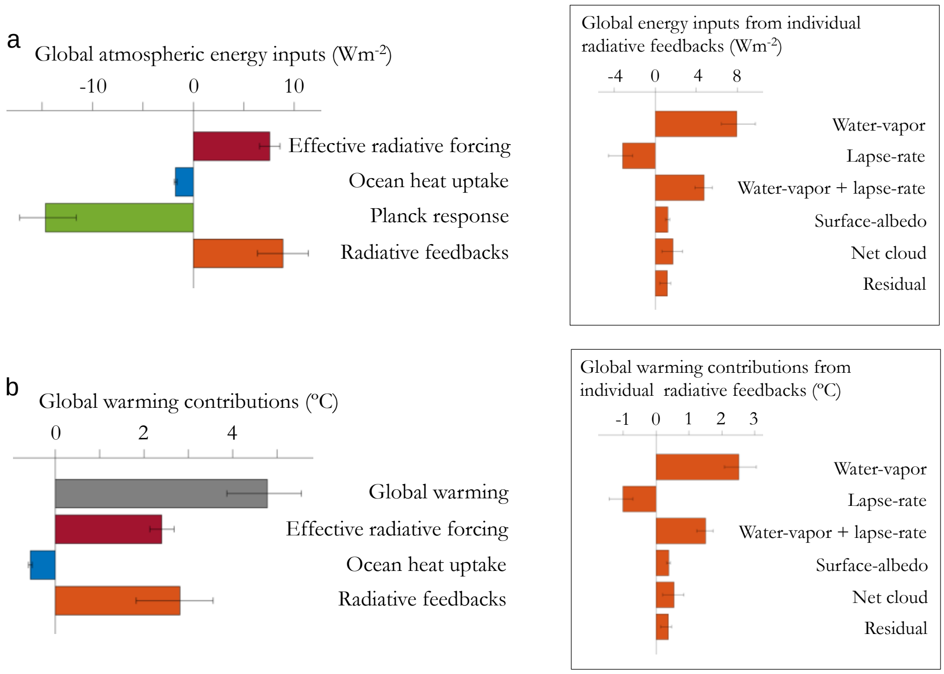

Figure 7.26: Contributions of effective radiative forcing, ocean heat uptake and radiative feedbacks to global atmospheric energy input and near-surface air temperature change at year 100 of abrupt CO_2 quadrupling simulations of CMIP5 models. **(a)** The energy flux to the global atmosphere associated with the effective CO_2 forcing, global ocean heat uptake, Planck response, and radiative feedbacks, which together sum to zero; inset shows energy input from individual feedbacks, summing to the total feedback energy input. **(b)** Contributions to net global warming calculated by dividing the energy inputs by the global Planck response (3.2 W m^{-2} $°C^{-1}$), with the contributions from radiative forcing, ocean heat uptake, and radiative feedbacks summing to the value of net warming; inset shows warming contributions associated with individual feedbacks, summing to the total feedback contribution. Uncertainties show 25% and 75% percentiles across models. Feedbacks are calculated using radiative kernels (Shell et al., 2008) and the analysis is based on that of Goosse et al. (2018). *[SOD: redo for CMIP6 models when available.]*

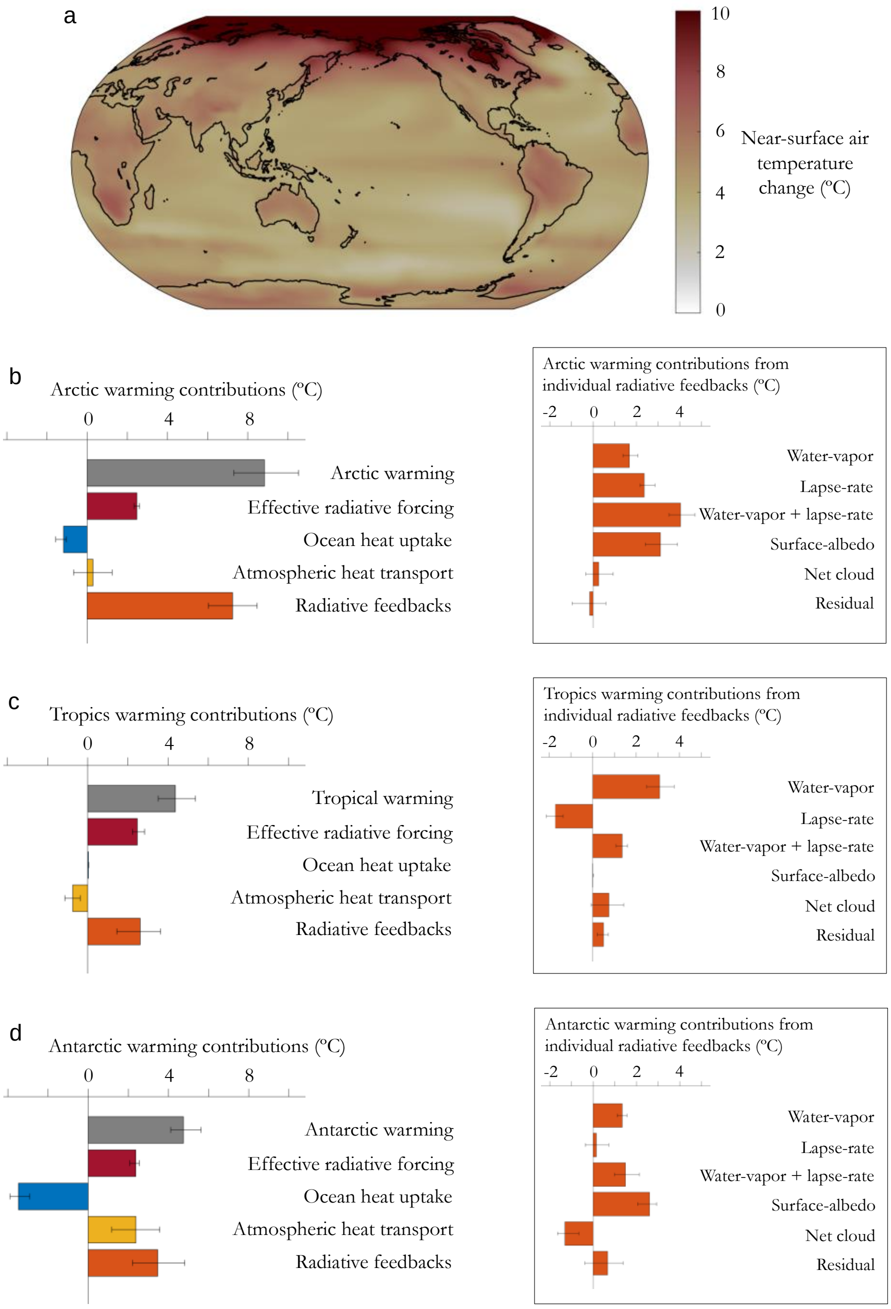

Figure 7.27: Contributions of effective radiative forcing, ocean heat uptake and radiative feedbacks to regional surface temperature changes at year 100 of abrupt CO_2 quadrupling simulations of CMIP5 models. **(a)** Pattern of near-surface air temperature change. **(b-d)** Contributions to net Arctic (>60°N), tropical (30°S-30°N), and Antarctic (<60°S) warming calculated by dividing regional-average energy inputs by the regional-average Planck response, with the contributions from radiative forcing, changes in atmospheric heat transport, ocean heat uptake, and radiative feedbacks summing to the value of net warming; inset shows regional warming contributions associated with individual feedbacks, summing to the total feedback contribution. Uncertainties show 25% and 75% percentiles across models. Feedbacks are calculated using radiative kernels (Shell et al., 2008) and the analysis is based on that of Goosse et al., (2018). *[SOD: Redo for CMIP6 models when available.]*

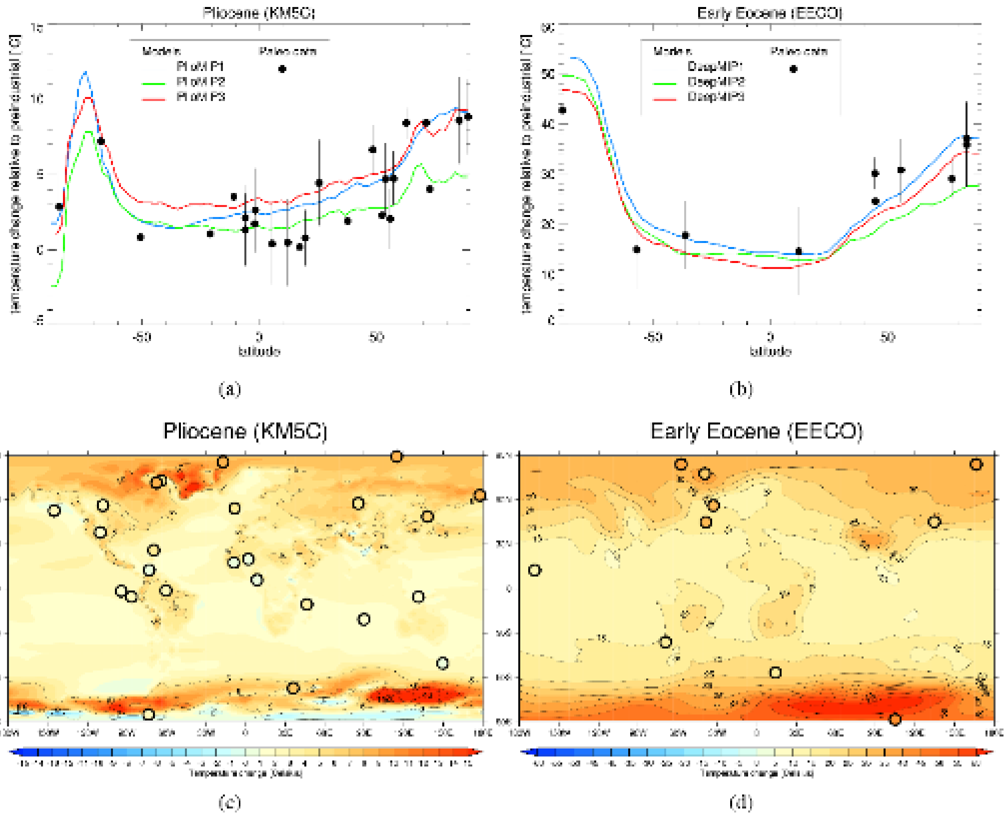

Figure 7.28: [N.B. that the model results in this figure are old simulations, and the data has been synthetically generated. This placeholder is just to show the style of the anticipated figure for SOD.]. Temperature changes compared with pre-industrial for the high-CO_2 MPWP and EECO time periods, from proxies and models. (a) proxy reconstructions of temperature change (black circles), including published uncertainties (vertical bars), for the MPWP (Stage KM5c), as synthesized by [PlioMIP data paper]. Coloured lines show the modelled zonal mean surface air temperature difference compared with preindustrial for 4 models from the PlioMIP ensemble [(b) proxy reconstructions of temperature change (black circles), including published uncertainties (vertical bars), for the early Eocene (EECO), as synthesized by Hollis et al. (submitted). Coloured lines show the modelled zonal mean surface air temperature difference compared with preindustrial. for 4 models from the DeepMIP ensemble (c) proxy reconstructions of temperature change (coloured filled circles) for the MPWP (Stage KM5c), as synthesized by [PlioMIP data paper]. Background colours show the mean surface air temperature difference compared with preindustrial for the ensemble mean of the PlioMIP ensemble (d) proxy reconstructions of temperature change (coloured filled circles) for the early Eocene (EECO), as synthesized by Hollis et al (submitted). Background colours show the mean surface air temperature difference compared with preindustrial for the ensemble mean of the DeepMIP ensemble.

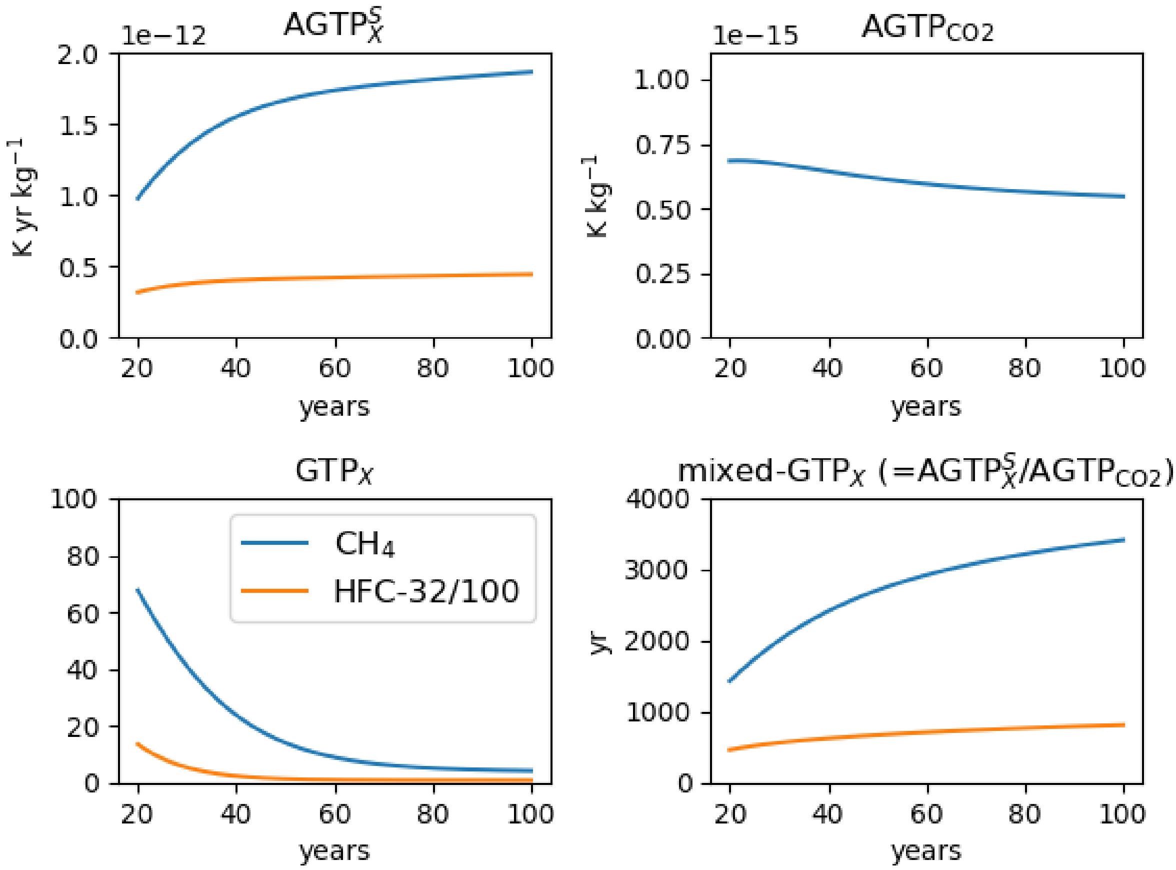

Figure 7.29: Climate metrics for two SLCFs: HFC-32 and CH_4, (lifetimes of 5.2 and 12.4) years. (a) temperature response to a step change in SLCF emission. (b) temperature response to a pulse CO_2 emission. (c) conventional GTP metrics (pulse vs pulse). (d) mixed-GTP metric (step vs pulse).

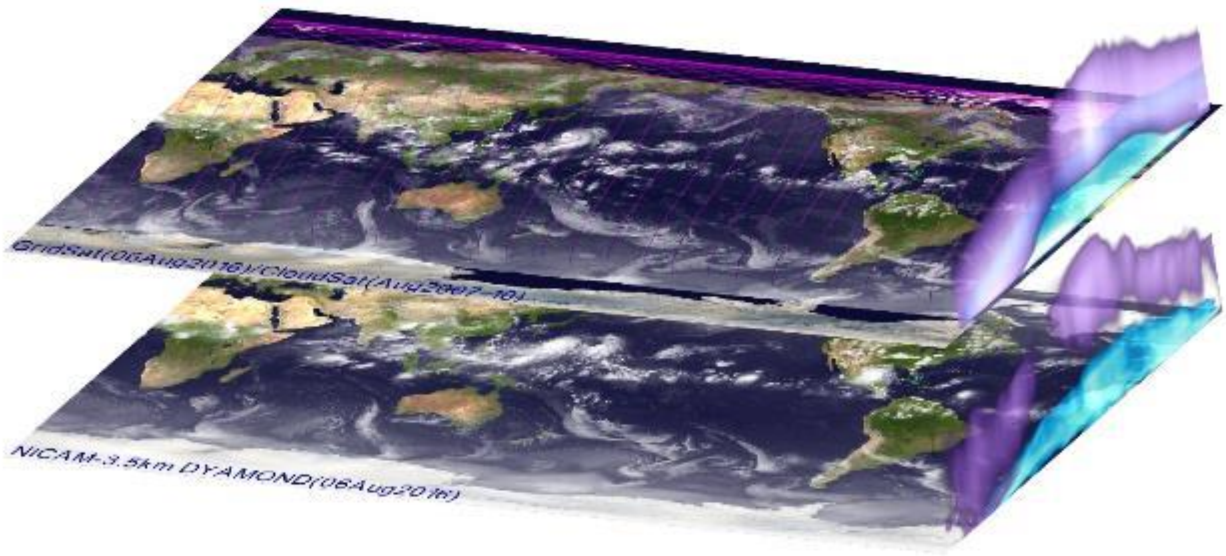

FAQ7.1, Figure 1: Global view of infrared brightness temperature (T_{bb}) on 6 August, 2016, and monthly- and zonal-mean cross section of cloud liquid (blue) and ice (purple) contents. T_{bb} has a low value where cloud covers surface and is used as a measure of cloud distribution from space. (Top) Satellite observations and (bottom) a global cloud-resolving simulation using 3.5 km NICAM. Colors are the same between the two panels. Thin purple curves in the top panel show the satellite paths along which the zonal mean is calculated.

References

Andrews, T., Gregory, J. M., Paynter, D., Silvers, L. G., Zhou, C., Mauritsen, T., et al. (2018). Accounting for Changing Temperature Patterns Increases Historical Estimates of Climate Sensitivity. *Geophys. Res. Lett.* 45, 8490–8499. doi:10.1029/2018GL078887.

Armour, K. C. (2017). Energy budget constraints on climate sensitivity in light of inconstant climate feedbacks. *Nat. Clim. Chang.* doi:10.1038/nclimate3278.

Armour, K. C., Siler, N., Donohoe, A., and Roe, G. H. (2019). Meridional Atmospheric Heat Transport Constrained by Energetics and Mediated by Large-Scale Diffusion. *J. Clim.*

Caldwell, P. M., Zelinka, M. D., Taylor, K. E., and Marvel, K. (2016). Quantifying the sources of intermodel spread in equilibrium climate sensitivity. *J. Clim.* 29, 513–524. doi:10.1175/JCLI-D-15-0352.1.

Cheng, L., Abraham, J., Hausfather, Z., and Trenberth, K. E. (2019). How fast are the oceans warming? *Science (80-.).* 363, 128–129. doi:10.1126/science.aav7619.

Cowtan, K., and Way, R. G. (2014). Coverage bias in the HadCRUT4 temperature series and its impact on recent temperature trends. *Q. J. R. Meteorol. Soc.* 140, 1935–1944. doi:10.1002/qj.2297.

Goosse, H., Kay, J. E., Armour, K. C., Bodas-Salcedo, A., Chepfer, H., Docquier, D., et al. (2018). Quantifying climate feedbacks in polar regions. *Nat. Commun.* doi:10.1038/s41467-018-04173-0.

Klein, S. A., Hall, A., Norris, J. R., and Pincus, R. (2017). Low-cloud feedbacks from cloud-controlling factors: A review. *Surv. Geophys.* 38, 1307–1329. doi:https://doi.org/10.1007/s10712-017-9433-3.

Loeb, N. G., Doelling, D. R., Wang, H. L., Su, W. Y., Nguyen, C., Corbett, J. G., et al. (2018). Clouds and the Earth's Radiant Energy System (CERES) Energy Balanced and Filled (EBAF) Top-of-Atmosphere (TOA) Edition-4.0 Data Product. *J. Clim.* 31, 895–918. doi:10.1175/Jcli-D-17-0208.1.

Loeb, N. G., Wang, H., Cheng, A., Kato, S., Fasullo, J. T., Xu, K.-M., et al. (2016). Observational constraints on atmospheric and oceanic cross-equatorial heat transports: revisiting the precipitation asymmetry problem in climate models. *Clim. Dyn.* 46, 3239–3257. doi:10.1007/s00382-015-2766-z.

Mauritsen, T. (2016). Global warming: Clouds cooled the Earth. *Nat. Geosci.* 9, 865–867. doi:10.1038/ngeo2838.

Meinshausen, M., Raper, S. C. B., and Wigley, T. M. L. (2011). Emulating coupled atmosphere-ocean and carbon cycle models with a simpler model, MAGICC6 – Part 1: Model description and calibration. *Atmos. Chem. Phys.* 11, 1417–1456. doi:10.5194/acp-11-1417-2011.

Nauels, A., Meinshausen, M., Mengel, M., Lorbacher, K., and Wigley, T. M. L. (2017). Synthesizing long-term sea level rise projections -- the MAGICC sea level model v2.0. *Geosci. Model Dev.* 10, 2495–2524. doi:10.5194/gmd-10-2495-2017.

Rayner, N. A., Parker, D. E., Horton, E. B., Folland, C. K., Alexander, L. V., Rowell, D. P., et al. (2003). Global analyses of sea surface temperature, sea ice, and night marine air temperature since the late nineteenth century. *J. Geophys. Res.* 108, 4407. doi:10.1029/2002JD002670.

Richardson, T. B., Forster, P. M., Smith, C. J., Maycock, A. C., Wood, T., Andrews, T., et al. Efficacy of climate forcings in PDRMIP models.

Shell, K. M., Kiehl, J. T., and Shields, C. A. (2008). Using the Radiative Kernel Technique to Calculate Climate Feedbacks in NCAR's Community Atmospheric Model. *J. Clim.* 21, 2269–2282. doi:10.1175/2007JCLI2044.1.

Smith, C. J., Forster, P. M., Allen, M., Leach, N., Millar, R. J., Passerello, G. A., et al. (2018a). FAIR v1.3: A simple emissions-based impulse response and carbon cycle model. *Geosci. Model Dev.* doi:10.5194/gmd-11-2273-2018.

Smith, C. J., Kramer, R. J., Myhre, G., Forster, P. M., Soden, B. J., Andrews, T., et al. (2018b). Understanding Rapid Adjustments to Diverse Forcing Agents. *Geophys. Res. Lett.* 45. doi:10.1029/2018GL079826.

Trenberth, K. E., and Stepaniak, D. P. (2003). Seamless poleward atmospheric energy transports and implications for the Hadley circulation. *J. Clim.* doi:10.1175/1520-0442(2003)016<3706:SPAETA>2.0.CO;2.

Wild, M., Folini, D., Hakuba, M. Z., Schär, C., Seneviratne, S. I., Kato, S., et al. (2015). The energy balance over land and oceans: an assessment based on direct observations and CMIP5 climate models. *Clim. Dyn.* 44, 3393–3429. doi:10.1007/s00382-014-2430-z.

Wild, M., Hakuba, M. Z., Folini, D., Dörig-Ott, P., Schär, C., Kato, S., et al. (2019). The cloud-free global energy balance and inferred cloud radiative effects: an assessment based on direct observations and climate models. *Clim. Dyn.* doi:https://doi.org/10.1007/s00382-018-4413-y.
Zelinka, M. D., Andrews, T., Forster, P. M., and Taylor, K. E. (2014). Quantifying components of aerosol-cloud-radiation interactions in climate models. *J. Geophys. Res. Atmos.* 119, 7599–7615. doi:10.1002/2014JD021710.
Zhou, C., Zelinka, M. D., and Klein, S. A. (2016). Impact of decadal cloud variations on the Earth's energy budget. *Nat. Geosci.* 9, 871–874. doi:10.1038/ngeo2828.
Zhou, C., Zelinka, M. D., and Klein, S. A. (2017). Analyzing the dependence of global cloud feedback on the spatial pattern of sea surface temperature change with a Green's function approach. *J. Adv. Model. Earth Syst.* 9, 2174–2189. doi:10.1002/2017MS001096.